國立臺灣大學生物資源暨農學院生物產業機電工程學系

博士論文

Department of Bio-Industrial Mechatronics Engineering

College of Bioresources and Agriculture

National Taiwan University

Doctoral Dissertation

應用往復式微流體於適體篩選、電化學感測
與電鍍效率增強之研究

Efficiency enhancements of aptamer selection,

electrochemical sensing and electrodeposition

by microfluidic shuttling

翁瑞鴻

Jui-Hong Weng

指導教授：陳林祈 博士

Advisor: Lin-Chi Chen, Ph.D.

中華民國 108 年 7 月

July 2019

國立臺灣大學博士學位論文
口試委員會審定書

應用往復式微流體於適體篩選、電化學感測與電鍍效率增強之研究

Efficiency enhancements of aptamer selection, electrochemical sensing and electrodeposition by microfluidic shuttling

本論文係 翁瑞鴻 君（D01631002）在國立臺灣大學 生物產業機電工程 學系、所完成之博士學位論文，於民國 108 年 7 月 16 日承下列考試委員審查通過及口試及格，特此證明

口試委員：

_____（簽名）

（指導教授）

張敏膀　　　　　魏志坤

盧彥文　　　　　謝博全

林正嵐

系主任、所長 _____（簽名）

致謝

　　人生不僅僅在於完成了多少成就，每一點滴的經歷都造就了我們的未來發展。在生機系這個大家庭中度過了許多重要的時光，13 年的日子裡，從懵懂學習到獨立自主。能有機會獲得如此的成長，除了要感謝各位師長與同學們的友善幫助，也要歸功於生機系自由開放、跨領域的研究學習環境。自從大三的夏天加入陳林祈老師的實驗室開始，我的研究之路也就此展開。沒想過會走上學術這條路的我，在實驗室學長姐的耳濡目染與陳老師的諄諄教誨下，對研究居然也玩出了興趣。被陳老師對研究的熱情所點燃的心，也讓我毅然決然地選擇攻讀碩士與博士班。除了學術上的指導，在人生的道路上，陳老師也宛如一展散發溫暖光芒的明燈，時時刻刻的給予建議與分享哲學體悟，讓我能有機會接觸到許多新事務。從一個人出國開會、管理實驗室帳務、籌辦研討會等，豐富了我的研究生生涯，也讓我學習到許多有趣的能力。雖然在博士班的求學過程中，一度有不務正業的接觸其他事務而耽誤了學位論文的進展，讓陳老師為我的畢業感到擔憂，真的感到很抱歉。但就像口試後，陳老師與我分享的"木魚與佛像"的故事，這些付出的時間會有它的價值。將博士班念到最後一刻，說起來很不好意思，但其中的經歷與收穫我覺得值得。

　　感謝洪敏勝教授、林正嵐教授、魏培坤教授、盧彥文教授以及謝博全教授擔任我的論文指導委員並撥冗參與口試，對於論文的統整與研究的細節提供了許多的建議與指導，讓我能更深的思考自己的研究。此外，也要感謝歐陽又新教授、李允中教授、賈精石技正與林益源技佐在機械加工技術上的指導，讓我能有機會精進各種加工方法。謝謝一路走來的好兄弟培鈞，引領我進入微機電的世界，也成為我實驗討論的好夥伴。謝謝 403 實驗室十多年來的各位夥伴，有電化學領域的專家(祥富、任遠、鴻昀、煥庭、誠專、伊敏、柔宣、奇翰、禮丞、唯里、聖丰)，也有生物領域的翹楚(業興、鈞瑋、登凱、紹任、育恩、蕙妤、修瑋、佩瑋、婉茹、惟甄)，除了在學術上的研討，與大家經歷每年的聖誕派對、熬夜趕實驗、出遊玩樂等點滴，都將成為我人生的重要回憶。

　　最後，要感謝我的家人與朋友。謝謝我的家人們一直以來的關心與支持，讓我能持續充滿正面能量的迎接各種挑戰，成為我挫折時的避風港，為我充飽電後繼續出發。也謝謝朋友們好事的督促，讓我的論文進度能急起直追。雖然門票到手，但真正學術研究的路才要開始，乘載著各位的祝福，我會全力以赴的！
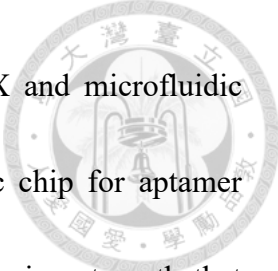
中文摘要

　　微流體平台是近年來廣為利用的化學、生物分析技術，其優點在於具備微量樣本與試劑的精準操控與自動化控制的發展潛力，可將傳統的各種分析技術優化並整合與微小晶片中。但隨著研究需求的增加，微流體平台的複雜度快速提升，許多新穎的結構設計與操作元件被附加上去。雖然有助於繁複的實驗操作，但也產生複雜的晶片製作程序與不友善的操作需求，這將不利於微流體分析技術與實場應用的拓展。因此，近年來有許多研究針對微流體平台的系統進行簡化，像是利用 paper-based 或 pump-free 等技術發展微型化感測應用。然而，如何有效的利用微流體的優勢並改善其層流限制仍是相當重要的議題。本研究提出以往復式微流體的操作策略進行層流效應與混合效應的探討。以簡單的微流道結構設計搭配彈性的微流體操作系統來取代繁雜的晶片設計，此微流體平台將具有更靈活的應用空間。針對此平台活用之微流體特性，將其應用於三種技術進行驗證與探討：適體篩選、電化學感測、電鍍製程。在適體篩選中，整合 single-bead SELEX 與微流體平台發展微珠陣列微流體晶片用於蛋白質適體篩選。往復式的流體輸送的確能增進結合速率與分離強度，使篩選效能提升。以 STAT3 作為標的，成功的篩選出具專一性與親和力的適體，且具有癌細胞基因調控的能力。在電化學感測應用中，微電極表面的氧化還原反應受到流動操作的影響，產生流動極化(flow-polarization)與促進質傳(facilitated mass transfer)的效果。此現象將增幅電化學訊號響應，並提升其感測靈敏度。在電鍍製程應用中，原先不穩定的普魯士藍(Prussian blue, PB)電鍍薄膜，在溶液流動狀態造成的表面物質更新與薄膜沖刷下，結構穩定的 PB 薄膜可以更牢固的貼附於電極上，以利後續的生化感測應用。針對微流體輸送產生之效應加以利用並改善微流體技術之限制，本平台之發展將有利於微流體應用之拓展。

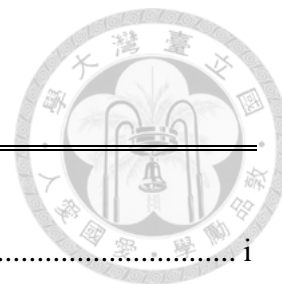關鍵字：適體、電化學感測、電鍍、往復式微流體、流動效應

Abstract

Microfluidic platform is a widely-used technology for chemical and biological analysis in the recent years. Its advantages include the precise modulation on micro-scale of samples and reagents and the potential of automatic controlling. The traditional analysis techniques can be optimized and integrated into a tiny chip. But, with the increasing needs of researches, the microfluidic platform becomes more complex, and a variety of novel structure design and operation units are embedded into the chip. Although the delicate chips benefit to operate the complicated experiment, the drawbacks like the difficult chip fabrication and un-friendly operation requirement still limit the development of microfluidic analysis in on-site application. Therefore, many researches focus on the simplification of microfluidic platform, for example, using paper-based or pump-free technology to develop miniaturized sensors. However, how to efficiently utilize the superiority of microfluidics and improve the limitation of laminar flow is still an attractive issue. In our study, the strategy of microfluidic shutting is proposed to explore the laminar flow effect and the mixing effect. Combining a simple microchannel structure and a convenient microfluidic operating system to replace the complicated chip design, this platform have a more flexible space of application. Aiming to the features of microfluidics which can be wisely used in this platform, three kinds of technology is applied to verify the assumption: aptamer selection, electrochemical sensing and
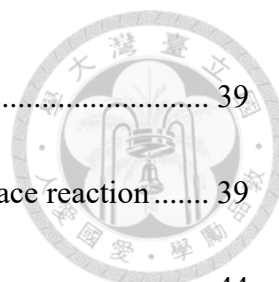
electrodeposition. In the aptamer selection, the single-bead SELEX and microfluidic platform are integrated to develop a microbeads-array microfluidic chip for aptamer selection. Shuttling liquid can enhance the binding rate and partitioning strength that improve the selection performance. STAT3-specific aptamers are identified with high specificity and affinity, and they show the ability of gene regulation in the cancer cell apoptosis. In the electrochemical sensing, the redox reaction on the microelectrode surface is influenced by flowing operation, and it produces the flow-polarization and facilitated mass transfer effects. This phenomenon can increase the electrochemical response and improve the sensitivity. In the electrodeposition, the Prussian blue film formed by electrodeposition is unstable under flowing condition. With the component refreshment on surface and film polishing which are caused by flowing liquid, the structure-stable PB film can firmly attach on the electrode that is beneficial to the following biosensing applications. Taking advantage of the effect generated by microfluidic transportation to improve the limitation of microfluidic technology, this platform shows the potential of expanding the current microfluidic applications.

Keywords: aptamer, electrochemical sensing, electrodeposition, microfluidic shuttling, flow effect

Contents

List of Figures

List of Tables

Chapter 1. Introduction

Microfluidic applications are widely-explored in many fields like the precious sample preparations, the simplification of complicated processes, and portable sensor developments. Among the diverse applications, DNA aptamer evaluation and symmetric electrochemistry are two attractive research topics in recent years. They exist the challenges of lengthy procedures and miniaturization requirement in micro-/nano-liter sample handling. The laminar characteristics in microchannels don't only limit the reaction efficiency in microfluidic, but also produce more possibilities of the assay improvement. Hence, many laminar-destroyed strategies are presented to achieve the micro-mixing. On the other hand, more and more researches make good use of the laminar features, for example, the hydrodynamic focusing and gradient generator. Both ways provide great potential to expand microfluidic applications.

Among the various paths to seek the possible solutions, we start with the shuttle flow which is one of the micro-mixing methods. Unlike other micro-mixing methods with complicated structure designs, transporting liquid back and forth repeatedly only needs a simple pump operation. To explore the shuttle flow effects, the aptamer selection and the symmetric electrochemistry are performed. Shuttle flow will enhance the interaction between DNAs and proteins, and it will also increase the partitioning strength to generate high-affinity aptamers. The dynamic electrochemical features on electrode surface are

1
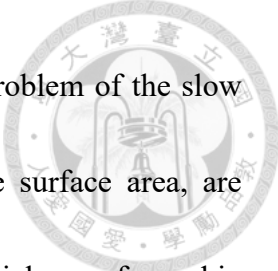
obtained under the flowing modes which induce an actively-refreshing effect.

In the following paragraphs, firstly, we will introduce how the modulation of liquid transporting enhance the reaction. Secondly, the niches of the aptamer development and how to execute the selection in an efficient way are mentioned. Finally, the state-of-the-art electrochemical biosensors for on-site applications are discussed.

1.1 Modulation of liquid transporting for reaction enhancement

Solution is the most common place for biomolecular reactions. The most of molecules can be dissolved in water to well interact with each other. But, as we know, when a solution is dropped into another, the reaction only happens around the drops until the drops are dispersed in the whole solution. According to the collision theory, a successful reaction carries out as the molecules have an effective collision. Therefore, the traditional solution-based reactions in the static state are slow because the rates are depended on the molecular diffusion. Stirring is an easy way to increase the reaction rate in a static and closed system. That's why we usually use the stirring bar to speed up the powder dissolving and to mix the solutions in the liquid-to-liquid reaction.

Liquid-to-solid interaction is another general situation of solution-based reaction. When the solution contacts the solid material, a surface reaction occurs to generate new substances. After the contents nearby the surface are depleted, the unreacted molecules

2

have to diffuse to the surface for a complement. To overcome the problem of the slow

reaction, the nanoparticle techniques, which considerably raise the surface area, are

widely developed in recent years. Several metal and non-metal material are reformed in

nano-scale like gold nanoparticle (gold NP), carbon nanotube (CNT) and Prussian blue

nanoparticle (nanoPB). Although the nanoparticles can improve the reaction efficiency,

they are too tiny to reserve and handle for demanding operation. So, the researchers begin

to immobilize the nanoparticles onto solid support like an electrode. Back to the origin,

the problem of how to enhance the liquid-to-solid reaction still exists. Fortunately, the

rotor disk electrode (RDE) is invented to provide a hydrodynamic condition for

electrochemical reactions. Unlike the stationary electrode, the rotating electrode of RDE

makes the solution flowing to replace the boundary layer around the electrode surface. It

causes facilitated diffusion to enhance the reaction. Jan Prasek *et. al* also proposes a new

hydrodynamic electrochemical arrangement that immerses an electrode in rotating conic

vessel containing reaction solutions (Prasek *et al.*, 2006). The current response can be

significantly improved in this hydrodynamic system. In biofuel cells, liquid transportation

also plays an important role that the flowing liquid can enhance the reaction to produce

more energy. If the biofuel cell runs in a close and stationary system, the efficiency of

energy production will be restricted due to the limited biofuel and diffusion effect.

Exchanging the reacted waste and fresh substance in the biofuel cell with an external

3

pump can increase the output power. It can be attributed to the proactive replacement of materials and hydrodynamic phenomena.

As a result of the interesting feature in hydrodynamic, the signal response obtained by flow injection analysis (FIA) provides much meaningful information. Just like the typical sensor fabrication, nanoparticles and reactants are fixed on the electrodes, and then the samples in solution are injected into the flow cell. When the samples flow through the electrode, they will interact with electrodes that lead to a peak in real-time. The peak heights are related to the sample concentration and reaction activity. It is convenient to measure the samples with tiny volumes by the FIA. However, the hydrodynamics in microfluidic still shows some difference. The laminar flow leads to some unique characterizations even during the flowing conditions. The details will be discussed in the following sections.

4

1.2   Efficient DNA aptamer selection

Aptamers are antibody-mimic biomolecules which can specifically bind to their targets. They are usually composed of DNAs or RNAs, which have four kinds of elements (ATCG or AUCG) to form various sequences and structures. Under particular buffer conditions, aptamers can fold into a secondary structure and show the key-and-lock feature to recognize the diverse targets like ions, proteins, cells, and tissues. High thermos-stability and easy synthesis are common advantages of the aptamers. Therefore, aptamers have a great potential to assist even replace the traditional antibodies in current bioassays and biosensors. The components of the aptamer are oligonucleotides that make them easy to label functional groups at both terminals and easy to get into cells because of the tiny size. According to the above superiorities, aptamers are widely applied to the development of biosensors and DNA drugs. The labeled aptamers can be immobilized on various material surfaces that play a role as probes to specifically bind to the targets. The DNA-target binding will induce the following reaction and the sensing mechanism. To generate excellent aptamers, systematic evolution of ligands by exponential enrichment (SELEX) is a typical method since 1987. A synthesis DNA library with random sequences is used to create an enormous variety of DNA structures and binds to the target. The bound DNAs and unbound DNAs are separated, and then the bound DNAs are enriched by polymerase chain reaction (PCR) to enlarge the dominant groups for the next selection

5
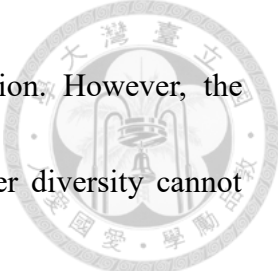
round. After several SELEX rounds, the sequences should become convergent, and it

means that some leading aptamer candidates emerge. The known sequences are verified

with a serial of validation experiments in order to identify the affinity and specificity.

SELEX typically contains a lot of steps including library generation, hybridization,

partitioning, amplification and ssDNA isolation. To generate an effective aptamer, it

needs to cost much time, money and labors to carry out the complicated processes. So,

how to improve selection efficiency becomes a major issue in the aptamer research.

● Smart designs of DNA libraries

According to Darwin's theory of evolution, an initial group with sufficient diversity

is necessary for the starting selection. With the specific filter conditions, only the most

suitable one can be saved, and the others are eliminated. For aptamer selection, the

original DNA library usually consists of a random region and two primer sites at both

terminals. The primer sites are designed for the PCR amplification, which can enrich the

selected groups. To ensure that the sequences are duplicated correctly, the primer dimer

should be prevented during the PCR process. Further, because the primers are involved

in the library throughout the whole selection, different primer pairs may lead to different

diversity. If the primers are directly deleted for the aptamer truncation, the affinity of

truncated aptamers could be distinct. The random region plays a major role in determining

library diversity. With a library containing 30 random bases (N30), about 10^{18} ($4^{30} = 2^{60}$

6

= 10^{18}) kinds of DNA sequences are generated in a stock solution. However, the recommended diversity for aptamer selection is 10^{15}, because lower diversity cannot create enough variation but higher diversity causes the poor sequence convergence. Hence, it's really a dilemma issue to choose an initial library with suitable diversity.

Sequence-constructive SELEX, which is developed by Wang *et. al*, is a novel strategy for screening DNA aptamer (Wang *et al.*, 2014a). A beginning library with a 15-base random region is chosen to accomplish the first SELEX procedure. It can ensure that all kinds of sequences will attend the selection. In the second round SELEX, the best sequence selected in the first round extends with 7 bases at both sides. It provides an additional diversity to carry out the aptamer selection. The same procedure as described for the second round is performed in the third round SELEX. Finally, the aptamer containing a 43-base core region is identified through the stepwise sequence-constructive SELEX. Another smart library design is proposed by Wang *et. al* that the individual DNAs are encapsulated in water-in-oil emulsion (Wang *et al.*, 2014b). Each emulsion contains a unique sequence to form aptamer particles (AP) after the emulsion PCR process. The APs incubate with fluorescence-labeled targets, and then the DNA-target complex will be sorted by fluorescence-activated cell sorting (FACS) to isolate the high-affinity aptamers. Instead of the mixed library, the design of one-sequence-one-particle performs a direct hybridization with targets. Further, this design can prevent PCR bias in order to preserve

7

the correctness of amplified sequences.

● *In silico* post-SELEX

Due to the sequence diversity and primer effect, you can always find a better aptamer for the same target. After the aptamer is identified by the complicated wet-bench SELEX process, the following validations of the aptamer affinity and specificity are necessary to verify the aptamer performance. In general, we can get the performance by using the typical biological assays like enzyme link oligonucleotide assay (ELONA), capillary electrophoresis (CE), electrophoretic mobility shift assay (EMSA), surface plasmon resonance (SPR), microarray, and so on. However, the above assays are time-consuming and labor-consuming, and they aren't suitable for a high throughput affinity measurement. To save the cost, the *in silico* methods are raised that the 3D structures of the aptamers and targets are predicted by software in order to simulate the interaction between each other (Jolma *et al.*, 2010). According to the calculated results, the pseudo affinity of aptamers can be evaluated, and the simulated molecular docking models reveal the possible binding domain. Additionally, the sequence alignment of the aptamer candidates for the same target is used to find out the special motif in the high-affinity aptamer. Optimization of the existing aptamers is a shortcut to create a better aptamer. If the known sequence is synthesized with the partial mutation, a re-constructive DNA library with artificial diversity is presented for a post-SELEX (Gao *et al.*, 2016).

8
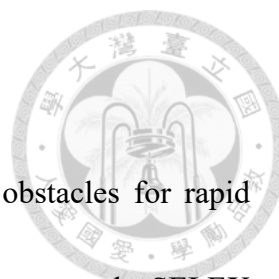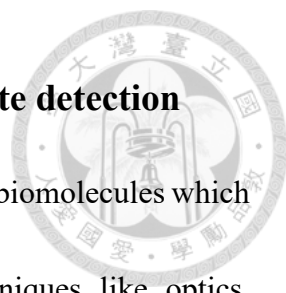
- Microfluidic SELEX

Complicated procedures in the aptamer selection are serious obstacles for rapid aptamer generation. Therefore, how to simplify the procedures or to automate the SELEX rounds are very valuable researches for achieving the efficient selection. Automated SELEX is the intuitive idea that an automated workstation is adapted for liquid sample transfer. But, workstation usually needs much space and requires hard settings. In addition to the automatized potential, the microfluidic technique can demonstrate the possibility of decreasing the size of the SELEX system. The microline-based system consists of controllable valves and a pump source. The microfluidic sample can be transported to the specified regions for the various selection procedures. In fact, there are more advantages to applying microfluidic to aptamer SELEX. In microfluidics, although the laminar flow restrains the efficiency of the DNA-target interaction, the high concentration due to the tiny volume still provide a rapid binding reaction. Even more, in the nanochannel, the reduced diffusion length results in an increasing collision frequency, and it leads to a faster interaction rate. To separate the weak bound and high-affinity aptamers, the microfluidic platforms can provide higher selection strength to refine the better aptamers. The development of microfluidic PCR chips is also widespread because it doesn't only reduce the size, but also shorten the time of PCR reaction.

9
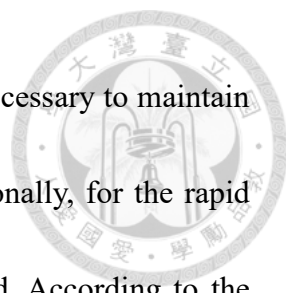
1.3   Miniaturized electrochemical biosensors for on-site detection

Biosensors are designed to recognize and quantify the particular biomolecules which are relative to diseases or environment pollutions. Various techniques like optics, thermodynamics, mechanics, magnetics and electrochemistry are studied to develop novel and robust biosensors. With the increasing demand for on-site and real-time diagnosis, the portable and miniaturized biosensors become attractive in recent years. Among the biosensor techniques, the electrochemical sensors (EC-sensors) are the most suitable method to reach the above purpose. The reactions happened on the electrode surface are measured in a short time, and the sensors have good sensitivities. Furthermore, with the benefit of micro-electromechanical systems (MEMS) development, electrodes can be scale-down to the micro or nano electrodes that greatly decrease the sensor volume. Glucose meter is just a practical case which has the well-developed instrument for signal processing and shows the feasibility of the mini-electrochemical biosensor.

Electrochemical detection comprises potentiometric, amperometric and impedimetric analysis, and all of them are based on the electrode reactions. The typical electrochemical system is based on the three-electrode configuration that contains a working electrode (WE), a counter electrode (CE) and a reference electrode (RE). However, this configuration results in an unstable measuring condition because the distances between electrodes are critical factors. Especially, for the on-site sensing

10
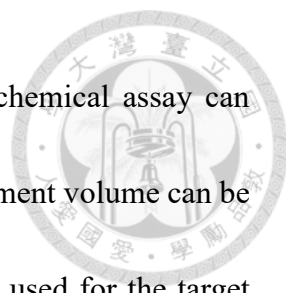
demand, the environment of analytes may be complicated, so it is necessary to maintain the consistent electrode configuration for reliable detection. Additionally, for the rapid examination, the lengthy experimental operation should be avoided. According to the above requirements, several techniques are developed to meet the need of the electrochemical sensors for on-site detection.

- Label-free electrochemical sensors

Label-free sensor is a novel strategy for the biomolecule quantification which can directly detect the target without any labels. In the traditional biomolecule measurement, the stable isotope compounds are labeled on the targets to enhance the signal because the size of the molecule is too tiny to observe in the common bioassays. However, not only the hazardous risk of an operating isotope is concerned, but also the labeled molecules may induce the feature change of the original targets. To eliminate the label requirement, the techniques based on explicit and sensitive instruments are developed for quantifying the original property of the targets. The difference in the size, mass or charge can be precisely measured and correlated to the target concentration. For example, mass spectrometry (MS) and surface plasma resonance (SPR) are well-known assays that use mass-to-charge ratio (m/z) and reflection angle (θ) as indicators respectively for the label-free detection.
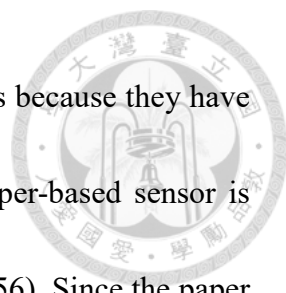
To measure the traces of targets precisely, the instruments usually have large

11

volumes and complicated control systems. In contrast, the electrochemical assay can

measure the original samples without additional labels, and its instrument volume can be

miniaturized into a chip. In the electrochemical sensing, the probes used for the target

recognition and binding are immobilized on the electrodes with various chemical

mechanisms. When the targets bind to the probes on the electrode surface, the surface

properties will be changed due to the electrostatic force and geometry obstruction. For

instance, three kinds of general electrochemical assays are mentioned below. (i) The

potentiometric sensor is a typical label-free electrochemical sensing platform for ions

measurement. Ion-selective electrode (ISE) like the pH meter can estimate the ions

concentration difference contributed from the biological reaction. (2) The amperometric

sensors use a soluble redox mediator as the reporter and mix analytes and mediators just

before dropping the mixture on the modified electrodes. The analyte-probe binding leads

to a barrier that limits the diffusion of the redox mediator to the electrodes. (3) In the

impedimetric assay, the slight interaction of analytes and probes can carry about obvious

impedance changes. It performs high sensitivity and label-free detection. Without the

complicated and lengthy molecule-labeling procedures, the label-free electrochemical

sensor can achieve rapid on-site detection.

● Paper-based electrochemical sensors

　　Paper is a common material for multiple applications. In recent years, paper-based

sensors draw much attention for developing the disposable test strips because they have the advantages of flexibility, versatility and low cost. The first paper-based sensor is demonstrated for semi-quantification of glucose in urine (Comer, 1956). Since the paper chromatography is invented for the rapid diagnosis in 1956, more immunochromatographic paper test strips are performed for different applications. The pregnancy test kit is a well-known example of approving the feasibility. The test paper contains a sample pad, a reagent pad, and a test line. As the urine is loaded to the sample pad, the liquid will migrate along the test line via the capillary force. When the samples flow through the probes fixed on the paper, they will be captured and generate the color change. According to the chromatographic spectrum, particular biomarkers can be detected and semi-quantified. But, this paper-based colorimetry is hard to calculate the precise concentration because the reading of color is subjective. Further, the reaction rate is limited by the diffusion of the samples.

The paper-based electrochemical sensor is widely developed on account of the screen printing technique. The conductive materials like carbon and silver are screen printed on the papers with electrode patterns. The features of high sensitivity and fast response in electrochemistry make the paper-based sensor more useful in rapid diagnosis. Moreover, the screen printing procedure is good for mass production, and it can reduce the cost of test chips. In reason of the cheap disposable test chip that prevents cross-

contamination, paper-based electrochemical sensors are suitable for developing the on-site detection.

- Microfluidic electrochemical sensors

In the last two issues mentioned in previous paragraphs, the electrochemical sensors show a lot of superiorities including high sensitivity, rapid response and label-free assays. To accomplish the purpose of miniaturizing sensors, the electrochemical sensors are integrated into the microfluidic chips. In microfluidics, the features of the liquid are so different compared to conventional electrochemistry in bulk solutions. The theory of typical electrochemistry may need some modification in this microscale laminar flow. The fabrication of microelectrodes is a key point to develop microfluidic electrochemical sensors. The complicated manufacturing procedures based on MEMS technique are performed to produce the tiny electrodes with good quality. After the microelectrodes are prepared, for biosensor applications, the biomolecules or nanomaterials are immobilized on the electrodes for the functional modification. The modified microelectrodes are assembled with microfluidic chips to control the tiny volume samples from the inlet to the detection region. However, the microelectrode fabrication of the traditional three-electrode structure is complex, especially the reference electrode. A simplified configuration – symmetric electrodes is proposed to solve this problem for efficient on-site detection.

14

1.4 Objectives

In this study, we aim to expand the possible applications of the microfluidic chips under flowing operations. Based on the advantage of channel-based reactor, which has short diffusion length for the rapid molecule interaction, the microfluidic reaction is carried out under the shuttle flow in order to enhance the efficiency. According to the dynamic responses obtained from the flowing-mode reaction, three flow effects including shuttle mixing, surface refreshment, and shearing effect are proposed to attempt to elaborate on the reasons for reaction enhancement under flowing conditions. Using the concept of microfluidic shuttling, the efficiency enhancement is achieved in three kinds of biochemical applications involving aptamer SELEX, electrochemical sensing, and electrodeposition. Combined or individual flow effects are expected to be found and verified in each research. With the improved performances like high-specificity aptamer identification, increasing electrochemical sensitivity, and high-charge-density film, the microfluidic shuttling is proven to be a valuable platform to produce the critical elements for the development of label-free electrochemical biosensors. The research framework is shown in Fig. 1.1.
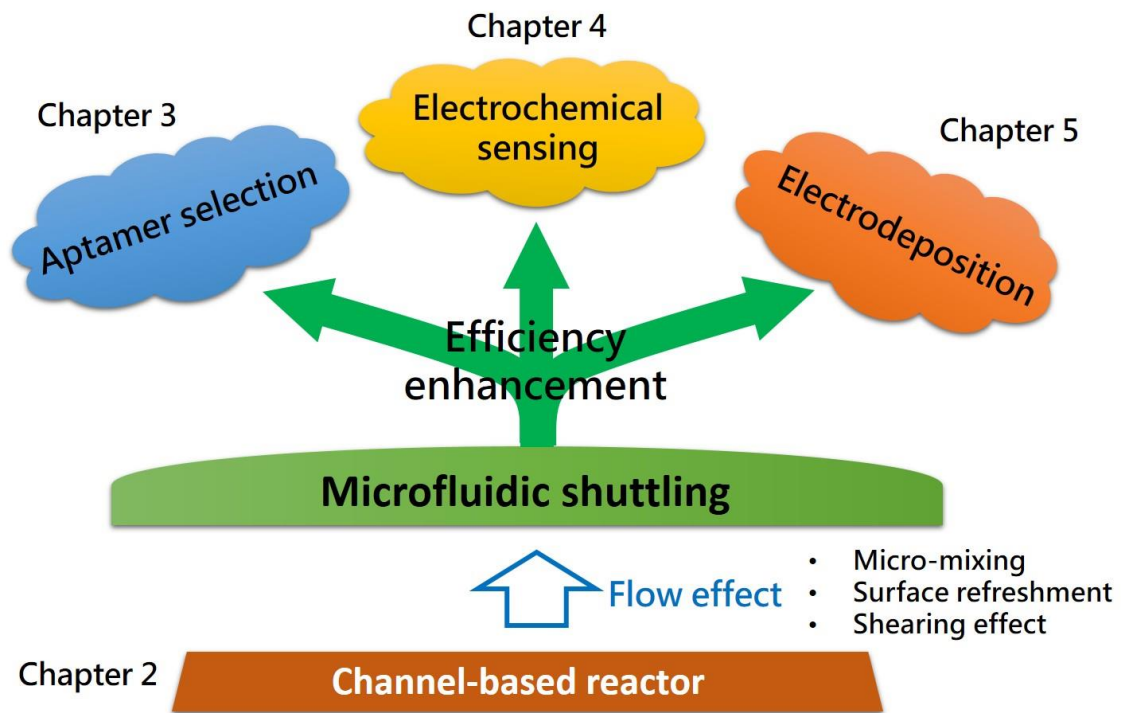
Figure 1.1 The research framework of this study. Based on the channel-based reactor, the characterization of microfluidic shuttling is explored, and three flow effects are proposed to explain the reaction enhancement in the applications of aptamer selection, electrochemical sensing, and electrodeposition.
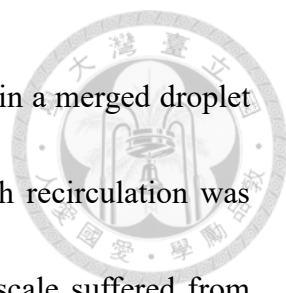
Chapter 2. The flow effects in the channel-based reactor

2.1　Introduction

Inspired by the research that Cheng *et. al* published in 2005, we are interested in the

flow effects on the fluidic reactions. Their works proposed a microfluidic device which

reduced the sample volume to 1 µl and the hybridization time to 500s for the DNA

microarray application (Wei *et al.*, 2005). A flat glass microarray was integrated with a

PMMA chip containing a serpentine microtrench, and continuous samples plugged into

the microchannel that formed discrete short plugs. The plugs were shuttled back and forth

across the microarray spots that considerably improved the DNA hybridization. Instead

of the long reaction time normally taking over 12 hours (overnight) in traditional DNA

microarrays (Stillman and Tonkinson, 2001), the shuttle hybridization provided a chaotic

advection mixing caused by the shearing interaction of the fluid in the plug with the wall

of the microchannel. The enhanced DNA hybridization was used to discriminate single-

base mismatch, and the detection limit of 19 amole was beneficial to study the gene

expression. In 2010, Huang *et. al* also presented a novel microfluidic device integrated

with microvalves and micropumps for rapid DNA hybridization using shuttle flow

(Huang *et al.*, 2010b). This device shortened the hybridization time to 90s and lowered

detection limit to 100 pM. The fast mixing performance depending on shuttle flow was

demonstrated through mixing water and dye indicator in the microchannel.

17

Some researchers also posed the shuttle mixing effect of flows in a merged droplet (Hosokawa *et al.*, 1999; Sassa *et al.*, 2008). A moving droplet with recirculation was proven to be potent for enhancing the mixing speed in the micro-scale suffered from diffusion limit. Besides of the droplet mixing attributed by shuttle flows, presumably, the moving liquid could lead to the overall influence of liquid reactions under diffusion-limited situations whether the liquid is shuttled or not. Recently, Dennison *et. al* introduced an electrochemical flow capacitor (EFC) for energy storage applications, and the capacitance and conductivity of EFC slurry electrodes were measured as a function of flow rate and flow cell channel depth (Dennison *et al.*, 2014). Accordingly, they speculated the variation in capacitance and conductivity was the result of boundary layer effects. The lowest conductivity was observed under static conditions because the boundary layer was thick at low flow rates that dominated the average conductivity. When the boundary layer thickness decreased along with increasing flow rates, the measured conductivity closed in the value in the free stream. Their finding supports our presumption that the flowing liquid can affect the reaction efficiency, and various flow conditions result in unique characteristics. This paper also mentioned the shear-thinning behavior of the slurry that produced special velocity profiles. Considering the above facts, we aim to study the flow effects that the flowing liquid may enhance the interfacial interaction according to disturb the diffusion layer for improving the reaction efficiency.

18
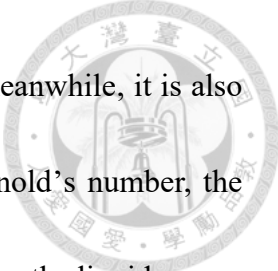
On the basis of mechatronic control and peristaltic pump, we build a programmable fluid controlling system that can transport the injected samples along the microchannel. With the CNC-machined manufacturing process, PMMA chips are designed and fabricated to investigate the flow effects. Originated from the cooperated researches with Prof. Hara's group (Iles *et al.*, 2007), we try to imitate the catalytic reaction between a metal catalyst and its substrate (Kobayashi *et al.*, 2010). A tiny iron sheet is placed in an intermediate chamber, and the inactive Prussian blue precursor is transported through the iron sheet. When the iron contacts the acid solution, it will be oxidized to Fe^{2+}. At the same time, the ferricyanide gets the electrons and forms the ferrocyanide which can react with the other components in the precursor to generate Prussian blue. Further, the techniques of the screen-printed electrode (SPE) and flow injection analysis developed by our lab (Chiu *et al.*, 2009) are extended to a three-electrode planar SPE to study the flow effects on electrochemistry. Among the electroanalysis under shuttle flow, the droplet-formed samples are used to save the reagent volumes, so the stability of droplet transportation should be ensured. Profiting from the MEMS process, the electroanalysis system can be miniaturized to a microchip. However, the three-electrode configurations have some hidden problems, so the two-electrode configuration is proposed. Below, we will show how we build the fluidic platform and develop the microfluidic chips, and the preliminary results can prove our assumption of the flow effect.

2.2 Literature review

2.2.1 Application of flowing operations in microfluidic chips

Microfluidics is a technology that handles microscale liquid in tiny channels or chambers. Based on the advantages of miniaturized volume, various traditional biological and chemical experiments can be scale-down and package into a chip called "Lab-on-a Chip (LOC)". Including the sample preparation, reagent reaction and target sensing, all stages in a complicated experiment can be sequentially accomplished. After the original samples are loaded into the chip, the tiny liquid should be transferred chamber by chamber. The syringe pump is the most common tool to drive the liquid because it can provide a precise and stable liquid control with the infusion and withdraw abilities. Positive pressure supplies a large driving force to push the liquid in tiny channels which have an enormous flow resistance. However, the huge pressure may damage the microfluidic chips if the seal is not robust enough. Therefore, negative pressure is an alternative way to transport liquid for preventing the chip breaking even though the pressure-supply is much less than positive pressure. The peristaltic pump is another tool to transport the liquid, and it has a faster flow rate and cycling-flow ability. Additionally, many researches focus on pump-free liquid transportation to further miniaturize the total system size. Using the centrifugal force, gravity, capillary, and electricity to drive the liquid have great novelty and development potential but they still have some individual limitations.

Laminar flow is a unique characterization in microfluidic and meanwhile, it is also the major limitation of microfluidic applications. According to Reynold's number, the flow can be divided into the turbulent and laminar flow. In laminar flow, the liquid moves layer by layer and doesn't interact with each other (shown in Fig 2.1(a)). When the flow rate is slow, the viscosity of the solution causes a higher shearing force than the inertial force. This laminar feature leads to a no-mixing and poor diffusion situation that reduces the reaction efficiency in microfluidic. In Fig. 2.1(b), driving liquid with a single direction is a common way in microfluidic applications, and we called "one-way flow" in this research. It's a continuous flow that can modulate the reaction time by the flow rate. Yet, it's still suffered from laminar problems and only exists a liquid-to-liquid interface interaction by the diffusion behavior. Actually, FIA is a breakthrough that applies the one-way flow to a liquid-to-solid reaction. When the liquid passes through, an instant surface reaction appears that leads to a considerable response. The facilitated surface refreshment results in a fast reagent compensation and the elimination of diffusion limit. Therefore, the one-way flow provides a new route to expand microfluidic developments.

However, there are still some disadvantages in the one-way flow operation. To provide a sufficient sample volume for the continuous one-way flow, the precious materials need to be diluted that cause a weak reaction efficiency. Furthermore, if there are routine processes in a chip, the device is crowded with repeated units that inhibit the

21
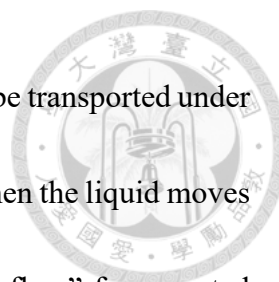
feasibility of miniaturization. To solve those problems, the liquid can be transported under different directions after the samples are loaded in the microchips. When the liquid moves back and forth in a microchannel, it can not only supply a "shuttle flow" for repeated transportation requirement (Carpenter and Roberts, 1999) but also keep the advantages of one-way flow conditions under a less sample volume (shown in Fig. 2.1(b)). Moreover, the shuttle rate is tunable to generate the chaotic flow, results from the sudden flow direction changes. Unlike the oscillation flow which only makes the droplet deformed by shaking the liquid in the microchannel, the shuttle flow in this research is defined as a completed movement that replaces the entire diffusion layer around the surface with a fresh liquid section. The micro-mixing effect under the shuttle flow condition is beneficial to overcome the laminar flow limitation in microfluidic applications.
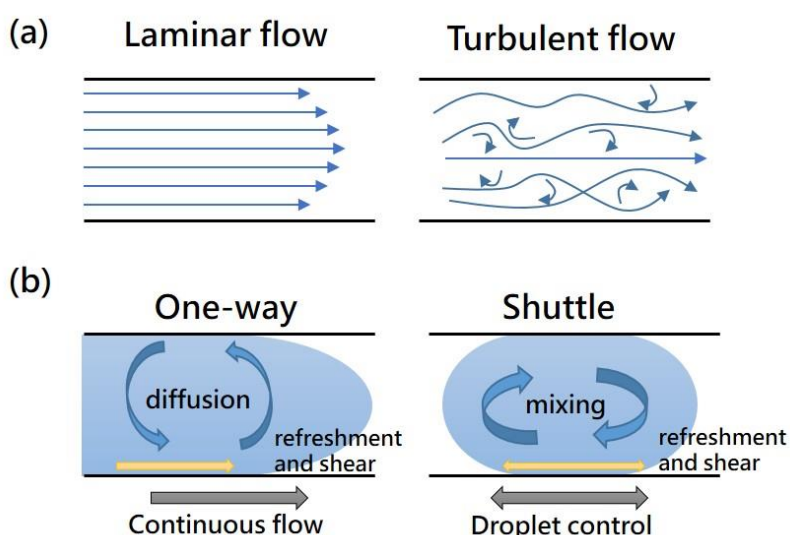
Figure 2.1 Schemes of (a) the laminar flow and turbulent flow and (b) the assumed flow effect under one-way and shuttle modes.

22

2.2.2 Shuttle flow for the micro-mixing and repeated reactions

In general, the laminar flow related to the low Reynold's number occurs in many microfluidic systems. The weak liquid mixing due to the diffusion limitation inspires many researches to interest in developing various mixing structures shown in Fig. 2.2 (Lee *et al.*, 2011). The T-mixer and Y-mixer are simple structures based on the lamination which twists and laminates two liquid flows to reduce the diffusion length (Nguyen and Wu, 2004). To reach a complete species mixing, the mixing channel should be long enough. Zigzag and serpentine structures are designed for more effective mixing in microchannels (Mengeaud *et al.*, 2002; Liu *et al.*, 2009). The fluid flows collide with each other passively due to the periodically changed flow directions. The chaotic advection and transverse dispersion are caused by the repeated flow impact. In addition to the channel design, the embedded barriers in the intermediate can provide the combination of multi-lamination and the chaotic effect that further enhances the mixing performance (Stroock *et al.*, 2002; Kim *et al.*, 2004). The micromixers with special structures have many advantages and disadvantages, and however, they indeed improve the mixing efficiency for diverse microfluidic applications.
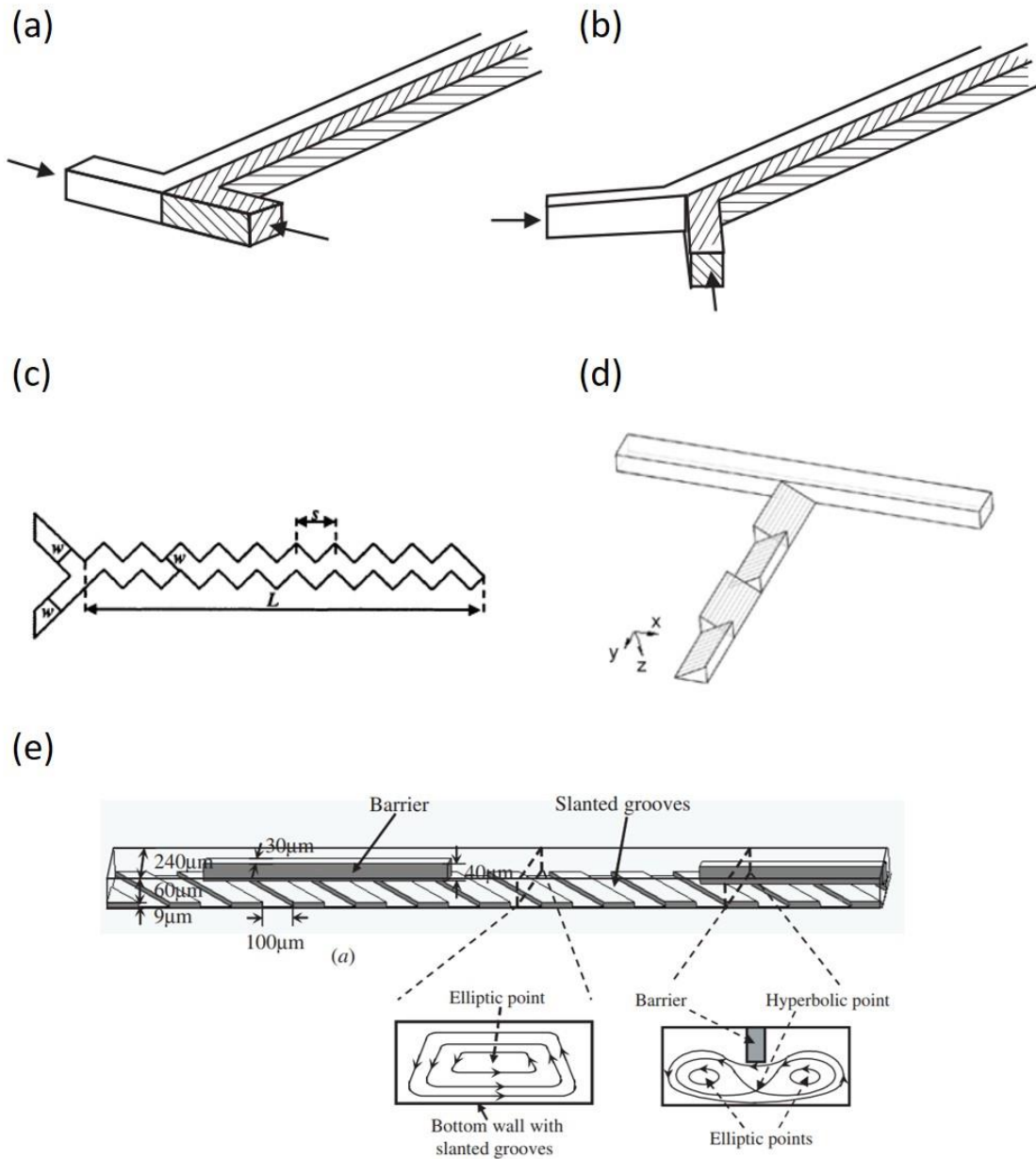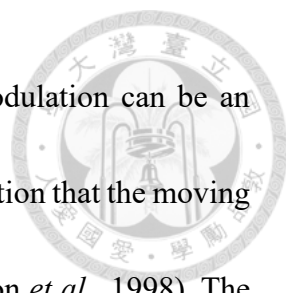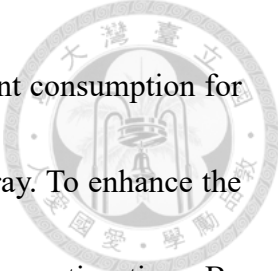
Figure 2.2 Micro-mixers in the microfluidic chips. (a) T-shape (b) Y-shape (Nguyen and

Wu, 2004) (c) Zig-zag (Mengeaud *et al.*, 2002) (d) stream twist (Lee *et al.*, 2011) (e)

embedded barriers (Kim *et al.*, 2004).

Instead of the special mixing structures, the particular flow modulation can be an alternative strategy for micro-mixing. Bolus flow is defined as the motion that the moving plugs of liquid separated by air form a recirculation pattern (Anderson *et al.*, 1998). The moving droplet has a stirring effect that can solve the "mixing problem". In general, when two droplets contact in a microchannel, the slow diffusion dominates the mass transfer. The homogenization of species should cost a few minutes in a stationary condition. In contrast, if the merged droplet is shuttled back and forth, the accelerated disturbance will achieve the complete mixing just in a few seconds. A simple experiment is executed to prove this phenomenon even in a pico-scale (Hosokawa *et al.*, 1999). When the droplets of water and fluorescein solution are merged in the microchannel, the fluorescent images are recorded to estimate the mixing degree. Without shuttling the droplet, it takes three minutes to get a uniform profile. In comparison, it takes 30 seconds to reach the whole merge after three shuttle operations. The shuttling operation is successfully proven to enhance the microfluidic mixing in this diffusion-dominated scale.

DNA hybridization assay is a critical step in DNA microarray for high throughput gene analysis. Unknown DNA targets in the solution bind to anchored DNA probes through heterogeneous DNA-DNA hybridization. Although DNA microarray is a powerful tool for all gene-related researches, the slow diffusion kinetic still limits the reaction. In fact, a normal DNA-DNA hybridization needs more than 12 hours to complete

the reaction (Huang *et al.*, 2010b). Besides the time cost, large reagent consumption for hybridization also restricts the practical application of DNA microarray. To enhance the hybrid efficiency, microfluidic devices are introduced to shorten the reaction time. By reducing the channel height, a shorter diffusion length leads to faster convection. However, the laminar flow in the microchannel hinders the effective mixing, and this problem evokes the following studies of micro-mixing. Instead of the active mixing, a passive micro-mixing based on the shuttle flow is adapted for the effective DNA hybridization (Wei *et al.*, 2005). The re-circulating flows resulted from the droplet feature in microchannel quickly mix the DNA molecules. The DNA probes for gene analysis are spotted on a microarray. Covered by a PMMA microchannel, the microarray forms a microfluidic chip, and then it is packaged by steel clamps. After the sample is loaded into the microchannel, the solution is pumped back and forth to generate scramble plugs. The plugs are shuttled through the probe spots to carry out the DNA hybridization. The results show an obvious improvement of hybridizing speed under the shuttle condition in comparison to the flat glass conditions. Huang *et. al* present a dedicated microfluidic chip consisted of microvalves and micropumps for rapid DNA hybridization under a shuttle condition (Huang *et al.*, 2010b). Forty-eight hybridization units are integrated into a microchip, and each hybridization can be finished in 90 seconds with merely 1 µl sample consumption.

26

In addition to DNA hybridization, shuttle flow can meet the other micro-mixing requirements. A simple reagent mixing before a PCR procedure is performed in a two-step gene synthesis chip (Huang *et al.*, 2009). Fresh PCR mixture and outer primers are pumped into a chamber in equal volume, and then the merged solution is shuttled between two chambers five times for uniform mixing. Interestingly, there is an additional feature in this two-chamber mixer. An abrupt opening at channel-chamber junctions causes chaotic advection and recirculates the flow. In a T-junction microfluidic device used to handle liquid plugs for bio/chemical analyses, the rapid mixing is implemented by shuttling the merge plug (Sassa *et al.*, 2008). This device can enable many liquid operations including plug division, plug sorting, plug formation, and plug attachment. Further, an enzymatic reaction involving L-glutamate oxidase (L-GlOx) and horseradish peroxidase (HRP) is demonstrated to prove the device performance. In the study of multiphase reaction, an oscillatory multiphase flow is proposed to eliminate the limitation from the traditional continuous multiphase flow (Abolhasani and Jensen, 2016). The continuous multiphase flow is utilized for high-throughput molecule screening and reagent preparation. Although this plug flow has the inter-circulation feature for micro-mixing, the residence time and reaction time are still limited by the length of the reactor. Hence, two oscillatory flow strategies, valve-based and syringe-based, are put forward to minimize the channel length. Two immiscible fluids are shuttled in a short space, and the

27
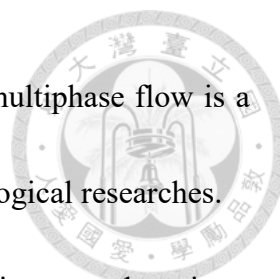
bi-phasic interfacial reaction conducts simultaneously. Oscillatory multiphase flow is a promising technology for the long-term process in chemical and biological researches.

The liquid transportation under oscillatory flow can not only improve the micro-mixing but also serves an optional liquid operation for recirculating reactions in lab-on-a-chip. Among the reactions, PCR is a well-known time-consuming biological reaction that can amplify DNAs through repeated temperature changes. In traditional PCR, the tubes containing PCR mixture are immersed in three water tanks in turn. Three different temperature conditions provide suitable environments for each PCR step. It takes time to move the tubes from a tank to another tank and to reach a thermal equilibrium between the liquids. Several kinds of thermal-cycler are developed to speed up the PCR procedure, but it's still limited by the heating and cooling rate of the PCR machine. Microfluidic PCR is an effective platform for rapid DNA amplification. Three heating regions are embedded in a microfluidic chip to provide the thermal-stable surroundings for the PCR. After the PCR mixture is loaded into the microchip, the droplet is shuttled between three regions to conduct the reactions (Wheeler *et al.*, 2004; Frey *et al.*, 2007; Sugumar *et al.*, 2010; Abolhasani and Jensen, 2016). This convectively driven PCR can reduce the cycle time for DNA amplification, and it also eliminates the possible bubble formation in a PCR microfluidic chips.

2.2.3 One-way flow for dynamic electrochemical responses

Dynamic electrochemistry is an attractive technology that can provide more information about the kinetic reaction. In traditional electrochemistry, most of the researches focus on the electrochemical response under steady states. Three-electrode system is commonly used to measure the signal while the surface reaction reaches equilibrium. As we know, the diffusion control restricts the signal response that leads to the typical electrochemical analysis profiles. When a potential is applied to the working electrode, the redox interaction occurs around the electrode surface. The charge transfer results in the current signal and consumes the component of the solution near the electrodes. In reason of the local consumption, a diffusion layer forms, and its width is determined by the diffusion rate. The diffusion effect can be illustrated in cyclic voltammetry (CV) and chronoamperometry analysis. In CV analysis, different potentials are swept with a particular scan rate. The current shows a sudden increasing when the applied potential is higher than the formal potential that means a rapid reaction happens. Basically, the higher potential is applied, the larger current response. Yet, instead of an exponential rising in redox current, there is a peak current resulted from the diffusion control. The same situation is observed in chronoamperometry. The current exponentially declines along with time until the zero-current equilibrium. To conquer the diffusion limit, the stirring bar and the rotor-disk electrode are used to create a dynamic surrounding for

29

electrochemical analysis.

FIA is an analytical method for bio/chemical detection (Ruzicka and Hansen, 1988). Typically, a FIA system consists of a pump, an injector, a reactor/cell and a detector in downstream (Xu *et al.*, 2005). A plug sample is injected into a flowing carrier stream via an external pump, and the sample volume can be accurately controlled. When the sample is transported to the detector, the components in the sample solution can be identified and quantified. In theory, the initially injected sample liquid has a rectangular profile, and then it transforms into a parabolic flow profile (Skoog *et al.*, 2017). When the sample is driven forward, the sample will disperse into the carrier flow via convection and diffusion that leads to the expanding profile width. After a few seconds, only the diffusion plays a significant contributor, and the flow profile becomes broad. This continuous flow analyzer is first described in the mid-1970s for the automated sample analysis (Ṙužička and Hansen, 1975; Ruzicka and Hansen, 2000). Besides the advantages of simple operation, rapid analysis, and versatile application, FIA is also an appropriate tool for dynamic sample detection. Especially in using the electrochemical detector, the e-FIA shows a wide variety of analyses. The targets can be environmental samples (Shitanda *et al.*, 2009) or clinical molecules (Yang *et al.*, 2008), and it's up to what kinds of modification on the electrodes.

The microfluidic-based flow-injection amperometric analysis integrates the

30

microelectrodes into a microfluidic chip. Combining the superiorities in FIA and microfluidic electrochemistry, this platform enables a fast, sensitive and less-reagent sample quantification. In the microfluidic chip, the complex samples can be purified by functional units before the targets reach the electrodes for quantification. Microelectrodes can be fabricated by various processes like CD etching (Daniel and Gutz, 2003) or thermal evaporator (Bäcker et al., 2013), and different electrode configurations are designed for versatile applications. The redox current peaks are proportional to the injected sample concentration, and it shows good repeatability on the peaks with the same concentration. A. Wisitsoraat's group report a flow injection microfluidic device for fast cholesterol detection. Functionalized carbon nanotubes are immobilized on the working electrode by an in-channel flow technique (Wisitsoraat et al., 2010). Ag and Pt are used as reference and counter electrodes, respectively. In the optimal pH and temperature conditions, an electrochemical sensor with high-throughput detection (60 samples/hr), low limit of detection (LOD) (50 mg/dl) and low cross-sensitivity are established.

In the flowing electrochemical detection under one-way flow, the continuous flow mode provides a simple way to measure the dynamic information. Further, some researches find that the flow rate is a critical parameter to improve sensor performance (Amatore et al., 2008; Wang et al., 2010). In Fig. 2.3(a), The deformed profiles of the linear sweep voltammetry (LSV) are also revealed in flowing amperometric detection

31
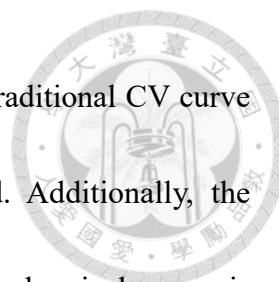
(Sansuk *et al.*, 2012). The sigmoidal curve which is distinct to the traditional CV curve may result from the facilitated mass transport in flowing liquid. Additionally, the dependence of anodic current responses with flow rates in an electrochemical sensor is shown in Fig. 2.3(b). It shows great potential to improve the performance of electrochemical sensors.
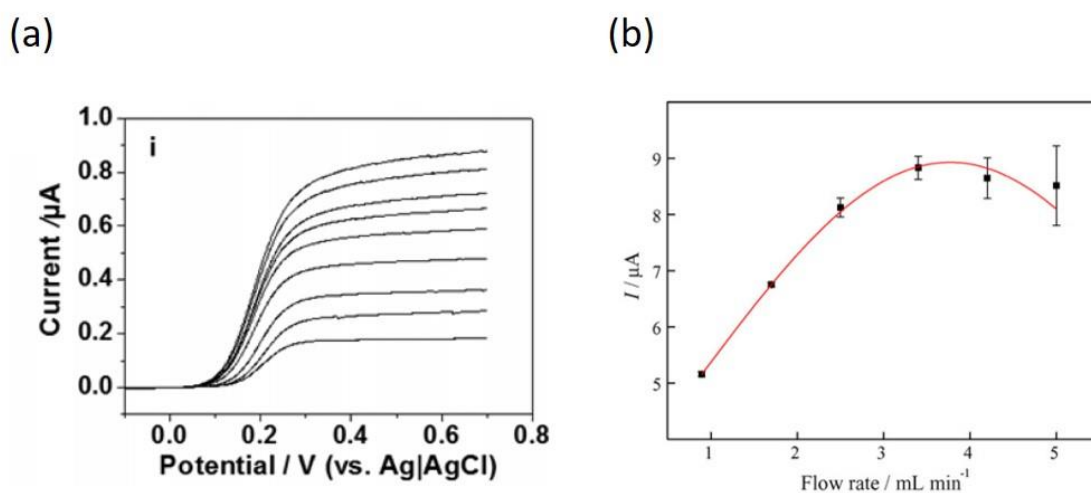
Figure 2.3 The hidden flow effects in the (a) deformation of LSV curve for the oxidation of redox components at an Au microband electrode under the flow rates of 0.01~2 ml/min (Sansuk *et al.*, 2012) and (b) the dependence of anodic current response with flow rate in an electrochemical sensor(Teixeira *et al.*, 2007).

2.3 Experimental

● Reagents and materials

The inactive Prussian blue precursor was prepared by mixing 20 mM $K_3Fe(CN)_6$, 10

mM KCl and 20 mM $FeCl_3$ in 0.1M HCl. The redox mediator solution was prepared by

equal-molar mixing, and the final concentration was 5 mM $K_3Fe(CN)_6$, 5 mM $K_4Fe(CN)_6$

and 0.1M KCl in ddH_2O. All reagents were purchased from Sigma-Aldrich. All organic

solvents like ethanol, acetone and isopropyl alcohol were obtained from HSIN MING

chemical instruments Co., LTD (Taipei, Taiwan). The PMMA blocks were purchased

from an advertising company (Wu-Mei, Taiwan). The components used for the fluidic

platform construction were obtained from commercial sources as follows: plastic tubes

and screw tubing (Superchroma, Taiwan), hardware parts (Tim Rong, Taiwan), O-ring

seal (CNL SEAL, Taiwan), electrical elements (YD-TECH, Taiwan), peristaltic pump

heads (SMP-23, Sun-way, Taiwan). The materials used for the screen-print electrode

fabrication were purchased from commercial sources as follows: PET slide (Kuang Nan

Fashion Shop, Taiwan), carbon paste and silver paste (Wellsuntec LTD., Taiwan), screen

board and cleaning solvent (Hocom, Taiwan). The materials and reagents used for the

construction of microfluidic devices and microelectrodes were obtained from commercial

sources as follows: glass slide (FEA, 1"x3", 1-1.2 mm thickness); gold slugs, Cr pieces

and boats (Guv Team International, Taiwan); S1813 photoresist (SHIPLEY); plastic

photo mask (TK, Taiwan); TMAH (Sigma); PDMS (BingBond, Taiwan); biopunch

(MILTEX, Japan).

- Construction of the programmable fluid controlling platform

The first few generations of fluid control platform were made of PMMA materials

because its transparent color made the liquid in the channel to be easily observed. The

channels were designed by the CAD software (SolidWorks), compiled by the CAM

software (Cut2D) and machined by CNC-milling machine (SIMENS). The channel

blocks were assembled with sealing elements (soft film or O-ring) and compacted with

strews to prevent the liquid leakage. Using peristaltic tubes to connect the pump and

fluidic device, the liquids were loaded into the channels with the aid of gas pushing which

was driven by the peristaltic pump head. The pump head was jointed to an electric motor,

and the motor could be programmably controlled by a mini Arduino controller and related

circuits (including a L298N chip for stepper control). The flow directions and flow rates

could be conveniently modulated via the precise control of rotating speed and direction.

- Fabrication of screen-print electrodes

Following the protocol of screen-print carbon electrode (SPCE) production

developed by our lab, the carbon and silver pastes were printed on the PET substrates to

form the electrode patterns. After the printing process, the electrodes were dried in a 200

°C oven for solvent removal and material curing. The 3M tapes were used as an insulated

layer to define the working area, and the copper tapes were used as a current busbar to avoid the connection problem.

- Manufacturing of the microelectrodes and PDMS chips

PDMS molding is a typical method to manufacture microfluidic chips, and the production of the photoresist master is a critical step along the whole process. The detail procedures are listed in Table 2.1. Two solvents of PDMS were mixed with the volume ratio of 10:1, and the mixture were degassed in a vacuum container before pouring the gel mixture on the master. And then, the master was heated by a hotplate at 120 ℃ for 10 mins to cure the PDMS gel. The PDMS chips were peeled off gently, and two holes (inlet and outlet) were punched by a puncher.

Microelectrodes are fabricated on glass slides by the lift-off process, and the detail procedures are listed in Table 2.2. The positive photoresist was used as a sacrifice layer that prevented the metal deposition on the glass slides. The electrode patterns were designed on the photomask which generated the difference of UV exposure. Cr and Au materials were deposited on the glass slide in order with the thickness of 20 nm and 80 nm, respectively. According to the principle of the lift-off process, only the films attached to the glass slide could be retained, and the left metal formed the electrode patterns.

The PDMS chips and microelectrode slides were bonded by the oxygen plasma treatment and heating at 120 ℃ for 10 minutes.

- Electrochemical analysis

The electrochemical analysis was carried out by AutoLab potentiostat. Using crocodile clips to connect the electrodes to the instrument, three-electrode configuration contained a pseudo-reference, a counter, and a working electrode. In the two-electrode configuration, reference and counter electrodes were combined to a single electrode. As the redox mediators were injected into the fluid devices, various electrochemical methods were utilized to measure the static and dynamic response under different liquid operation modes. Cyclic voltammetry (CV) was performed to verify the fundamental characteristics of electrochemistry. The electrodes were analyzed by applying a 100-cycle CV scan with a scan rate of 0.1 V/s, and the current profiles could imply much information about redox reactions. Chronoamperometry (CA) was performed to observe the real-time current response. In general, a constant voltage (0.4 V) was applied to the electrodes, and the corresponding currents were continuously measured.

36

Table 3.1 The detail procedures of producing the SU-8 photoresist master

Procedure	Parameters
Wafer cleaning	Sonicated for 10 mins in each solution Acetone – Methanol – DIW Dry at 120 ℃ for 5 mins Cool to room temperature
SU-8 coating	Gently spread the SU-8 on the wafer Spin coating by 500 rpm 10 s and 4000 rpm 50 s
Soft baking	65 ℃ 3 mins 95 ℃ 5 mins Cool to room temperature
Exposure	15 mW/cm^2 UV for 30 s
Post-exposure	65 ℃ 1 mins 95 ℃ 5 mins
Developing	Immersing in developer for 240 s
Rinse and Dry	Rinsed by IPA and dried by air blowing
Hot baking	160 ℃ 30 mins
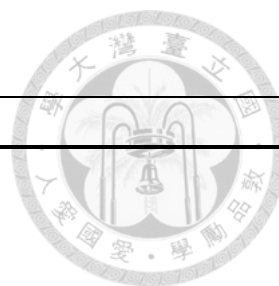
Table 3.2 The detail procedures of lift-off process

Procedure	Parameters
Glass cleaning	Sonicated for 10 mins in each solution Acetone – Methanol – DIW Dry at 120 ℃ for 5 mins Cool to room temperature
S1813 coating	Drop the S1813 on the substrate Spin coating by 1000 rpm 20 s and 4000 rpm 60 s
Soft baking	115 ℃ 1 mins Cool to room temperature
Exposure	15 mW/cm^2 UV for 10 s
Developing	Immersing in developer for 60 s
Rinse and Dry	Rinsed by DIW and dried by air blowing
Hot baking	130 ℃ 10 mins
Thermal evaporated deposition of metals	Cr as adhesion layer 20 nm Au 80 nm
S1813 removal	Sonicated in acetone
Dry	120℃ 5 mins

2.4 Results and Discussion

2.4.1 Automatic microfluidic reactor for enhancing the surface reaction

The concept of the automatic microfluidic reactor is shown in Fig. 2.4. In traditional

catalysis experiments, the tube-based reaction is a common strategy to evaluate catalysis

efficiency. However, the yield and the rate determined from the heterogeneous catalysis

are probably underestimated due to a retarded mass transfer of the substrate between the

bulk solution and the surface. Considering this issue, we attempt to develop an automatic

microfluidic reactor to enhance the surface catalysis on a metal chip. A PMMA device

containing a straight channel and a small chamber in the middle is manufactured, and a

piece of iron sheet (1x1 mm) is placed in the chamber before the assembly of the device.

After the device is connected to the peristaltic pump with tubes, the liquid can be loaded

into the channel through operating the pump under the withdraw mode. The pump is

driven by a DC motor which can rotate CW and CCW according to the applying voltages.

In addition to the optional flow direction, the flow rates are tunable through a set of

controlling circuit that regulated the rotating speed of motors shown in Fig. 2.5(a). In the

control circuit shown in Fig. 2.5 (b), four buttons are set for different motor motions

including a CW button for infusing liquid, a CCW button for withdrawing liquid, a

PROGRAM button for shuttle flow and a STOP button for ending the program. The

shuttle program contains a repeated infused and withdrawn motion, and the round-trip

39

time is 7s. The maximum of flow rate is about 1,932 μl/min under the suggested motor

operating voltage (DC 12V), and the flow rates are nearly proportional to the applied

voltage to the motor (shown in Fig. 2.5(c)). In the practical operating process, after a plug

liquid with the length of 10 mm (equal to 110 μl) is loaded into the channel and

transported near the chamber by continuously pressing the CW button, the PROGRAM

button is pressed to carry out the shuttle process shown in Fig. 2.6 (a).

In this work, we use the Prussian blue precipitation reaction for demonstration of this

proof-of-principle device. An iron chip is put into the tube-based and channel-based

reactors shown in Fig. 2.6(b), and then the inactive PB precursor is loaded into the reactor.

When the acid solution (reagents dissolved in 0.1M HCl) contacts the iron metal, it leads

to the oxidization of iron and reduces ferricyanide to ferrocyanide simultaneously. Mixing

ferrocyanide and ferric chloride can bring about a spontaneous reaction of Prussian blue

precipitation. After several repeated interactions with the iron sheet, the solution becomes

bluer which is attributed to the increasing PB precipitation. The yield of PB formation is

quantified by using UV-VIS spectroscopy analysis, and the blue color can be measured

according to the absorption spectra shown in Fig. 2.6 (c). In comparison, the tube-based

reaction is executed with the same reaction time, and the apparent difference of profile

can be seen around 720 nm. The results imply that the microfluidic reaction is more

efficient than a tube based reaction.
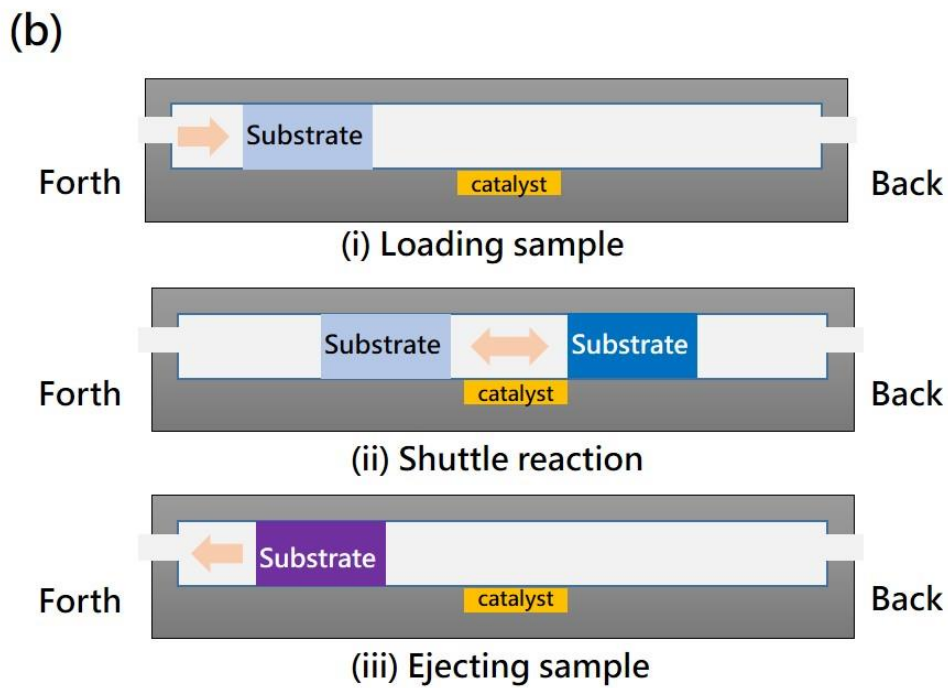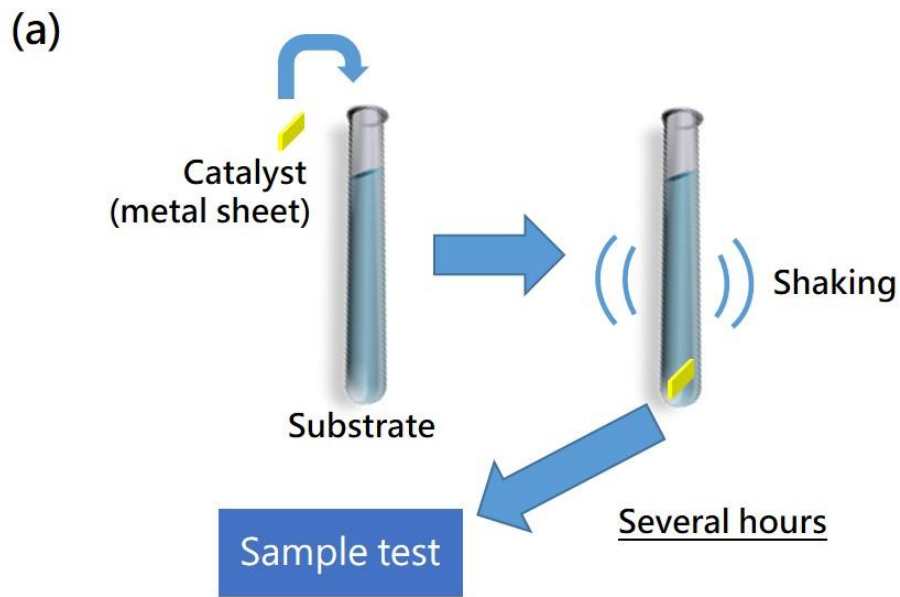
Figure 2.4 The catalyst reaction can be implemented in a traditional (a) tube-based reactor with a lengthy shaking process or (b) the channel-based microfluidic reactor with the shuttle flow.

(a)

(b)
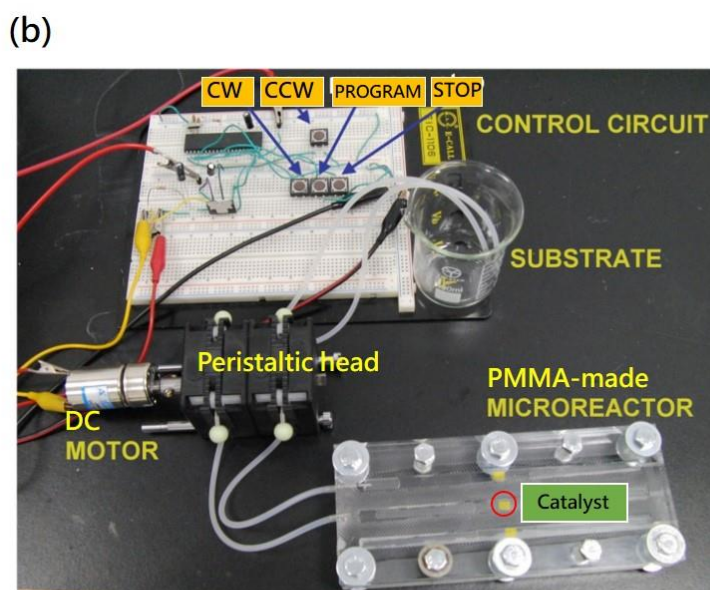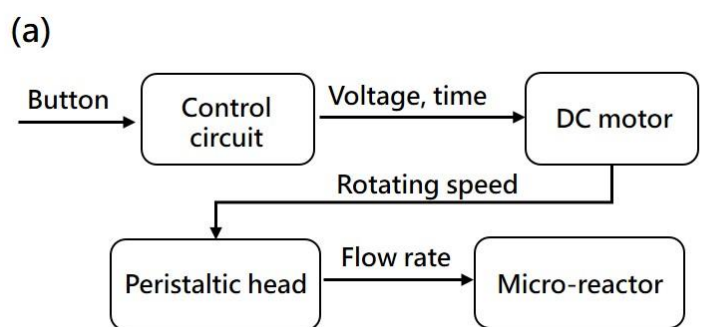
Channel : W5.5 x H2 x L150 (mm)

(c)
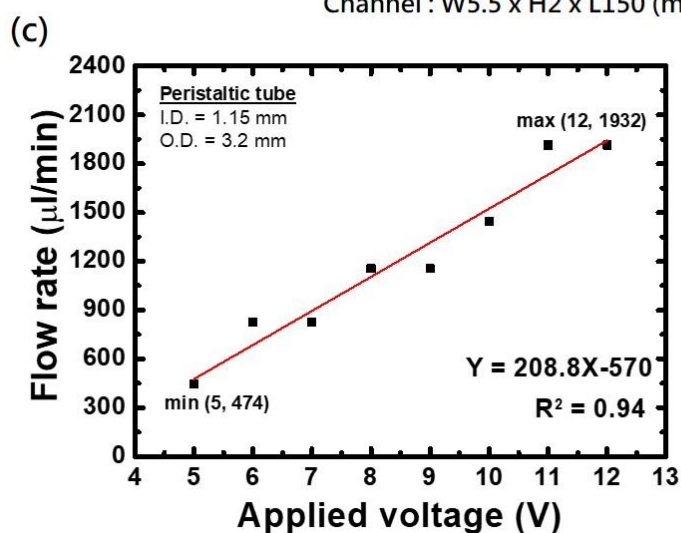
Figure 2.5 The automatic microfluidic system is controlled by (a) a serial of electrical signals after pressing a button, and (a) the system includes a circuit, pump, and microreactor that can (c) produces different flow rate depended on the applied voltages.
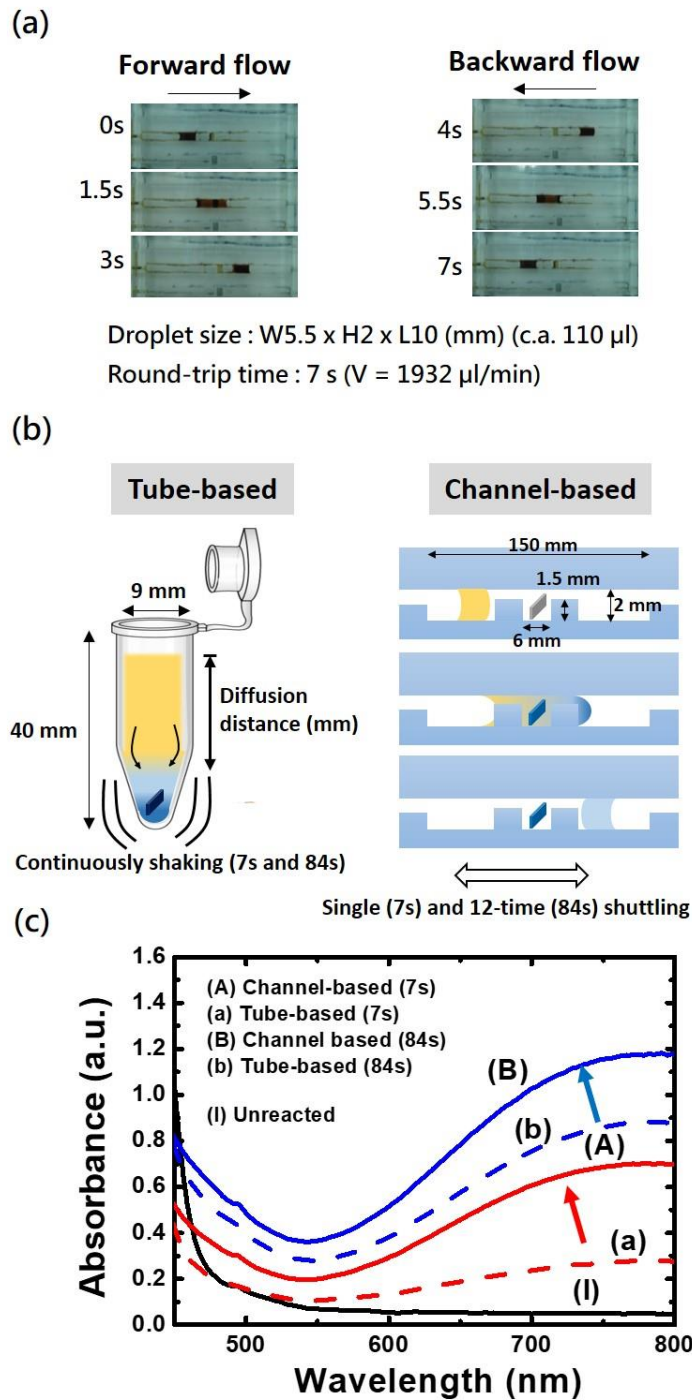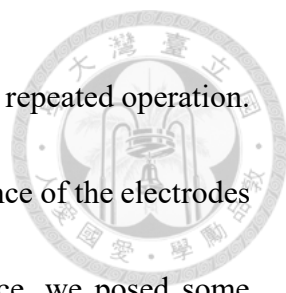
Figure 2.6 The shuttle flow performance is demonstrated by (a) the animation-division images of the device-operating process, and its enhancement is verified by (b) the comparison between tube-based reaction and channel-based reaction with shuttle flow on (c) the production of Prussian blue precipitation.

2.4.2 The flow effect on droplet-based electroanalysis

In the previous experiments, we confirm that the microfluidic reactor operating with shuttle flow has a higher reaction efficiency than the tube-based reaction. Further, this strategy can not only reduce the reaction time but also save the consumption of liquid samples. However, these experiments can merely obtain the reaction difference after reaching an equilibrium state, so the real-time response is hard to monitor. If we can detect the immediate signals during the reaction process under flow conditions, the dynamic information can be acquired to analyze the flow effect. Compared to optic methods, the electrochemical methods have a fast signal response and high sensitivity that benefits to study the flow effect and get more dynamic information.

Therefore, screen-printed electrode (SPE) is chosen to construct an electrochemical system containing a three-electrode configuration shown in Fig. 2.7(a). A silver electrode is used as a pseudo-reference electrode, and two carbon electrodes are served as working (WE) and counter (CE) electrodes. Among the two carbon electrodes, the counter electrode has a larger surface area in order to prevent the current limitation from the CE. Additionally, the CE is close to the WE for eliminating the diffusion resistance, and the CE is close to the RE that supplies a stable reference potential. The performances of these screen-printed electrodes are characterized through the typical ferricyanide redox reaction with 100-cycle CV analysis shown in Fig 2.7(b). After 100 cycles, the CV profiles show

44

a slight current degrade that means the electrodes are stable under the repeated operation. Yet, the shift of current peak still reveals that the high internal resistance of the electrodes leads to the delay redox reactions. In this case of the fluidic device, we posed some improved designs shown in Fig 2.8 (a), which involves a strew tubing and an O-ring for reducing the liquid leakage. The motor is fixed by a fixture shown in Fig 2.8 (b) to stabilize the rotating of the pump head. To carry out the experiments, the redox mediator is infused into the device in the form of a droplet, and a constant potential (0.4 V vs. RE) is applied to the WE for measuring the current immediately. In the chronoamperometry under one-way flow shown in Fig. 2.9, when a droplet flows through the electrodes, a set of current response occurs with a negative peak followed by a positive peak. This profile is different from a typical FIA signal, but we can still observe this unique profile under various flow rate conditions. Hence, we assume that the phenomenon may result from the order of droplet contacting the electrodes. Different from the FIA which has a continuous carry buffer providing a conductive surrounding, the droplet is flanked by air that causes an unstable situation. Under the shuttle conditions shown in Fig. 2.10, although the negative peak disappears, two peaks in a single current response are observed. The issue of contacting order is eliminated due to the fast shuttling which keeps the electrode wet, so the conductive state can be maintained. Moreover, we find that the backward signal is lower than the forward signal, and it may imply that the redox mediator is consumed.
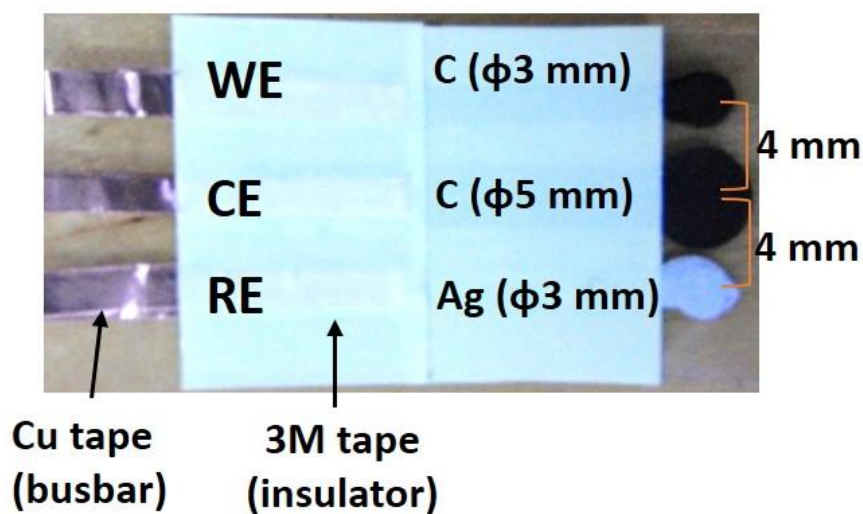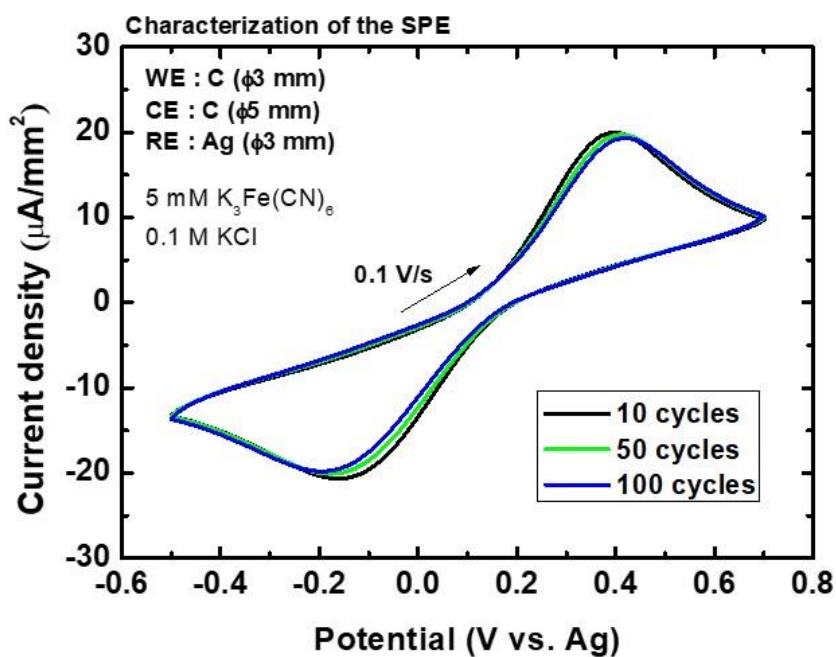
Figure 2.7 Electroanalysis platform for studying the flow effect contains (a) a three-electrode screen-printed electrode which has high stability after (b) 100-cycle cyclic voltammetry analysis.
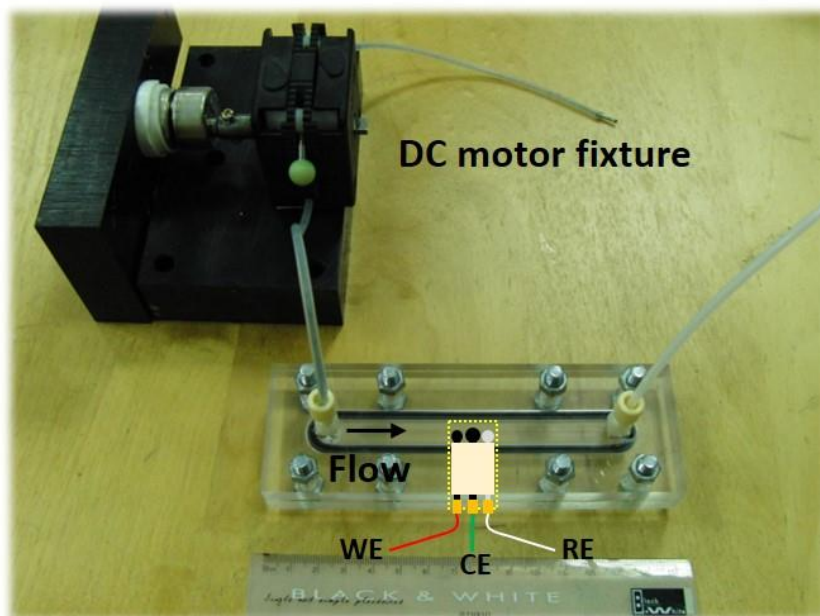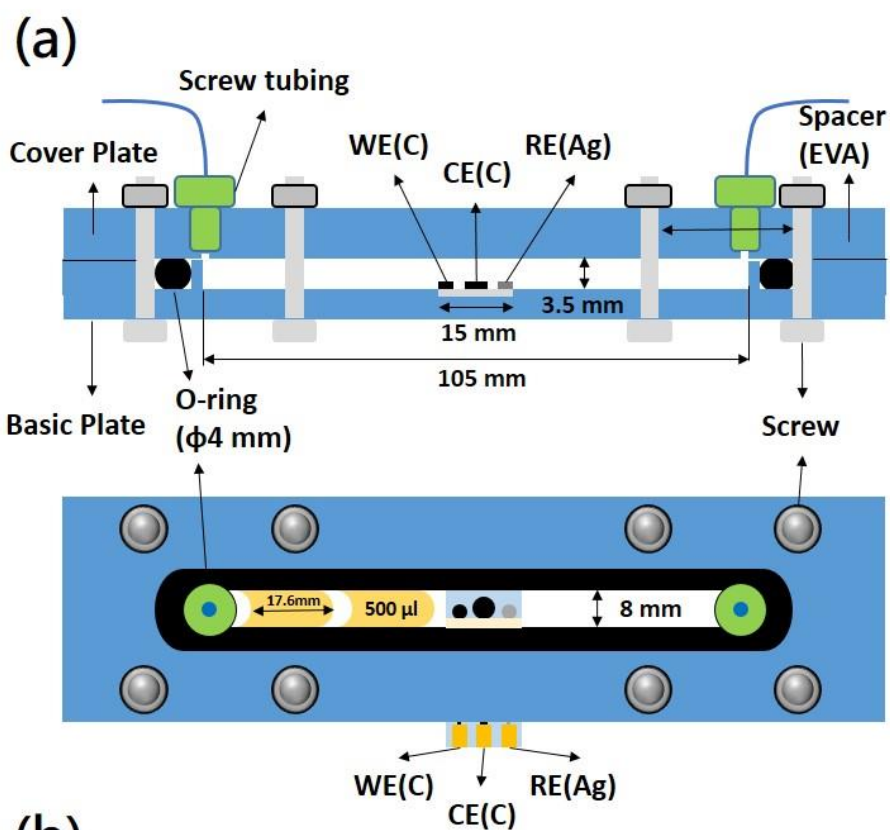
Figure 2.8 The improved channel-based reactor using (a) strew tubing and O-ring for

reducing the liquid leakage, and (d) a motor fixture to stabilize the pump system.

47
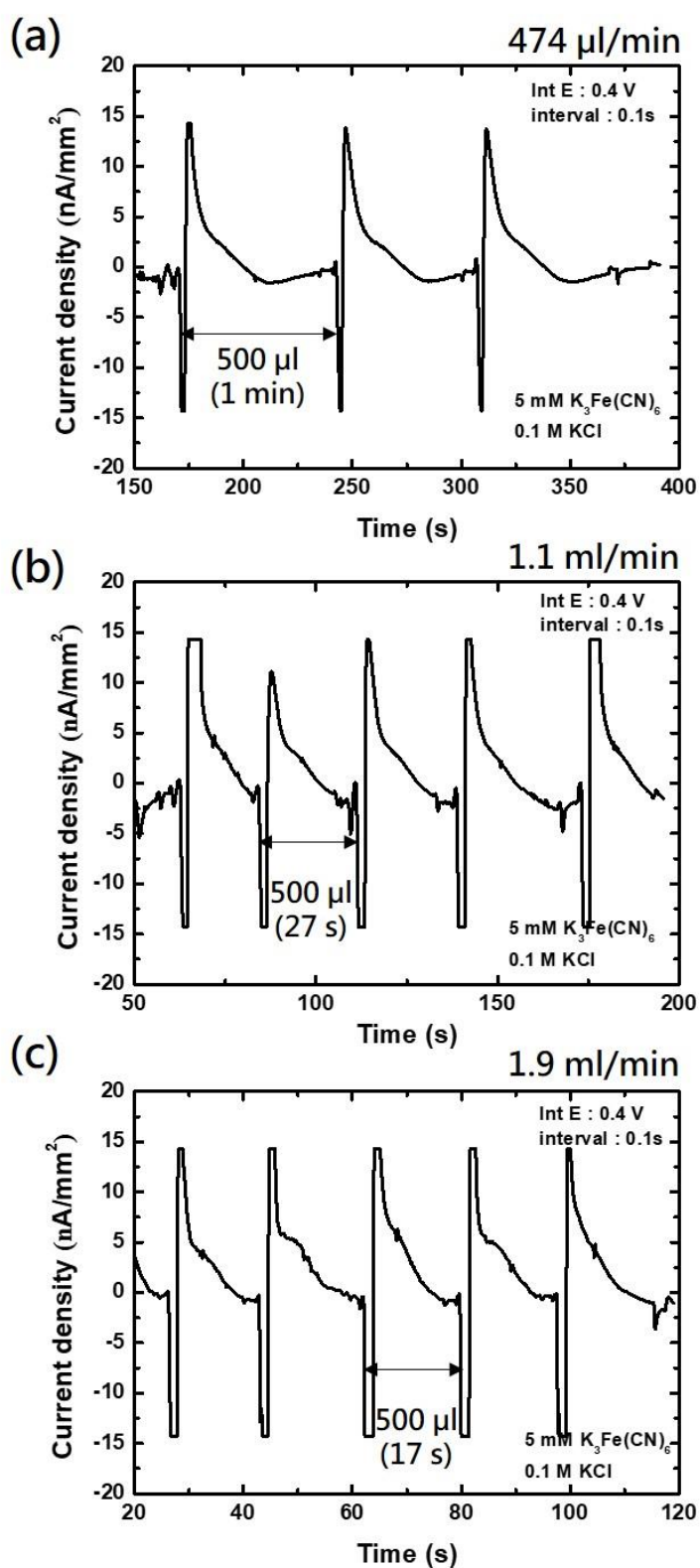
Figure 2.9 Chronoamperometry of the droplet-formed redox mediator under one-way

flow with different flow rates. (a) 0.474 ml/min (b) 1.1 ml/min (c) 1.9 ml/min.

48
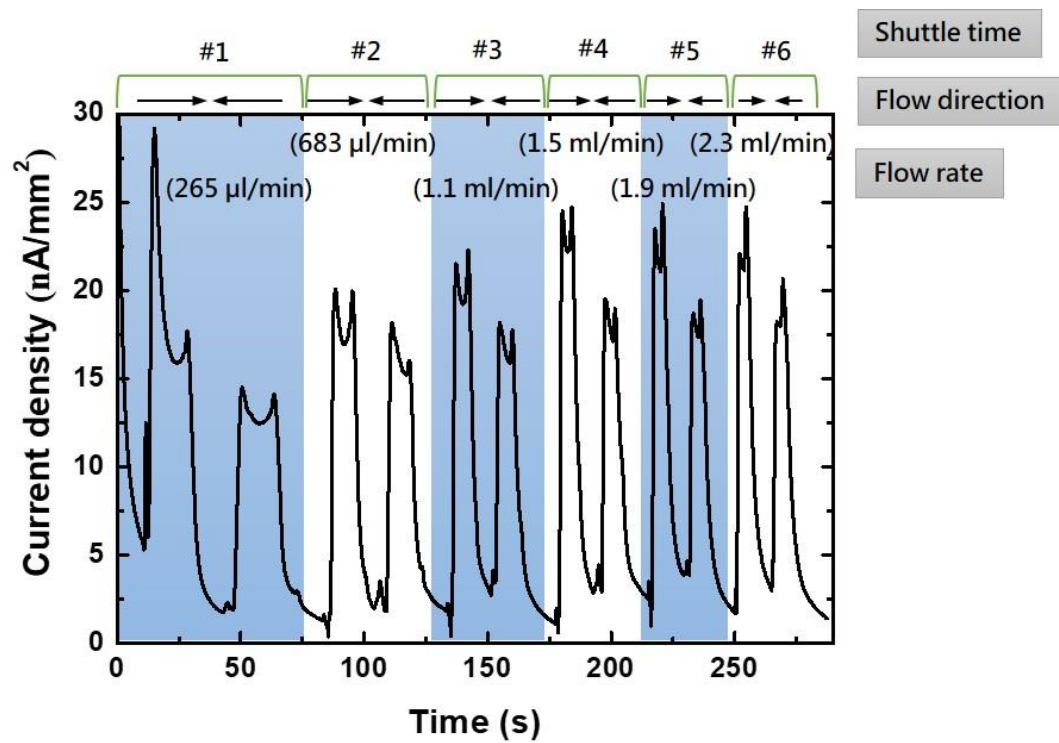
Figure 2.10 Chronoamperometry of the droplet-formed redox mediator under shuttle flow with different flow rates. The droplet size is 8 mm width, 3.5 mm height, and 17.6 mm length (volume is c.a. = 500 μl).
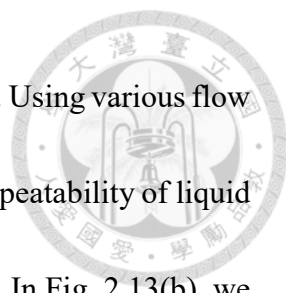
2.4.3 Calibration of the automatic pump system

Precise flow control can be achieved through a series of pump calibration. To operate the pump accurately, a stepper motor is used to drive the pump head with a programmable circuit shown in Fig. 2.11. The Arduino microcontroller has built-in functions that can easily control the stepper motor through entering the parameters of rotating speed, direction and delay time. The peristaltic pump head connected to the motor has several rotors which press the tube and push the gas forward during the rotating process. The flow rates depend on the rotating speeds of the motor, so it can be calibrated according to recording the moving distance of a droplet in the tube after the motor rotates a half turn with different speeds shown in Fig. 2.12(a). In Fig. 2.12(b), the moving distances are similar under slow rotating speed (less than 100 rpm), but the distances decrease as the speeds are up to 120 rpm. The failing liquid movement may be attributed to the incomplete gas pushing procedure due to the too fast rotor behavior. The flow velocities are determined by dividing the moving distance to the rotation time (shown in Fig. 2.12 (c)), and the flow velocities have good linearity to the rotating speeds in the range of 0~100 rpm. With this calibration curve, we can calculate the flow velocity directly through the applied motor speeds.

After that, the accuracy of shuttle transportation is analyzed with the pump rotating with alternatively changed directions. Owing to the continuous action of pressing tubes,

there possibly has the dead volume which affects liquid transportation. Using various flow rates and moving distances to manipulate the shuttle frequency, the repeatability of liquid positions is compared after 20 shuttle rounds (shown in Fig. 2.13(a)). In Fig. 2.13(b), we find that the position shifts of liquid are small under the shuttle flow with a short moving distance (2 cm), and the cases of long moving distance (4 cm) show a systematic shift to the downstream shown in Fig 2.13 (c). The position shifts may accumulate along with the long moving path, and the shift problem may lead to a detached situation which fails the electroanalysis after more shuttle rounds. Although the cases of short moving distance have a less position shift, the individual positions in each shuttle round under the fast shuttle frequency (5.3 Hz) show an unstable oscillation shown in Fig. 2.14. The following experiments will refer to the above calibration results and the limitation of shuttle frequency.
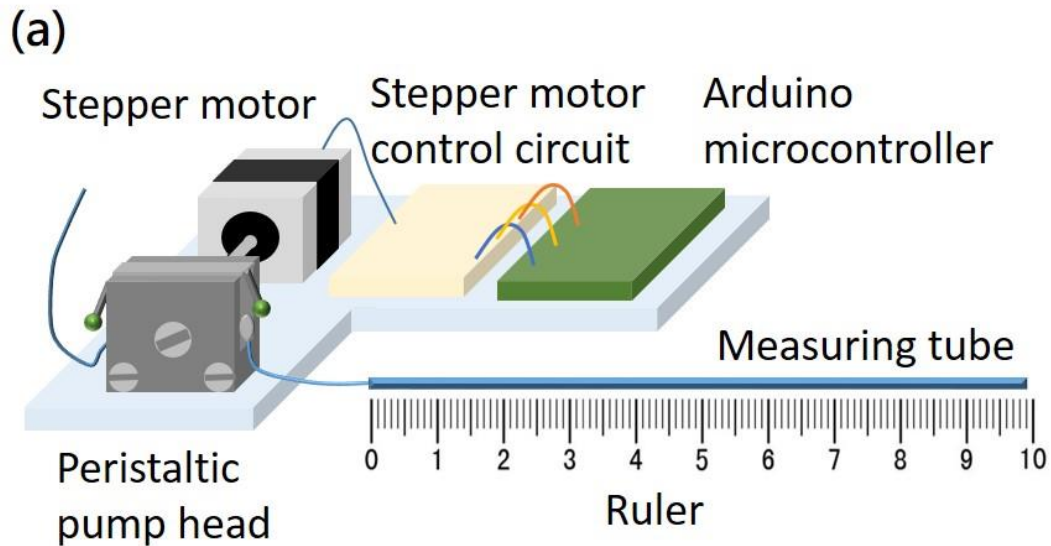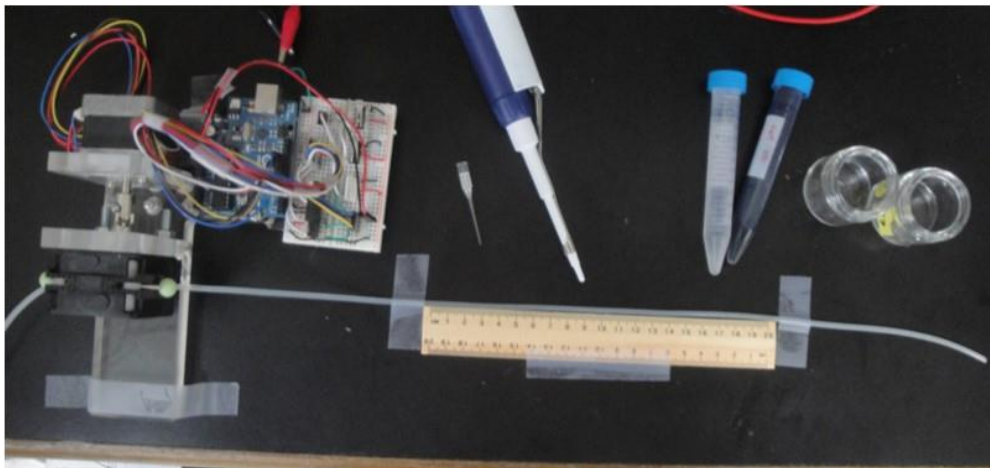
Figure 2.11 The improved pump system for the flow rate calibration. (a) A stepper motor

is connected to the peristaltic pump, and it can be modulated by a control circuit and a

Arduino microcontroller. (a) After the dye droplet is injected into the tube, the position of

the droplet is recorded with a ruler under different flow conditions.
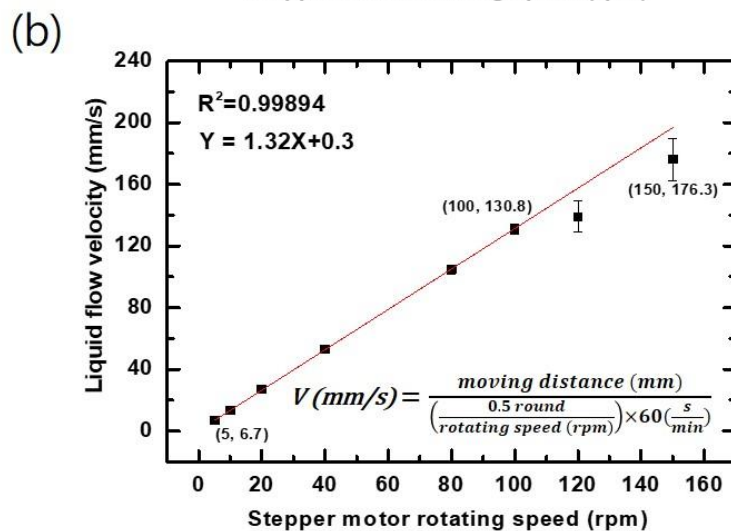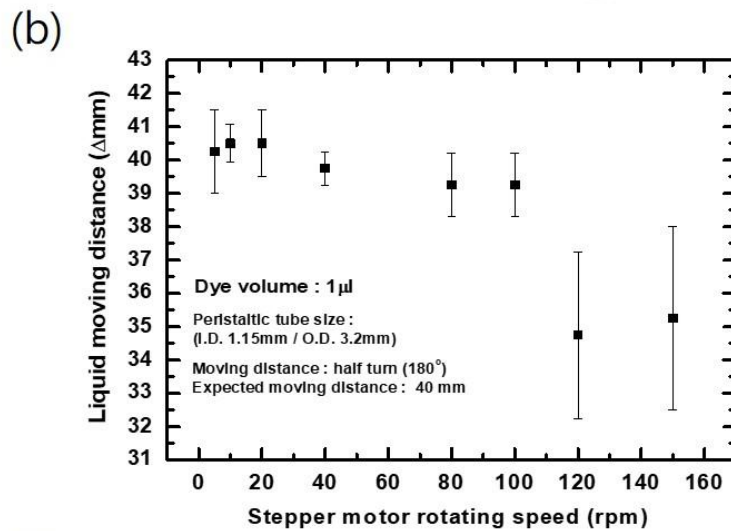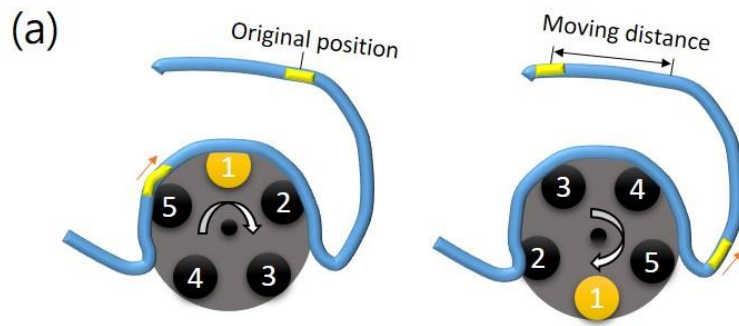
Figure 2.12 Calibration of motor speed and flow velocity. (a) The peristaltic pump is

rotated with a half-turn, and the moving distance of the droplet is recorded to find (b) the

correlation between the rotating speeds of the stepper motor and the liquid moving

distances, and (c) the calculated flow velocities.

53
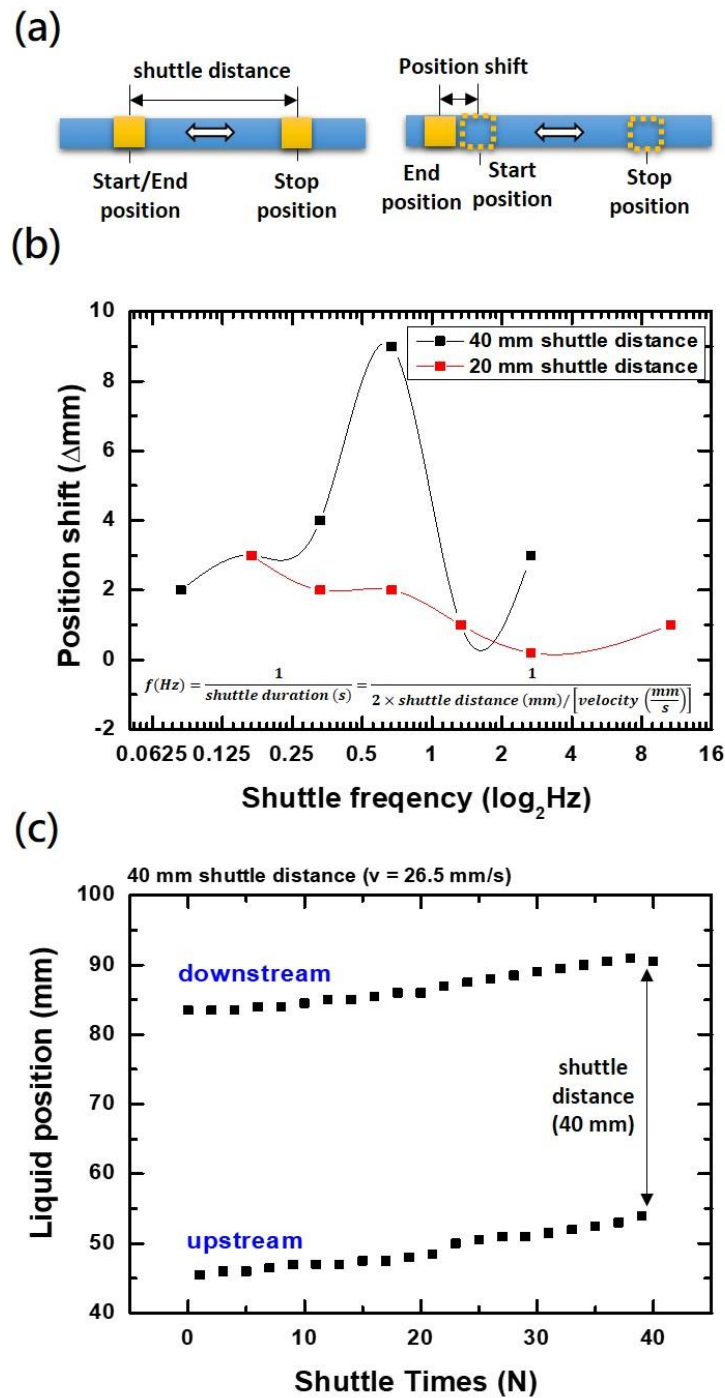
Figure 2.13 Position calibration of shuttle liquid droplet according to (a) the position deviation of droplet after a 20-time shuttle procedure (b) under different shuttle conditions, and (b) the terminal positions in each shuttle cycle are presented to observe the liquid shift process..
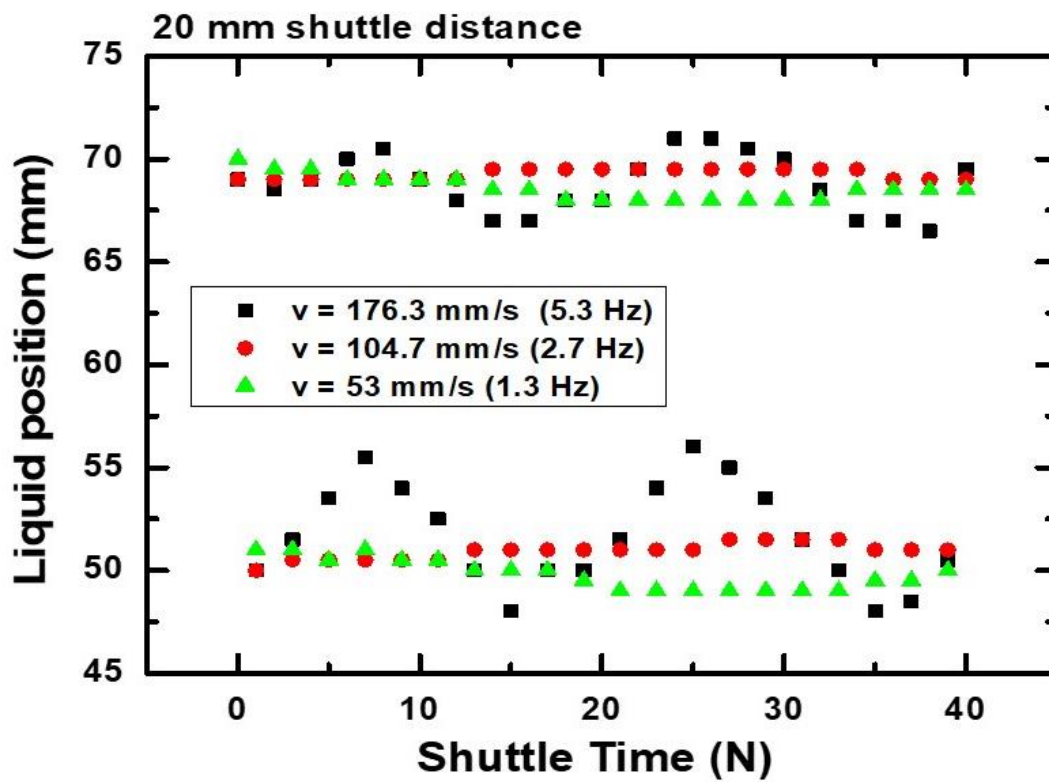
Figure 2.14 The positions of the liquid droplet when the shuttle flows with a small moving

distance (2 cm) are applied to the droplet with various shuttle frequencies.

2.4.4 Miniaturized fluidic device with microelectrodes and PDMS chips

After the electroanalysis methods and a precise pump system are established, we aim to further miniaturize the microfluidic device in order to observe the flow effect under a much smaller scale. Introducing the microelectromechanical systems (MEMS) technique involving a PDMS-based microfluidic channel and the microelectrodes, the previous experiments of droplet electroanalysis can be carried out in a mini device. A special structure of PDMS microchannel is designed with a flat chamber, main channels and gradient diffusers shown in Fig. 2.15(a). The chamber with a small height can reduce the diffusion length, and contrarily the main channels have a high height to lower the flow resistance. Additionally, the gradient diffusers are used to eliminate the sudden flow change when the liquid flows from the main channel to the chamber.

The fabrication of microelectrodes is based on lift-off process which can easily generate metal patterns on the substrate for electrode application. Firstly, considering the arrangement issue of electrodes encountering in the previous experiment, two kinds of three-electrode gold microelectrode chip are designed with different configurations. Three microelectrodes are aligned in serial and parallel sequences shown in Fig. 2.15(b). In the serial configuration, it is similar to the design of the screen-printed electrode which has a large CE and the same sequence of CE, RE and WE. In the parallel configuration, a major change of electrode sequence is presented that three electrodes have the opportunity

56

to contact the liquid at the same time. Interestingly, if the liquid flows in the opposite

direction, very different contacting sequences of the electrodes may happen that leads to

the unexpected current response. Finally, the PDMS microchannel and the

microelectrodes are assembled by the oxygen plasma treatment to produce a microfluidic

device for the following experiments of electroanalysis.
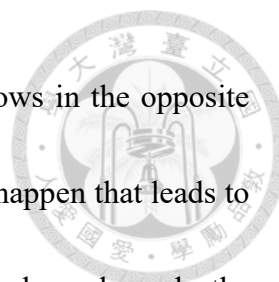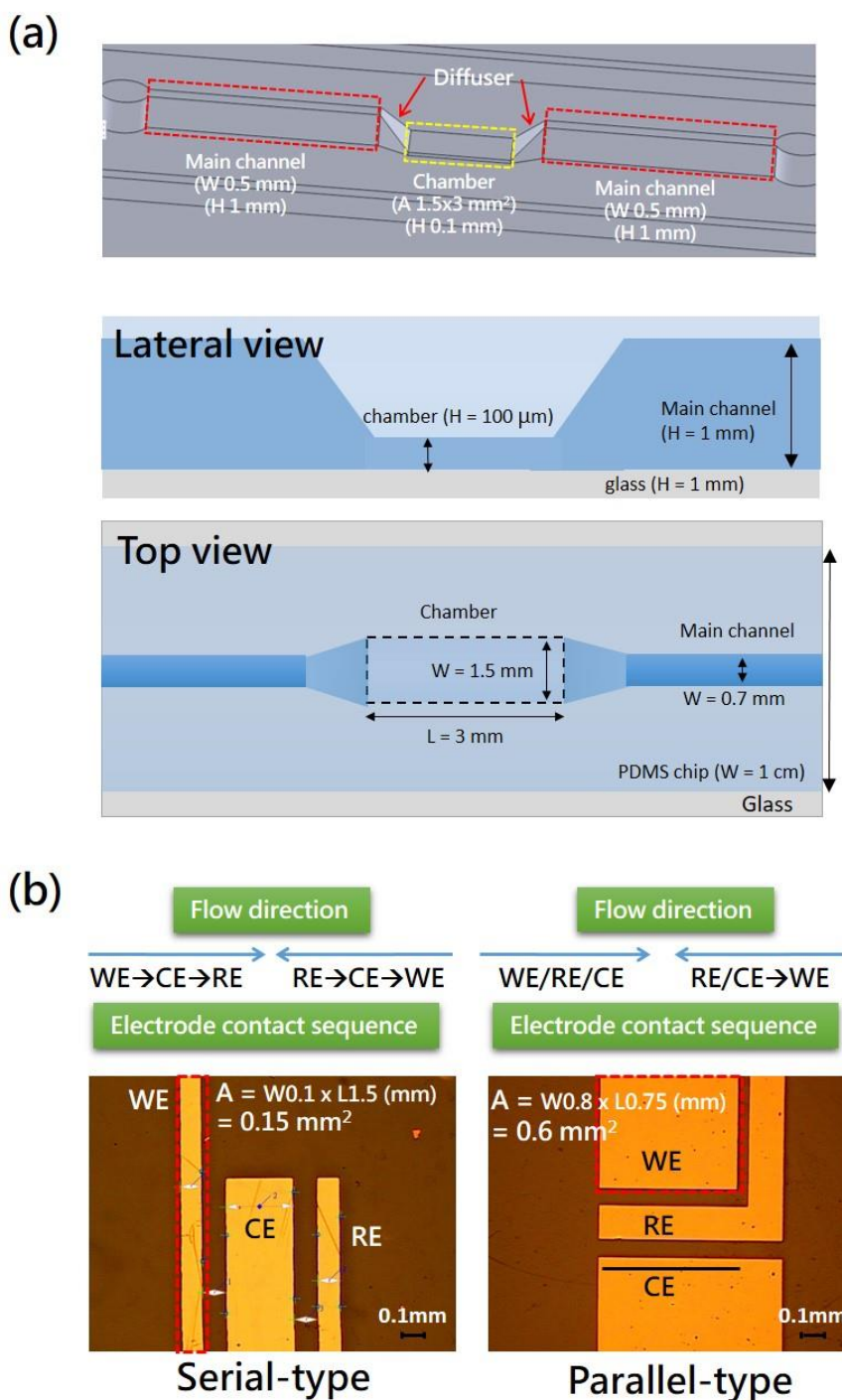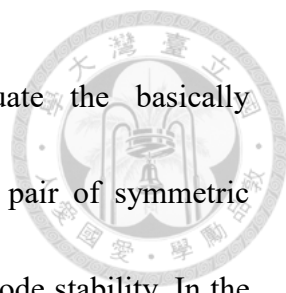
Figure 2.15 Miniaturized microfluidic electroanalysis devices combine (a) a special microchannel design including a flat chamber, two main channels and two gradient diffusers and (b) a three-electrode gold microelectrode chips with the serial and parallel arrangement.

Cyclic voltammetry (CV) is an ideal method to evaluate the basically electrochemical characterizations of microfabricated electrodes. A pair of symmetric redox peaks can be used to access the charge transfer and the electrode stability. In the CV profiles of the serial-type microelectrode chips shown in Fig. 2.16(a), the typical CV curves are found in a 20-cycle CV scan, and their peak currents decrease along with scan cycles. The decreasing current peaks may result from the tiny electrode surface that limits the charge transfer. The redox peak separation is small (0.1 V) because of the good conductivity of gold. Besides, the position of formal potential (-0.5 V) is also different from the SPE (+0.1 V), since the pseudo-reference is made of a gold electrode which has a distinct reference potential. With different CV scan rates, the corresponding peak currents raise along with increasing scan rate, and the diffusion constant can be calculated by Randles–Sevcik equation (shown in Fig. 2.16 (b)).

In the CV profiles of the parallel-type microelectrode chips shown in Fig. 2.17(a), the similar CV profiles are also obtained, and their peak currents enhance along with scan cycles until it reaches a steady state after 15-cycle CV scan. The increasing peaks may result from the activation of electrodes, and they show a twice height compared to the serial-type electrodes. With different CV scan rates, the corresponding peak currents raise along with increasing scan rate, and the diffusion constant can be calculated by Randles–Sevcik equation (shown in Fig. 2.17(b)).

59
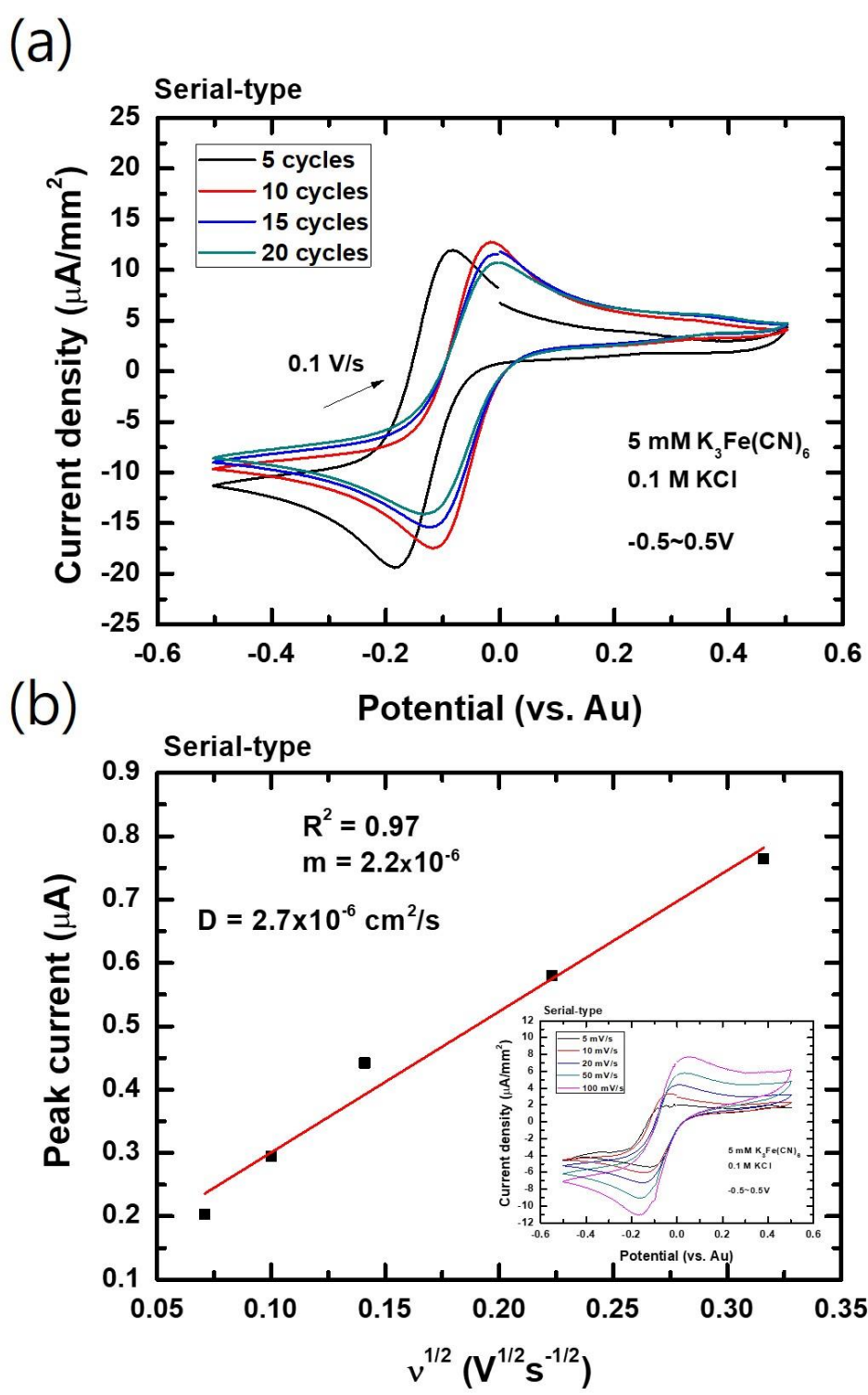
Figure 2.16 Electrochemical characterization of microelectrodes with the serial arrangement. (a) Stability in 20-cycle CV analysis and (b) diffusion constant obtained from CV scans with different scan rates.

60
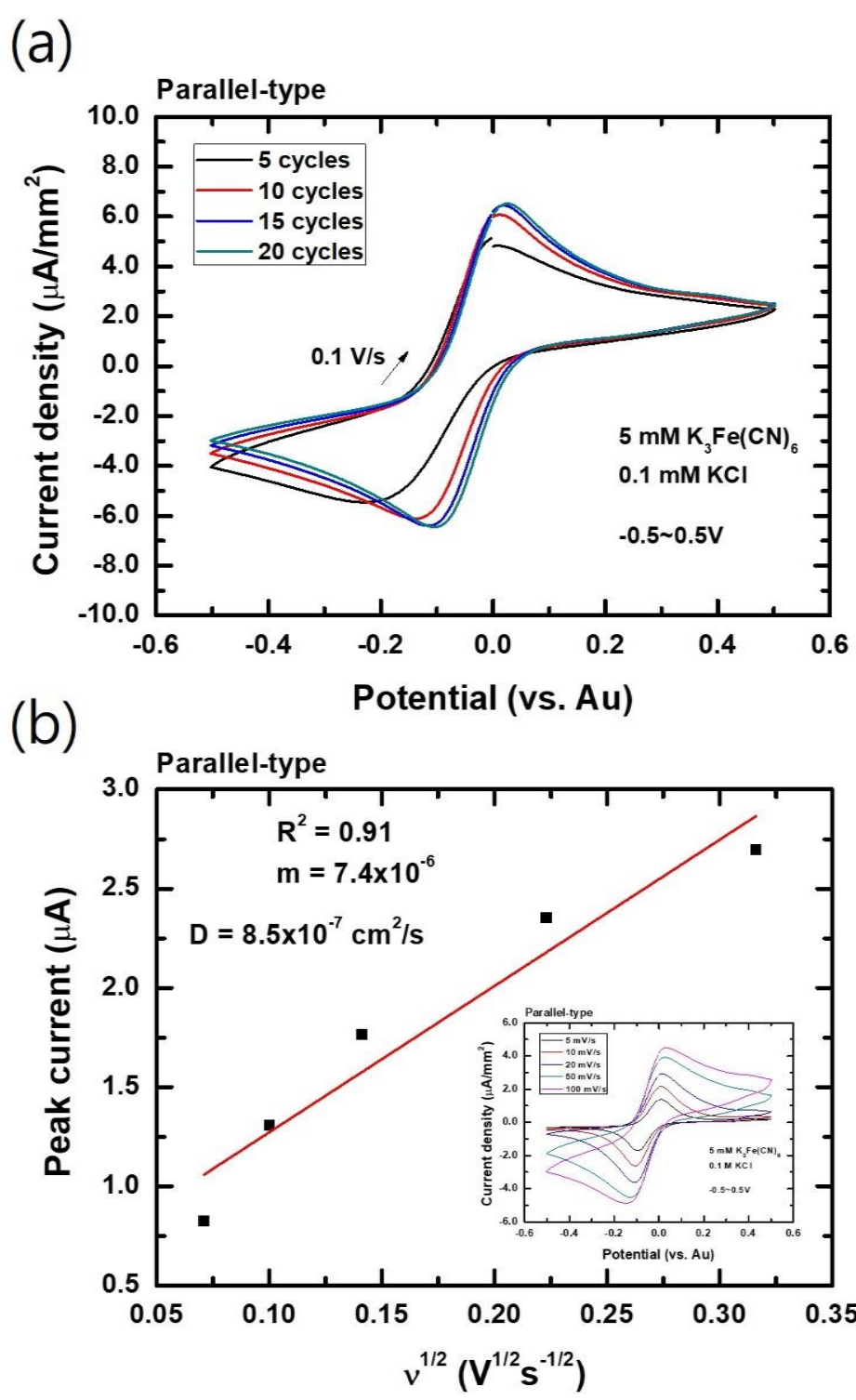
Figure 2.17 Electrochemical characterization of microelectrodes with the parallel arrangement. (a) Stability in 20-cycle CV analysis and (b) diffusion constant obtained from CV scans with different scan rates.

61
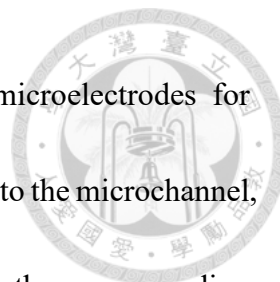
To investigate the real-time flow effect executed with the microelectrodes for dynamic electroanalysis, the droplets of redox mediator are injected into the microchannel, and the droplets are transported with various flow rate to produce the corresponding shuttle frequencies. As a constant voltage is applied on microelectrodes, the redox currents are measured *in-situ* to monitor the reaction response affected by the flow effect. In similar with the previous results obtained from SPE system, when the droplet flow through the serial-type electrodes, the negative current peaks occur unexpectedly (shown in Fig. 2.18). The peak profiles seem to be no obvious tendency, and the peaks overlay is observed as the shuttle frequencies enhance. It may result from the unstable reference electrode setting that reacts the redox mediator under different voltages. Further, the confused profiles may be related to the incomplete liquid cover on the electrodes which is mentioned before. Hence, this electrode configuration seems to be unsuitable for the droplet electroanalysis under flow conditions.

In parallel-type electrodes, the more regular peaks are observed, but the profiles are different with various shuttle frequencies (shown in Fig. 2.19). The first peak is usually small that echoes the above assumption of electrode activation. When the flow rate is slow, the redox mediator can be consumed completely that leads to a depletion zone. Additionally, because of the laminar flow in the microfluidics, the fresh redox mediator is hard to diffuse to the electrode surface that causes the decreasing current peaks along

with shuttle cycles. As the flow rate increases, the depletion-induced current decay slows

down because of the rapid mediator supplies attributed to the micro-mixing effect under

shuttle flow. The consistent peak heights are achieved under the flow rate of 53 mm/s

(rotating speed = 40 rpm). Nevertheless, when the shuttle frequency is too fast, the merged

peaks also occur that may be due to the improper interval (interval 0.1s) of data

acquirement in the instrument.
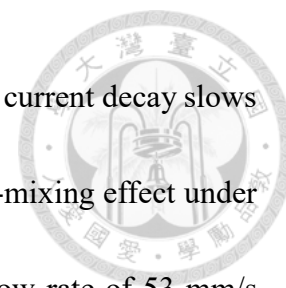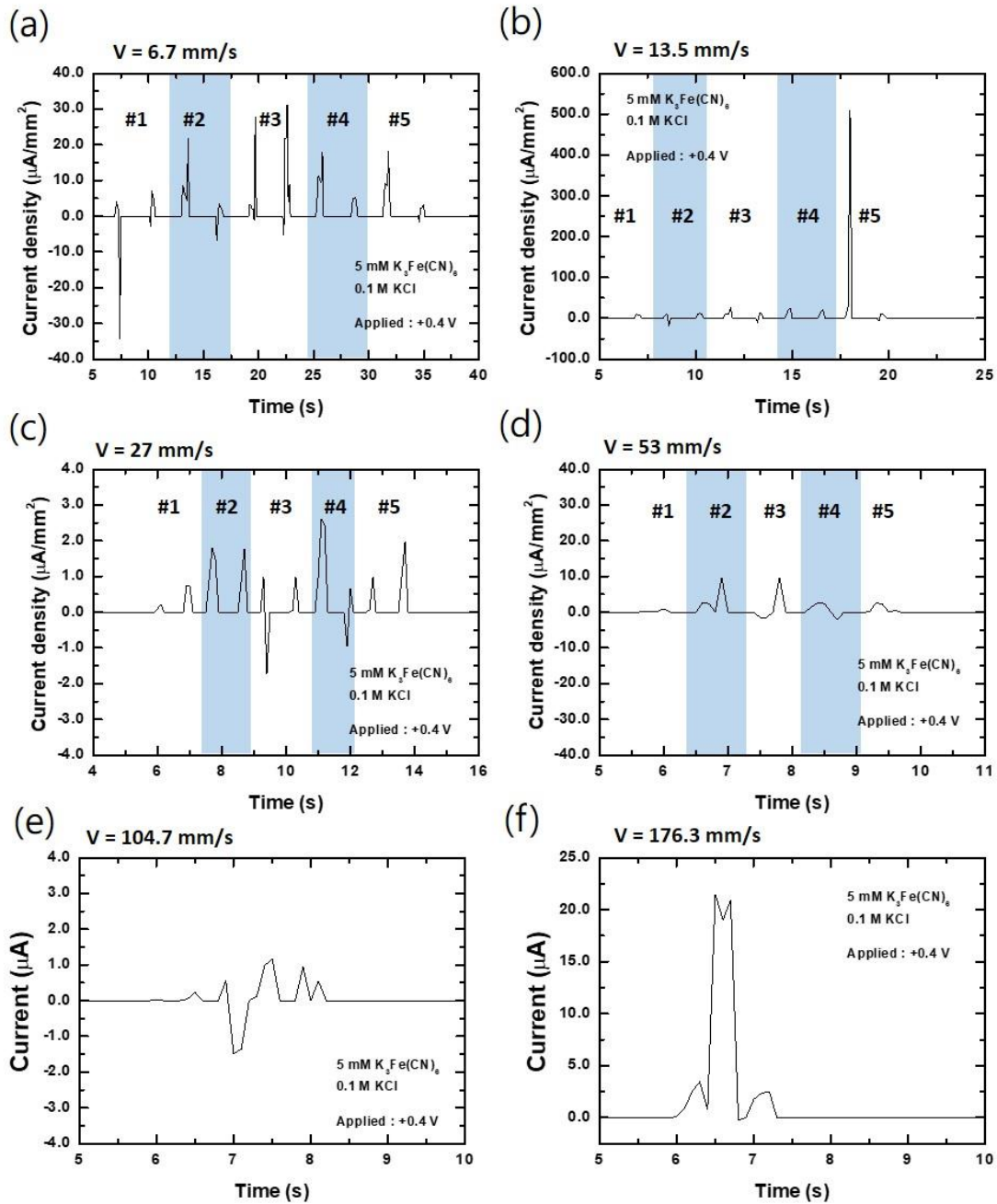
Figure 2.18 Chronoamperometry of serial-type microelectrodes under shuttle flow conditions. (a) 5 rpm (b) 10 rpm (c) 20 rpm (d) 40 rpm (e) 80 rpm (f) 150 rpm.
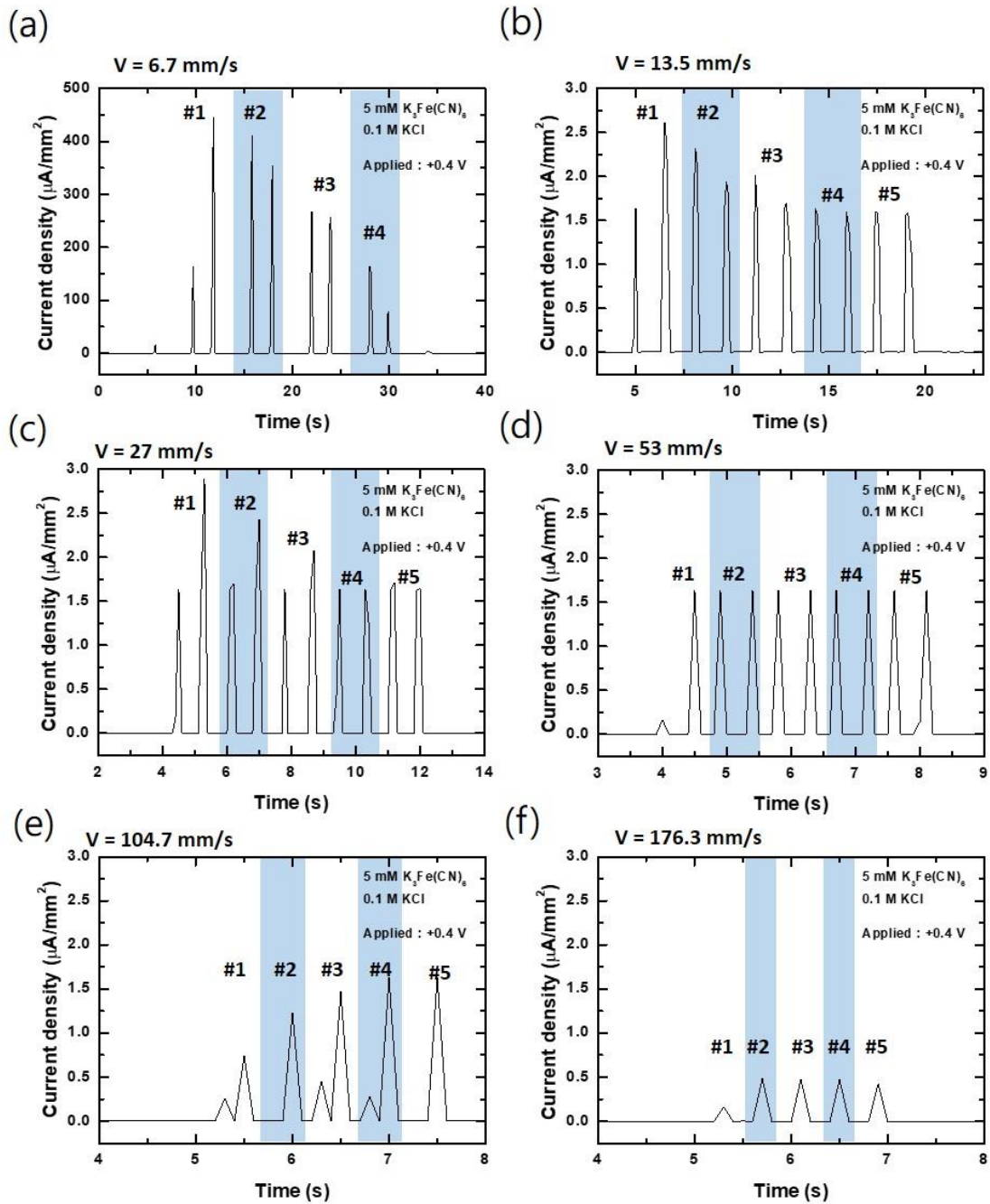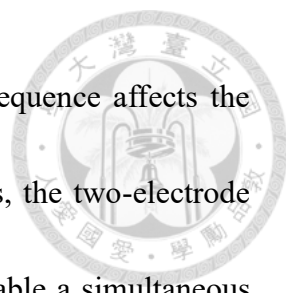
Figure 2.19 Chronoamperometry of parallel-type microelectrodes under shuttle flow conditions. (a) 5 rpm (b) 10 rpm (c) 20 rpm (d) 40 rpm (e) 80 rpm (f) 150 rpm.

In three-electrode configurations, we find that the electrode sequence affects the current response, especially under the shuttle flow conditions. Thus, the two-electrode configuration with the parallel-type arrangement is fabricated to enable a simultaneous contacting between the liquid droplet to the microelectrodes under shuttle flow. In the basic electrochemical analysis based on CV shown in Fig. 2.20(a), the phenomenon of electrode activation is also observed according to the increasing peak current along with the scan cycles. The peak separation of CV profile is larger, and a capacitance seems to occur. It may result from the electrode polarization which is induced by the redox reaction on both electrodes. By the reason of polarization, the double layer capacitance may generate that leads to a slower decay of diffusion-controlled current. With the increasing CV scan rates, not only the peak current raises, but also the peak separation expands. It may result from the too sudden voltage change that consumes the mediators around the surface and produces a depletion zone. The resistance of charge transfer makes the peak tending to the larger voltage, and the capacitance effect is erased via diffusion-induced depolarization process. The diffusion constant can be calculated by Randles–Sevcik equation (shown in Fig. 2.20(b)). In chronoamperometry of two-electrode chips under shuttle flow shown in Fig. 2.21, the similar peak heights imply a rapid compensation of redox mediator, but the fastest shuttle frequency can still cause a current decay due to the late supply.

66
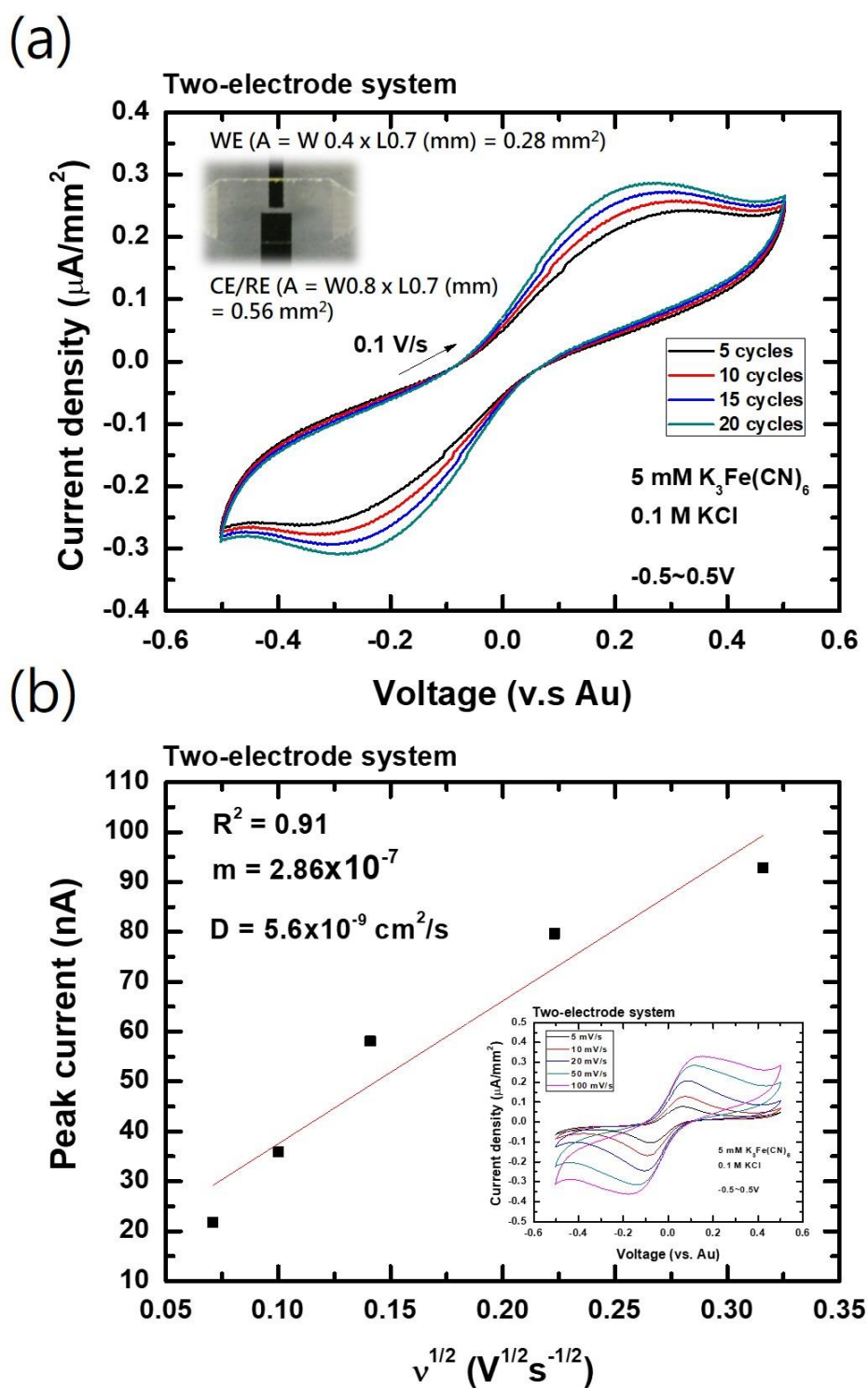
Figure 2.20 Electrochemical characterization of microelectrodes with a two-electrode configuration. (a) 20-cycle CV analysis. (b) CV scans with different scan rates. (c) Calibration curve for diffusion constant calculation.

67
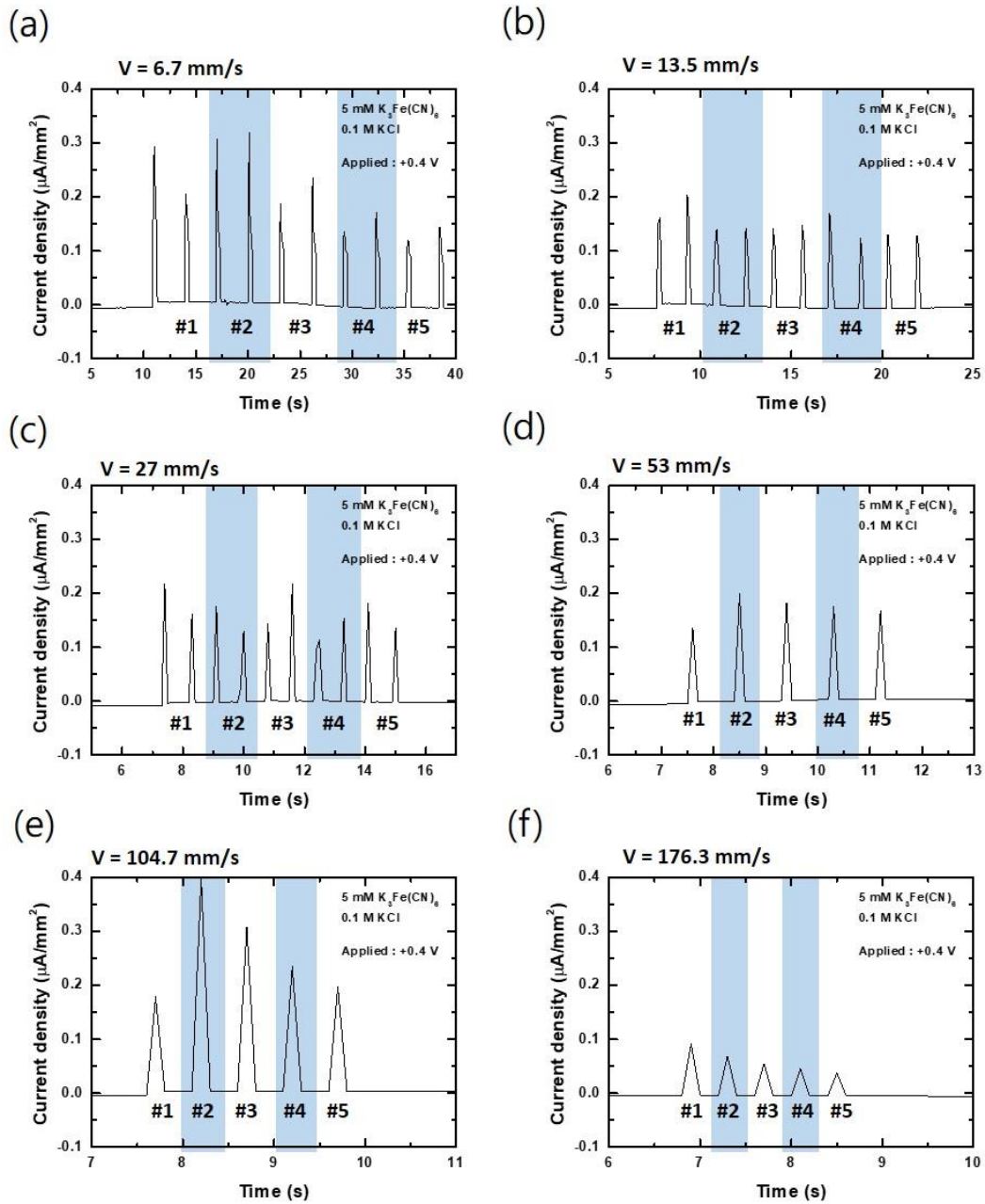
Figure 2.21 Chronoamperometry of two-electrode microelectrodes under shuttle flow

conditions. (a) 5 rpm (b) 10 rpm (c) 20 rpm (d) 40 rpm (e) 80 rpm (f) 150 rpm.

68

2.5　Chapter Summary

In this chapter, we successfully establish a fluid control system and miniaturize the system into a microfluidic chip. Aiming to investigate the flow effect, the reaction improvement is preliminarily proven via demonstrating the Prussian blue precipitation. Tube-based and chip-based reactors are compared to evaluate the reaction efficiency, and an efficient reaction is found in the chip-based system according to the more PB production. Moreover, the droplet electroanalysis can provide dynamic information of the redox reaction under flow conditions. Despite the unknown current response caused by the electrode sequence of the three-electrode system, the evidence of flow effect is still acquired through the chronoamperometry profiles. In the microfluidic chip embedded the microelectrodes, the tendency of mediator consumption and the mixing effect during the shuttle flow are discovered. Furthermore, to simplify the complicated responses in the three-electrode system, the two-electrode system is adapted, and it shows a great potential to perform a real-time detection for studying the flow effect in microfluidic electrochemistry. According to the above observations, the flow effect plays an important role to affect the reaction in the microfluidics. The extending applications in view of flow effect will be discussed in the following chapters.
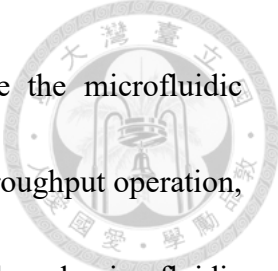
Chapter 3. 1D microbeads array for STAT3 aptamer selection

3.1 Introduction

Along with the development of the aptamer application, how to generate high-affinity aptamers in a short time becomes a very important issue. Especially, the high throughput and multiplex aptamer selection procedures are attractive research topics. To achieve the efficient aptamer evolution, the concepts of Darwin's Theory of Evolution involving sufficient variation, conditional competition, and survival of the fittest are key points to improve selection efficiency. Since the *in vitro* aptamer selection method called systematic evolution of ligands by exponential enrichment (SELEX) is invented by Ellington and Szostak in 1990 (Ellington and Szostak, 1990), the specific target-binding aptamers are generated through a great variety of strategies and platforms. In addition, among the complicated SELEX procedures, the partitioning of unbound DNAs plays an important role to accelerate the selection progress. With the aids of the techniques of protein immobilization including NC membranes, magnetic beads, and affinity columns, the researchers are not only able to easily separate the protein-binding DNAs and unbound DNAs, but also able to apply stricter washing conditions to remove the low-affinity aptamers. However, these diffusion-based DNA binding assays usually cost a lot of time to wait for a complete incubation which needs one hour at least.

More and more researchers tend to develop the microfluidic SELEX that carries out

70

the aptamer selection procedures in a microfluidic chip. Because the microfluidic technique shows the advantages of less reagent consumption, high throughput operation, and enhanced reaction. Huang *et. al* presented a magnetic bead-based microfluidic SELEX to automate the aptamer screening process (Huang *et al.*, 2012). In the microchannel which reduces the diffusion length from flow stream to the targets, the incubation time took only five mins utilizing a micromixer. After several selection rounds, the aptamers with high affinity and specificity were identified. However, although the magnetic beads can improve the reaction rate according to the large surface area, the tiny particles still have the risk of loss during the operation. Further, the targets need additional modifications (biotinylation) that may affect the unique structure of targets. Park *et. al* demonstrated the use of sol-gel arrays of proteins in a microfluidic system for efficient aptamer selection (Park *et al.*, 2009). The sol-gel matrix could entrap the protein in their native state without capture tags or molecular labels. Additionally, this platform could be used for multiplex selection if the different targets were trapped in the sol-gel array. Unfortunately, both methods can merely provide a 2D target exposure that may lead to a limited interaction. In the laminar-dominated microfluidics, although the DNAs near the surface can interact with targets rapidly, the DNAs in the stream are hard to diffuse to the surface. This characteristic may lead to miss the potential aptamer candidates. Hence, if the target immobilization becomes a 3D surface, more binding opportunities appear to

71

enhance the incubation process.

Inspired by the single bead SELEX technique developed by our lab (shown in Fig. 3.1) (Yang *et al.*, 2014), a 3D target immobilization system solving the above problem comes to mind. In the single bead SELEX, target proteins could be covalently bound to the epoxide-beads with the original amine groups without any modification. This method prevented the structure change of proteins, and the usage amount of proteins could be decreased. After the DNA incubation, the bead-binding DNAs could be analyzed and enriched individually that eliminates the influence of PCR bias. Moreover, the real-time evolution monitoring via qPCR analysis was proposed to trace the selection progress. Here, we assume that if the single bead SELEX is integrated into a microfluidic chip, not only the characteristics of short diffusion length and less sample consumption benefit to the aptamer selection, but also the configuration of bead array can achieve the high throughput aptamer screening. Besides, according to the discovery from chapter 3, the droplet mixing induced by the shuttle flow may further improve the reaction rate, and the repeated liquid transportation increases the washing strength to enhance the aptamer affinity. By establishing the bead-array SELEX platform, the flow effect on biological reaction enhancement is proven, and the improved features of the micro-mixing for effective incubation and the shearing effect for strict washing are demonstrated to produce the STAT3-specific aptamers.
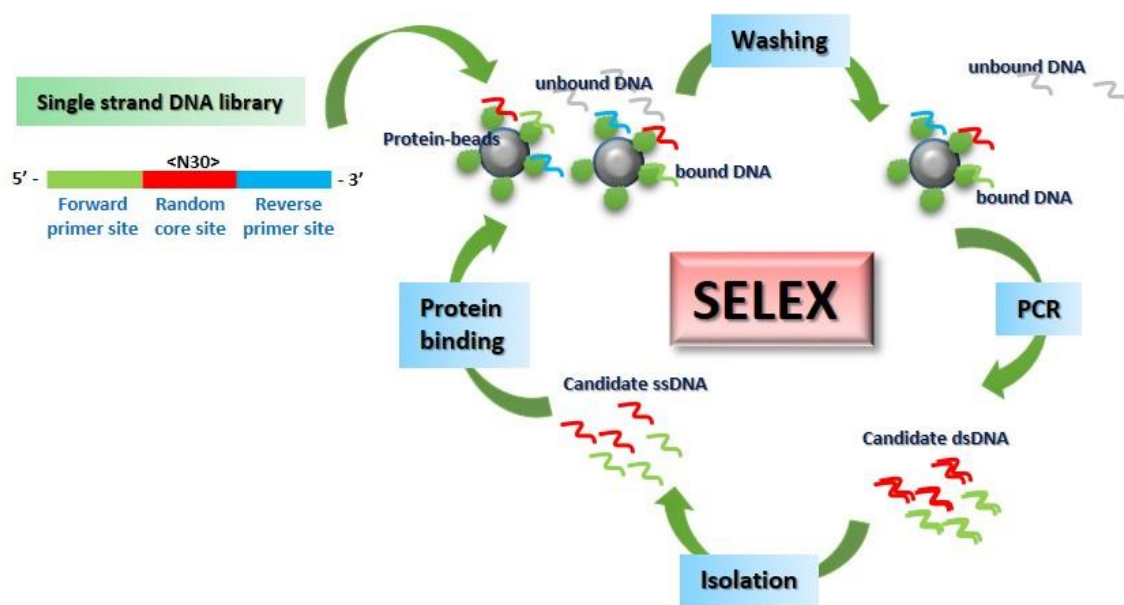
Figure 3.1 Single-bead SELEX includes four major processes in a single aptamer

selection round.
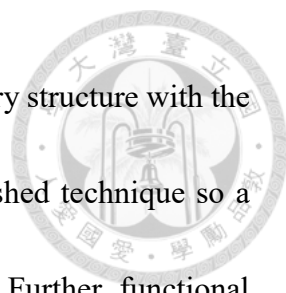
3.2 Literature review

3.2.1 Efficient selection of DNA aptamers in microfluidics

Aptamer is a promising artificial ligand which can specifically bind to its targets just like an antibody. Aptamers can consist of DNAs, RNAs or peptides, which are all sequence-dependent biomolecules. With different permutation of nucleotides or amino acid, the chain-like molecules can fold into a particular structure. Just like the key-and-lock model mentioned in the antibody, the specific structure can recognize its corresponded target according to the geometry match. Via hydrogen bonding, van der Waals and electrostatic interactions, the aptamers can attach to its target with high affinity. The targets of aptamer involve tiny molecules (ions, small molecules, peptides) and big things (proteins, cells, tissues). It reveals the versatile functionality of aptamers and potential biological applications. In comparison to the antibody, aptamers have many advantages including easy synthesis and modification, high thermal stability, *in vitro* generation, small size and low immunogenicity. With the superiorities, aptamers can well-assist the current antibody-based assays and even replace antibody in the future. Actually, a lot of aptamer applications are well-studied in the biosensors, environmental monitoring, and disease therapy.

DNA aptamer is an oligonucleotide having typically from 15 to 40 nucleotides in length. Four kinds of nucleic acid (A, T, C, G) are used to compose various

74

oligonucleotide chain. The long chain tends to form a stable secondary structure with the aid of particular ions (Na^+, Mg^{2+}). DNA synthesis is a well-established technique so a large number of DNA aptamers can be easily generated in a batch. Further, functional groups can be conjugated at the terminal of aptamers in the synthesis process. The extra functional groups are useful for aptamer immobilization and stability improvement. Because of the flexible structure in DNA molecules, even if the DNA aptamer is denatured at high temperature, it can refold to the initial structure when the temperature decreases.
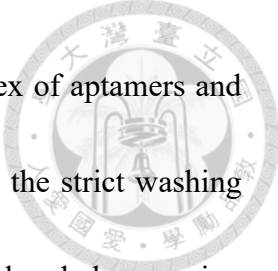
Before the DNA aptamer researches, there are already several studies on protein-binding oligonucleotides called small interfering RNA (siRNA). siRNA is usually a 21-base double-strand RNA which is generated by dicer enzyme. After the siRNAs are transfected into cells, they will interact with particular genes and proteins that lead to a gene knockdown. Decoy oligonucleotide (dODN) is another kind of DNA molecule for gene regulation in recent years. Decoy ODNs are used to block the transcription factors in cells that lead to the upgrade or downgrade gene regulations.

Both aptamers and dODNs can be generated by *in vitro* selection. However, selection procedures are complicated and time-consuming. To enhance the selection efficiency, the microfluidic platform is introduced to decrease the reagent consumption and to increase incubation and partitioning performance. Efficient selection of DNA aptamers is an attractive topic for the next generation aptamer researches.

75
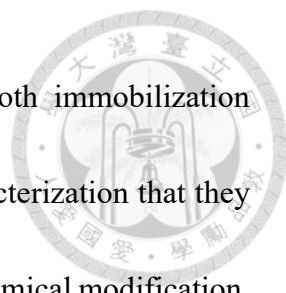
3.2.2 Systematic evolution of ligands by exponential enrichment
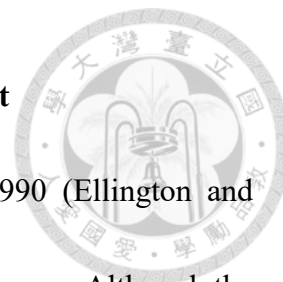
SELEX is a typical aptamer selection method presented in 1990 (Ellington and Szostak, 1990), and it becomes well-developed in the following few years. Although the complicated procedures in SELEX make the experiment last from a few weeks up to a month, this method still provides a standard for aptamer production. At the beginning of the selection, an artificially synthesized DNA library is prepared, and it usually has a core random region with flanked primer sites. The library includes up to 60-mer random sequence because it determines the diversity of the initial DNA library (Sampson, 2003). Low random level causes an insufficient diversity, and excess random level leads to the diversity leak in a single selection. After the DNA library is refolded through a thermal denaturing and an air cooling, the DNA molecules will form stable structures in the particular buffer condition. Mixing the library and target molecules, the binding reaction is carried out to capture the DNAs. With serial washing steps, unbound and weak-bound DNAs are removed. This partitioning process is a critical step to identify a high-affinity aptamer before the following PCR amplification. To enrich the retained DNA pools, several PCR cycles are utilized along with the designed primer sets. DNA isolation is used to generate single-strand DNA for the next SELEX round. Through a number of selection rounds, potential aptamers are sequenced, and its affinity and specificity are evaluated by various assays.
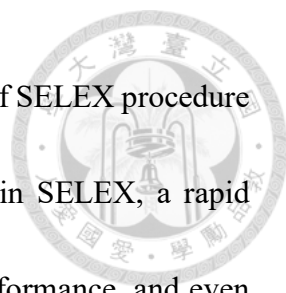
In order to separate the soluble materials which mean the complex of aptamers and targets, one of them should be fixed on a solid support for enduring the strict washing steps. In comparison to DNAs, the targets like proteins and peptides already have amino acid and carboxylic groups for target immobilization without extra labeling. Additionally, instead of the covalent bonding which needs a complicated procedure, polyvinylidene difluoride (PVDF) membranes and nitrocellulose (NC) membranes can adsorb proteins via hydrophobic and dipole interactions (Pristoupil and Kramlovă, 1968; Liu *et al.*, 2012). The protein binding capacity of PVDF and NC are 170 to 200 $\mu g/cm^2$ and 80 to 100 $\mu g/cm^2$, respectively. Target proteins can be easily immobilized on the membranes by directly dropping the protein solution on the membrane. After the DNA library is added to interact with proteins on the membrane, the washing step starts to eliminate the unbound DNAs. Recently, magnetic beads provide another option of solid supports for the protein immobilization. Various functional groups and ligands including amino-, carboxyl-, epoxy- and streptavidin are available on magnetic beads via relative chemical conjugations (Stoltenburg *et al.*, 2005). Moreover, a large surface area of magnetic beads provides higher protein binding capacity. Although the particle sizes of magnetic beads are small, the complex instrument is unnecessary for beads operation. Collection of beads can be achieved by an external magnet, and dispersion of beads can be accomplished by vortex mixing. Using biotin-streptavidin as an example, the target proteins should be

77

biotinylated before the protein is mixed with magnetic beads. Both immobilization methods of the membrane and magnetic bead have a common characterization that they preserve the natural property of target proteins. Without additional chemical modification, the proteins can be kept in an original state which is more similar to a practical situation. However, these methods also induce an orientation problem that the proteins may attach to the surface with different directions (Filali *et al.*, 2019). It means the exposed binding epitopes may be distinct.

Aptamer validation is an important step to evaluate aptamer performance. Affinity and specificity of aptamers can be quantified by various bioassays. In affinity measurement, k_d values are usually used as a factor of comparison. Estimation of k_d values can be employed by all-solution methods and partner-immobilization methods. In all-solution methods including isothermal titration calorimetry (ITC), capillary electrophoresis (CE), chromatography and nuclear magnetic resonance (NMR), the demands of high sample concentration make the assays hard to reach high throughput applications. The dissociation constant (k_d) is estimated in an equilibrium condition. In contrast, the partner-immobilization methods including surface plasmon resonance (SPR), enzyme-link aptamer assay (ELAA) and thermofluorimetric analysis (TFA). They can provide the dynamic dissociation constant closed to the true k_d. Especially, SPR is a gold standard for the affinity validation which can reveal the real-time binding response.

78

To enhance the efficiency of aptamer selection, the optimization of SELEX procedure and platform is necessary. Among the various experimental steps in SELEX, a rapid incubation and a rigorous partitioning can improve the selection performance, and even the selection can be completed in a single round. Single-round SELEX can not only save much time on the complicated SELEX procedures but also prevent the PCR bias which may cause an unfair sequence amplification. Therefore, it becomes a noticeable research topic in aptamer development.

3.2.3 Microfluidic SELEX

Microfluidic technology shows a lot of advantages for biological and chemical developments. According to the limitations of traditional SELEX, the microfluidic platform can provide corresponding solutions to improve selection performance.

First, the automatic microfluidic system based on programmable pumps and valves can accomplish all the complicated SELEX procedures by a designed program. A microfluidic SELEX prototype having microline-based assembly is displayed for the anti-lysozyme aptamer selection (Hybarger *et al.*, 2006). The liquid is automatically transferred to the protein binding region and the RT-PCR region in turn. The automated workstation is also a powerful tool for efficient aptamer selection (Cox and Ellington, 2001). The robot integrates various units including a thermal cycler, magnetic particle separator, vacuum filtration manifold, pipette tip carousel, and enzyme cooler. All the

79

elements can be controlled by a personal computer. A microfluidic SELEX based on the magnetic beads is carried out for finding anti-lysozyme aptamers. After twelve rounds taking about 48 hours, the selected aptamer can successfully inhibit the lysozyme and prevent the cell lysis.

Second, the precise behavior control under micro-scale is a beneficial feature for micro-fluid and micro-particle operation in a microfluidic system. In the typical bench-top operating of magnetic beads, the loss of beads during the repeated liquid transfer causes a serious problem. Additionally, the magnetic beads may aggregate together under incorrect operation, and the aggregated beads will reduce their binding capacity. The micromagnetic separation (MMS) chip is developed to generate large magnetic field gradients in the microchannel (Qian *et al.*, 2009). The magnetic field can efficiently trap the aptamer-bound magnetic beads. With MMS chips, a more stringent selection condition is applied to accelerate aptamer selection with small amounts of target proteins. The streptavidin aptamers are identified through three SELEX rounds and its affinity display dissociation constant arranging from 25 to 65 nM. Shortly, an improved MMS chip is presented with the name of continuous-flow magnetic activated chip-based separation (CMACS) (Lou *et al.*, 2009). A multi-stream laminar fluidic architecture is utilized to produce the hydrodynamic focusing that achieves a high partition efficiency. The localized magnetic field gradients supplied by magnetized nickel strips forces the

80

aptamer-bound beads to transport from sample stream into the central buffer stream. According to the serious selection conditions, aptamers against recombinant *Botulinum* neurotoxin type A are found after a single round SELEX.

Third, except for the incubation time taking one hour, the PCR amplification occupies most of the time in a SELEX round. The time-consuming procedure results from the slow heating and cooling rate in traditional PCR machines. To carry out the PCR amplification, it takes incredible time for various thermal equilibrium which is owing to the thermal conductivity. PCR microchip based on microfluidic technique can solve this problem. A micro-fabricated chamber containing few amounts of PCR mixture is heated to particular temperatures by micro-heaters, and the temperature is monitored by micro-thermometers to maintain the stability of temperature. Although the tiny volumes of PCR reagent already speed up the amplification via rapid thermal equilibrium, the whole reaction is still slowed down due to the limited heat source in the static condition. Therefore, many researchers aim to develop the flowing microfluidic PCR in order to overcome the thermal problems. Continuous flow PCR (Kopp *et al.*, 1998) and oscillatory (shuttle) flow PCR (Sugumar *et al.*, 2010) are common strategies that transport the PCR mixture from one temperature zone to the others. Three heating blocks set with different temperatures are settled in a microfluidic chip. Because the temperatures in each heat zone are pre-equilibrium before the PCR procedure, only the thermal equilibrium between liquid and
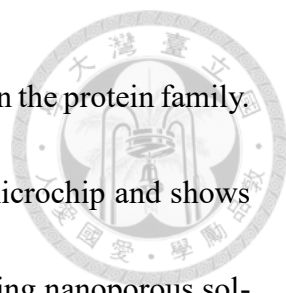
blocks is needed that saves much time in a multi-cycle PCR. Furthermore, digital PCR (Hindson *et al.*, 2011) and emulsion PCR (Williams *et al.*, 2006) are invented according to the micro-droplet technology. Using special microchannel designs, PCR mixture can be formed to micro-droplets, and there is only a single DNA template in each droplet. This mechanism can eliminate the PCR bias since the sufficient and fair PCR components are provided for each DNA template in micro-droplets. Hence, the microfluidic SELEX chips integrated microfluidic PCR are developed to enhance the selection efficiency (Huang *et al.*, 2012). In this chip, the DNAs bounded on the magnetic beads can be amplified *in situ* after a serial of incubation and washing steps. The aptamers against C-reactive protein (CRP) (Huang *et al.*, 2010a) and even cancer cells (Hung *et al.*, 2014) are generated after a few SELEX rounds. This microfluidic SELEX only takes three days to accomplish all the procedures.
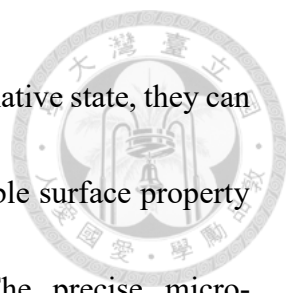
Fourth, it is hard to handle the aptamer selection targeting on more than one target simultaneously in traditional bench-top, because the separation of different DNA-bound targets is difficult. If one SELEX procedure spends a few weeks, it should take several months to achieve the aptamer selection against multi-targets. The reason to develop the multiplex SELEX is the niche of the aptamer cocktail which can improve the affinity via multi-epitope binding. In the cancer cell research, many protein families are discovered as the relevant biomarkers, and they are usually similar in structure and property. It

82

becomes an important issue to know how to distinguish the members in the protein family. The microfluidic platform can integrate many operation units in a microchip and shows great potential for high-throughput screening. A microfluidic chip using nanoporous sol-gel arrays with integrated micro-heaters is performed for multiplex aptamer selection (Park *et al.*, 2009). Five sol-gel binding droplets imbedding target proteins are spotted on the PMMA pad, and the gelled droplets can enable the entrapment of proteins in their native state. Two duplications of TFIIB and TBP aptamer SELEX and one counter SELEX are carried out in a single microchannel. The eluted DNA pools obtained from each round are compared according to the affinity assay. The microfluidic SELEX platform successfully improves the selection efficiency for multiplex selection. Furthermore, this device can be extended to execute the aptamer selection against five different proteins including BSA, TBP, TFIIB, eGFP, and HSF (Lee *et al.*, 2013). A cross-contamination-free SELEX platform using pneumatic valves to serially load samples and seal the adjacent elution chambers is demonstrated to prove the parallelization of chemical processes.

Fifth, the microfluidic system is able to automatically control various parameters in a micro-environment. Various micro-sensors and micro-actuators can be integrated into microfluidic chips for monitoring the conditions in this tiny reactor. Additionally, it is convenient to modify the channel surface through injecting reagents into the microchip.

Although the surfaces of PDMS and glass are both hydrophobic in a native state, they can be turned into hydrophilic by treating oxygen plasma. This changeable surface property makes the chips suitable for various material modification. The precise micro-environment control provides a great platform for cell culturing and analysis. To provide a comfortable surrounding for cell growth, the buffer condition and CO_2 amounts should be exactly controlled. A microfluidic chip system is developed to improve the efficiency of cleaning non-specific binding DNA from the cell surface (Weng *et al.*, 2012). After the target cells are assembled on the chip, the ssDNA library will incubate with cells. The electrophoresis applies into the chip for unbound DNA partitioning, and then the bound DNAs are collected for PCR enrichment. Moreover, ovarian cancer (OvCa) cells and tissues are seeded on a chip for the aptamer screening (Hung *et al.*, 2014). Similar to typical SELEX procedure, the aptamers with high affinity are identified after several selection rounds. However, in comparison to the typical SELEX, cell-SELEX can implement the selection with uncovered information from whole cells. Instead of using recombinant protein as selection targets, the aptamers obtained from real cells show great feasibility of clinical applications.

Table 3.3 Aptamer selection in a microfluidic chip
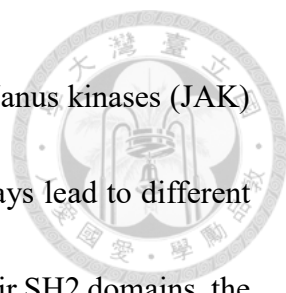
Method	Target	Performance	Ref.
Microline	lysozyme	31 nM / 12 rounds	(Cox and Ellington, 2001)
MMS device	streptavidin	25 to 65 nM / 3 rounds	(Qian *et al.*, 2009)
CMACS device	Botulinum neurotoxin type A	33 nM / Single round	(Lou *et al.*, 2009)
Integrated PCR	AFP	2.37 nM / 6 rounds	(Huang *et al.*, 2012)
sol-gel arrays	TBP	4 nM / 8 rounds	(Park *et al.*, 2009)
Microcolumn	hHSF	< 20 nM / 3 rounds	(Latulippe *et al.*, 2013)
Micro-bead array	STAT3	High specificity to HSA / 5 rounds	This work

85

3.2.4 Meaningful biomarker for aptamer selection - STAT3 protein

The targets for aptamer selection can be peptides, proteins, and whole cells. Finding a meaningful target among considerable numbers of known biomarkers becomes a considering issue. Since the thrombin aptamers are identified and continuously studied, they act as a standard target for proving the novel sensing or selection platforms. Recently, the biomarkers related to cancer cells are highly attractive because there show dawns for the possible therapeutic of deadly cancer diseases. Intracellular and extracellular biomarkers are widely studied for early cancer diagnosis and cancer inhibition. For example, mucin 1 (MUC1) is an extracellular protein showing overexpression on the surface of cancer cells. Hence, MUC1 aptamers are useful probes to recognize the cancer cells for further treatments. On the other hand, the abnormal proliferation of cancer cells results from the failed gene regulation. If the relevant gene about cell apoptosis can be well-controlled via artificial molecules, the molecules may become an effective drug for cancer therapy.

Signal transducer and activator of transcription (STAT) proteins are intracellular transcription factors, and there are seven members in their family including STAT1, STAT2, STAT3, STAT4, STAT5a, STAT5b, and STAT6. They play an important role to mediate the cellular signal transduction which is related to cell proliferation, apoptosis, and differentiation. Generally, the signal transmission begins from the stimulation of

86

cytokines and growth factors on the cell membrane. The stimulated Janus kinases (JAK)

induces the primary activation of STAT proteins, and various pathways lead to different

gene regulations. As the activated STAT proteins form a dimer via their SH2 domains, the

complex can transport to the nucleus with the aid of importins. In case the STATs get into

the nucleus, they will recognize the consensus DNA called gamma-activated sites (GAS)

in the promoter region. After the STAT-DNA binding, a series of transcription and

translation starts to express the particular proteins. Finally, the mission-completed STATs

dissociate from the gene, and they are deactivated to the origin states.

STAT3 is a member of the STAT protein family. Under the activated state of STAT3,

the tyrosine 705 and serine 727 can be phosphorylated by JAKs and MAPKs, respectively.

The activated STAT3 can form homodimers and heterodimers, and translocated to the

nucleus for the gene regulation (shown in Fig. 3.2). STAT3 mediates a lot of genes in

response to cell growth and apoptosis, and it is found to be related to abnormal

proliferation and immunosuppression in tumors. In the cancers, the dysregulation of the

STAT3 pathway is usually observed, and it enhances the survival of tumors and

immunosuppression. According to the gene knockout experiments, the importance of

STAT3 on the immune system and tumor surveillance is proven. STAT3 overexpression

is discovered in many cancers including head and neck cancers (Sen *et al.*, 2012; Mali,

2015) and breast cancers (Banerjee and Resat, 2016), and so on. Therefore, a variety of

researches focusing on STAT3 inhibition occur to find the therapeutic potential of cancer disease.

In accordance with the principle of STAT3-related cancer growth, the inhibitors targeting three major aspects (phosphorylation inhibiting, SH2 domain shielding and DNA-binding domain blocking) are developed by various selection strategies. Phosphotyrosine (pTyr)–SH2 domain interaction is disrupted by small molecules which are created by computational modeling (Leung *et al.*, 2015). After fluorescence polarization (FP) assay and SPR, analysis, the small molecules are proven to induce an antitumor response in human breast tumor. Stattic is another small-molecule STAT3 inhibitor which blocks the SH2 domain whether STAT3 is activated or not (Schust *et al.*, 2006). A specific STAT3-binding peptide is generated as a novel "aptide" to block STAT3 phosphorylation and reduce expression of STAT targets (Kim *et al.*, 2014). The results show that aptide can suppress the viability and proliferation of cancer cells. An imidazole analog is synthesized to suppress the phosphorylation and induce apoptosis in myeloma and lung cancer cells (Liby *et al.*, 2006). Gene microarray assay is used to verify the gene profiles in cell extract after cancer cells are treated by inhibitors. The small molecule can also target on DNA-binding domain to inhibit the cancer cell proliferation (Huang *et al.*, 2014). It can selectively inhibit the DNA-STAT3 binding without affecting the activation of STAT3 dimers. The results of electrophoretic mobility shift assay (EMSA) prove that

the small molecule has the same binding epitope with *c-fos* consensus. Mentioning the inhibition of DNA-binding in STAT3, decoy oligonucleotide (dODN) is a promising strategy to inhibit tumor angiogenesis (Tadlaoui Hbibi *et al.*, 2009). Deriving from the promoter sequence, dODN can bind to the activated STAT3 dimers before they transport into the nucleus. This mechanism successfully induces cell death in a human colon carcinoma cell line.
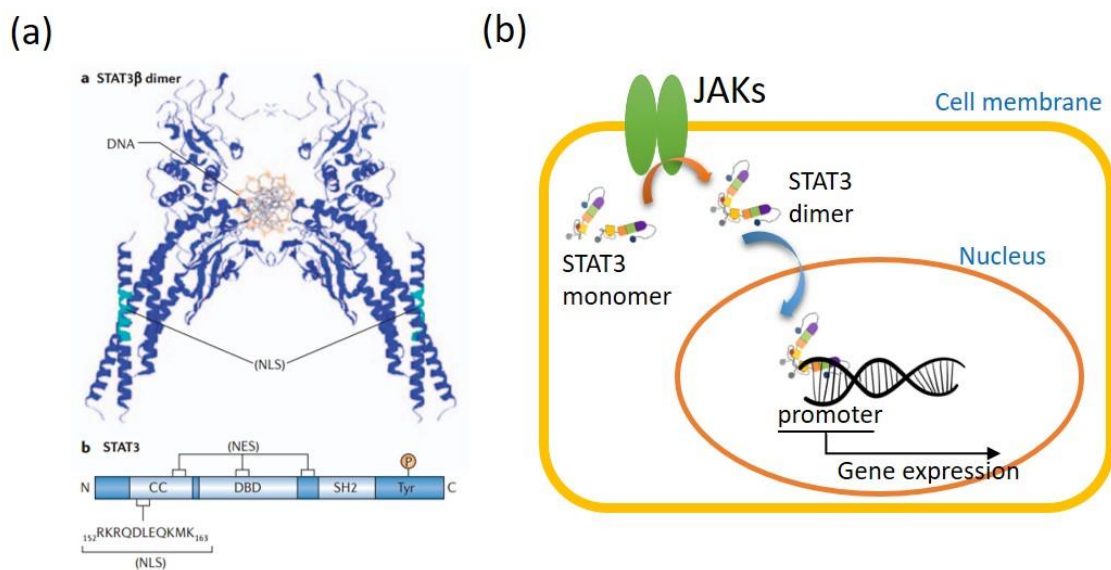
Figure 3.2 STAT3 protein forms (a) a heterodimer with three major domains (Sgrignani *et al.*, 2018), and (b) the activated STAT3 dimer is transported into the nucleus to regulate the gene expression.

3.3   Experimental

● Reagents and materials

The glass beads (0.5 mm diameter) are purchased from Scientific Biotech Corp. The recombinant full-length human STATs proteins (SignalChem) are purchased from Bio-Genesis LTD. Human serum albumin (HSA), 3-Glycidyloxypropyl-trimethoxy silane (GLYMO), glycine, ampicillin, betaine (5M), DMSO, NaOH, and agarose are purchased from YU HO REFRACTORIES Co., LTD. 35% H_2O_2, 98% H_2SO_4, 95% ethanol, toluene, 10x SSC buffer, and acetone are purchased from HSIN MING CHEMICAL INSTRUMENTS Co., LTD. Bradford assay kit is purchased from Genmall Biotechnology Co., LTD. Glass slide and peristaltic tube are purchased from HonDwen Co., LTD. Electronic components used in pump controlling circuit are purchased from YD-TECH. PDMS is purchased from Bingbond Co., LTD. PTFE tube is purchased from Leo Flon Co., LTD. Single strand DNA library and oligonucleotide primers (R9R/RPF and T7/SP6) are synthesized by Integrated DNA Technologies, Inc. The qPCR premix (Rotor-Gene SYBRs Green PCR kit) is purchased from Qiagen LTD. The DNA polymerase (ProTaq Plus DNA Polymerase), dNTP, DNA ladders (bio-25 and bio-100), gel loading dye (4x) and 5x TBE buffer are purchased from Protech Technology Enterprise Co., LTD. SYBR safe gel dye (Invitrogen) are purchased from GenedireX. The ligation kit (pGEM®-T easy vector kit) and magnetic beads (Streptavidin MagneSphere®

90
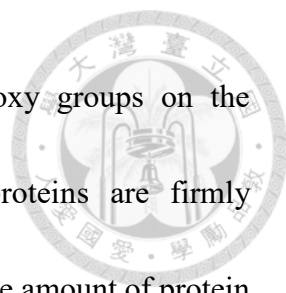
Paramagnetic Particles) are purchased from GeneLabs Life Science Corp. The non-heat shock competent cell (RBC HIT-DH5α), agar (AGR001, bacteriological grade) and LB broth (Lennox) are purchased from BIOMAN Scientific Co. LTD. The ExoSAP- IT® kit is purchased from Thermo Fisher Scientific.

● Preposition of epoxide-functionalized microbeads and the protein immobilization

Piranha solution (35% H_2O_2 and 98% H_2SO_4 are mixed in 1:4 ratio by volume) is prepared carefully for the cleaning and activation of glass microbeads (c.a. 500 μm). The silicon oxides on the glass microbeads are oxidized at 60 °C for an hour and form the activated oxygen molecules for the following reaction. After washing twice with DIW, the microbeads are rinsed with 95% ethanol and dried at 100 °C in an oven for an hour to completely remove the water molecules. After that, the microbeads are placed in a 4% (v/v) 3-Glycidoxypropyl-trimethoxy silane (GLYMO) diluted in toluene, and the coupling reaction is carried out by shaking overnight at room temperature. Residual GLYMO solution is removed by rinsing twice with toluene and 95% ethanol, and the epoxide-functionalized microbeads are dried at 100 °C in an oven for an hour. The epoxy-beads should be preserved in a dark and dry surrounding for remaining the activity of epoxy groups.

Protein immobilization is executed by mixing the protein solutions (c.a. 1 μg protein dissolved in 30 μl 1x PBS buffer, pH7.4) and the epoxide-functionalized microbeads (c.a.

91

0.03 g) at 4 °C overnight. A spontaneous reaction between epoxy groups on the microbeads and amine groups on the protein happens, and proteins are firmly immobilized on the surface of microbeads with covalent bonding. The amount of protein bounding on the microbeads is estimated by subtracting the amount of initial protein loading and final supernatant. The amount of proteins in the solution can be qualified by Bradford assay. After target protein immobilization, the residual epoxy groups on the microbeads are blocked by immersing in 1 M glycine solution (dissolved in 1x PBS buffer, pH 7.4) at 37 °C for 2 hrs. Washing twice with 1x PBS buffer, the liquid is removed, and the protein-microbeads can be stored at 4 °C for use. STAT1, STAT2, STAT3 and STAT4 proteins served as selection targets are conjugated on the microbeads according to the above procedures, and HSA-coated microbeads are also prepared under similar conditions for the counter selection and a control target.

- Single bead-based pre-SELEX for the potential sequence enrichment

A 60-mer ssDNA library consisted of a randomized central sequence flanked by two primer regions (5'-CCCTACGGCGCTAAC-$(N)_{30}$-GCCACCGTGCTACAA-3') is synthesized to provide the high diversity of DNA structures. However, the 30-mer random region can produce about 10^{18} ($=4^{30}$) kinds of sequence that exceeds the initial diversity suggested for an aptamer selection (10^{15}). To supply adequate opportunities for each sequence to incubate with target proteins, a pre-SELEX round is performed to collect the

92

protein-binding DNAs via a simple selection, and it can reduce the diversity of sequence before carrying out the following SELEX rounds.

First, five protein-bound microbeads are picked up into a microcentrifuge tube and rinsed by SELEX buffer twice for conditioning. The ssDNA library dissolved in the SELEX buffer is heated to 95 ℃ for 5 mins and gradually cooled to 25 ℃ for DNA structure refolding. The protein-bound microbeads are mixed with 20 μl refolded ssDNA library in a 200-μl PCR tube, and the mixture is incubated at 25 ℃ for 1 hr. After the incubation, the five protein-bound microbeads are washed with SELEX buffer three times to remove the unbound DNAs. And then, the microbeads are transferred individually by a tweezer into PCR tubes containing 25 μl PCR premix (Rotor-Gene SYBRs Green PCR kit, the forward primer (5'-CCCTACGGCGCTAAC-3') and the biotin-labeled reversed primer (5'-(biotin)-TTGTAGCACGGTGGC-3')). The protein-binding DNAs on the microbeads are amplified by using a qPCR machine (Rotor-Genes Q, Qiagen) with the real-time qPCR process (initial Taq activation for 5 mins followed by 12 cycles of two-step PCR reaction including 95 °C for 5s and 60 °C for 10s). After confirming the PCR products through an electrophoresis analysis (3% agarose gel stained by SYBR safe, 120V/30mins), the biotin-labeled dsDNAs are isolated by the Streptavidin MagneSphere® Paramagnetic Particles (SA-PMPs) kits (Promega). The washed SA-PMPs in 10x SSC buffer are incubated with the biotinylated PCR amplicons at 25 °C for
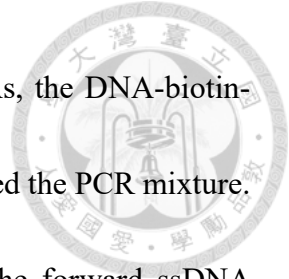
1 hr. After the streptavidin proteins capture the biotin-labeled DNAs, the DNA-biotin-SA-PMPs are washed four times to purify the DNAs from complicated the PCR mixture. Instead of the biotin-anchored reverse strand of binding DNAs, the forward ssDNA strands are separated by 50 mM NaOH solution. Finally, the DNA dissolving buffer is exchanged to SELEX buffer by a G-25 column, and this pre-SELEX pool is stored at 4 °C for use.

● Fabrication of the bead-array chips and establishment of the flow system

The chip molding master is made of CNC-machined aluminum instead of SU-8 photoresist because the aluminum master has great mechanical strength that can endure many times of molding process. A straight channel containing five isometric microwells is designed, and the size of microwell is optimized to hold a 500-μm microbead. The PDMS mixture (reagent ratio 10:1) is poured into the master and heated at 120 °C for gel curing. The cured PDMS chip is peeled off from the master, and two holes are punched as inlet and outlet. Microbeads are transferred into the microwells by a tweezer, and a glass slide covers the PDMS chip to seal the microchannel. The PDMS chip and glass slide are fixed by an aluminum fixture to assembly a beads-array microfluidic device. This device has a reversible assembly that benefits to open the device and collect the microbeads for further analysis after performing the selection process.

One terminal of the PTFE tube is inserted into the inlet/outlets hole, and another is

94
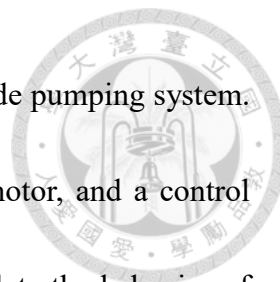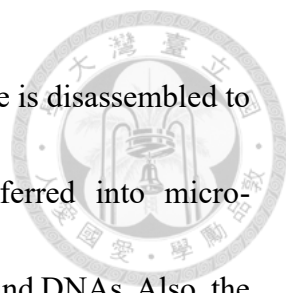
connected to the peristaltic tube which is assembled on the homemade pumping system. The pumping system contains a peristaltic pump head, a stepper motor, and a control circuit. Arduino-based controlling circuit is programmable to modulate the behavior of stepper motor that regulates the liquid flow rate and direction. Shuttle frequency can also be controlled according to adjusting the flow rate and moving distance.

● Bead-array micro-shuttle SELEX

Protein-microbeads are placed into the microwells individually, and the glass slide covers the PDMS chip to form a beads-array microfluidic device. For STAT3-specific aptamer selection, STAT3-microbeads and HSA-microbeads are alternatively arrayed to perform multiple micro-reactors for simultaneous target/counter SELEX. For STATs protein multiplex SELEX demonstration, the microbeads coated STAT1, STAT2, STAT3 and STAT4 are arranged sequentially to collect the specific binding DNAs, and a HSA-microbead which locates at the first microwell plays the role of intercepting non-specific binding DNAs.

20 μl enriched ssDNA pool (evoluted by pre-SELEX) is injected into the beads-array microfluidic device, and then the liquid is shuttled across the microbeads several times for rapid DNA-binding reactions. The flow rates and shuttle times can be controlled according to the experimental requirement. After the incubation process, the wash buffer (SELEX buffer containing 150 mM NaCl) is shuttled in the microfluidic device to remove

95
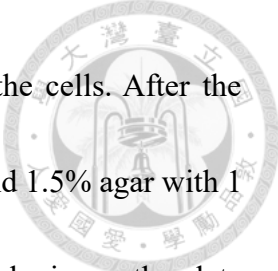
the redundant DNAs. As the washing process is completed, the device is disassembled to recover the DNA-bound microbeads. The microbeads are transferred into micro-centrifuge tubes containing real-time qPCR premix to amplify the bound DNAs. Also, the real-time qPCR is used to quantify the amount of DNA-binding on each microbead that may imply the preliminary binding affinity.

- Aptamer candidate sequencing, sequence alignment and structure prediction

Although the sequences should be converged during the selection process, the PCR products still have a lot of sequences in the solution. To identify the single sequence, a TA-cloning method is adapted to prepare the samples for DNA sequencing. Firstly, the potential DNA pool is enriched again by PCR reaction with the reverse primer without biotin-label. 2 μl DNA pool is added to a 23 μl PCR premix (containing 2.5 μl 10x ProTaq buffer, 0.5 μl forward primer, 0.5 μl reverse primer, 5 μl betaine, 0.25 μl DMSO, 0.5 μl dNTP and 0.25 μl ProTaq polymerase), and the PCR tubes are put into the PCR machine to carry out a 30-cycle PCR (initial Taq activation at 95 °C for 5 mins followed by 95 °C for 20s, 60 °C for 30s and 72 °C for 20s, and a final extension at 72 °C for 5mins).

2 μl product is mixed with the pGEM®-T easy vector kit (5 μl 2X Rapid ligation buffer, 1 μl p-GEM®-T easy vector, 1 μl T4 DNA ligase and 1 μl Q-H$_2$O) for the DNA ligation. The mixture is shaken at 25 °C for 1 hr and incubated at 4 °C overnight. When the DH5α (RBC HIT competent cell, 100 μl) is thawed one-third, 10 μl ligated vector is

96
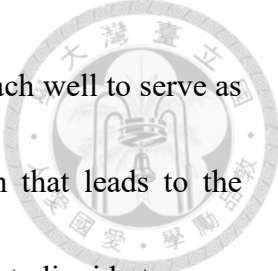
added and put on the ice for 10 mins to transfect the vector into the cells. After the

transfection, the cells are plated on the LB agar plate (2% LB broth and 1.5% agar with 1

µg/ml ampicillin), and incubated at 37 °C overnight. The individual colonies on the plate

are picked up and transferred into the PCR premix (the same components except the T7

and SP6 primers). The particular sequence flanked by T7/SP6 primers is amplified

through a 30-cycle PCR, and the products (240 bp in length) are confirmed by agarose

electrophoresis. The amplicons with correct length are chosen for DNA sequencing.

Before sending the sequencing samples to Technique Center, the selected aptamer

candidates are purified by the ExoSAP- IT® kit (mixing 5 µl product and 2 µl kit reagent

at 37 °C for 15 mins, and heating to 80 °C for 5 mins). The concentration and purity of

DNA samples are verified by the UV-absorption spectrum measured by ELISA reader

(BioTek, Epoch) with Take3 micro-volume plate.

- Immuno-qPCR assay for affinity estimation

The principle of immune-qPCR assay is shown in Fig. 3.3. Target proteins are diluted

to 1 mg/ml with 1x PBS buffer (pH7.4) and added into the 96-well plate for protein

immobilization at 4 °C overnight. After proteins adsorb on the well, 1 M glycine solution

is added to block the empty spaces at 37 °C for 2hrs. The candidate ssDNAs are serially

diluted with the SELEX buffer and added into the protein-coated wells for DNA-protein

hybridization. After the incubation, the wells are washed by the SELEX buffer three times

97

to remove the unbound DNAs. 100 µl SELEX buffer is loaded into each well to serve as the elution buffer. The whole plate is heated to 95 °C in an oven that leads to the dissociation of the DNA-protein complex. Transferring the hot liquid to new microcentrifuge tubes as soon as possible, the solution contains the ssDNAs released from proteins. The amounts of ssDNA in solution are quantified by real-time qPCR analysis. If a lot amount of DNA molecules is used as a template, the qPCR signal will raise in the early PCR cycles that cause a low cycle threshold (Ct) value. According to the Ct values, the amounts of DNA-binding can be evaluated. The loading DNA concentration and DNA-binding amount are plotted an affinity curve, and the dissociation constant (kd) can be calculated by one-site binding equation.

- MTT assay for the estimation of cell viability

The cell viability of DNA-treated cells are assessed with Vybrant® MTT cell proliferation assay. 500 µL of 0.4x MTT solution (diluted from 2x MTT by medium) is added to each well. After the incubation for 2 hrs, the MTT solution is removed and 100 µL DMSO is added into each well to dissolve the purple crystal. After several times pipetting, the samples are measured for the absorbance at 540 nm.
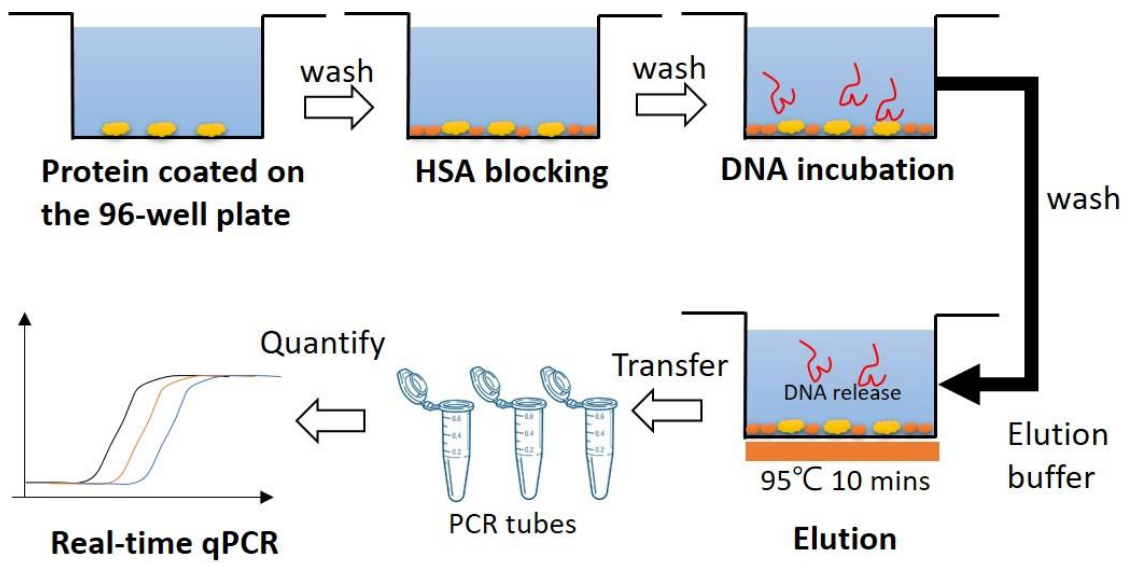
Figure 3.3 The procedures of immuno-qPCR analysis for evaluating the binding affinity of the selected aptamers.

3.4 Results and Discussion

3.4.1 Pre-SELEX of STAT3-specific binding DNA pool

The sequence diversity of the ssDNA library is a critical factor for aptamer selection. Low diversity may lead to the missing of potential sequences, but high diversity may cause the decreasing opportunity of molecule collision. Hence, a selective sequence enrichment is executed to acquire a suitable diversity of initial library. Pre-SELEX is performed by single-bead SELEX which is based on epoxide glass beads. The epoxide microbeads shown in Fig. 3.4(a) are produced by GLYMO modification which is a kind of silane reaction for glass functionalization. The epoxy groups can react with amino groups on the protein molecules in order to immobilize the protein on glass microbeads (shown in Fig. 3.4(b)). The amount of immobilized protein can be estimated by measure the reduction of protein concentration after the protein-bead incubation (shown in Fig. 3.4(c)). The condition of GLYMO modification is optimized according to the temperature and concentration parameters. In Fig. 3.5(a), the modifications carried out under room temperature provide more protein immobilization. In Fig. 3.5(b), using carbonate buffer (pH 9.5) for protein immobilization can fix more protein on the microbead surface. Five STAT3-microbeads prepared with 3% GLYMO at RT are incubated with the library to carry out the pre-SELEX shown in Fig. 3.6(a). The bound DNAs are amplified by qPCR shown in Fig. 3.6(b) and verified by agarose electrophoresis shown in Fig. 3.6(c).
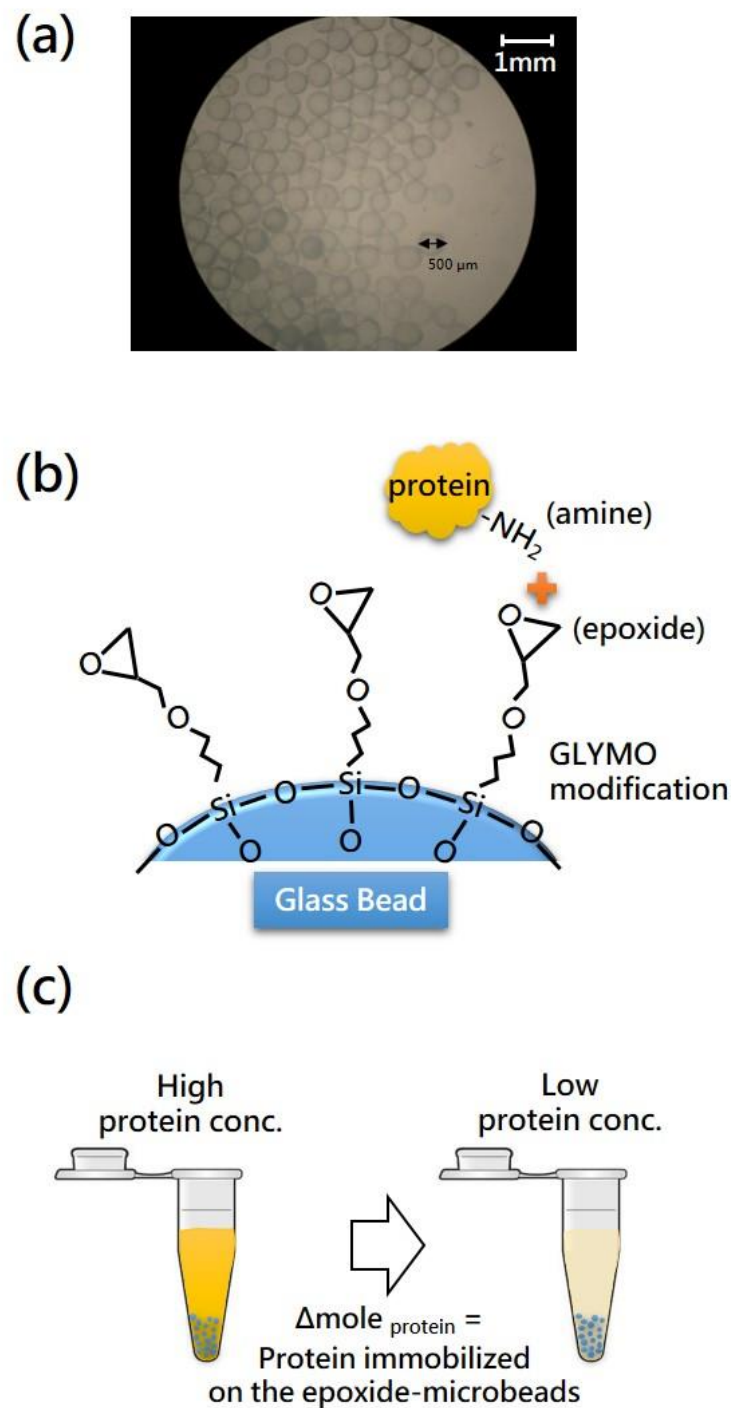
Figure 3.4 Microbeads modification based on GLYMO silanization for protein immobilization. (a) 500 μm glass microbeads. (b) protein immobilization via amine and epoxide interaction. (c) The fixed proteins are quantified by measuring the reduction of STAT3 concentration in the supernatant.
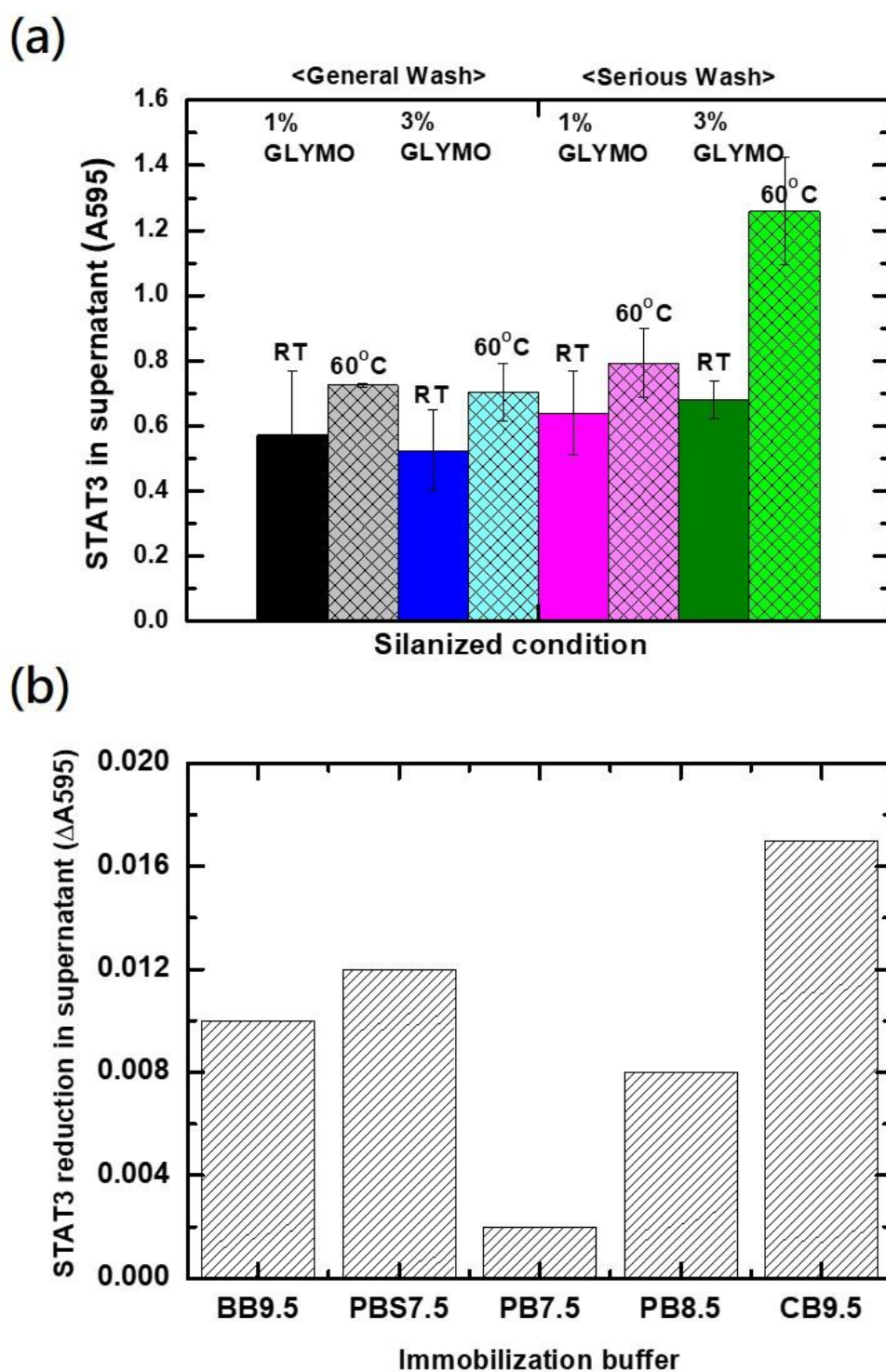
Figure 3.5 Optimization of protein immobilization according to (a) various silanized

conditions of glass microbead and (b) different buffers for protein reaction.
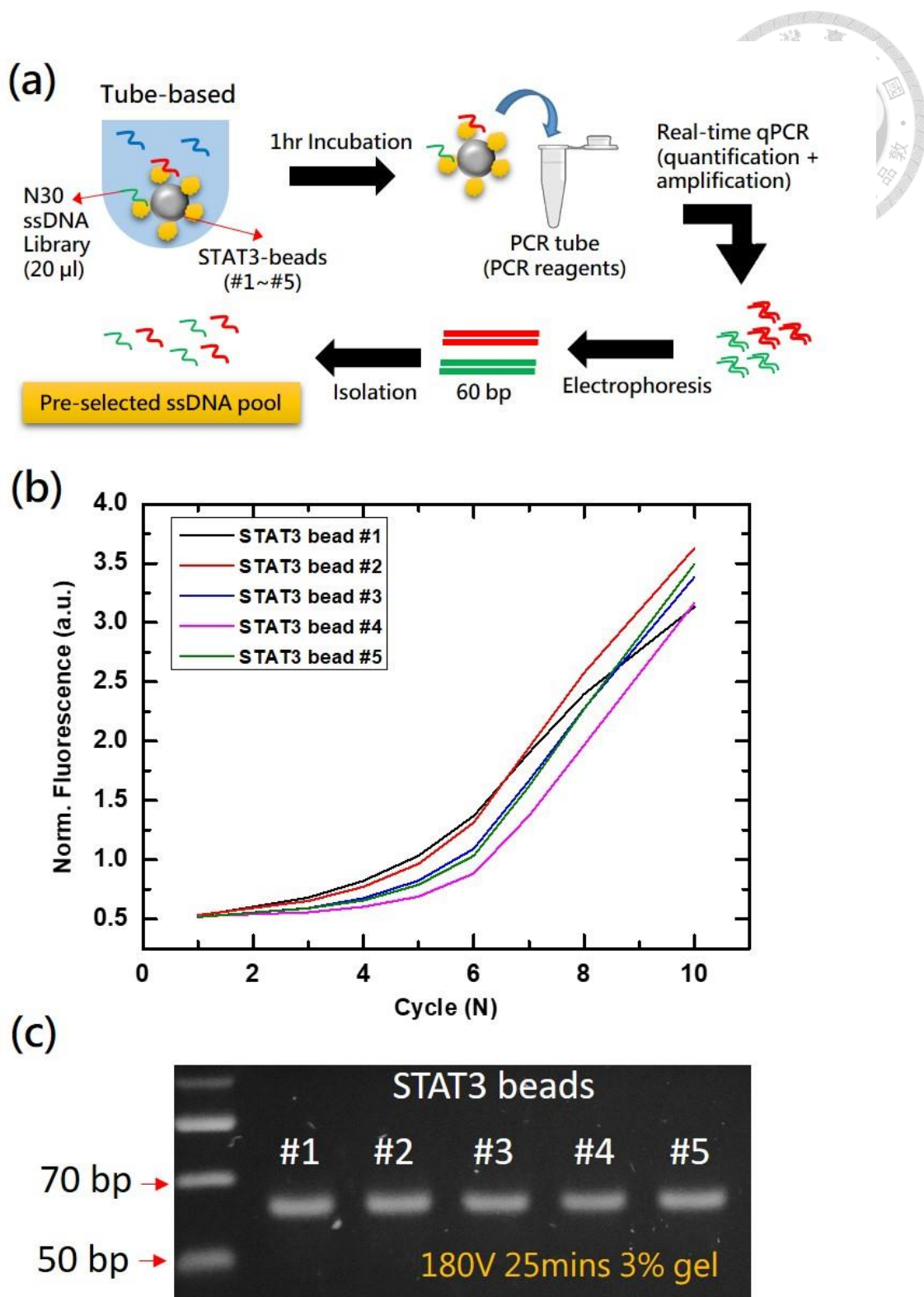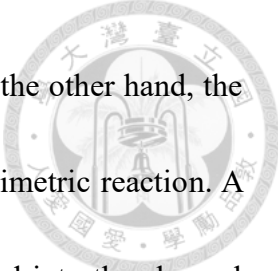
Figure 3.6 Pre-SELEX is executed by (a) the tube-based single bead SELEX which can

monitor aptamer evolution in real-time with (b) the qPCR analysis and (c) agarose gel

electrophoresis.

3.4.2 Beads array microfluidic chip

To get a high-affinity aptamer in fewer selection rounds, a stringent selection condition is needed. A series of experiments demonstrates the concept and feasibility of the microfluidic SELEX platform which reduces the needs of target molecules and performs extensive washing process. The precious target molecules can be immobilized on microbeads to save the consumption of targets and reagents. Moreover, the narrow microfluidic channels provide short diffusion distance between DNA and target molecules (shown in Fig. 3.7(a)), and an enforced molecular collision occurred in a microscale channel. In addition, the fluidic-flow status provides the binding and washing process at the same time to generate a high-affinity aptamer (shown in Fig. 3.7(b)). Also, the SELEX with parallel microfluidic channels or microbeads can be further developed as a multiplex platform to run a number of *in vitro* aptamer selection processes in parallel. In this work, we conducted a proof-of-concept study about microfluidic SELEX with one-dimensional microbead array shown in Fig. 3.8(a) for future single-round, high-throughput aptamer screening application.

To explore the fluid field in bead array chips, a simple microfluidic chip containing two inlets is fabricated. When two color dyes flow into the channel without microbeads at the same time, an obvious interface is formed between two dyes, and the interface results from the laminar flow. As the microbeads exist, the fluids will pass along the beads

and induce an interference of laminar flow shown in Fig. 3.8(b). On the other hand, the

shuttle effect in microfluidics is also demonstrated in a simple colorimetric reaction. A

blue substrate solution and a transparent enzyme solution are injected into the channel

sequentially. In Fig. 3.8(c), it needs about one minute to complete the enzymatic reaction

which changes the blue substrates to yellow products under a static state. The molecules

need to interact with each other by diffusion, and this effect can be observed by the blue

color change shown in Fig. 3.8(d). In contrast, the shuttle flow mixes the liquid in less

than ten seconds, and this mixing strategy is also proved in many researches about the

DNA hybridization or enzymatic reactions.
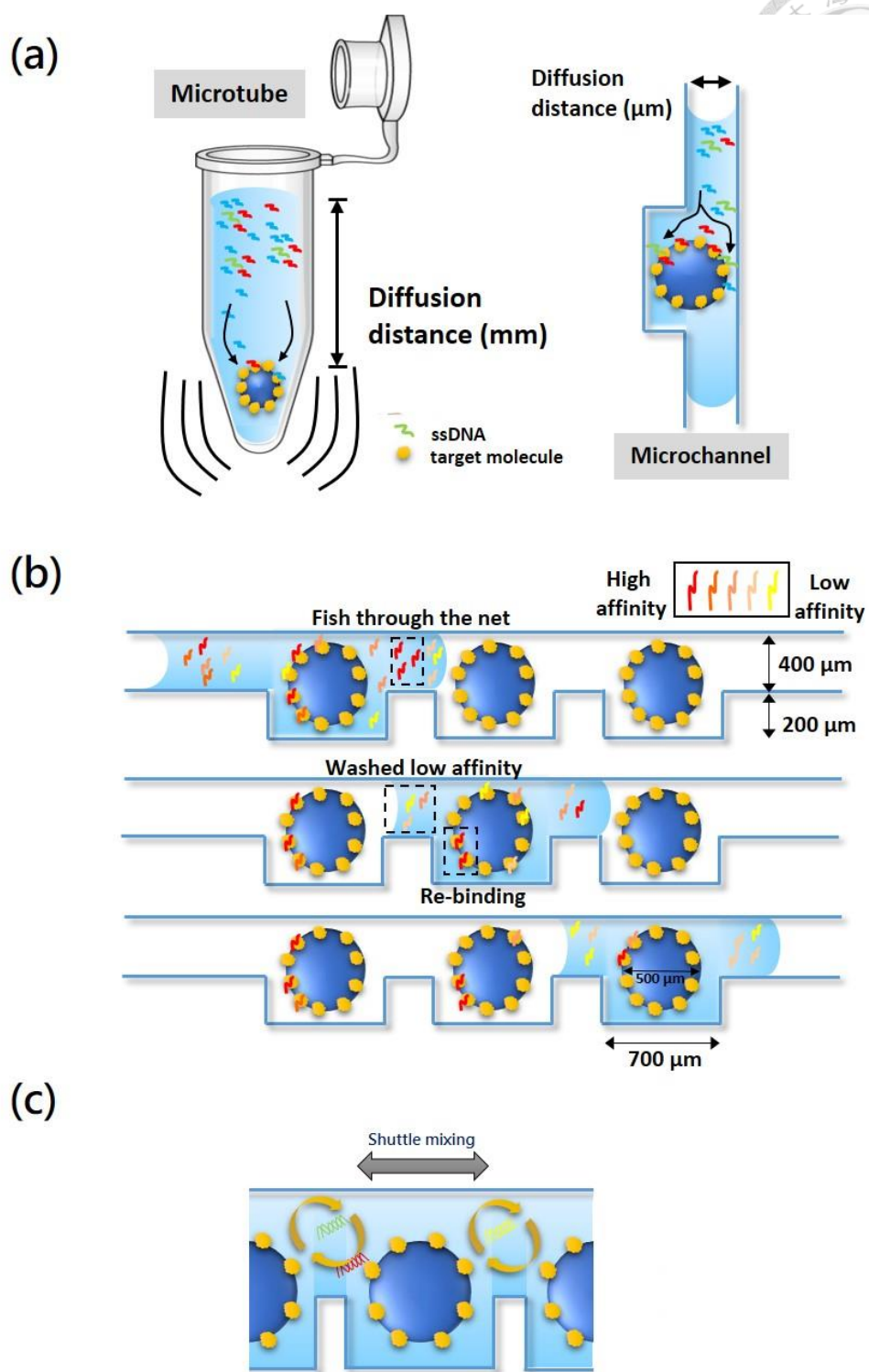
Figure 3.7 Comparison of DNA binding effect (a) in microtube (long diffusion distance)

and in microchannel (short diffusion distance) with (b) microbeads array which has a

unique binding mechanism and (c) shuttle mixing effect.
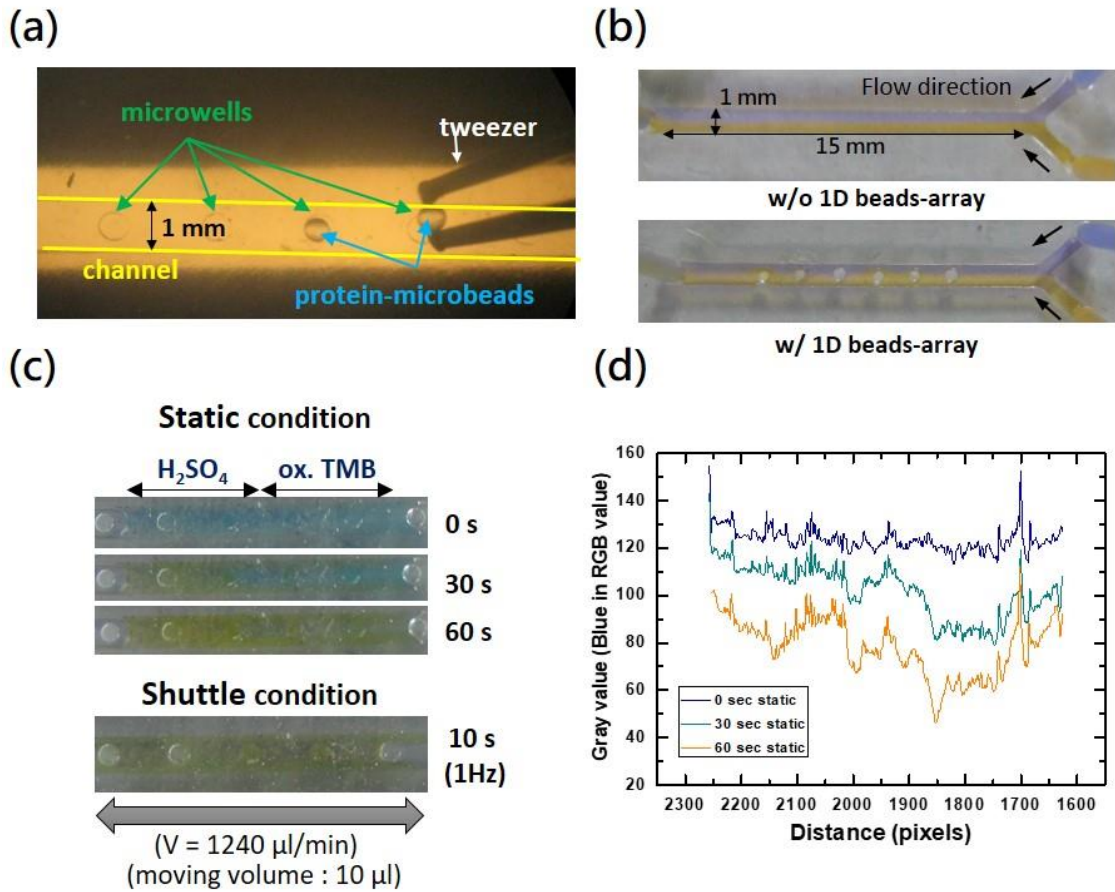
Figure 3.8 Microbeads-array microfluidic device fabricated by (a) picking the protein-microbeads into the microwells shows the effects of (b) laminar flow interference and (c) shuttle mixing which is demonstrated by the H_2SO_4-triggered color change of oxidized TMB substrate. (d) The degrade of blue color measured by image analysis implies the diffusion effect in the static condition.

107

To achieve an efficient aptamer selection, the pre-selected ssDNA pool of STAT3 protein was pumped into a microbead array chips with one-way and shuttle flow shown in Fig. 3.9. The liquid flow rate is related to the DNA-protein interaction time and the unbound-DNA washing strength. According to the concentration of bound-DNA on each bead, the variation in the affinity of distinct microwells can be obviously observed. In high flow rate condition, the front beads would capture the most DNA molecules which produce an unequal DNA-binding situation (shown in Fig.3.10(a)). However, the fast liquid transportation provided a strict binding condition that the selected-DNA has a high affinity to STAT3 protein compared with HSA (shown in Fig. 3.10(d)). In contrast, the low specificities of STAT3-binding DNAs were selected from low flow rate conditions. It may result from the sedimentation of DNA molecules onto microbeads, and it produces the non-specific binding. Moreover, the slightly washing conditions under a slow flow rate also decrease the specificity of selected aptamers.

A repeated transient DNA-protein interaction was performed by a shuttled liquid flow. The liquid consisted of pre-selected ssDNA was pumped through the microchannel back and forth in order to improve the binding efficiency and washing strength. In the shuttled flow selection, the high specificity aptamer candidates could be evaluated even in the lower flow rate (shown in Fig. 3.11(d)).

108
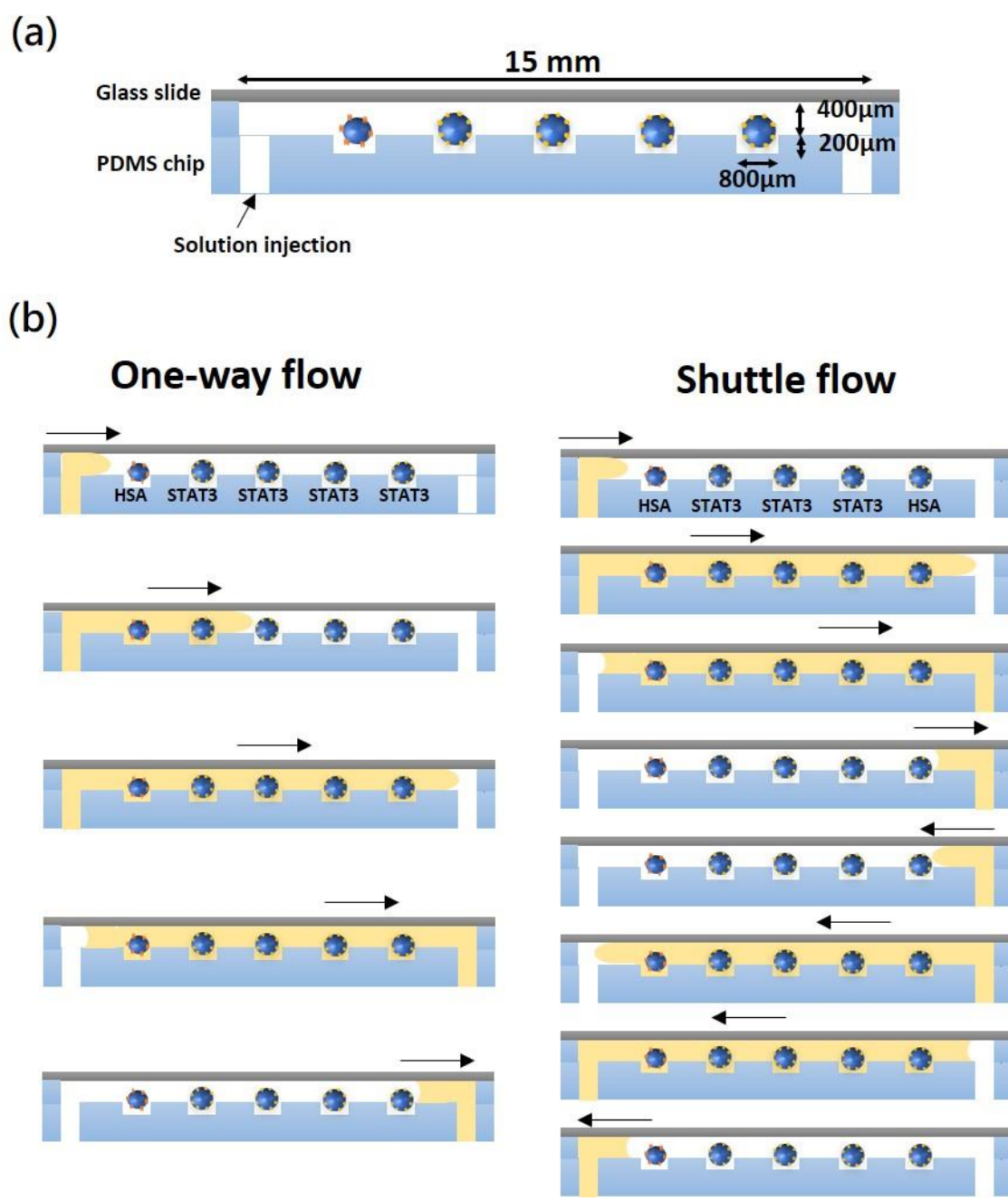
Figure 3.9 The schematics of (a) the lateral view of 1D microbeads-array microfluidic chip containing five protein-microbeads in the individual microwells and (b) the operation procedures of the one-way flow and the shuttle flow.
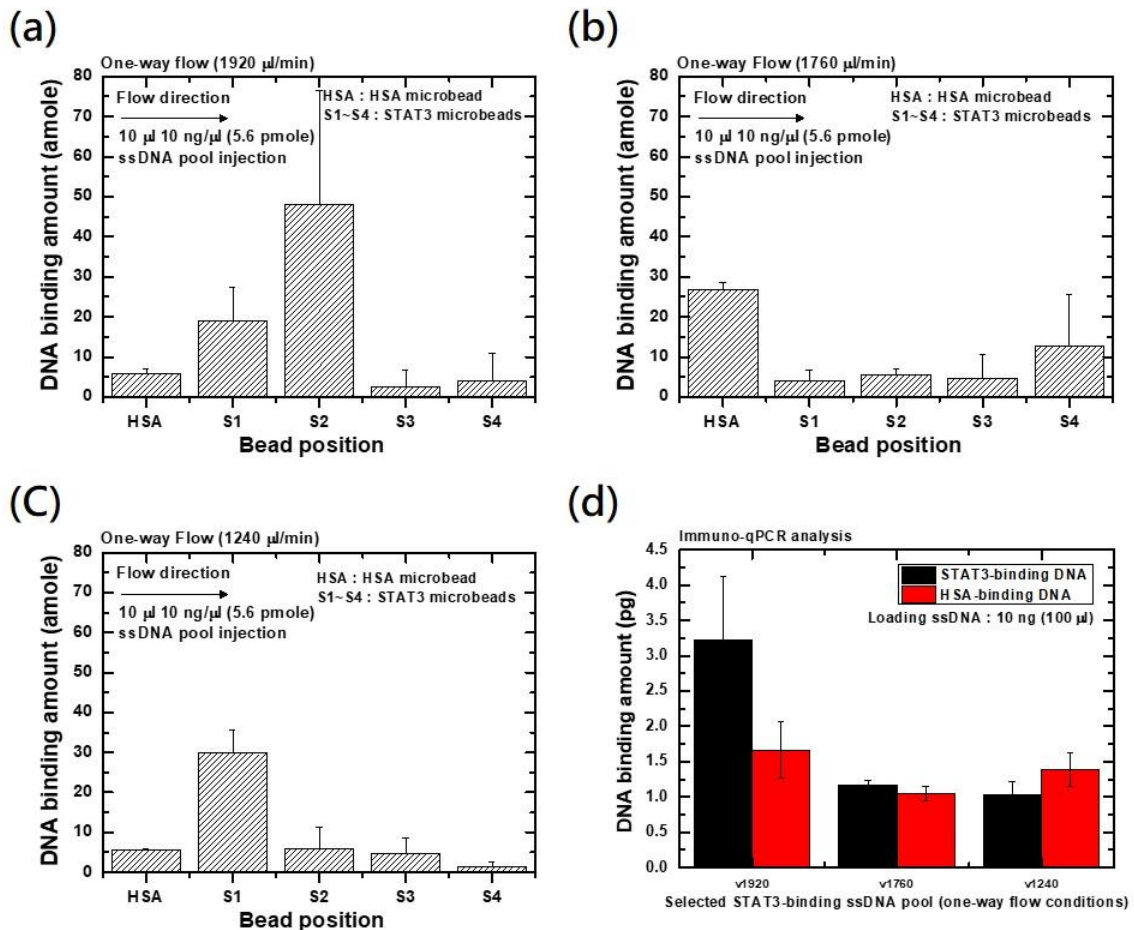
Figure 3.10 STAT3-preferred DNA binding in the microbeads-array microfluidic device under one-way flow with the velocity of (a) 1920 μl/min, (b) 1760 μl/min and (c) 1240 μl/min. (d) The STAT3-bound DNAs are incubated with STAT3 and HSA for evaluating the affinity and specificity of selected DNA pools.
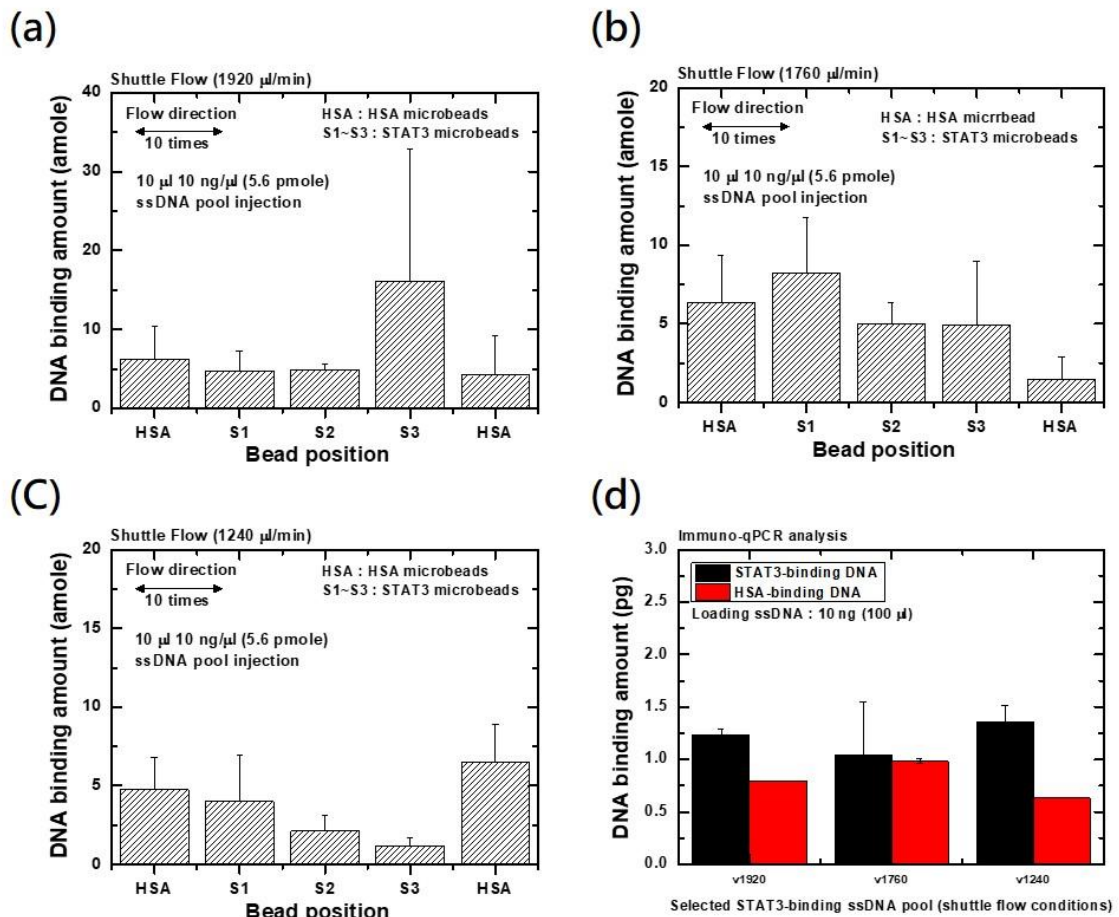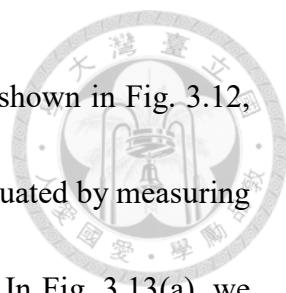
Figure 3.11 STAT3-preferred DNA binding in the microbeads-array microfluidic device

under shuttle flow with the velocity of (a) 1920 μl/min, (b) 1760 μl/min and (c) 1240

μl/min. (d) The STAT3-bound DNAs are incubated with STAT3 and HSA for evaluating

the affinity and specificity of selected DNA pools.

To further explore the shuttling effect for the aptamer SELEX shown in Fig. 3.12, the DNA captured capability in various interaction strategies are evaluated by measuring the remaining DNA concentration after protein-binding procedures. In Fig. 3.13(a), we find that the one-way flow interaction captures more DNA than tube interaction, and the shuttling flow carries out much higher DNA capture ability which confirms our assumption for shuttle effect.

The washing effect is verified by an indirect way that the washing solutions are collected after each washing step and quantified the DNA concentration to evaluate how many unbound DNAs are washed in three washing steps. Figure 3.13(b) shows that the one-way flow provides a weak washing result which can still recover DNA even after three times washing. In the shuttle flow condition, most unbound DNAs are removed in the first washing step, and no detectable DNA molecules are recovered in the third washing step. It means that the shuttling flow provides a more efficient washing effect in microfluidic chips. High DNA binding ability indicates that the captured DNAs have high affinity but the specificity of them are not confirmed.

Figure 3.14(a) shows the DNA accumulation on STAT3-coated microbeads during the shuttling process, and it reveals the binding phenomenon of each bead in various positions. The HSA protein is chosen as a control protein to verify the specificity of the STAT3-binding DNA pools selected by 1D microbeads array shown in Fig. 3.14(b). The

DNA pools selected by one-way flow have low specificity compared to the DNA pools generated from shuttling flow SELEX.

To estimate the binding results of the microbead in microfluidics, a set of experiments was designed to provide the shuttling effect. The STAT3 aptamer candidate library was introduced into the microfluidic chip consisted of five STAT3 protein beads. The binding effect could be evaluated by measuring the amount of bound DNA which quantified by qPCR analysis. And then, the single and shuttle flow operations were applied to manipulate the binding condition. The diluted DNA libraries were used because we assumed that the less DNA amount, a more obvious difference between single and shuttle flow was observed. The various concentrations of DNA libraries were injected into microfluidic chips, and the liquids were operated in single and shuttle flow. In Fig. 3.15(a), the DNA binding ratio is declined from the front bead to the end. This result met the hypothesis we had mentioned before. That is shuttle flow also provided a balanced binding efficiency which shown in Fig. 3.15(b).

113
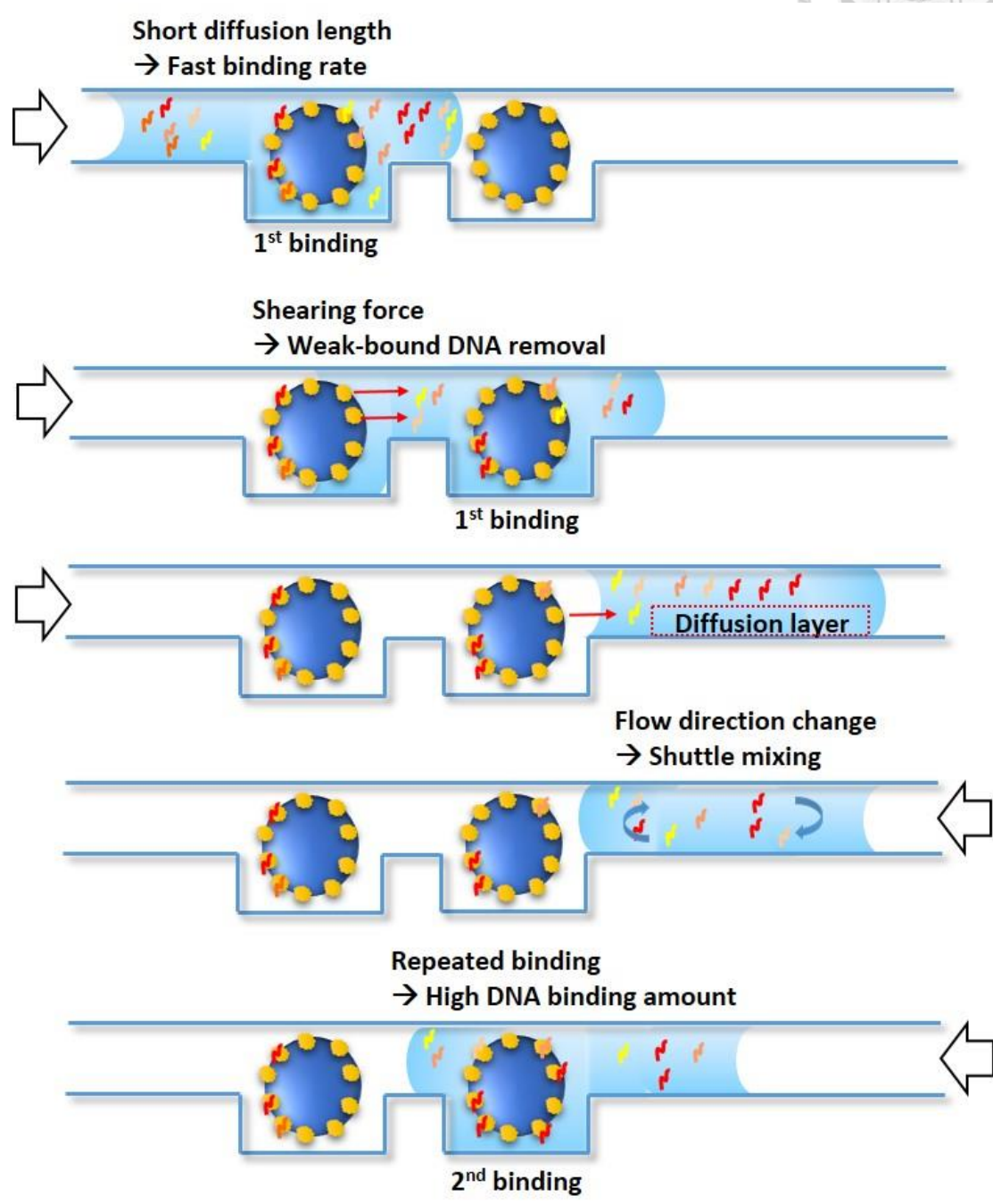
Figure 3.12 The mechanism of microbeads-array SELEX with shuttle flow. Several

effects including rapid DNA binding reaction, the shearing force washing, shuttle mixing,

and repeated binding are happened to enhance the selection efficiency.
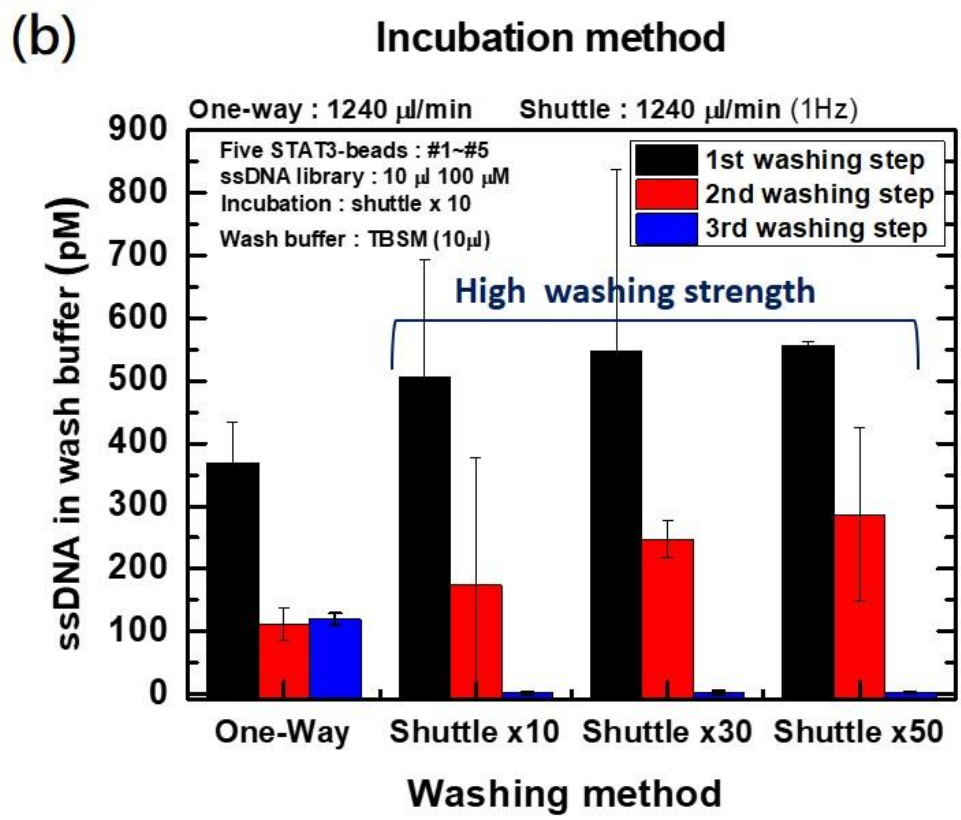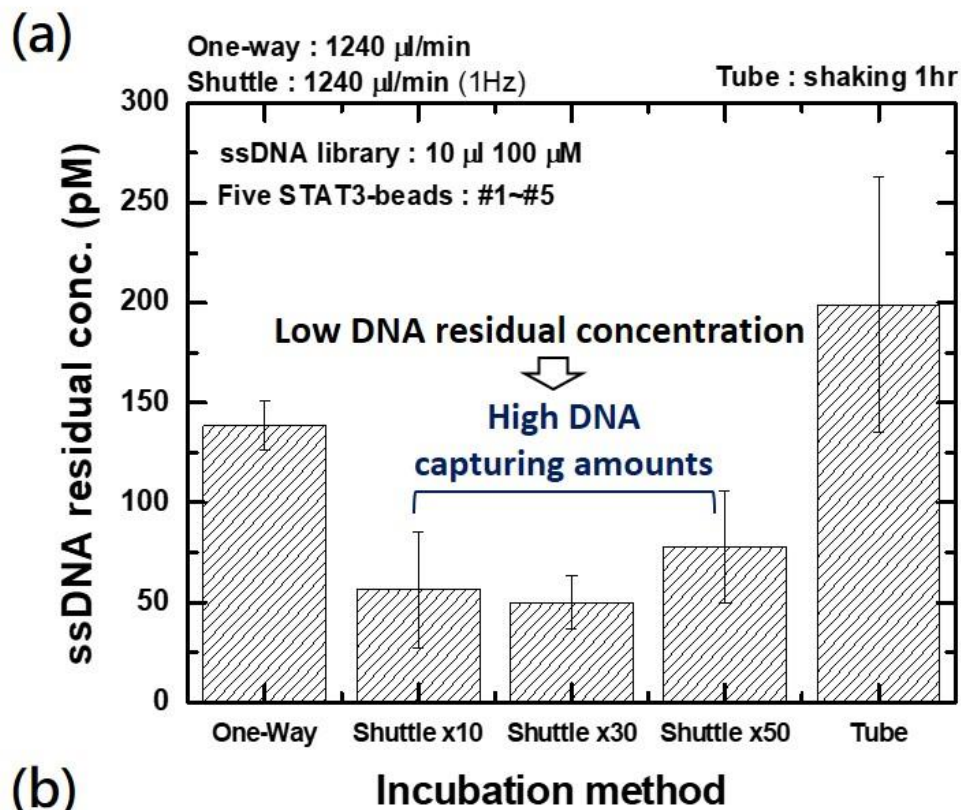
Figure 3.13 The effect of shuttle flow on (a) high DNA binding efficiency to shorten the incubation time and (b) high washing strength to remove low-affinity DNAs.

115
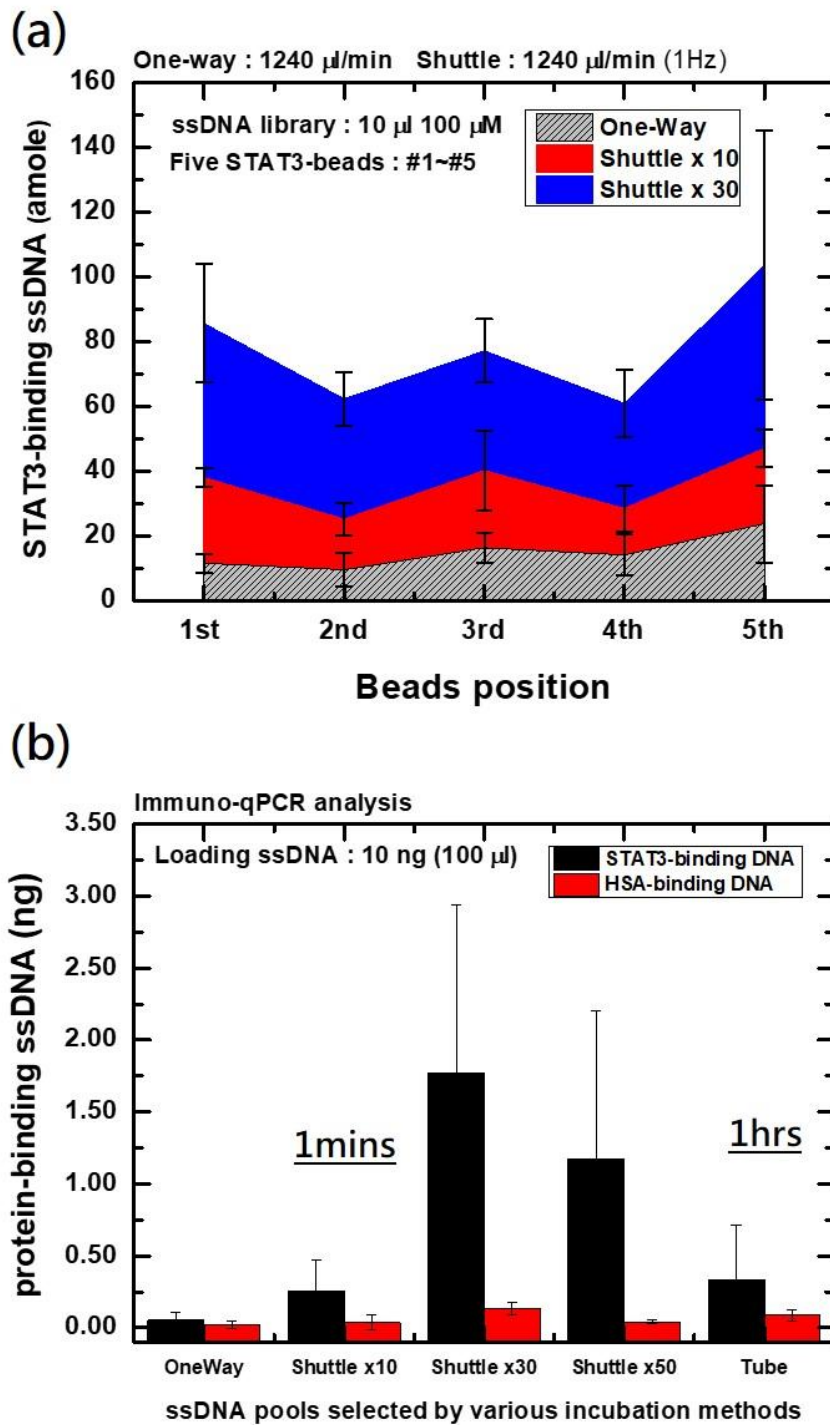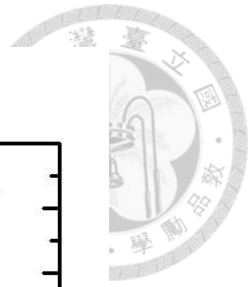
Figure 3.14 The increasing shuttle times enhance (a) the affinity according to the high

DNA binding amount and (b) specificity according to the affinity difference compared to

HSA proteins of STAT3-binding DNA pools.

116
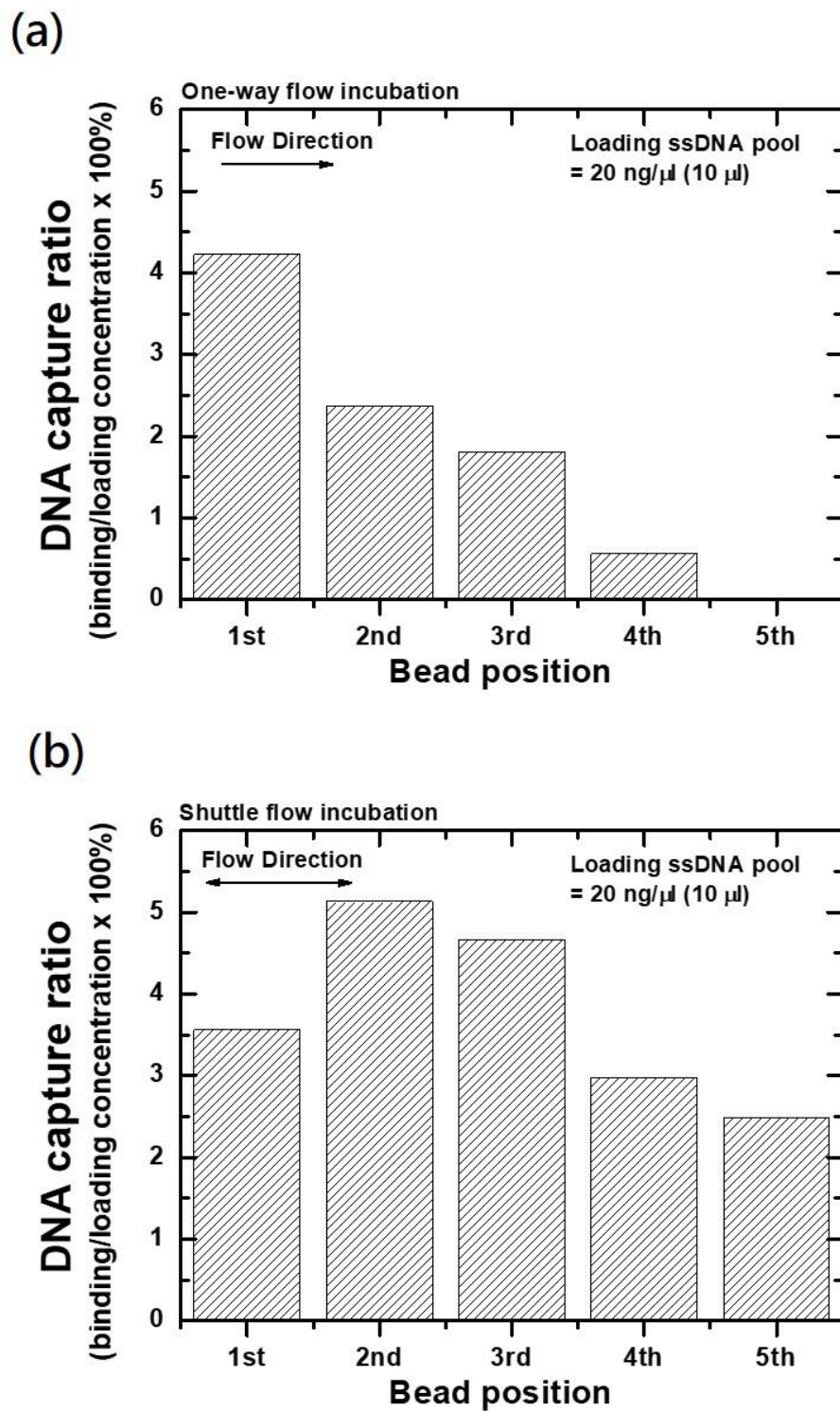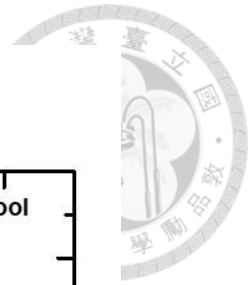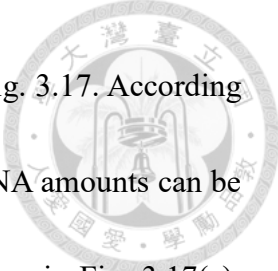
Figure 3.15 DNA capture ratios at each microbeads under (a) one-way flow and (b) shuttle

flow modes.

3.4.3 STAT3 aptamers generated by beads-array microfluidic SELEX
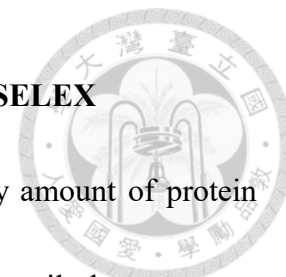
Microbeads SELEX technology has the advantages of the tiny amount of protein usage for aptamer selection, and the microbeads can be transferred easily by a tweezer that is considered to be a micro-reactor unit. To combine with the microfluidic technique, a 1D bead array microfluidic chip can supply a multiplex aptamer selection. Besides, the shuttle liquid transportation makes the microfluidics which has a laminar flow well-mixed in the microchannel. Therefore, we propose a six-bead 1D bead array shown in Fig. 3.16(a), and the STAT3 proteins and HSA proteins are immobilized on the microbeads by the way of an epoxy-amine reaction. These two kinds of protein beads are alternatively placed into the microwell by a tweezer. After the 1D bead array chip assembling, a DNA library with random sequences is injected into the chip to carry out the protein-DNA interaction. With the detachable assembly design, the microbeads in the chip can be recovered after the binding process, and the DNAs bound on STAT3 and HSA microbeads are amplified by qPCR process. Only the DNAs bound on STAT3-microbeads are collected and isolated for the next selection round. Similar to the traditional SELEX process shown in Fig. 3.16(b), through several SELEX rounds, the selected DNA pools (involving STAT3 and HSA) obtained from the final round are sequenced to identify the individual aptamers.

The amounts of bound DNA on the STAT3-microbeads and the HSA-microbeads in

each selection round are evaluated by the qPCR analysis shown in Fig. 3.17. According to the standard calibration curve generated by the N30 library, the DNA amounts can be precisely quantified via the threshold cycles. In the first round shown in Fig. 3.17(a), considerable DNA binding amounts are observed because the loading library has a large diversity and high concentration that leads to serious non-specific DNA binding. After the initial selection, the diversity of DNA pools decreases that results in the low DNA binding amount shown in Fig. 3.17(b). In the fourth selection round, the DNA binding amounts increase because of the sequence convergence. However, the over-selection is observed in the fifth selection round shown in Fig. 3.17(e) due to the sequence mutation among the PCR process.

The STAT3-bound and HSA-bound DNAs in the 4th selection round were collected individually and amplified to further enrich the DNA pools. In the immuno-qPCR, the STAT3-coated (100 nM) and HSA-coated (10 μM) 96-well plate were incubated with isolated ssDNA libraries (100 nM) for 1hr at room temperature. To remove the non-specific binding DNA, three times buffer washing was applied. The elution was carried out with adding 100 μl buffers into wells and heating in an oven at 95 °C for 10 mins. The eluted DNAs were quantified by qPCR analysis to compare the specificity and affinity of the selected libraries in different positions. The S1 library showed a great specificity to HSA, and the S2 and the S3 libraries also had the binding difference (shown in Fig. 3.18).
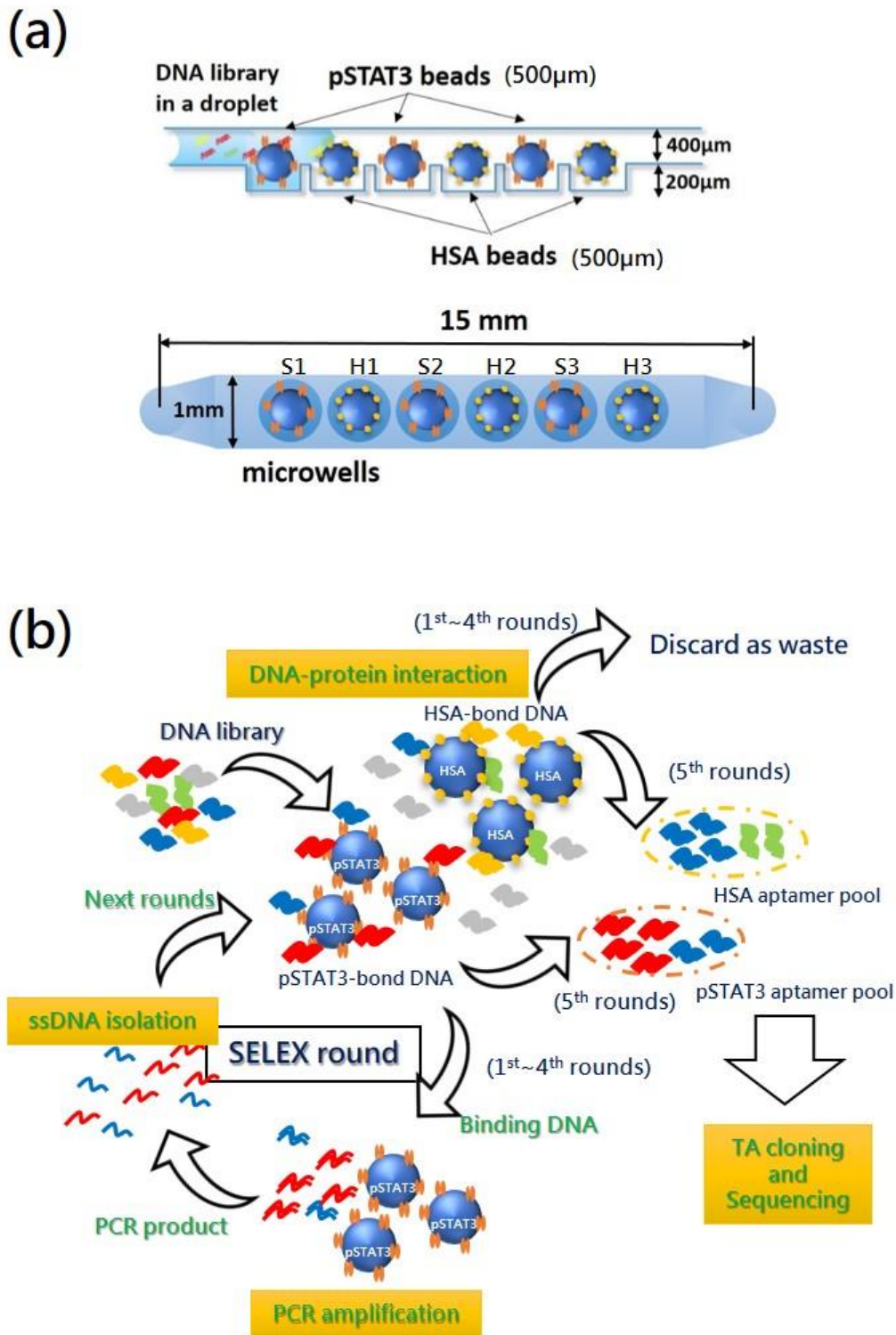
Figure 3.16 Microbeads-array microfluidic device (a) containing three STAT3-microbeads and three HSA-microbeads arrayed in serial for (b) rapid STAT3 aptamer selection against HSA as a control.

120
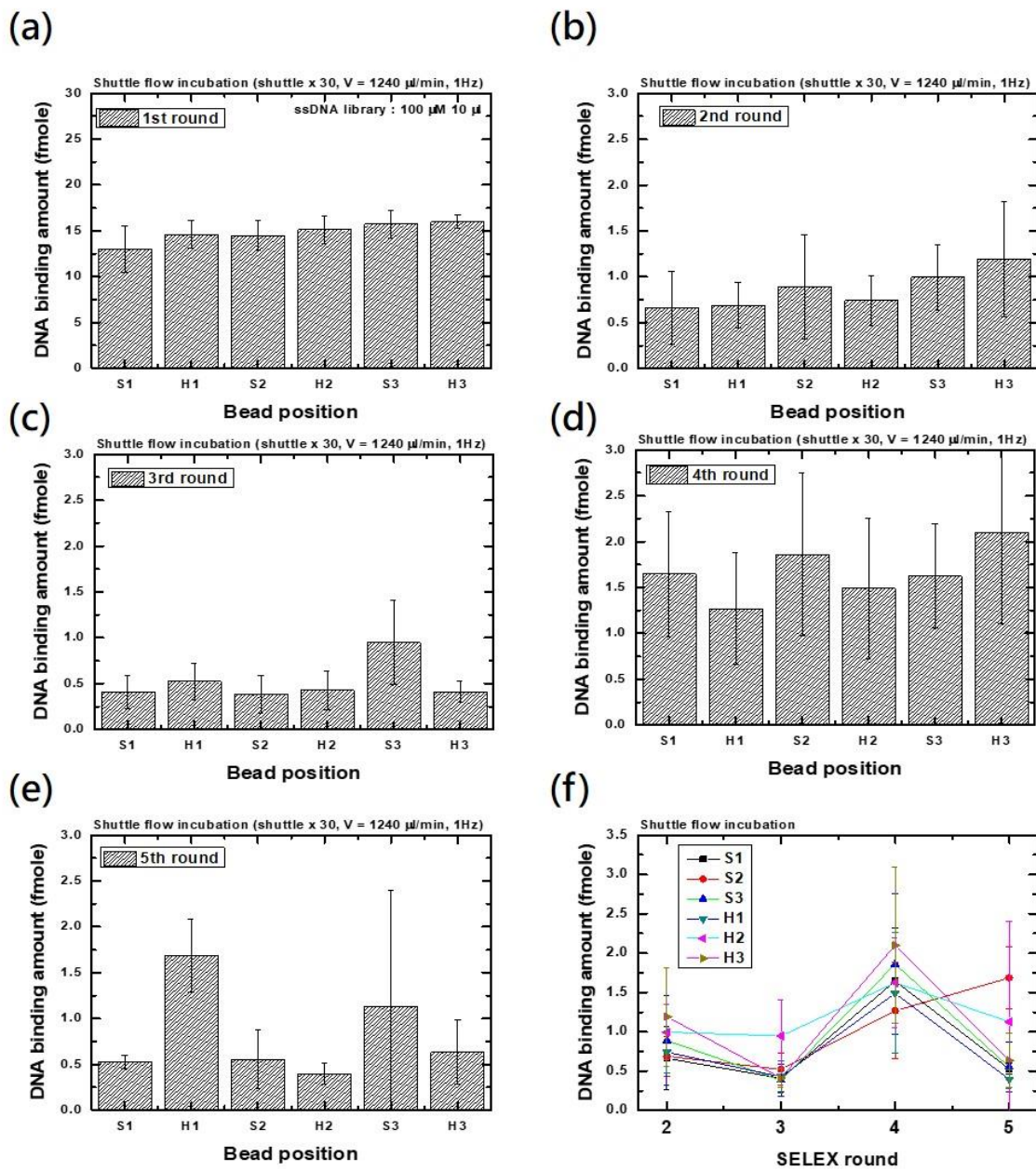
Figure 3.17 The DNA binding amounts on each protein-microbead in (a) 1st, (b) 2nd, (c)

3rd, (d) 4th and (e) 5th rounds. (f) The tendency of overall amounts of DNA binding with

increasing SELEX rounds.

121
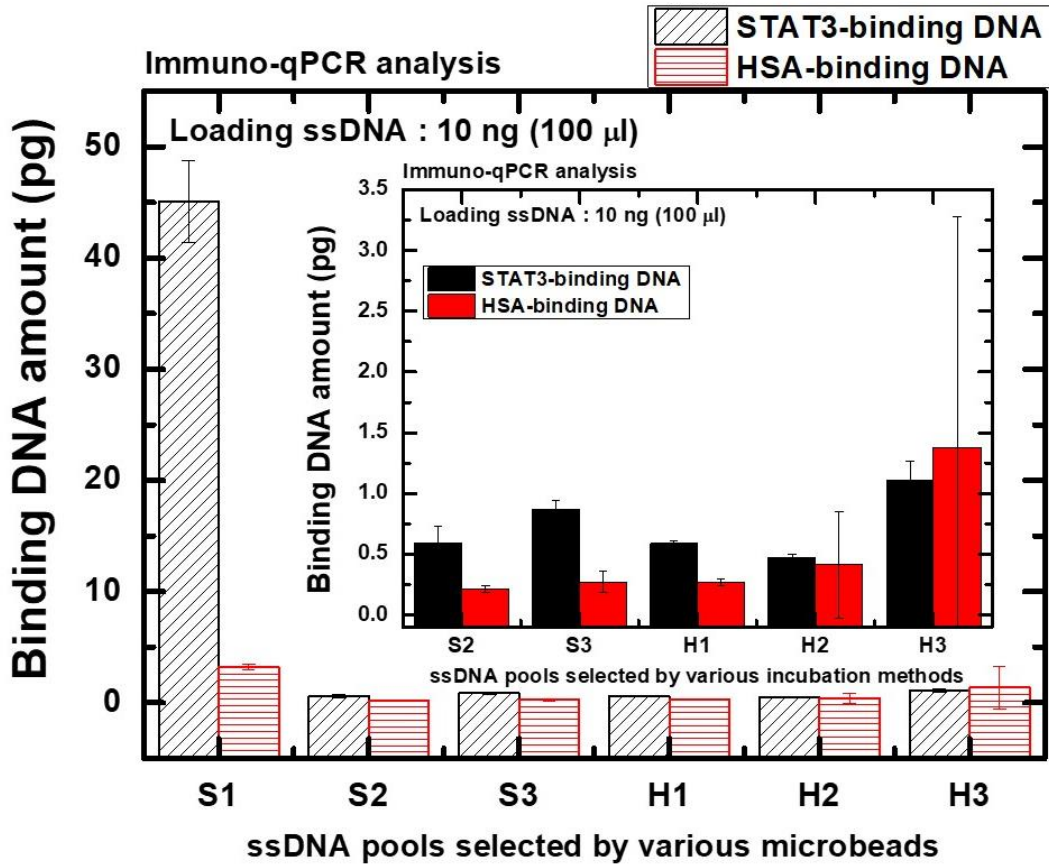
Figure 3.18 The specificities of STAT3-specific ssDNA pools compared with HSA protein binding. The insert diagram shows the zoom-in results of DNA binding amount on microbeads of S2 to H3.

3.4.4 ssDNA pools sequencing and sequences alignment

The Six groups of the DNA pools from each bead are cloned into the plasmid DNA by a TA-cloning kit. Because there is only one plasmid DNA can get into a single cell, one cell colony provides an identical sequence after the cell culture. The colonies are taken out to apply the PCR amplification, and then the PCR products are purified for the sequencing analysis (shown in Fig. 3.19). The total sequence is 96 including the 16 sequences obtained from each microbead. At first, the sequence similarity within groups of the STAT3-binding (shown in Fig. 3.20(a)) or the HSA-binding DNA (shown in Fig. 3.20(b)) are compared, and some sequences are marked by the green color to present a higher similarity. The identified sequences imply to have a converged motif after several selection rounds. Next, the STAT3-specific and HSA-specific sequences are compared again to find the similar sequence. The STAT3-specific aptamer named S304 has a similar motif to the HSA-specific aptamer named H107, and it implies that this aptamer has the possibility to bind both STAT3 and HSA showing a non-specific binding property. The DNA structures of the selected sequences are predicted by the online software (shown in Fig. 3.21). The aptamers named S213 and 206 show a similar configuration containing two loops. Thus, the non-specific sequence named S304 has more double-strand structure, and it might be attributed to the transcription protein feature of the STAT3 protein that is easily bound to the dsDNAs.

123
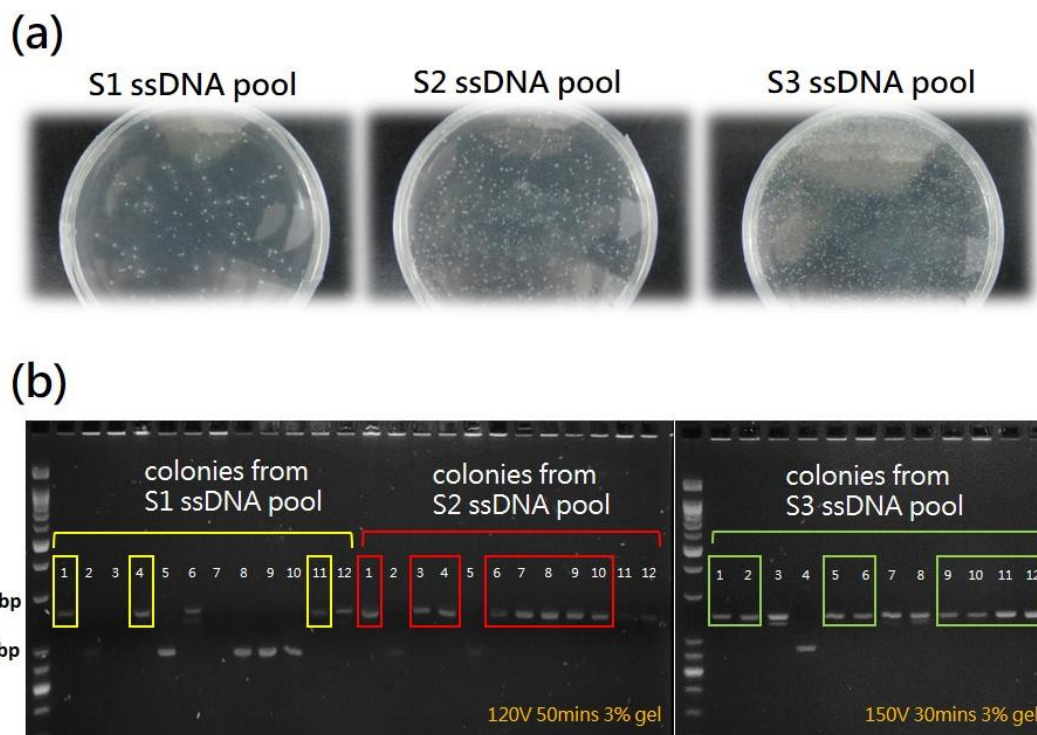
Figure 3.19 Identifying individual ssDNAs from selected pools by TA-cloning which (a)

transfects the ssDNA into the competent cells to form the colonies, and (b) the transfected

sequence can be confirmed by agarose (3%) electrophoresis.

(a)

(b)

(c)

	H110	H114	S216	H314	S204	S206	H113	S102	H107	H115	S304	H102	H209	H213	S213	H104	H203	H214
H110	100	100	31.03	35.71	34.78	24.14	28	26.09	25	25	23.81	34.62	30.77	30.77	39.29	24.14	25	25
H114	100	100	31.03	35.71	34.78	24.14	28	26.09	25	25	23.81	34.62	30.77	30.77	39.29	24.14	25	25
S216	31.03	31.03	100	37.04	37.5	21.43	19.23	16.67	40.74	40.74	40	36	32	32	22.22	35.71	37.04	37.04
H314	35.71	35.71	37.04	100	38.1	37.93	30.43	38.1	36.67	36.67	39.13	42.86	32.14	32.14	33.33	41.38	30	30
S204	34.78	34.78	37.5	38.1	100	27.27	17.86	40	38.1	38.1	35.71	31.58	31.58	31.58	23.81	27.27	38.1	38.1
S206	24.14	24.14	21.43	37.93	27.27	100	50	22.73	34.48	34.48	18.18	22.22	14.81	14.81	51.72	30	31.03	31.03
H113	28	28	19.23	30.43	17.86	50	100	28.57	43.48	43.48	31.25	23.81	23.81	23.81	34.78	37.5	39.13	39.13
S102	26.09	26.09	16.67	38.1	40	22.73	28.57	100	33.33	33.33	35.71	36.84	36.84	36.84	28.57	31.82	33.33	33.33
H107	25	25	40.74	36.67	38.1	34.48	43.48	33.33	100	100	60.87	32.14	32.14	32.14	26.67	34.48	36.67	36.67
H115	25	25	40.74	36.67	38.1	34.48	43.48	33.33	100	100	60.87	32.14	32.14	32.14	26.67	34.48	36.67	36.67
S304	23.81	23.81	40	39.13	35.71	18.18	31.25	35.71	60.87	60.87	100	36	48	48	26.09	45.45	30.43	30.43
H102	34.62	34.62	36	42.86	31.58	22.22	23.81	36.84	32.14	32.14	36	100	43.33	43.33	22.22	62.96	28.57	28.57
H209	30.77	30.77	32	32.14	31.58	14.81	23.81	36.84	32.14	32.14	48	43.33	100	100	17.86	48.15	28.57	28.57
H213	30.77	30.77	32	32.14	31.58	14.81	23.81	36.84	32.14	32.14	48	43.33	100	100	17.86	48.15	28.57	28.57
S213	39.29	39.29	22.22	33.33	23.81	51.72	34.78	28.57	26.67	26.67	26.09	22.22	17.86	17.86	100	20.69	20	20
H104	24.14	24.14	35.71	41.38	27.27	30	37.5	31.82	34.48	34.48	45.45	62.96	48.15	48.15	20.69	100	37.93	37.93
H203	25	25	37.04	30	38.1	31.03	39.13	33.33	36.67	36.67	30.43	28.57	28.57	28.57	20	37.93	100	100
H214	25	25	37.04	30	38.1	31.03	39.13	33.33	36.67	36.67	30.43	28.57	28.57	28.57	20	37.93	100	100

Figure 3.20 Sequence alignment according to the online software (MUSLE) that provides the match scores of sequences from (a) STAT3-binding and (b) HSA-binding ssDNA pools. (c) The similar sequences from both pools are matched again to exclude the non-specific binding aptamers.

125
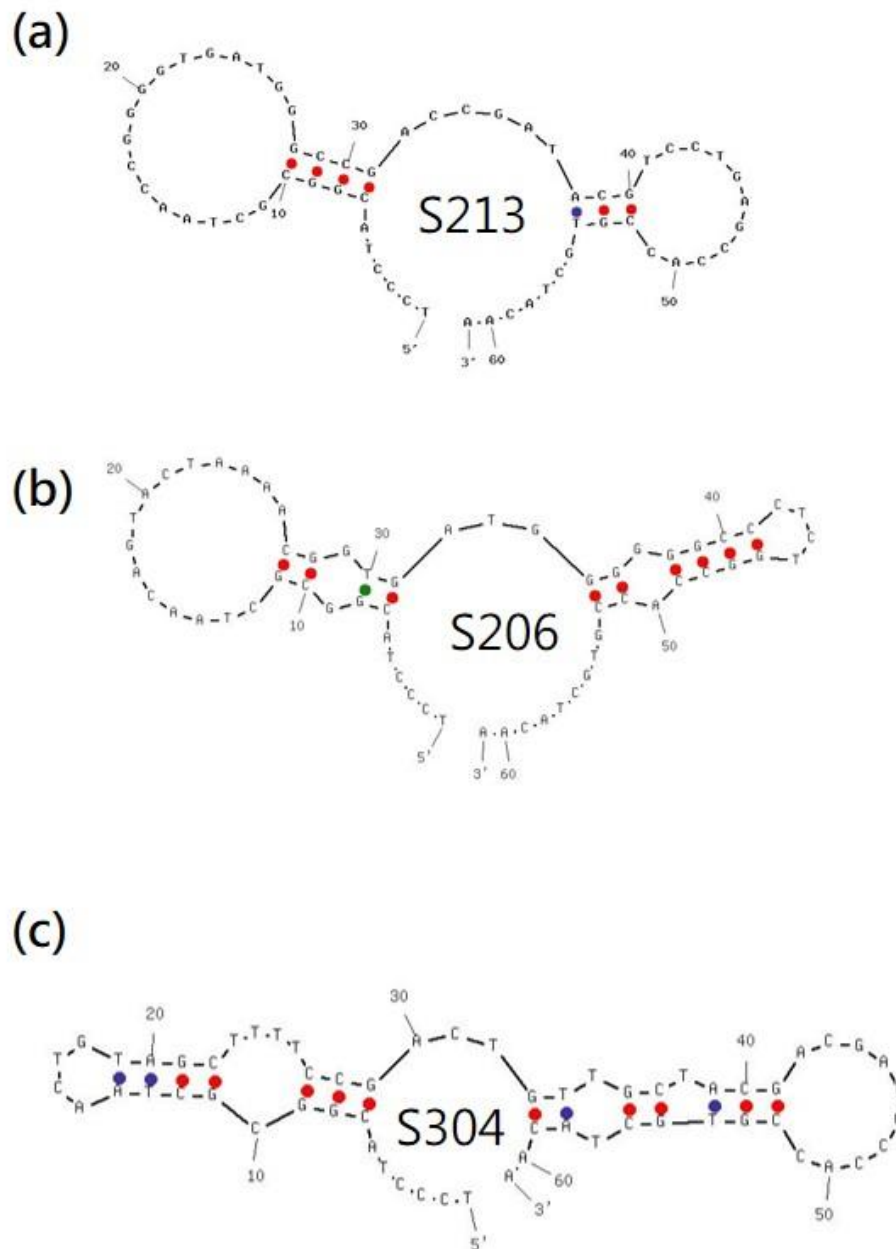
Figure 3.21 Structure prediction of possible STAT3-binding aptamers named (a) S213 and

(b) S206 and assumed non-specific binding aptamer (c) S304.

126

3.4.5 The influence of STAT3 aptamers on cancer cell

STAT3-specific aptamers can bind to the STAT3 protein which is a key molecule for the gene regulation of cell anti-apoptosis. In cancer cells, because of the failed gene regulation, the STAT3 proteins are over-activated which leads to the up-regulation of anti-apoptosis and over-proliferation. If the over-activated STAT3 proteins can be inhibited via the epitope binding of STAT3-specific aptamers, the cancer cells may be killed according to the corrected cell apoptosis process. The DNA-based STAT3-specific aptamers are transfected into cells by the lipofectamine which can prevent DNA degradation.

The STAT3-specific aptamers selected by the microbeads-array microfluidic device are transfected into breast cancer cells (MCF7) to estimate the performance of STAT3 inhabitation. In Fig. 3.22, all aptamers with the concentration of 100 nM seem to have high cell killing efficiency that may be resulted from the high charge density. Except for the S304 and S216 aptamers, the other aptamers show a dose-dependent response with increasing aptamer concentration.

In Fig. 3.23, The STAT3-specific aptamers (S304 and S206) are used as anti-cancer drugs to treat Clone9 and MCF7 cells with different concentration (1 nM, 10 nM, 25 nM, 50 nM, 100 nM, 200 nM). The IC50 ((half maximal inhibitory concentration) is ranged from 25 nM to 50 nM in the condition that Clone9 treated by S304 (shown in Fig. 3.23(a))

127

In comparison, the IC50 is ranged from 10 nM to 25 nM in MCF7 treated by S304 (shown in Fig. 3.23(b)).

The safety of using STAT3-specific aptamers as anti-cancer drugs is verified by measuring the cytotoxicity of drugs to primary liver cells shown in Fig. 3.24(a). Besides, the drugs are tested to know whether the liver cells can metabolize the drugs or not. Additionally, the performance of inhibiting cancer cells with the drugs is evaluated, and the metabolites of cancer cells are analyzed to measure the hepatotoxicity. After the drugs and MCF7 are incubated for 24 hrs, the medium containing metabolites is transferred to Clone9 cells. According to the results shown in Fig. 3.24(b), the drugs can kill the cancer cells, but the metabolites don't affect the Clone9 cells. On the other hand, after the drugs and Clone9 are incubated for 24 hrs, the medium containing metabolites is transferred to MCF7 cells. According to the results shown in Fig. 3.24(c), the drugs can also kill the liver cells (Clone9), and the used medium seems to have no inhibition to cancer cells. It may result from that the liver cells can degrade the drugs in the medium before the medium transferring process. Hence, cancer cells can still stay alive. However, the problem of hepatotoxicity is still needed to be solved.
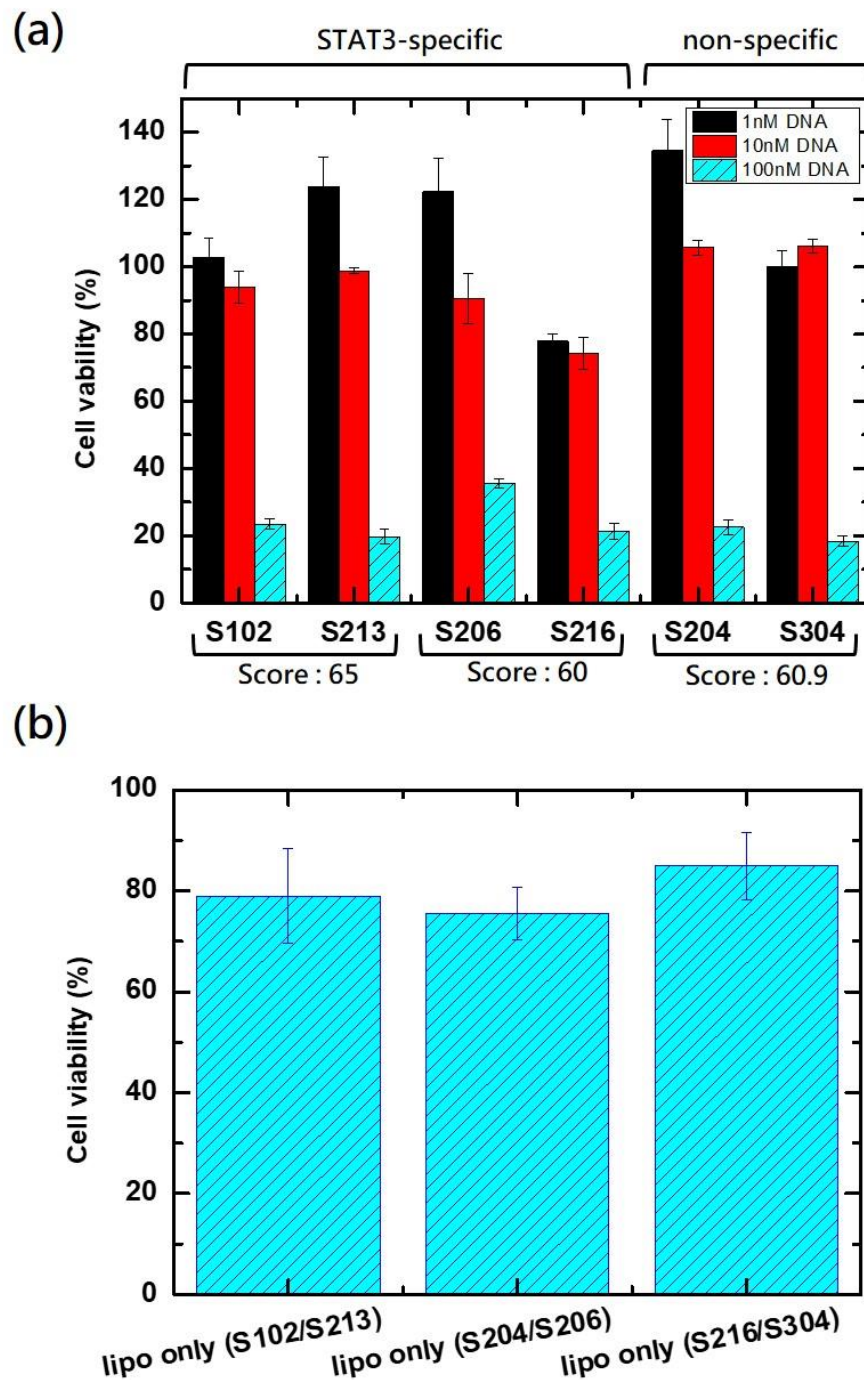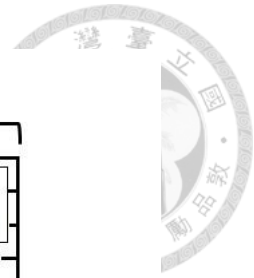
Figure 3.22 The death of breast cancer cells (MCF7) caused by the STAT3-related gene regulation. (a) Cell viability of cancer cells treated by the selected STAT3 aptamers with different DNA concentrations. (b) Lipofectamine shows few cytotoxicities even in the highest prepared concentration (for 100 nM DNA preparation).

129
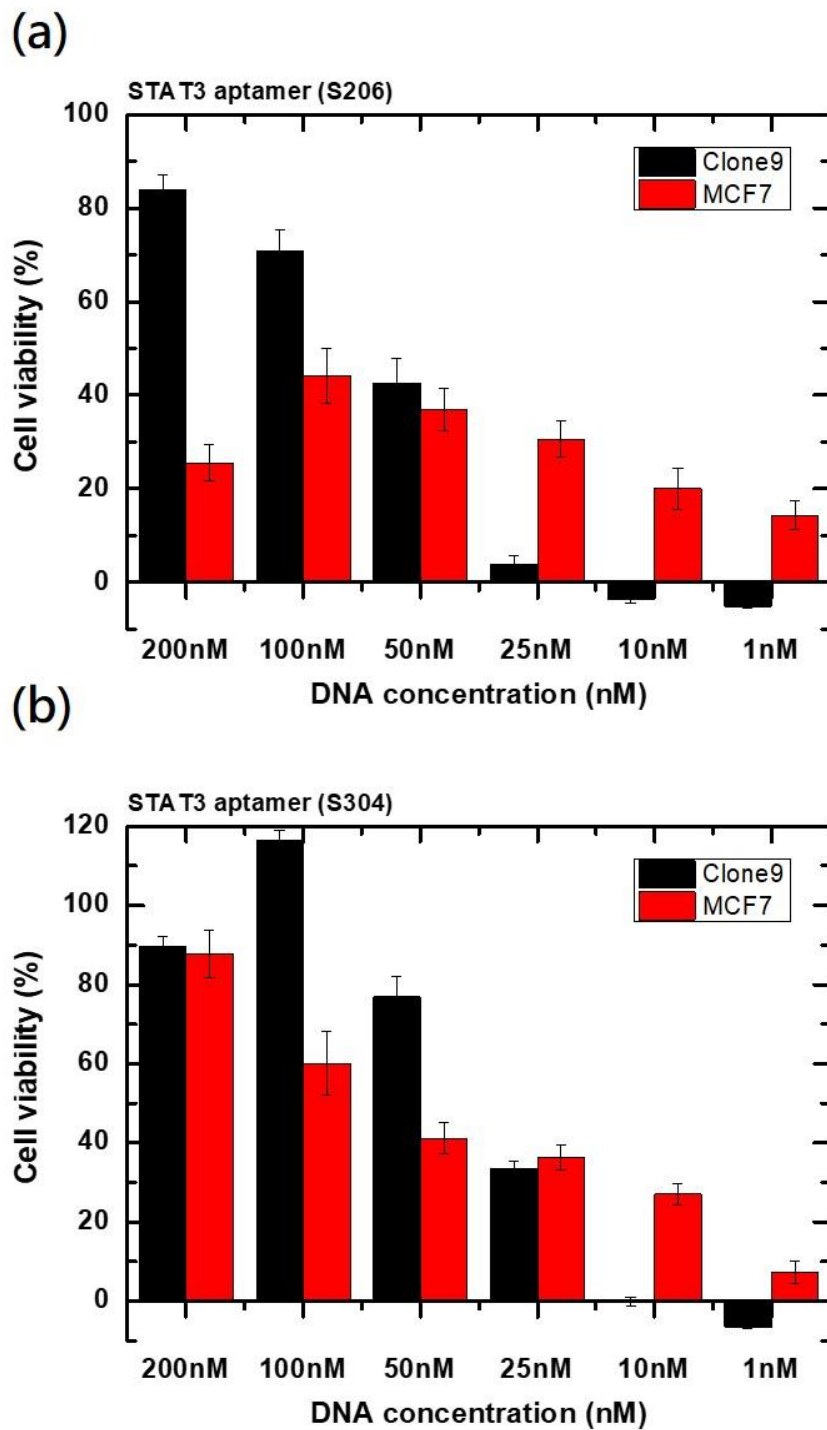
Figure 3.23 The selectivity of aptamer-induced cell death on liver cells (Clone9) and

breast cancer cells (MCF7) wit (a) S206 and (b) S304 aptamers.

130
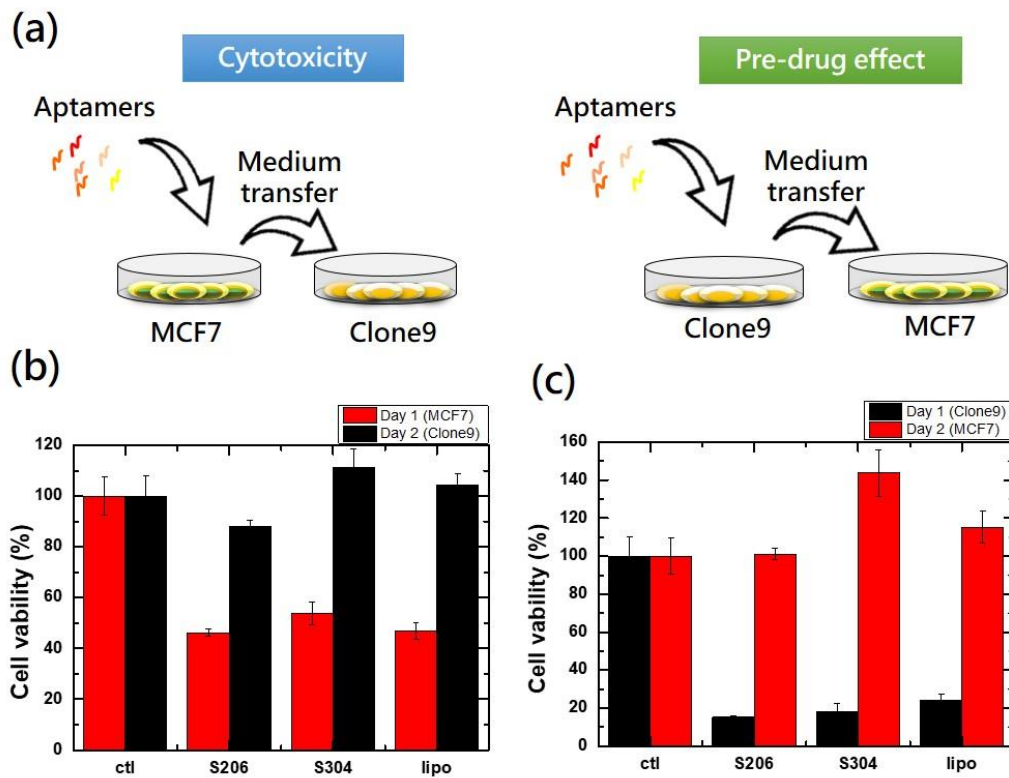
Figure 3.24 Influence of the metabolites produced by aptamer-treated cells. (a) The schemes describe the experimental designs for studying the cytotoxicity and pro-drug effects. The MTT assay quantifies the cell viabilities affected by (b) cytotoxicity and (c) pro-drug effect.

3.5   Chapter summary
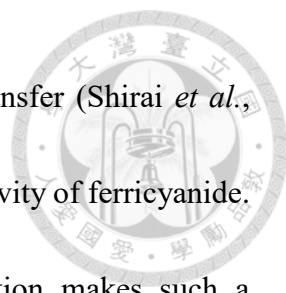
Single-bead SELEX is already proven as a powerful aptamer selection tool for rapid aptamer generation. To integrate the singe-bead SELEX into a microfluidic chip for improving the selection efficiency, a microbeads-array microfluidic device is constructed to carry out the multiplex aptamer selection. In traditional tube-based SELEX, the long diffusion distance leads to a long hybridization time and weak partitioning strength. Using the microfluidic device, the DNA-protein interaction can be performed in microchannel which has short diffusion distance that enhances the hybridization efficiency. Moreover, the shuttle flow is applied to transport the ssDNA solution across the microbeads repeatedly that causes a micro-mixing effect to enhance the DNA binding. Additionally, the shuttle flow can provide a serious washing strength which may be resulted from the shear stress around the surface of microbeads. The assumption is verified according to the shuttle washing experiments. The STAT3-specific ssDNA pools are identified after five selection rounds, and the individual STAT3-specific aptamers are also determined by software analysis and the validation of cancer cell inhibition.

Chapter 4. Microfluidic amperometry with microelectrodes
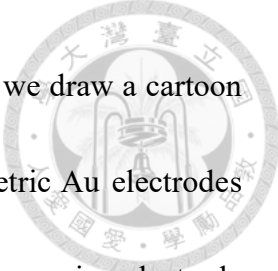
4.1 Introduction

Electrochemical detection of ferricyanide with an electrode chip in a microfluidic channel has been extensively applied in developments of various lab chips for bioassays, ranging from enzymatic to affinity-based molecular recognition. Being an ideal redox mediator, ferricyanide has been employed as an electrochemical reporter that probes the electrode surface in response to analyte sensing. Although the electrochemical characteristics of ferricyanide in a classical three-electrode system have been thoroughly studied and well understood for decades, precise control of the redox electrochemistry at two symmetric Au electrodes and enhancement of ferricyanide signal are still important issues for microfluidic biochips (Horny *et al.*, 2016). Fabrication of a biochip with a pair of Au electrodes is simple due to eliminating the tedious steps for growing a solid-state reference electrode on a chip. In addition, an Au electrode has well-established surface chemistry for decoration with versatile bio-recognition elements, such as antibodies, and aptamers. However, a two-electrode measurement by setting one Au electrode as the working electrode (WE) and the other as the counter and reference electrodes at the same time (CE/RE) is rather an electrolytic cell process than a single electrode analysis. This makes the three-electrode electrochemistry difficult to apply to two-electrode chips directly. Furthermore, when the electrode chip is placed inside a microfluidic channel, the

133

diffusion limit and laminar flow often show downsides in mass transfer (Shirai *et al.*,

2014), respectively, and both effects decrease the redox signal sensitivity of ferricyanide.

Besides, the two-electrode measurement plus microfluidic operation makes such a

biochip detection an interesting research problem, which is similar to redox

characterization of a miniature electrolytic cell with flow electrochemistry (Marschewski

et al., 2015). Motivated by the above reasons, we aim to study the electrochemical

detection of ferricyanide with a pair of Au microelectrodes under different microfluidic

manipulations and to provide a better insight into two-electrode microfluidic

amperometry.

Microfluidic amperometry means performing electrochemical current

measurements by controlled-potential techniques, such as chronoamperometry (CA) and

cyclic voltammetry (CV), with microelectrodes embedded in a microfluidic device.

Having the advantages of minute sample requirement, adjustable flow mode, and on-chip

microanalysis, microfluidic amperometry can be developed as a powerful analytical

platform for both sample characterization and analyte detection. In practice, a pair of

microelectrodes are usually fabricated on a glass chip with lithography for microfluidic

amperometry, and both are made of Au for reducing the process cost (cf. three-electrode

system) and for biomolecule immobilization through thiol-gold interaction. Thus,

microfluidic amperometry is presumed to be influenced by the microelectrode dimension

134
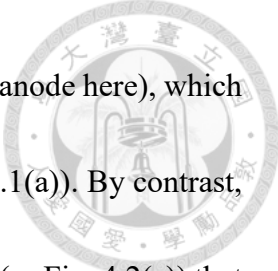
and pattern design (Kidner *et al.*, 2007). To better address this point, we draw a cartoon

to illustrate the presumed ferricyanide redox reaction at two symmetric Au electrodes

with an applied voltage bias and provide the pattern details of the three microelectrode

chips studied in this work in Fig. 4.1. From Fig. 4.1(a), we can imagine that an equal

molar mixture of ferri/ferro-cyanide stays at its equilibrium at zero bias. The redox

reactions triggered by exerting a forward and reverse bias with the same voltage across

the two Au electrodes are symmetrical and should result in the same redox current despite

opposite electrode polarization. Also, there is a redox cycling phenomenon while the two

electrodes have a small gap in between. From Fig. 4.1(b), it shows the three different Au

microelectrode pairs studied in this work with potential redox cycling of ferri/ferro-

cyanide under an applied bias. The electrodes are micro-fabricated on a glass chip and

aligned with interdigitated array (IDA), parallel symmetry (PAR), and serial symmetry

(SER) designs, respectively. From the figure, we can realize that the electrode dimensions

and pair alignment are important factors to determine the redox signal. They determine

the inter-electrode gap distance for triggering the redox cycling between Fe^{3+} and Fe^{2+}

(White and McKelvey, 2018). They also influence the electrode sequence to contact redox

species carried by the microfluidic flow, which can result in "flow polarization" (Kim

et al., 2007) that promotes the downstream electrode reaction due to a facilitated transport

of redox species from the upstream (see Fig. 4.2). The latter consideration brings another

135

important factor in addition to microelectrode design to our attention. That is the flow condition, which is an indispensable factor in microfluidic analysis.
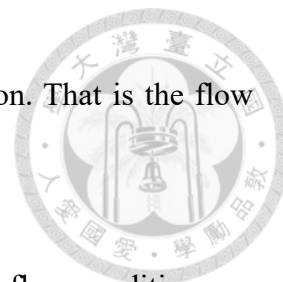
To understand how microfluidic amperometry is modulated by a flow condition, we investigate the influences of one-way flow and shuttle flow on the microfluidic amperometric detection of ferricyanide in this work. Taking a SER-based device as an example, we draw a cartoon in Fig. 4.2 to explain how one-way and shuttle flows exert distinct effects on the microfluidic amperometry. When a forward bias (i.e., WE = anode; CE/RE = cathode) is applied to the SER microelectrodes under a static condition (shown in Fig. 4.2(a)), the voltage bias results in a corresponding concentration polarization of ferri/ferro-cyanide on the anode and cathode, respectively. Under this circumstance, the redox current would gradually decay with the square root of time due to the Cottrell's diffusion current behaviour. Yet, if a one-way flow is applied to this two-electrode amperometry (as Fig. 4.2(b)), a facilitated mass transfer of ferricyanide occurs. It not only renews the surfaces of both electrodes but also increases the transfer rate of ferri/ferro-cyanide in the microfluidic channel. Thus, the redox current is supposed to be significantly enlarged and to be increased with the flow rate. Moreover, the flow rate would determine the ratio of convective mass transfer speed to diffusional mass transfer speed for the redox mediator. This provides a chance to tune the electrochemical characteristics from the aspect of microfluidic transport phenomenon. Besides, there is

136

supposed to be an accompanying flow polarization effect (cathode-to-anode here), which

breaks the two-electrode symmetry under a static condition (as Fig. 4.1(a)). By contrast,

if the flow condition is changed to a specialized mode – a shuttle flow (as Fig. 4.2(c)) that

moves a tiny drop of the redox couple back and forth at a certain rate for repeated reaction,

the redox species will "swing" on the electrode area. Moreover, the flow polarization

direction would be altered periodically. The effect turns to be micro-mixing that reduces

the concentration gradients of ferri/ferro-cyanide across the two electrodes. Then the

current characteristics should be highly correlated to the shuttle speed and distance, and

it can become a unique approach for in situ determination of the degree of micro-mixing.

According to the above "thought experiments," we design and perform a series of

experiments to show how one-way and shuttle flows modulate the microfluidic

amperometry differently as discussed below.
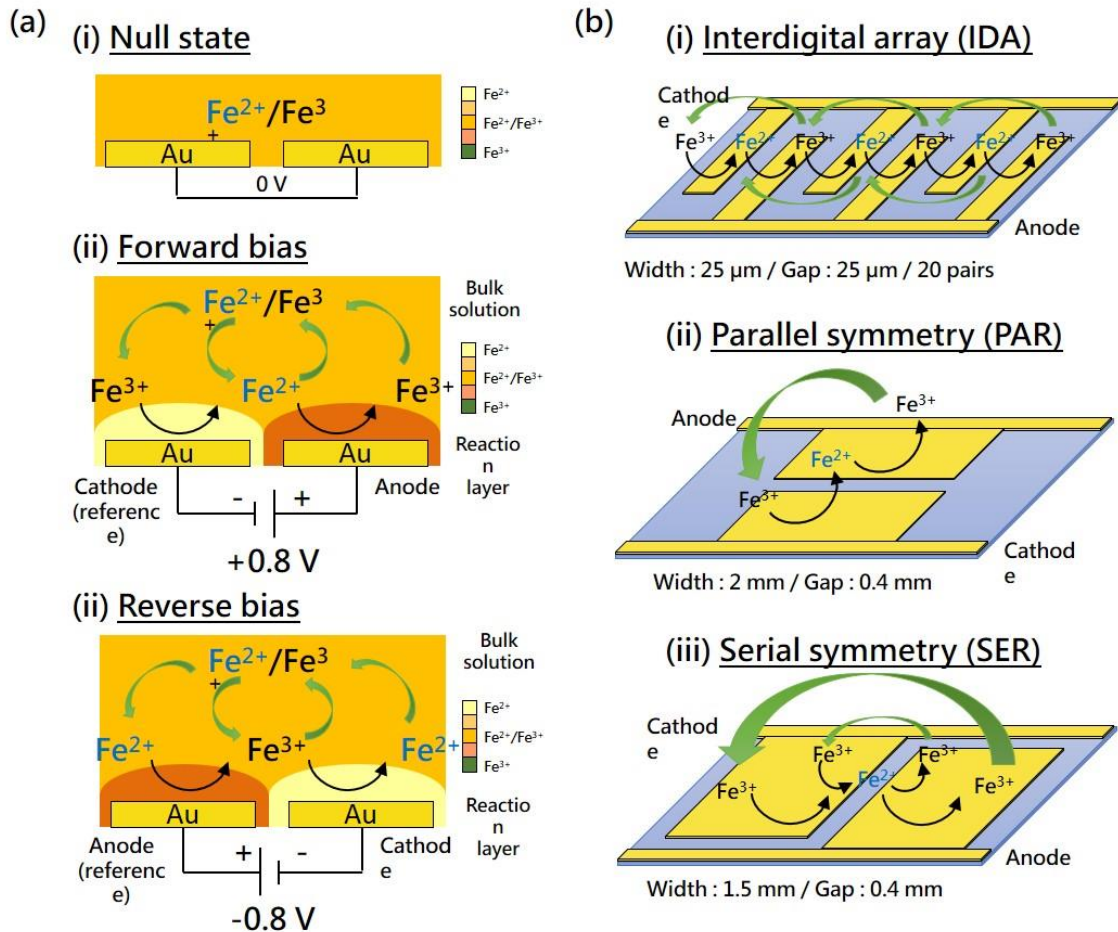
Figure 4.1 Presumed redox cycling and electrode pattern effects for amperometric analysis of ferri/ferro-cyanide at two symmetric Au microelectrodes. (a) Redox reactions under (i) zero bias, (ii) forward bias and (iii) reverse bias. (b) The three Au microelectrode pairs with different alignment designs (IDA, PAR, SER) and illustrated with presumed redox cycling of ferri/ferro-cyanide under an applied bias.
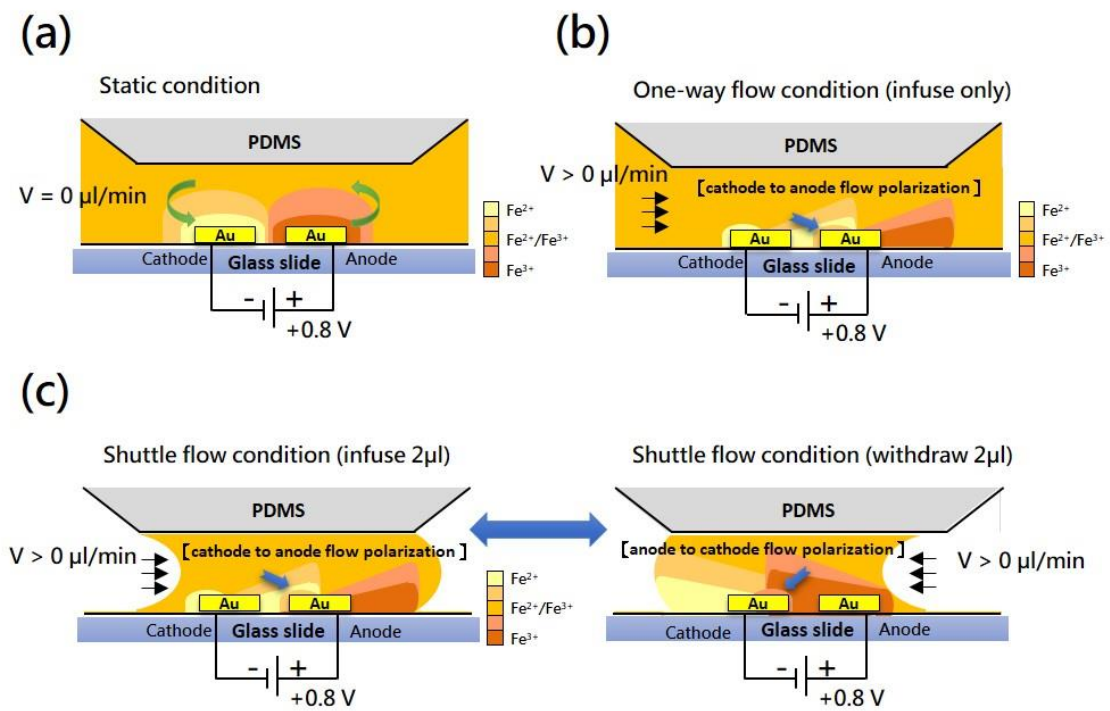
Figure 4.2 Presumed flow polarization and mediator distribution effects for the microfluidic amperometry of ferri/ferro-cyanide at two symmetric Au electrodes under the (a) static, (b) one-way and (c) shuttle flow conditions.
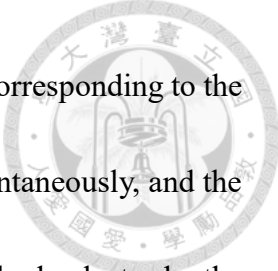
4.2   Literature review

4.2.1   Electrochemistry applied to sensor development
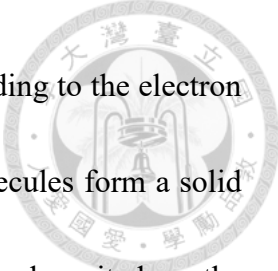
Electrochemistry is a technique studying the relationship between chemical reaction

and electricity. The measurable physical quantities are produced by either an externally

applied current, as in electrolysis, or a spontaneously chemical reaction, as in a battery.

The electrochemical reaction happens due to the electric charges transporting between

electrodes and an electrolyte. Reduction and oxidation generally called redox reaction are

identified as the electron transfer behavior between molecules in a narrow definition. Both

reactions are symmetrical that means the reduction and oxidation occur simultaneously.

However, electrons are hardly transported in the electrolyte, so an external electric circuit

is necessary to supply another road for the electron transfer. The uneven distribution of

electrons leads to an electric potential difference, and it generates the electron flow named

current. According to the amount of current response, the extent of reaction can be

estimated. On the contrary, as the sufficient electrical energy is supplied on electrodes,

the corresponding chemical reaction takes place with uncertainly proportional levels.

The most classic electrochemical device is electrochemical cells (also named battery)

that store the electric energy via a spontaneous redox reaction. They have two conductive

electrodes as anode and cathode, which is defined as an oxidation electrode and a

reduction electrode, respectively. In a galvanic cell, two different metal electrodes are

immersed in an electrolyte which contains the positive-charged ions corresponding to the metal electrodes. At the anode electrode, the oxidation undergoes spontaneously, and the metal of the electrode is oxidized to a positive-charge ion. At the cathode electrode, the metal ions in the solution are reduced to the solid metal through the reception of electrons. The loss and gain of electrons among the anode and cathode electrodes are connected by an external circuit where the electron flow occurs.

The tendency of electron transfer is determined by the standard electrode potential (E°) which implies the pulling force of the substrate undergoing reduction reaction on electrons in the standard state. All the standard electrode potentials are referenced to the standard hydrogen electrode (SHE), and the E° values are tabulated into a table for the prediction of the cell potentials. A spontaneous reaction occurs as long as two half-reactions are matched with appropriate E° values. The electrode having higher E° acts as the cathode, and the other electrode acts as the anode which needs to reverse the reaction direction in the half-reaction table. In contrast, an unspontaneous reaction like electrolysis and electrodeposition can be driven by an external voltage. The electrons flow via the potential difference that compels the reduction and oxidation reaction at each electrode. In electrolysis, the electrical energy can trigger the component reorganization in the electrolyte. Most of the products from the electrolysis are gases, so bubbles usually occur on the electrode surface during the reaction. Instead of the decomposition in electrolysis,

the formation of films can also be induced by external energy. According to the electron

transfer between the electrode and ions in solution, the aqueous molecules form a solid

state which attaches on the electrode substrate. Materials are electrodeposited on the

electrode surface, and the thickness of the film is determined by the parameters including

deposition time, solvent concentration and applied voltage.
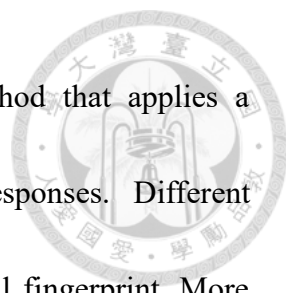
The electron-based reaction in electrochemistry shows a rapid and sensitive response.

This feature makes the electrochemical tools suitable to develop an efficient sensing

platform. The following subsections will further introduce the electrochemistry in sensing

amplifications. From a typical three-electrode system to a novel symmetric configuration,

the standard analysis methods and superiorities are discussed in detail. Moreover, the

miniaturization and geometry effect of electrodes are compared for the optimization of

sensing performance.

142

4.2.2　Three-electrode system for electrochemical sensing

To measure the electrochemical reaction in the electrolyte, the two-electrode system is a common configuration containing a working electrode (WE) and a reference electrode (RE). As a negative voltage is imposed on RE, the WE will be relatively positive and induce an oxidation reaction which releases the electrons from high potential to low potential. Both electrodes are connected to an operation amplifier (OPA) for converting the tiny current response into readable voltage values. According to Ohm's law, the output current can be calculated by the resistance and applied voltage. With the tunable potential-control, the electrochemical instrument named potentiostat is used to measure the current. However, a fatal disadvantage of the two-electrode configuration occurs in long-term measurement. When a large current passes through the RE, an undesired reaction may damage the electrode that leads to an incorrect reference potential.

A counter electrode (CE) is introduced to form a three-electrode electrochemical system. CE and RE are connected via another OPA which has large input impedance to prevent the current-induced breaking of the reference electrode. With the aid of CE, although the potential is not exactly the same as RE, the CE which carries out the counter reaction still saves the RE from destruction. Based on the three-electrode system, several electrochemical methods are developed for various applications. According to the detecting quantity, the methods can be divided into voltammetry and impedimetric. In

voltammetry, cyclic voltammetry (CV) is a classic analysis method that applies a continuously changing potentials and monitors the current responses. Different electrolytes lead to distinct CV profiles just like an electrochemical fingerprint. More voltammetric methods are derived to improve the sensing performance, for instance, linear sweep voltammetry (LSV), differential pulse voltammetry (DPV), and square wave voltammetry (SWV). In impedimetric, electrochemical impedance spectroscopy (EIS) is a powerful tool for redox resistance measurement. Multiplex information about the redox reaction can be provided through the impedance spectrum. With the versatile electrochemical tools, the three-electrode system is not only widely developed in traditional chemical engineering, but also becomes an addressing biological technique for environment monitoring, disease diagnosis and food safety.

Integrated with microfluidic technology, electrochemical sensing platform can be miniaturized into a small chip. The mini chips consume fewer reagents for the electrochemical detection, and the miniature size of the device is suitable for portable sensor development. The most important thing about miniaturization is the fabrication of the microelectrodes. In general, the microelectrodes are manufactured through standard photolithography with designed patterns. Instead of the traditional etching process, the lift-off process is a method of producing patterned microelectrodes. After the photoresist is coated on the substrate that acts as a sacrificial layer, the materials of microelectrodes

144

are deposited on the chip. Because of the stepped structure of photoresist, a discontinuous material film is generated. Finally, the sacrificial layer is removed by immersing the chip into acetone, and then the patterned microelectrodes are accomplished.

On the other hand, the microelectrodes have some drawbacks on electrochemical sensing. The small working area of the electrode causes a small current response that may be interfered by some background noise. Additionally, the small area also reduces the amount of functional material immobilization which may correspond to the sensing performance. To connect the electrodes to the potentiostat instrument, the connecting pad and conductive wire are integrated with microelectrodes. But, following the theory of sheet resistance, the narrow wires cause a large conductive resistance which may suppress the electron transfer efficiency.

Fang's group present a three-electrode microfluidic device for DNA analysis (Fang *et al.*, 2009). The device contains three platinum electrodes serving as a working electrode, a counter electrode and a pseudo-reference electrode. The microelectrode array is located on a glass substrate, and each electrode set forms a detection station for electrochemical sensing. The chip has a multi-layer structure including a heater, microelectrode array and a PDMS microchannel. The working principle of DNA analysis is based on real-time qPCR. A continuous flow PCR is used to carry out DNA amplification. When the DNA template is amplified via PCR process, the particular DNA-intercalating molecules,

145

methylene blue (MB), bind to enriched DNA. More DNA is produced during PCR, less

MB retains in the solution. The MB concentration is determined by SWV analysis, and

the peak currents have a negative correlation to the DNA amount.
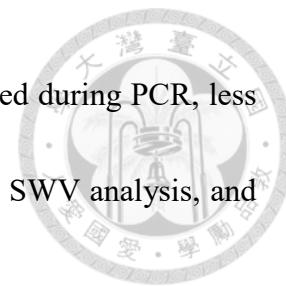
Zou's group demonstrate the heavy metal ions measurement through a

microfabricated chip embedded a bismuth (Bi) electrode (Zou *et al.*, 2008). This three-

electrode system consists of a Bi working electrode, an integrated Ag/AgCl reference

electrode and a gold counter electrode. Square wave anodic stripping voltammetry

(SWASV), which has lower background noise, is used for Pb(II) detection. This

disposable sensor has a detection limit of 8 ppb in a 60s deposition that is appropriate for

online direct measurement.

Wu's team fabricate a disposable electrochemical immunosensor for

carcinoembryonic antigen (CEA) detection (Wu *et al.*, 2006). A three-electrode screen-

printed carbon electrode (SPCE) system involve graphite-based working and counter

electrodes, and a Ag/AgCl reference electrode. The CEA antigens are embedded in an Au

colloid and chitosan membrane. A competitive assay that the CEA and HRP-labeled anti-

CEA are incubated with modified electrodes is executed for the immunoassay. The HRP

catalyzes the H_2O_2 to H_2O, and the reduced H_2O_2 concentration leads to a decreasing

catalytic current through DPV analysis.

Wisitsoraat *et. al* develop a flow injection microfluidic device for fast cholesterol

146

detection (Wisitsoraat *et al.*, 2010). The functionalized carbon nanotubes are immobilized on a gold working electrode. Integrated with a silver reference and a platinum counter electrode, the three-electrode system is constructed for FIA applications. Cholesterol oxidases are fixed on the CNTs by in-channel flow technique. Sample plugs are injected into the carry buffer stream, and the current response is continuously monitored at a constant potential vs. Ag reference electrode.
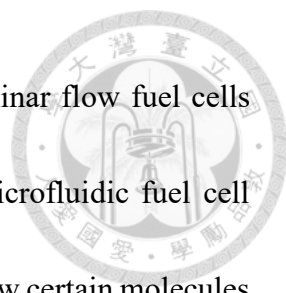
Hadar's team report a controlled microfluidic electrochemical lab-on-a-chip for DNA hybridization analysis (Ben-Yoav *et al.*, 2015). The counter and the working electrodes are made of gold, and the reference electrode is made of platinum. The DNA probes are immobilized on the working electrodes via the gold-thiol covalent bounding. As the target DNAs hybrid to the probe DNAs, the repulsion forces between negative-charged dsDNA and the electro-active species like ferricyanide and ferrocyanide increase that leads to a higher charge impedance. According to the impedance change, the concentration of target DNAs can be quantified through a label-free sensing platform.

4.2.3 Symmetric microelectrode for miniaturized biosensors
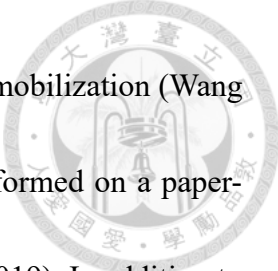
Although the three-electrode system is a typical configuration for electrochemical sensing which can provide a stable potential due to the protected reference electrode, however, the manufacturing process of the microelectrodes is too complicated to achieve the mass production. If the microfabricated device wants to mimic the elements of the traditional three-electrode system, an inert metal as the counter electrode and a planar Ag/AgCl as the pseudo-reference electrode are necessary to assembly the detection platform. However, it makes the process complicated because three electrodes are made of different materials. Patterned electrodes are deposited on substrate through a layer-by-layer procedure or masked evaporation. To simplify the electrode fabrication, the two-electrode system is re-proposed that the counter and reference electrodes are combined to a single electrode. Meanwhile, the novel strategies for improving the drawbacks of the two-electrode system are widely developed in order to enhance the feasibility of commercialization.

Actually, the two-electrode system is a common configuration in microfluidic fuel cells. Two electrodes serving as anode and cathode electrodes are embedded into a microfluidic chip which has two laminated inlet flows. Kjeang *et. al* demonstrate a microfluidic fuel cell using the formic acid (HCOOH) fuel and hydrogen peroxide (H_2O_2) oxidant (Kjeang *et al.*, 2007). Two Pd-modified electrodes are used to measure the power

148

density generated from fuel cell reaction. However, the two co-laminar flow fuel cells usually encounter a crossover problem. Hence, a membraneless microfluidic fuel cell containing a leak-free PEG membrane is performed to selectively allow certain molecules and ions diffusion (Ho *et al.*, 2016). In this device, two Pt electrodes are deposited on a plastic film, and the other two plastic films are used to form the microchannel and cover lid. Furthermore, a pump-free microfluidic fuel cell is presented to achieve the autonomous point-of-care (Esquivel *et al.*, 2014). Two patterned gold electrodes are evaporated on a paper substrate. According to the capillary forces, the liquids move through the electrodes under laminar flow situation. The two-electrode system can successfully harvest the energy generated from the biological samples during analysis.

The symmetric microelectrode configuration is also employed to the electrodeposition under microfluidic conditions. Polysaccharide hydrogels such as chitosan and alginate are biocompatible scaffolds which can be microfabricated through the electrical and flow control (Cheng *et al.*, 2012). As a constant voltage applies to the cathode, the reduction of hydrogen ions causes a pH gradient. The high pH value near the electrode surface induces the electrodeposition of chitosan hydrogel. According to the deposition mechanism, chitosan film can be assembled on addressable electrodes for further immobilization of biological components(Liu *et al.*, 2011). Layer-by-layer (LBL) assembly of alginate and chitosan is available in symmetric microelectrode microfluidic
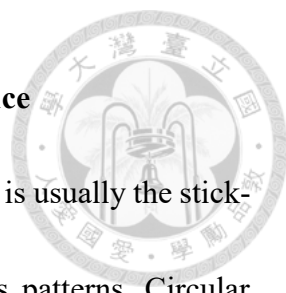
chips, and the LBL structure can offer a mild condition for protein immobilization (Wang

et al., 2011). Additionally, the chitosan electrodeposition can be performed on a paper-

based microfluidic device for enzyme immobilization (Wang *et al.*, 2019). In addition to

the biomaterials deposition, a silver deposition is also performed in a microchannel

embedded with two electrodes (Kozicki *et al.*, 2005). The silver electrodeposition

changes the fluid-surface interaction and serves as a valving element.

Electrical impedimetric sensing can be compiled by symmetric electrodes without a

three-electrode system. A simple two-electrode chip is fabricated for monitoring of blood

coagulation process (Lei *et al.*, 2013). The equivalent electrical model of the whole blood

is established. The capacitance and resistance contributed from blood cells and solution

are calculated via the impedance spectrum analysis. A printed gold electrode chip and a

microfluidic flow cell are developed for sensitive and selective detection of transgenic

protein Cry1A (Jin *et al.*, 2017). Two gold disk electrodes are used to measure the

impedance changes resulted from the target binding. When the anti-Cry1Ab aptamer

coated magnetic beads capture the target proteins, the negative-charged beads are

neutralized due to the electrical nature of Cry1Ab surface. Because of the low

conductivity, the impedance decreases along with increasing protein binding. To further

improve the sensitivity of impedimetric sensing under symmetric electrode configuration,

the microfluidic device integrating the gold interdigitated array microelectrode is
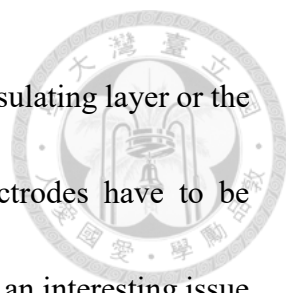
constructed for protein detection (Wang *et al.*, 2014c). With a similar sensing mechanism,

Bode diagrams of impedance spectra are compared under different protein concentration.

A suitable sensing frequency is identified that has good linearity with the concentrations

of protein and the detection limit is 0.01 nM. Interdigitated array (IDA) microelectrode is

an interesting configuration for electrochemical analysis. Using the IDA electrode, the

self-anchoring nickel microelectrodes are used to measure conductivity via impedance

spectroscopy analysis (Paredes *et al.*, 2015).

4.2.4 Geometric effect of microelectrodes on sensing performance

Unlike the traditional electrodes used in bulk solution system that is usually the stick-shaped or disk-shaped, microelectrodes are fabricated with various patterns. Circular patterns shown in Fig. 4.3(a) are commonly used to minimize edge effects at the corner, and the circle shape is suitable for uniform dispersion of drop coating. Two symmetric gold disk electrodes connecting to conductive wire are employed for stationary impedimetric detection (Jin *et al.*, 2017). Additionally, two asymmetric electrodes are fabricated with an inner small working electrode and a surrounding counter electrode having a large area (Lin *et al.*, 2010). Based on the electrochemical principle, the counter electrode serves as a charge sink for carrying out the complementary reaction of the working electrode. Hence, the area of counter electrodes should be larger than the working electrode in order to eliminate the possible current limitation. An interdigitated concentric circular design maximizes the surface area of the sensing site for the detection of antibiotic contaminants in water (Jacobs *et al.*, 2013). In the three-electrode system, a central circular working electrode is surrounded by the meniscus-shaped counter and reference electrodes, and a larger CE is also observed (Ali *et al.*, 2017).
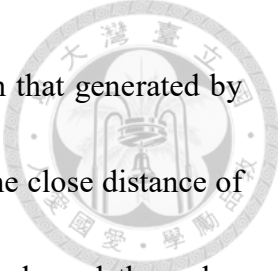
Bar-shaped electrode shown in Fig. 4.3(b) is another optional configuration, especially applying to microfluidic applications. This electrode can be easily fabricated by various processes involving photolithography, lift-off depositing, and screen printing.

The square shape makes it easy to control the working area via the insulating layer or the microchannel. However, in the narrow microchannel, the bar electrodes have to be arranged in serial. The arranging sequence of the electrodes becomes an interesting issue which may affect the electrochemical response. In the flowing microfluidics, the flow direction can define the upstream and downstream where may show different electrochemical reactions. Three-electrode system can produce six kinds of arrangement, but most of the researches choose only four types involving RE/CE/WE, RE/WE/CE, WE/RE/CE and CE/RE/WE. It seems that the RE should be at the upstream to provide a stable potential basis (Ko *et al.*, 2017), and it would be better to place the CE and WE nearby for a short diffusion length (Mayorga-Martinez *et al.*, 2013).

More designs of microelectrode are proposed to improve the sensing performance. Vertical electrode configuration shown in Fig. 4.3(d) which deposits the microelectrodes on the walls of microchannel can prevent the gravity-induced sedimentation (Wang *et al.*, 2011), and the effect may reduce the non-specific binding on electrodes. Different geometries of working electrode affecting on electrochemical detection are compared in various flow conditions. The model of the mass charge transport on a channel with one bumped, inlaid, or recessed electrode and two bumped electrodes shown in Fig. 4.3(e) are studied (Al Khatib *et al.*, 2018). The bumped geometry has the better collection percentage and higher current yield. Recently, IDA electrode shown in Fig. 4.3(c) attracts

153

great interest because the electrochemical signal is much higher than that generated by

single electrodes (Shim *et al.*, 2013; Wang *et al.*, 2014c). Owing to the close distance of

two array electrodes, the nonplanar diffusion occurs to each electrode and the redox

cycling results in considerably increasing signal response. The width of the electrodes

and the gap between the electrodes are tunable to optimize the geometric design of

microelectrodes for signal improvement. As the width and gap are decreased, the time of

reaching a steady-state is reduced. In this case, the abnormal CV profiles and EIS

spectrums can be discovered, and the principle should be further discussed.
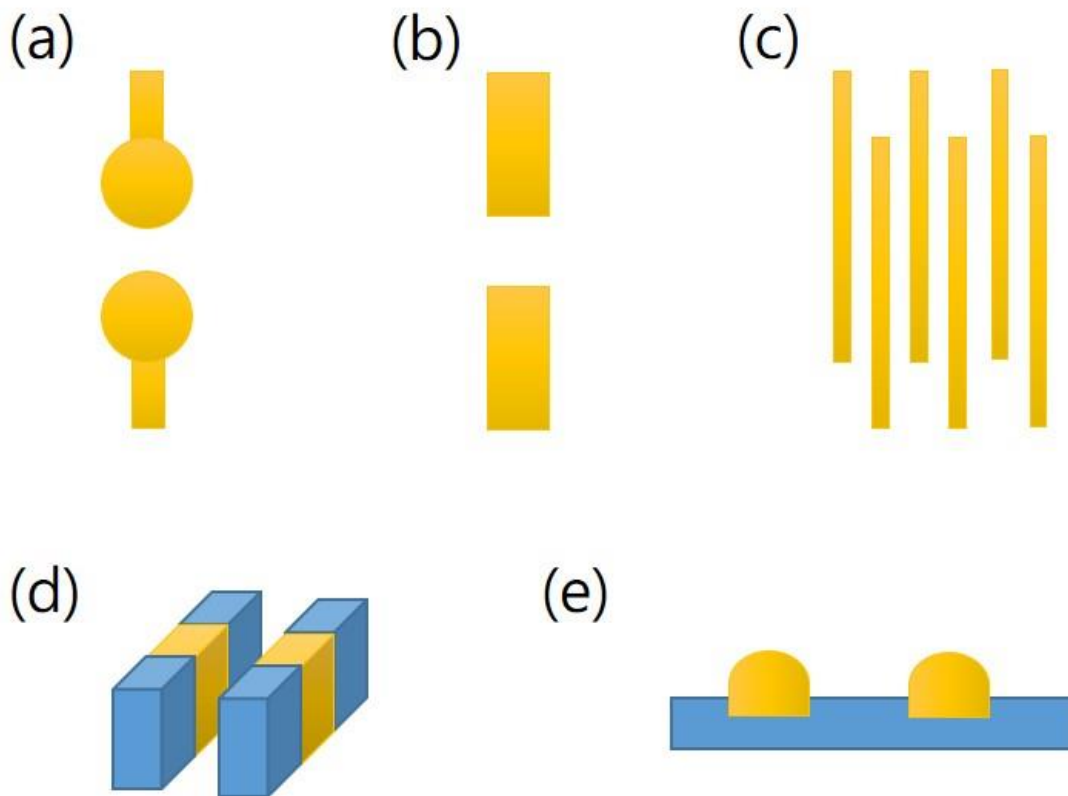
Figure 4.3 Different geometries of the symmetry electrodes. (a) Circular-shaped electrode.

(b) Bar-shaped electrode. (c) Interdigital array-shaped electrode. (d) Vertical electrode. (e)

Bumped electrode.

Table 4.1 Microelectrodes for electrochemical reaction in microfluidic chips

Type	Electrodes	Method	Application	WE dimension	Ref.
Three-electrode	WE/RE/CE : Au (bar)	CP	Copper electrodeposition	W 2.5 mm	(Saito *et al.*, 2015)
	WE/CE : Au (bar /circle) RE : Ag (bar)	SWV	Biomarker Analyses	W 500 μm	(Lee *et al.*, 2017)
	RE/CE/WE : SWCNT (bar)	CV	Hydrogen peroxide detection	W 100 μm	(Ko *et al.*, 2017)
	WE/RE/CE : Au (bar)	CP	cholesterol detection	W 200 μm	(Wisitsoraat *et al.*, 2010)
	WE/CE : Au (bar /circle) RE : Ag/AgCl (bar)	EIS	Soil nitrate detection	W 25 mm	(Ali *et al.*, 2017)
Two-electrode	WE/RE : Au (circle)	EIS	Cry1Ab Detection	ϕ 2.2 mm	(Jin *et al.*, 2017)
	WE/RE : Ni (mushroom)	EIS	KCl detection	W 50 μm	(Paredes *et al.*, 2015)
	WE/RE : Au (interdigital)	EIS	Aptamer-based bioassay	W 20 μm	(Wang *et al.*, 2014c)
	WE/RE : Au (vertical)	CP	Layer-by-Layer Assembly	W 1.0 mm	(Wang *et al.*, 2011)
	WE/RE : Au (bar)	CP	Microdroplet size measurement	W 80 μm	(Elbuken *et al.*, 2011)
	WE/RE : Au (bar)	CV/CP	Ferricyanide detection/PB deposit	W 1.5 mm	This work

4.3   Experimental

● Reagents and materials

The redox mediator solution was prepared by equal-molar mixing, and the final concentration was 5 mM $K_3Fe(CN)_6$, 5 mM $K_4Fe(CN)_6$ and 0.1M KCl in ddH_2O. All reagents were purchased from Sigma-Aldrich. All organic solvents like ethanol, acetone and isopropyl alcohol were obtained from HSIN MING chemical instruments Co., LTD (Taipei, Taiwan). The materials and reagents used for the device construction were obtained from commercial sources as follows: glass slide (FEA, 1"x3", 1-1.2 mm thickness); gold slugs, Cr pieces and boats (Guv Team International, Taiwan); S1813 photoresist (SHIPLEY); plastic photo mask (TK, Taiwan); TMAH (Sigma); PDMS (BingBond, Taiwan); biopunch (MILTEX, Japan).

● Fabrication of the device for microfluidic amperometry

Two symmetric Au microelectrodes were fabricated on a glass slide by a standard lift-off process. Firstly, the glass slides were cleaned with acetone, isopropyl alcohol and ddH_2O sonication, and then they were dried by N_2 and 120 ℃ hotplate. Secondly, the positive photoresist S1813 was coated on the cleaned glass slides by spin coating at 1000 rpm for 20 s and then at 4000 rpm for another 60 s. After the soft baking at 115 ℃ for five minutes, the cured photoresist was exposed to UV light ($15mW/cm^2$) for 10 seconds. Thirdly, the unexposed photoresist was developed in TMAH for 1 min, and then the chip

157

was baked at 130 ℃ for 10 mins. Next, the photoresist-patterned chips were put into a thermal coater which deposited a Cr (30 nm) and an Au (80 nm) layer on the glass slides by heat evaporation. According to the lift-off principle, the electrode patterns appeared after the chips were immersed in acetone for a few minutes. Again, taking the SER-based device as an example, we illustrate the details of the device assembled with an Au microelectrode chip (at the lower position) and a PDMS chip with ramped diffuser microchannel pattern (at the upper position) in Fig. 4.4. The consistent areas of the two electrodes were defined by the microchannel (Fig. 4.4(a)). The microchannel was designed for reducing the fluidic resistance and enhancing the reaction efficiency. A shallow-height chamber was connected to two wide-height channels with a ramped diffuser, which smooths the liquid flow through the height-difference channel (Fig. 4.4(b)). For microchannel fabrication, PDMS (standard mixing ratio is 10:1) was poured into an aluminum mold (fabricated by a CNC machine) and cured at 120 ℃ for 10 mins. Later, the cured PDMS chip (4 mm in thickness) with microfluidic patterns were peeled off, and two tiny holes were punched for the tubing installing. Finally, the upper PDMS chip with micro-channels and the lower Au microelectrodes on a glass slide were bonded by oxygen plasma for a robust sealing through a relatively large contact area between PDMS and glass (Fig. 4.4(c)).

158
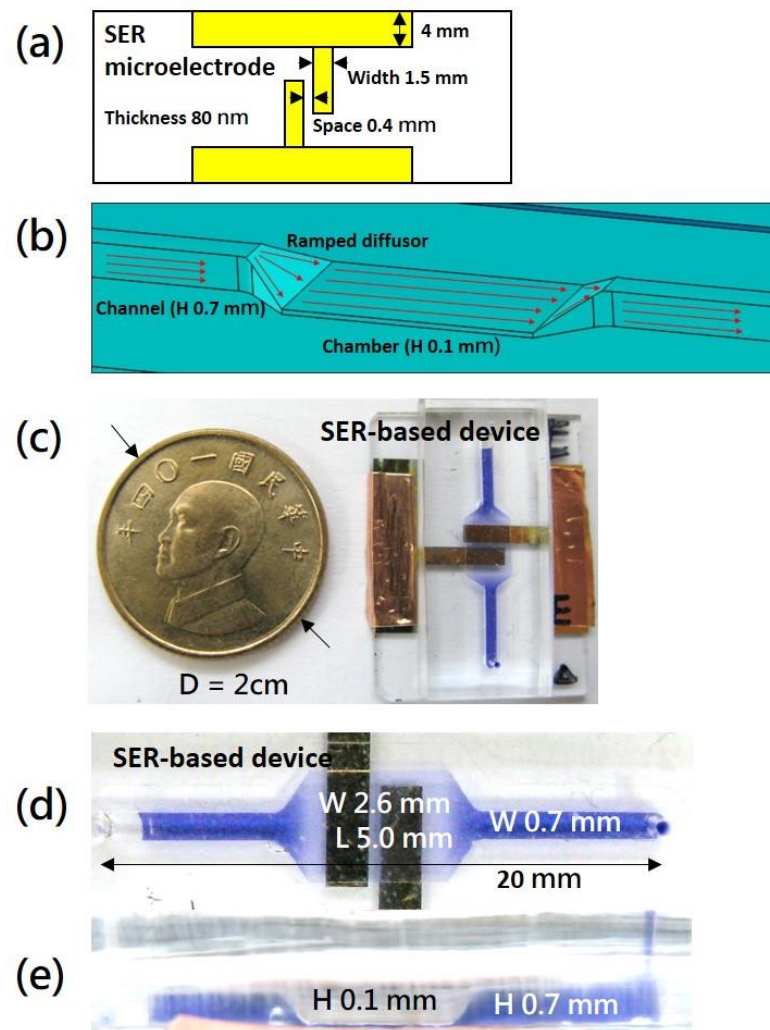
Figure 4.4 Fabrication of a device for microfluidic amperometry with two serial (SER) symmetric Au microelectrodes and a ramped diffuser microfluidic chip. (a) The dimensions of the serial symmetric Au microelectrodes and the pad-connecters for conduction. (b) A ramped diffuser applied into the microchannel design to reduce the fluidic resistance in microfluidics. (c) The PDMS microchannel and the microelectrodes bonded by oxygen plasma treatment. (d) The top view and (e) lateral view of the microfluidic device.

159

- Electrochemical characterization

After the device's microchannel was rinsed by ddH$_2$O, 10 µl redox mediator solution ($K_3Fe(CN)_6$/$K_4Fe(CN)_6$/KCl) was injected into the chamber to carry out the electrochemical characterization of the devices with different electrode pattern designs (i.e., the IDA, PAR, and SER –based devices) and different flow modes (i.e., the one-way and shuttle flows). For symmetric two-electrode measurement, one of the gold electrodes was used as the CE/RE, and the other gold electrode was used as the WE. The measurements were performed by a potentiostat/galvanostat (CH Instruments). In CV measurements, the scan window was set from -0.8 V to +0.8 V so that the redox mediators could be completely oxidized and reduced at either electrode. The scan rates of CV analysis were varied to investigate the diffusion and flow effects. In electrochemical impedance spectroscopy (EIS) measurements, an initial voltage (equal to open circuit potential) and a small AC oscillatory voltage (5 mV) with different frequencies (10^{-1}~10^5 Hz) were applied to measure the impedance spectroscopy. The obtained Bode plots were fitted by the software (EC-Lab), and the relative parameters were identified by the fitting models. In CA measurements, a potential step (+0.8 V) was applied to oxidize the mediators at the working electrode (while reduced at the counter electrode) for 300 seconds.

● Liquid transportation and flow mode control

The liquid transportation in the microfluidic device was driven by a syringe pump

(Kd Scientific) with both infuse and withdraw capabilities. A 100 μl syringe (HAMILTON)

was used in this research, and the maximum flow rate was about 250 μl/min. A PTFE

tubing was used to connect the syringe and the device. In one-way flow experiments, the

ferri/ferro-cyanide mixture was continuously infused into the channel until the analysis

was completed. In shuttle flow experiments, a drop (20 μl) of the redox mixture was

injected into the device at first, and then the drop was transported back and forth on the

electrode area via a shuttle flow, which was achieved by switching the infuse and

withdraw modes of the pump periodically. The microfluidic manipulations of one-way

and shuttle flow modes are detailed in Fig. 4.5.

● Amperometry sensitivity for the redox mediator detection

The redox mediator stock solution (5mM $K_3Fe(CN)_6$, 5mM $K_4Fe(CN)_6$ and 0.1M

KCl) was serially diluted into four dilutions (4 mM, 3 mM, 2 mM and 1 mM) with ddH_2O.

The steady currents and oxidation peak currents in response to different concentrations of

the redox mediator were recorded from CA and CV analysis, respectively. The calibration

curves of the above amperometric measurements were obtained by plotting the current

signal versus the mediator concentration. The sensitivity values of ferricyanide detection

under different flow conditions were then determined by linear regression.
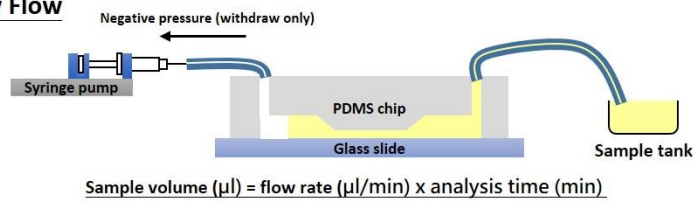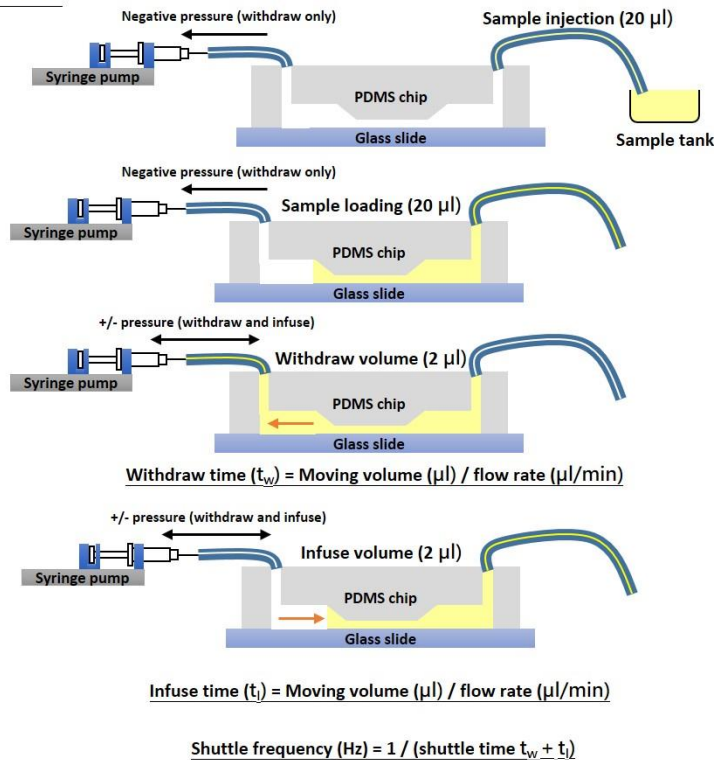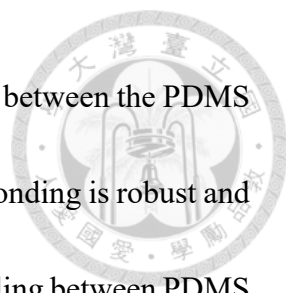
Figure 4.5 The schematics of the detailed operation for one-way and shuttle flows. (a) In one-way flow experiments, a syringe pump was used to provide a negative pressure, which withdrew the sample into the microchannel. The volume of the consumed sample was proportional to the flow rate. (b) In shuttle flow experiments, the same syringe pump supplied either a negative pressure or a positive pressure. Firstly, a sample drop (20 μl) was loaded into the device, and then the drop was driven back and forth through the electrodes with a specified moving volume (e.g., 2 μl). The shuttle frequency (f) was determined by the moving volume (V) and the flow speed (v). (f = v/2V)

4.4   Results and Discussion

4.4.1   Characterization of microfluidic device assembly

To visualize the flow in microfluidic channels, we injected a purple dye solution into a SER-based device and took pictures as shown in Fig. 4.4(d) and Fig. 4.4(e). As we can see in Fig. 4.4(d), when the dye solution flows from the main channel (H = 700 μm) through the ramped diffuser and then into the shallow reaction chamber (H = 100 μm), the colour becomes lighter from a top-view angle. In contrast, from the side-view angle (Fig. 4.4(e)), we observe that the solution colour has no significant changes throughout the distinct channel regions. Considering these observations along with the Beer law, we know that the colour gradient in Fig. 4.4(d) reflects the change in the channel height (as well as the optical path length), not dilution of dye concentration. Thus, the uniform colour appeared in the chamber zone from both top and side views indicates that the chamber with 100 μm in height does not collapse or deform during operations, although PDMS is a relatively soft material. We presume the reason is that the main body of the PDMS chip has a thickness of 4 mm, which can provide a sufficient mechanical strength to sustain the microfluidic structures when bonding with the lower electrode chip. To avoid possible influences of PDMS deformation on the microfluidic amperometry study, we also construct microfluidic devices based on PMMA, which is a more rigid than PDMS, to confirm important experiments.

163

The microfluidic device is assembled by typical plasma bonding between the PDMS chip and the glass slide with microfabricated Au electrodes. Plasma bonding is robust and irreversible; however, this method is ineffective and yields a weak sealing between PDMS and gold surfaces. This raises the concerns of solution leakage and trapping issues in the contact region between the PDMS and Au microelectrodes in our device. To check if a solution leakage occurs from the PDMS-Au interface, we operate a fluorescein solution (10 μg/ml) in the device in the shuttle mode for 1 hour. Then we take both phase-contrast and fluorescent microscope images of the used device as shown in Fig. 4.6 along with device structure illustrations. As can be seen in Fig. 4.6(e), there is no fluorescein solution trapped in the PDMS-Au interface, and all fluorescein sample is remained in the chamber zone after 1-hour shuttle operation. This suggests that the bonding between the PDMS chip and the electrode chip in our device is robust and does not suffer from solution leakages. The reason can be explained by Fig. 4.4(c). From which, it is seen that there is a large surface area in contact between the PDMS chip and the glass slide for plasma bonding, and the PDMS-Au interface only takes a small portion of the surface area. To further check if there is a solution-trapping problem that affects the measurement, a cycling sensing experiment is performed using the microfluidic device by alternate amperometric detection of 1 mM and 5 mM redox mediator samples. If cross-contamination occurs due to the trapped liquid, the current response of 1 mM sample

164

should increase with the sensing cycle. From the experiment, we find that the current

response of 1 mM nearly remains the same (despite with small variation) in all sensing

cycles, as shown in Fig. 4.7. Thus, it is evidenced that there is no solution-trapping effect

on the measurement, either. From above discussions, the robustness of the PDMS-based

microfluidic device assembly is assured.
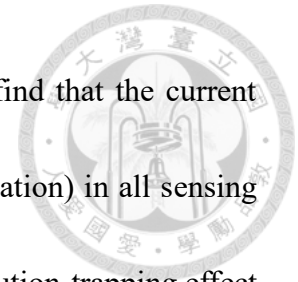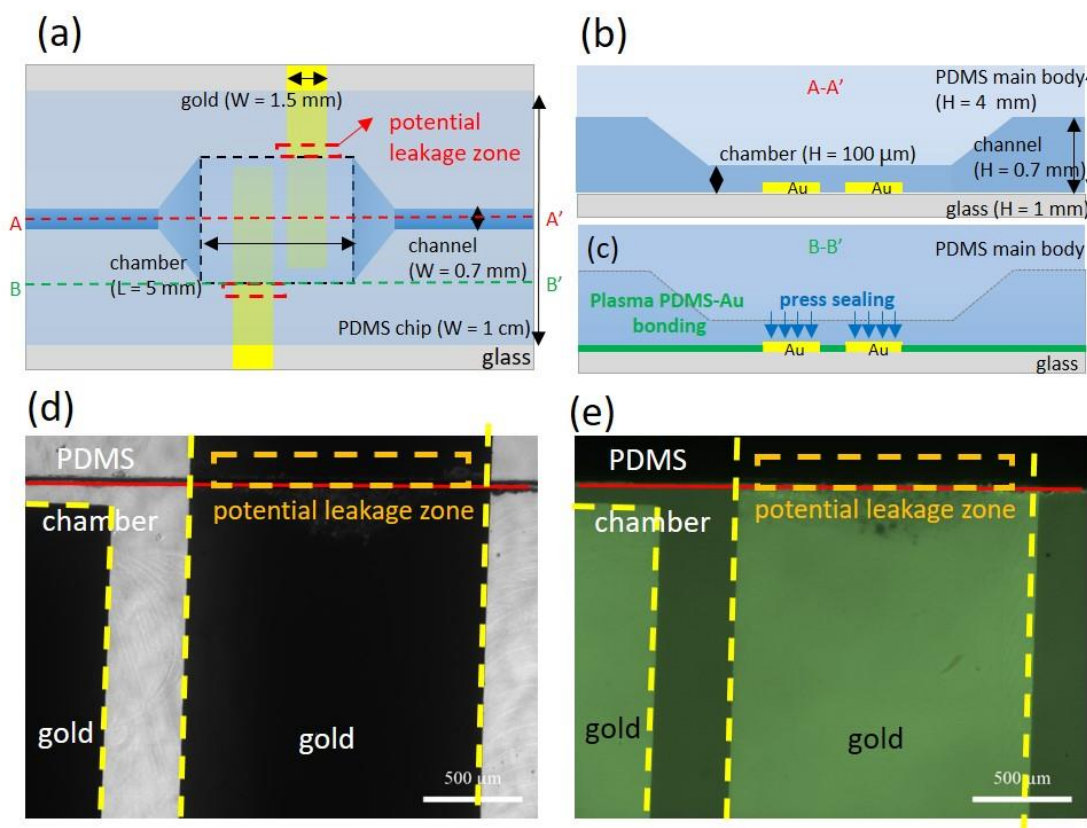
Figure 4.6 The schematics of the device assembly from different view angles: (a) Top-view scheme, which shows there is a large contact area between PDMS and glass for effective plasma bonding. (b) Side-view scheme, which highlights the microfluidic chamber region of the PDMS chip atop the electrode chip, and it is noted that the thickness of the PDMS main body is 4 mm providing a strong structure support for bonding. (c) The illustration of plasma-assisted bonding between the PDMS chip and electrode chip on a glass slide. The microscope images of the microfluidic device after 1-hr shuttling operation of a fluorescein solution (10 μg/ml): (d) phase-contrast mode and (e) fluorescent mode (ex. 480 nm/em. 520 nm).

166
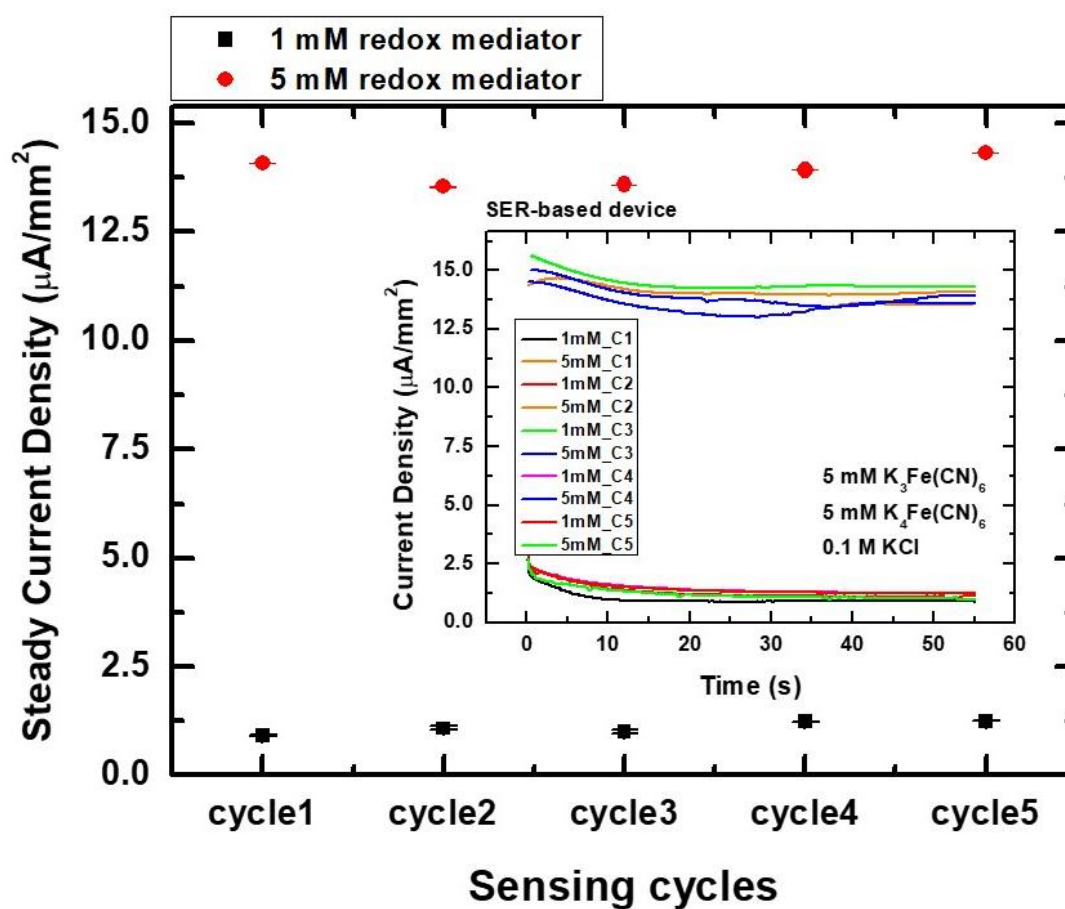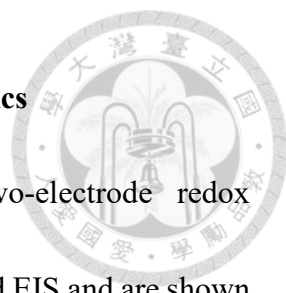
Figure 4.7 Cycling sensing test with alternate amperometric detection of 5 mM and 1 mM

mixed ferri/ferro-cyanide sample in the microfluidic device. The steady current values

are determined by taking the average of the last five-second current response.

167

4.4.2 Two-electrode redox electrochemistry in static microfluidics

The influences of the microelectrode pattern on the two-electrode redox electrochemistry in static microfluidics are characterized with CV and EIS and are shown in Fig. 4.8. The data compare the IDA, PAR, and SER microelectrodes, as illustrated in Fig. 4.1(b). All two-electrode CV curves in Fig. 4.8(a)-(c) present a highly symmetric pair of redox waves with the peak voltages symmetric to 0 V. This is an evidence of a highly reversible ferri/ferro-cyanide redox reaction attained on the symmetric two-microelectrode chips. To study the effect of using Au as a pseudo-RE and the difference between two-electrode and three-electrode setups, we also perform CV experiments of ferri/ferro-cyanide with bulk gold disk electrodes (GDEs) under the following conditions: (a) WE = Au, CE/RE = Au; (b) WE = Au, CE = Au, and RE = Ag/AgCl; (c) WE = Au, CE = Au, and RE = Au. The results are compared in Fig. 4.9. When compared to the CV measured with two symmetric Au electrodes (case (a)), the three-electrode setup with an Ag/AgCl RE (case (b)) results in a CV with a higher current and a positive shift of +0.22 V for E_o (estimated by $(E_{pa}+E_{pc})/2$). In case (c), we observe an increased current signal along with an oxygen evolution peak at 0.8 V, and the formal potential is the same as that of case (a), implying that an Au pseudo-RE can provide a stable reference potential in this system. From Fig. 4.9, it is shown that the two-electrode setup gives the highest CV symmetry, although the current is reduced due to the shared CE/RE configuration. This

168

finding supports the perfect symmetry in two-electrode CVs for the microelectrodes in

Fig. 4.8(a)-(c), and such CV symmetry provides an important basis for the study of flow

polarization and flow rate-tuned characteristics in microfluidic amperometry.
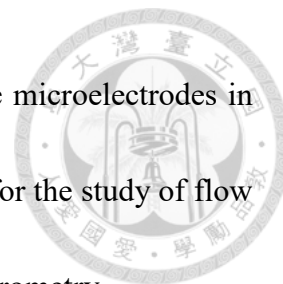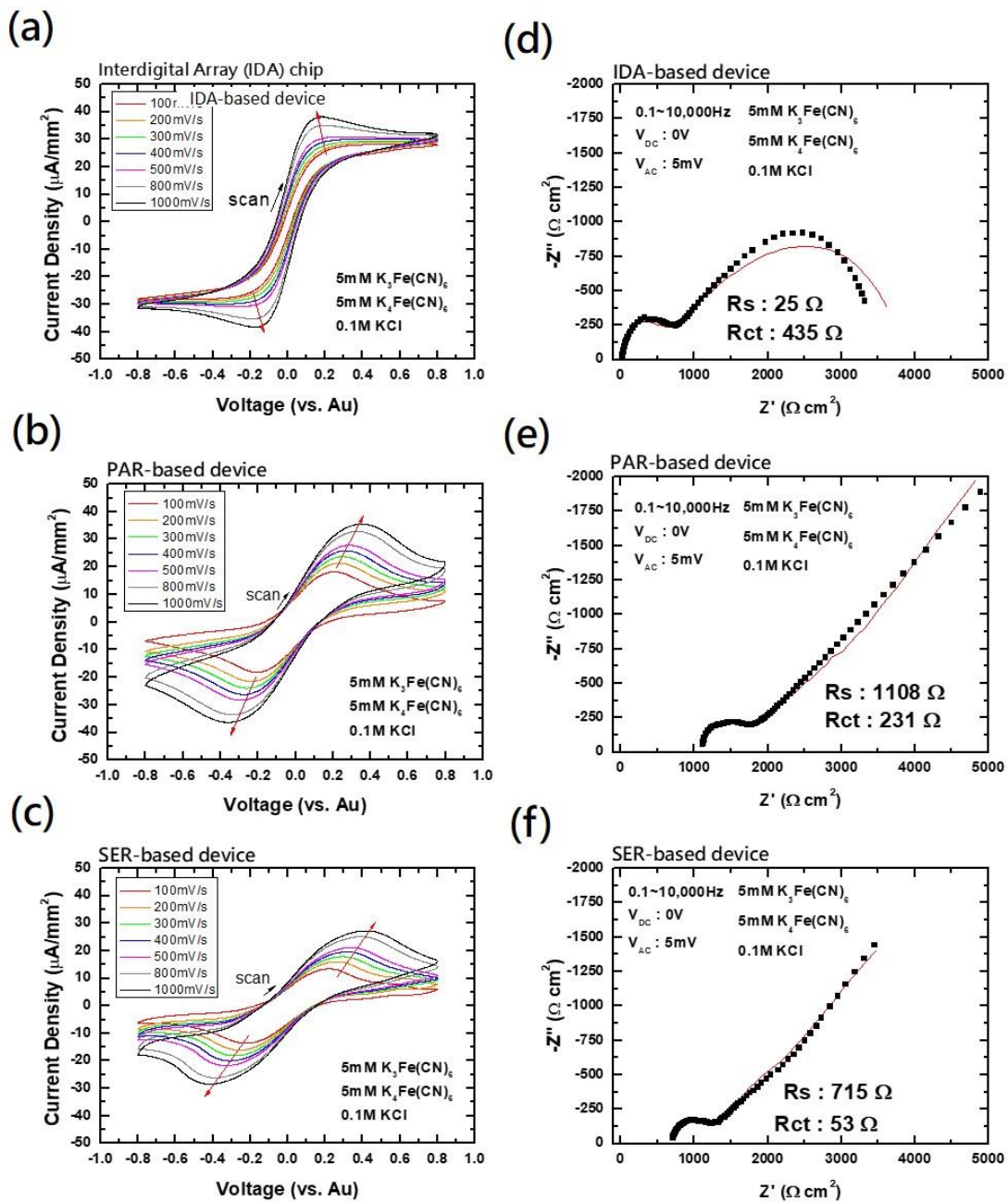
Figure 4.8 The electrochemical characteristics of two-electrode ferri/ferro-cyanide redox

reaction on the interdigital array (IDA), parallel symmetry (PAR) and serial symmetry

(SER) microelectrodes. (a)-(c) Cyclic voltammograms at different scan rates; (d)-(f) EIS

spectra with the trend lines. The patterns and detail dimensions of IDA, PAR and SER

microelectrodes are illustrated in Fig. 4.1.

170
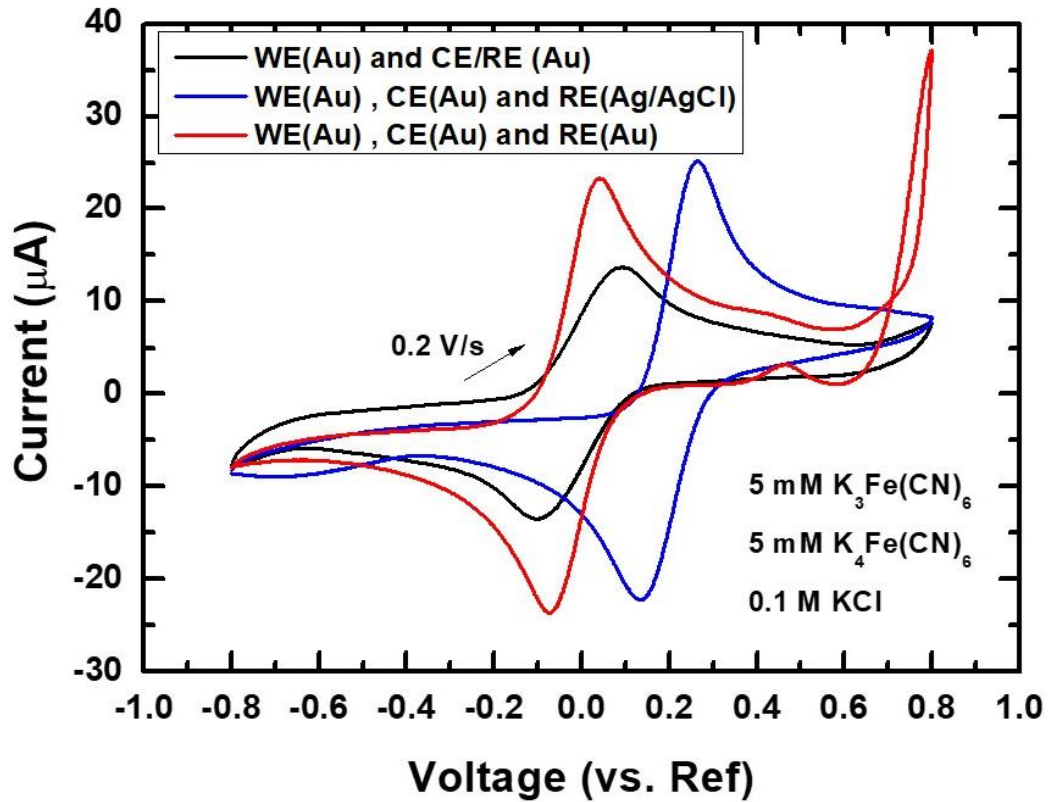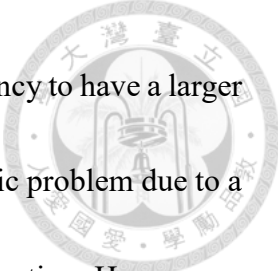
Figure 4.9 CV diagrams measured in a solution of 5 mM ferri/ferro-cyanide and 0.1 M

KCl under the following electrode configurations: (a) WE = Au, CE/RE = Au (two-

electrode setup); (b) WE = Au, CE = Au, and RE = Ag/AgCl (three-electrode setup); (c)

WE = Au, CE = Au, and RE = Au (three-electrode setup). Note: Au = bulk gold disk

electrode (GDE).

171

It is also found in Fig. 4.9 that a two-electrode system has a tendency to have a larger $\triangle$ Ep in CV than a three-electrode system does. This can be an intrinsic problem due to a weak instrumental IR compensation under the shared CE/RE configuration. However, a two-electrode chip in microfluidics indeed can lead to an even larger $\triangle$ Ep in CV (Fig. 4.8(b) and Fig. 4.8(c)) as compared to the bulk gold electrode system. When compared with the CV diagrams measured from two identical bulk GDEs (Fig. 4.10), it is found that the CV peak separation of the two-electrode GDE system is obviously smaller and less affected by the scan rate than that of either a microfluidic PAR-based (Fig. 4.8(b)) or SER-based (Fig. 4.8(c)) device. In addition, either microfluidic two-electrode device shows flatter CV diagrams and larger peak separations than the bulk gold electrode system. Moreover, the peak separation is even larger at a higher scan rate. We presume that this phenomenon is attributed to a "depletion effect" in the microfluidic device. In other words, it takes more time in a static microfluidic system than in a bulk system to supply redox mediators for sustaining the electrochemical reaction. As the scan rate increases, the redox mediators are consumed at the microfluidic electrodes at a higher rate and generates a larger depletion zone for diffusion-based compensation. As a consequence, the higher the scan rate is; the larger reaction resistance and peak separation will be in the static microfluidic system. This presumption is supported by Fig. 4.11. Comparing the insets in Fig. 4.11(a) and Fig. 4.11(b), we find that the peak separation is

172

significantly reduced for the SER-based device after applying a one-way flow. It is because that the flow enhances the mass transfer as well as the rate of supply of fresh redox mediators in the microfluidic device.
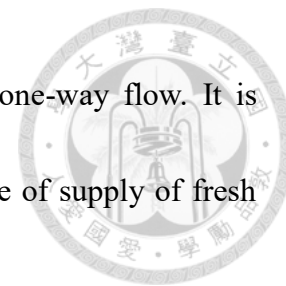
In addition, obtaining the distinct shapes between the CV curve of the IDA microelectrode and that of the PAR and SER microelectrodes, we proves that the microelectrode pattern indeed plays a determinant role in the redox electrochemistry. It can be seen that the IDA microelectrode shows a quasi-steady state I-V polarization curve, which is characterized to be the feature of an ultramicroelectrode (UME) effect, instead of a typical two-wave CV response. By contrast, both the PAR and SER microelectrodes have similar CV characteristics of a semi-infinite planar electrode showing increasing peak current and peak separation with the scan rate. The difference in the CV response between IDA and PAR/SER can be further explained by the dimensions of the microelectrode and the gap distance between the electrodes. For the IDA microelectrode, the electrode's characteristic dimension fits the definition of a UME (25 μm), and the electrode gap is as small as 25 μm, which is close enough to promote the redox cycling phenomena depicted in Fig. 4.1. As a result, the redox reaction is less affected by diffusion control. Moreover, we perform the CV experiments for IDA with a wider scan-rate range (from 10 mV/s to 3 V/s), shown in Fig. 4.12. We find that a low scan rate (e.g., 10 mV/s) shows no significant change in the sigmoidal curve feature, while a high scan rate (e.g.,

173

3 V/s) makes IDA exhibit typical CV waves, implying that the diffusion effect is predominant only at a high scan rate. This is why we consider that the steady state current response (i.e., the sigmoidal I-E curve) of IDA is resulted from the redox cycling effect. The sigmoidal curve in an IDA electrode system was reported in other literature. Mikkelsen's group published a paper on Analytical Chemistry in 2011 (Rahimi and Mikkelsen, 2011). They discussed the biamperometry in a microinterdigitated electrodes system. In that work, a sigmoidal CV curve was found and was also explained as a result of the redox cycling effect. In addition, Baeumner's group presented a DNA sensor based on an IDUA system in 2006 (Kwakye *et al.*, 2006). They mentioned that the steady-state current responses of IDA were resulted from the significant radial diffusion to the edge of fingers, and it delivered the redox species to the microelectrodes at a rapid speed which was equal to the electrolysis rate. This argument might explain more details of the redox cycling of IDA.
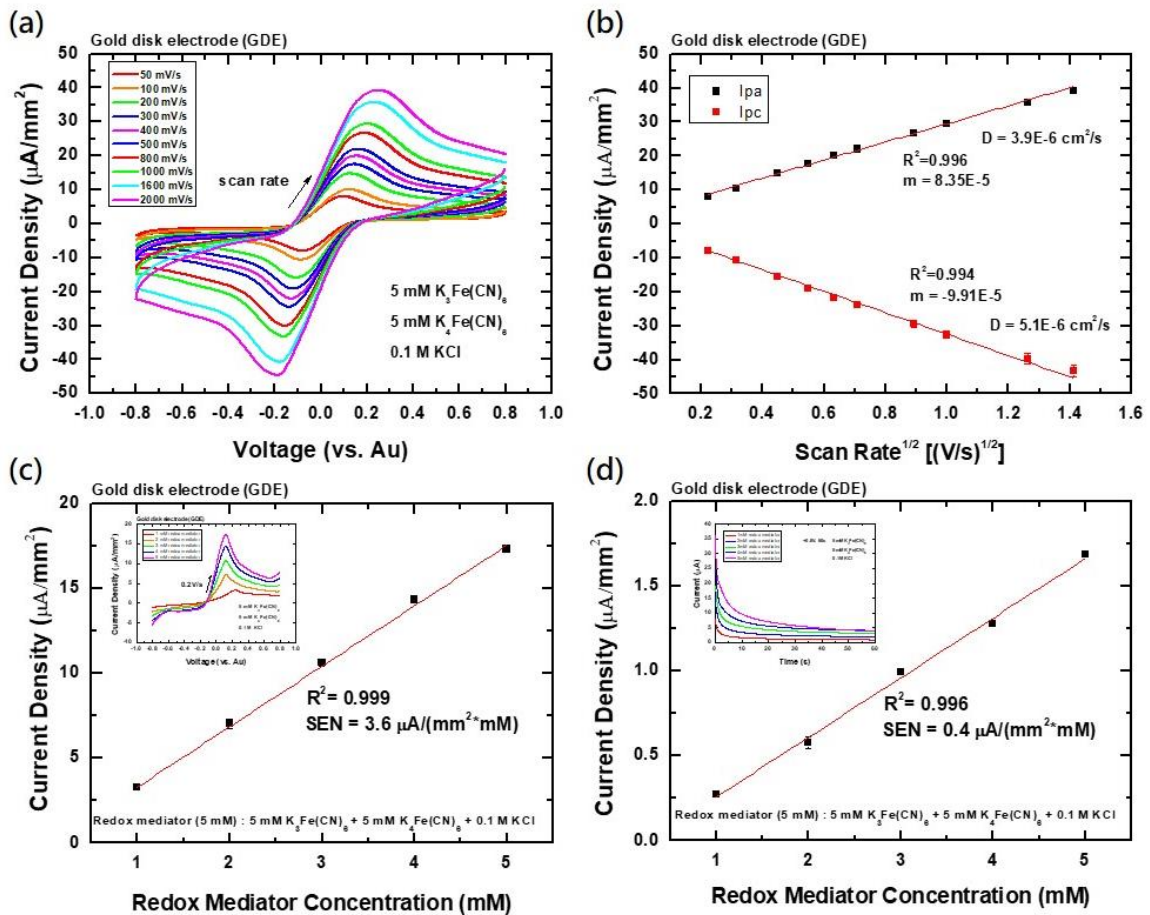
Figure 4.10 Ferricyanide redox reaction characterized by two identical gold disk electrodes (GDEs). (a) CV responses at different scan rates. (b) CV peak currents as a function of the square root of the scan rate for diffusion coefficient determination. (c) LSV detection of ferricyanide concentration. (d) CA detection of ferricyanide concentration.

175
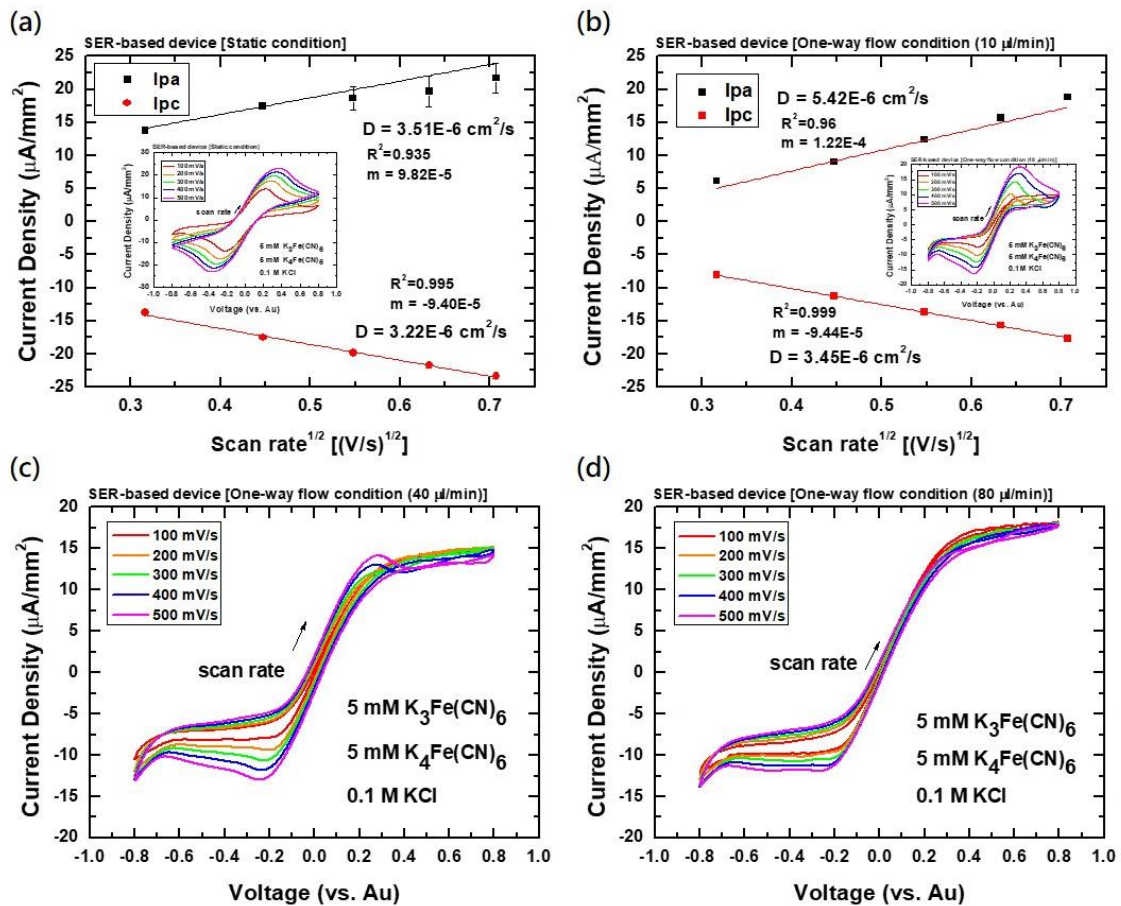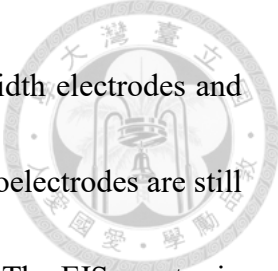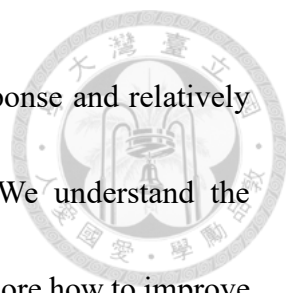
Figure 4.11 Cyclic voltammetry at different scan rates for the ferricyanide redox reaction

on the SER-based device under (a) static condition, (b) one-way flow at 10 μl/min, (c)

one-way flow at 40 μl/min, and (d) one-way flow at 80 μl/min.

176

In comparison, the PAR and SER microelectrodes use 2 mm-width electrodes and have an electrode gap of 0.4 mm, so the redox reactions on both microelectrodes are still strongly governed by the diffusion limit under a quiescent condition. The EIS spectra in Fig. 4.8(d)-(f) support the above discussions. It is found that a relatively small uncompensated solution resistance (R_s = 25 Ω) is obtained on the IDA microelectrode due to the adjacent electrode distance as compared to that of PAR (R_s = 1108Ω) and that of SER (R_s = 715Ω), which are the results of wider electrode gaps. This large resistance can also be explained by the same reason as the microfluidic depletion effect for slowing down the supply speed for consumed redox mediators and resulting an increased reaction resistance in two-electrode CV measurement. In addition, the higher charge transfer resistance (R_{ct}) and the presence of the secondary, large hemi-circle in the lower frequency domain shown in Fig. 4.8(d) imply that the ferricyanide redox reaction is under kinetic control rather than diffusion control on the IDA microelectrode. In contrast, the PAR and SER microelectrodes (Fig. 4.8(e) and Fig. 4.8(f)) have an EIS spectrum with the Warburg-like diffusion behaviour in the lower frequency domain. Therefore, the data in Fig. 4.8 suggest that microfluidic amperometry is significantly subject to the microelectrode pattern, and the electrochemical characteristics of a redox couple can be tuned by the electrode size and electrode gap. Nonetheless, since the main objective of this work is to study how a flow mode affects the microfluidic amperometry, we choose

177

the SER microelectrode, which has a typical diffusion-type CV response and relatively small R_s and R_{ct}, for carrying out the subsequent experiments. We understand the advantages and benefits of IDA electrodes. However, we hope to explore how to improve the SER electrodes to match or exceed the performance of IDA electrodes, since the symmetric SER electrodes are often used in biosensor applications. In addition, we want to discuss the flow polarization effect and flowing mixing effect in the microfluidic amperometry. The IDA electrodes already have a sigmoidal CV curve under the static condition and have an interdigitated electrode arrangement, so we can neither find a flow rate-tuned CV characteristics nor observe the flow polarization effect, which are thought be interesting features for two-electrode microfluidic amperometry. Regarding the PAR-based device, it has no sequential arrangement of the symmetric Au electrode, either. Thus, the flow polarization effect is supposed not existed for PAR, although the flow rate-tuned CV characteristic is presumed valid for PAR, too. According to these considerations, we choose the SER electrodes for penetrative analysis.
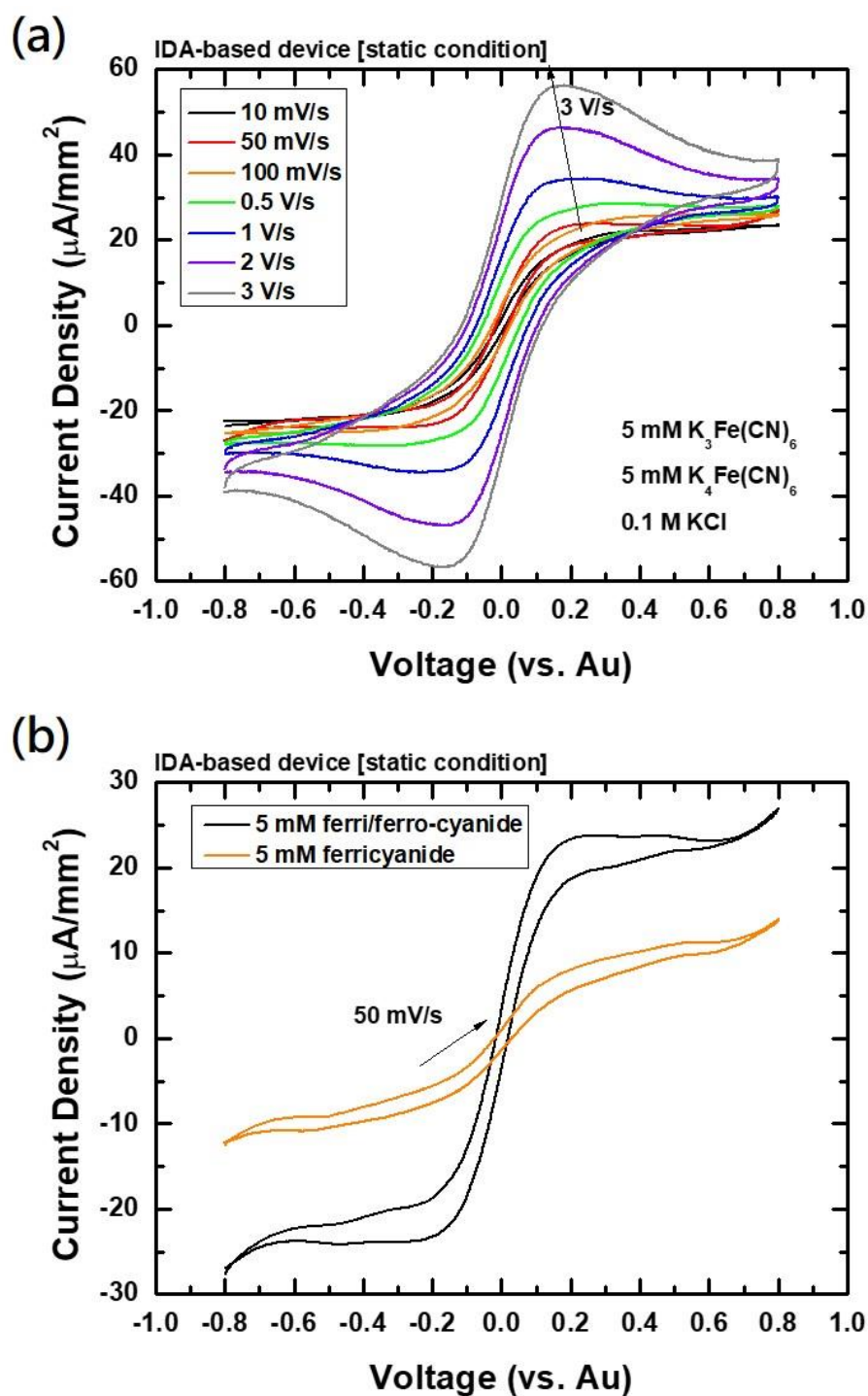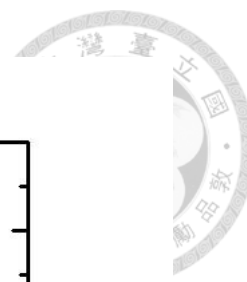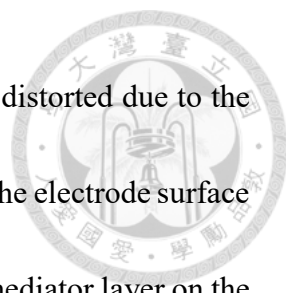
Figure 4.12 (a) The CV diagrams of ferri/ferro-cyanide measured with a static IDA-based

device at different scan rates ranging from 10 mV/s to 3 V/s. (b) The CV diagrams of

mixed and single mediators measured by the IDA-based device.

4.4.3 Tuneable microfluidic amperometry under one-way and shuttle flow

From the thought experiment in Fig. 4.2, we have deduced that the electrochemical behaviours of the ferricyanide redox reaction are supposed to be very different under one-way flow and shuttle flow conditions. The thought experiment is first proven with the CV data from the SER-based device in Fig. 4.13. From Fig. 4.13(a), it can be seen that the CV profile of a SER-based device can be tuned from a diffusion-type CV curve to a steady-state sigmoidal I-V polarization curve under the one-way flow condition. The data shows that the CV current declines initially and then increases with the flow rate. This can be attributed to the formation of a pre-adsorbed redox mediator layer on the quiescent electrodes that causes a higher CV current under the static condition but is then removed after applying one-way flow. Kizek's group published a paper in Biosensor (2006) (Prasek *et al.*, 2006) discussing the hydrodynamic electrochemical arrangement. In their article, the CV diagrams in different arrangements of electrochemical analysis were compared. The phenomenon of current decreasing under flowing conditions was also observed, but they didn't provide further explanation. Here, we can provide some proof-of-principle data to support the pre-adsorbed effect. In Fig. 4.14(a), it can be seen that the CV peak current of a SER-based device increases with the scan cycle when the liquid sample is static. This implies adsorption of ferri/ferro-cyanide on the Au electrode surface of a SER microelectrode. In contrast, the CV curve has no dependence on the scan cycle

180

under one-way flow mode in Fig. 4.14(b), although the CV shape is distorted due to the

flow polarization effect. This implies that the mediator adsorption on the electrode surface

is washed away under a flow condition. Thus, a pre-adsorbed redox mediator layer on the

Au electrode under a static condition is considered to be existed. Hence, a reduced CV

current is obtained with one-way flow initially. With increasing the flow rate, a facilitated

mass transfer effect similar to stirring is taking place for the CV response. Not only the

steady I-V curve but also the increased current response is obtained at a higher flow rate

that supplies a facilitated mass transfer. Also, it can be noted that there is asymmetry

between the anodic and cathodic waves at higher flow rates in Fig. 4.13(a), which is the

proof of the flow polarization effect as depicted in Fig. 4.2(b).
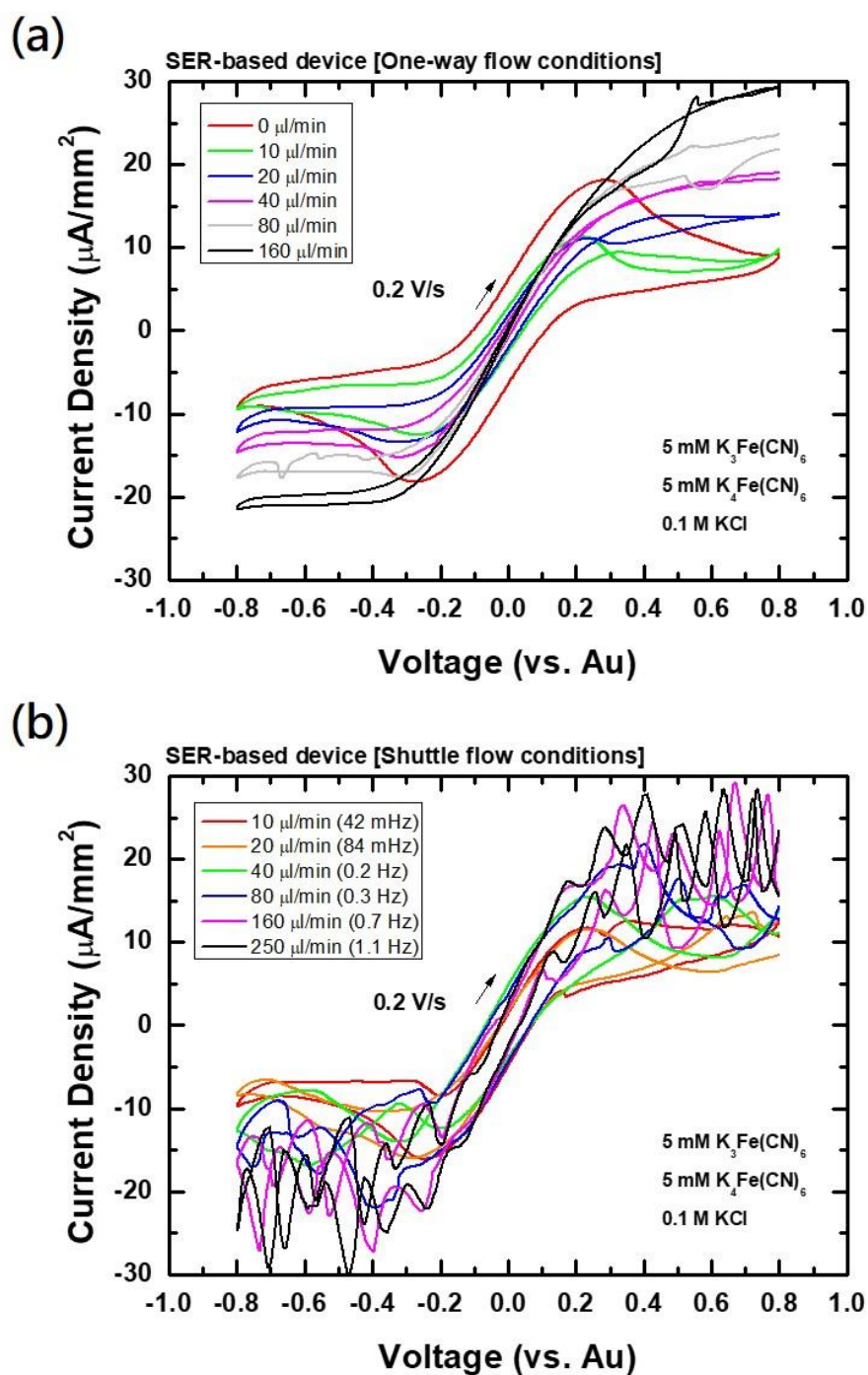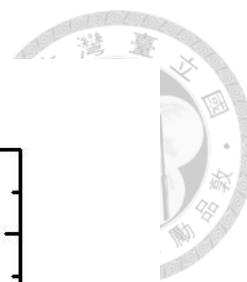
Figure 4.13 Two-electrode cyclic voltammograms for ferri/ferro-cyanide redox reaction

on the SER-based device under different microfluidic flow conditions. (a) One-way flow

mode with different flow rates. (b) Shuttle flow mode with different shuttle rates. The

moving volume is 2 μl in both directions.
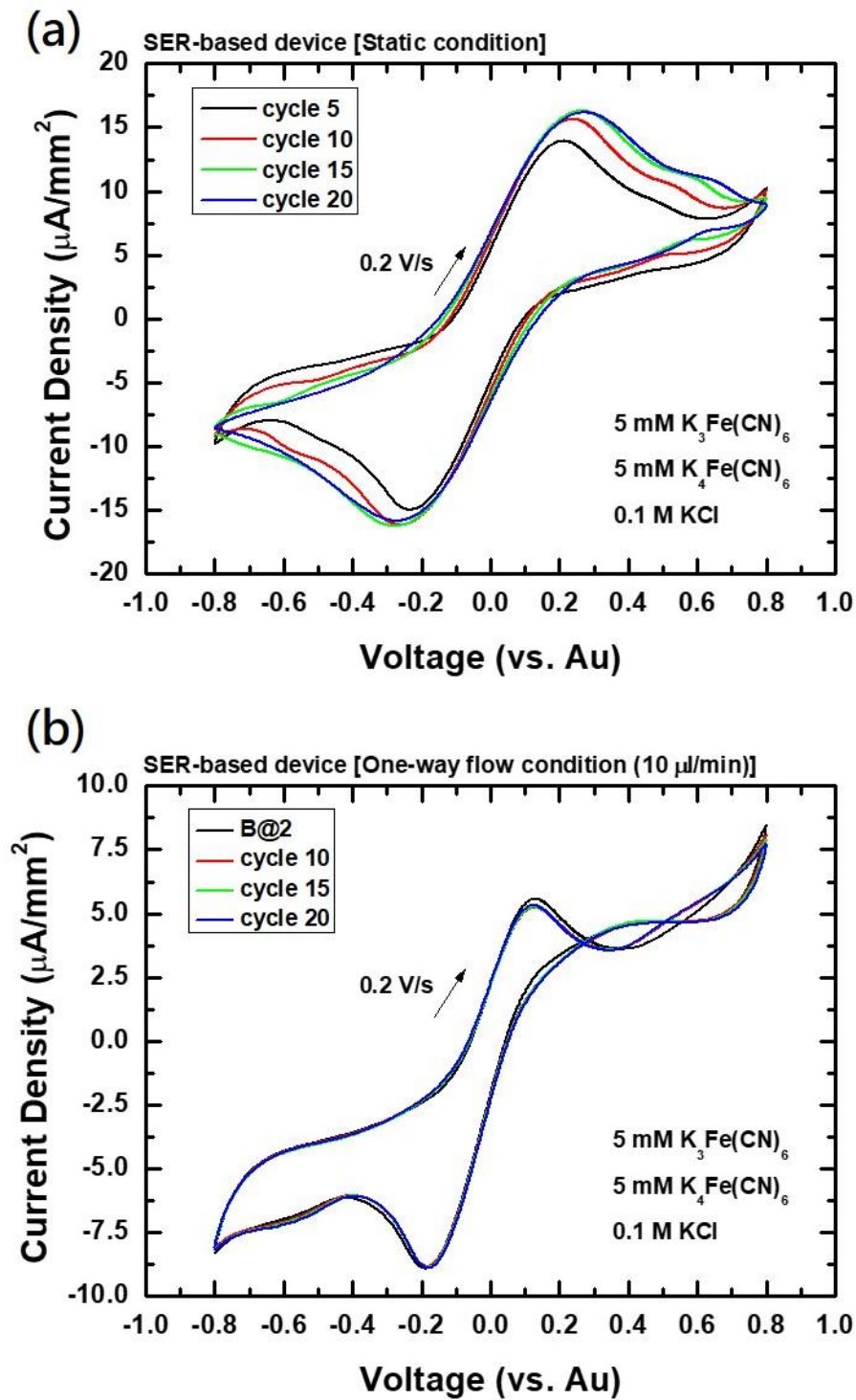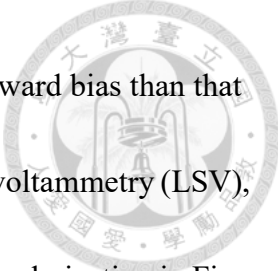
Figure 4.14 The CV diagrams of ferri/ferro-cyanide of different scan cycles under (a)

static and (b) one-way flow conditions.

The flow polarization effect here gives a larger current at the forward bias than that at the reverse bias. The same effects are also observed in linear sweep voltammetry (LSV), as shown in Fig. 4.15. According to the schematic illustration of flow polarization in Fig. 4.2(b), the reduced mediator (ferrocyanide, Fe^{2+}), generated on the upstream cathode, is brought by the flow and increase the local concentration of ferrocyanide (Fe^{2+}) on the downstream anode. In addition, the resulted ferricyanide (Fe^{3+}) on the anode is removed by the flow quickly. As a consequence, when the anode (WE) is placed on the downstream of the one-way flow and the cathode (CE/RE) is placed on the upstream, the anodic current response is to be higher than the cathodic one. We call this "flow polarization" effect. When the flow direction is reversed, the cathode becomes the downstream electrode and gives a higher cathodic current in response to the opposite flow polarization. In Fig. 4.16, the one-way flow CV data with opposite flow directions are compared, and the flow polarization effects are clearly seen: (1) cathodic polarization with larger cathodic currents due to a downstream cathode (Fig. 4.16(a)) and (2) anodic polarization with larger anodic currents due to a downstream anode (Fig. 4.16(b)). Regarding the current plateau issue, the anodic current is possible to reach a constant plateau at a slow flow rate in practice. Taking Fig. 4.2(b) as an example, the anodic flow polarization is also influenced by the competition between diffusion control and kinetics control. Because if the rate of convective mass transport of Fe^{2+} from the upstream is slower than

the reaction kinetics on the downstream anode, a plateau limiting current (independent of electrode potential) is obtained due to diffusion control. However, when the flow rate increases, the convective transportation of Fe^{2+} from upstream becomes faster. Local concentration (accumulation) of F^{e2+} on the downstream anode breaks the diffusion-limiting situation and plateau condition. In such a case, the anodic current is kinetic-controlled and keeps increasing with a potential bias. According to the above discussions, we can know that the one-way flow mode is a useful strategy to tune the two-electrode CV behaviour for a redox mediator and to increase the CV sensitivity.

185
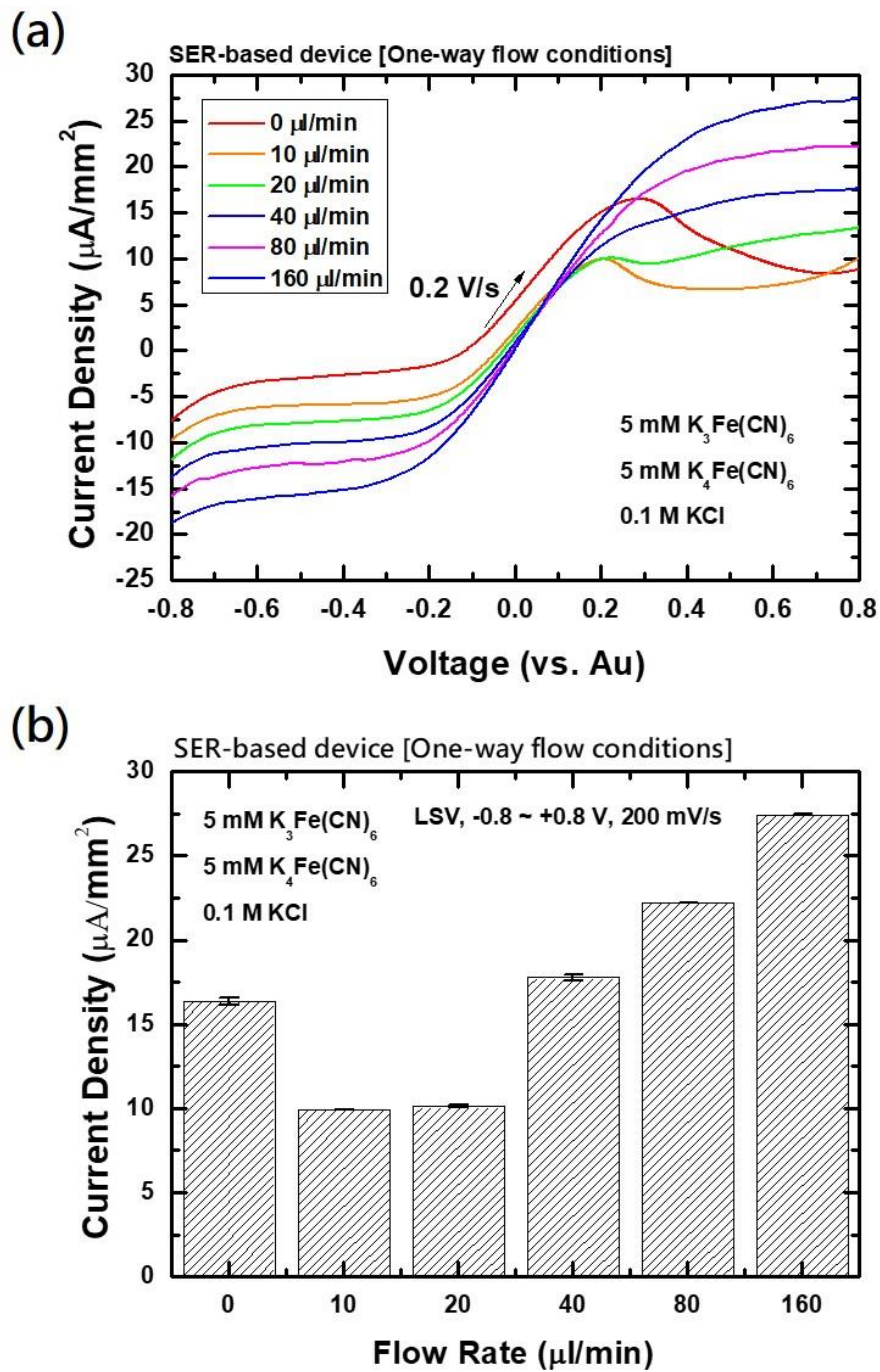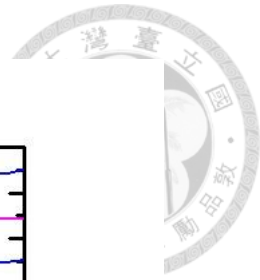
Figure 4.15 The influence of the one-way flow rate on the current response in the linear

sweep voltammetry (LSV) analysis. (a) The LSV curves obtained from various flow rates.

(b) The maximal current response increases linearly with the flow rate when the rate is

higher than 20 μl/min.

186
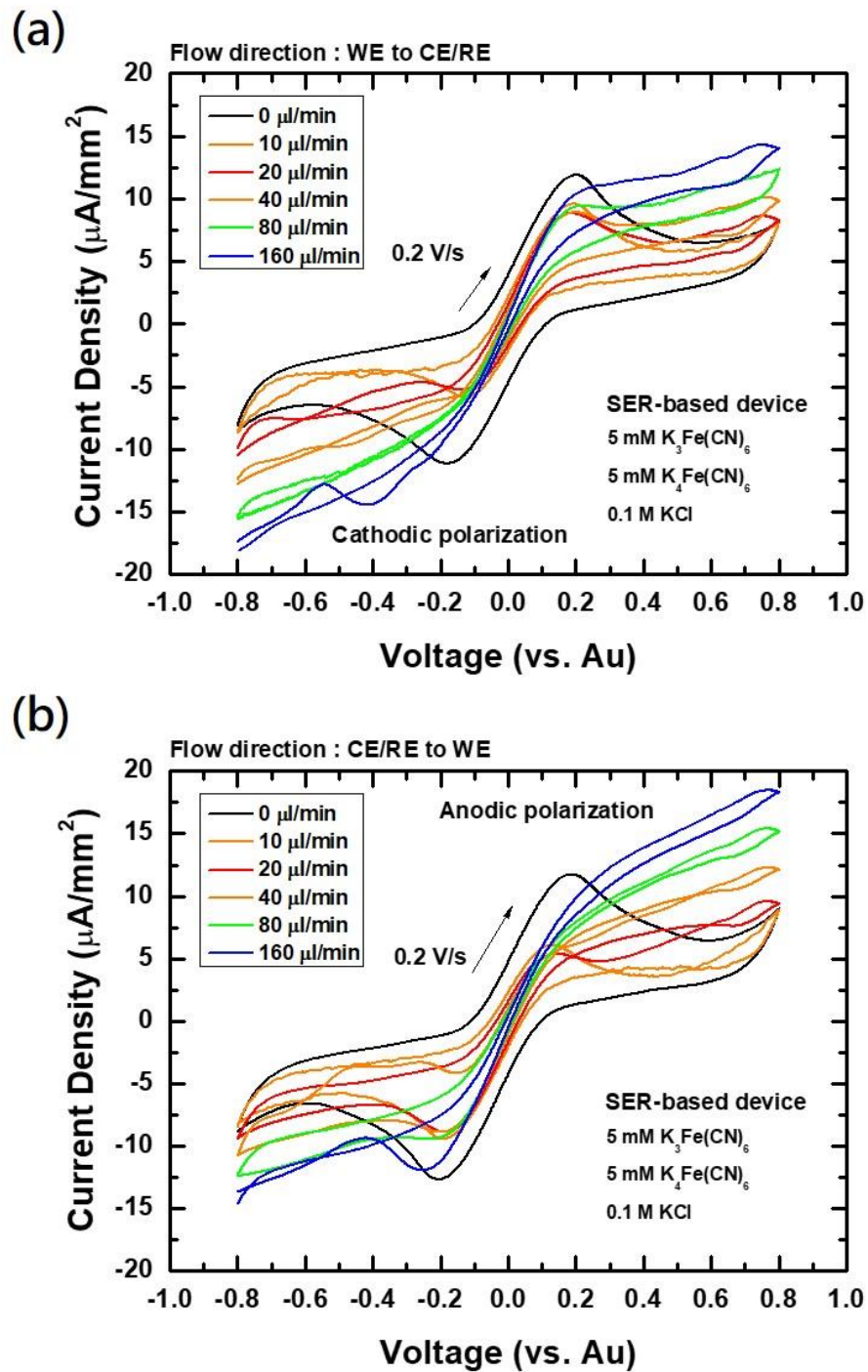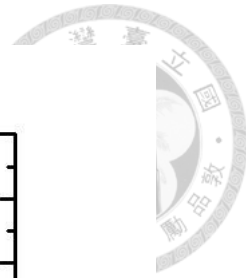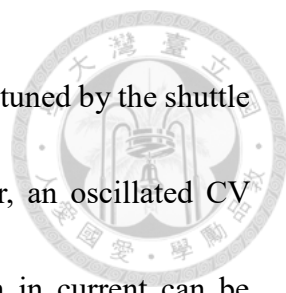
Figure 4.16 The flow polarization effects identified by comparing the SER chip's CV responses at different flow rates with opposite directions in one-way flow mode. (a) From WE to CE/RE (with a downstream cathode) and (b) from CE/RE to WE (with a downstream anode).

In the shuttle flow condition (Fig. 4.13(b)), the CV curve is also tuned by the shuttle speed and has a similar transition shown in Fig. 4.13(a). However, an oscillated CV profile is seen, especially at higher shuttle speeds. The oscillation in current can be resulted from the repeated equilibrium-seeking situation whenever the flow direction changed. This makes the shuttle flow not friendly for microfluidic CV detection. Yet, the current signals at the forward and reverse biases are similar in scale, which implies that the net flow polarization effect (Fig. 4.2(c)) can be diminished after serval shuttles. This is a primary proof of the micro-mixing effect under the shuttle flow and shows a distinct strength of this flow mode. To exclude the consideration that the current fluctuation might be attributed to the disordered flow control or channel deformation, a PMMA-based microfluidic chip is constructed by CNC-based manufacturing and assembled to a SER-based device. PMMA is a more rigid material than PDMS so the channel volume change can be ignored even under the flowing conditions. After the shuttle flow is applied, the current fluctuation still occurs as shown in Fig. 4.17. Since PMMA is a more rigid material than PDMS, this experiment indicates that the current oscillation is not because of the channel deformation. The current oscillation is resulted from the shuttle motion of the liquid sample.
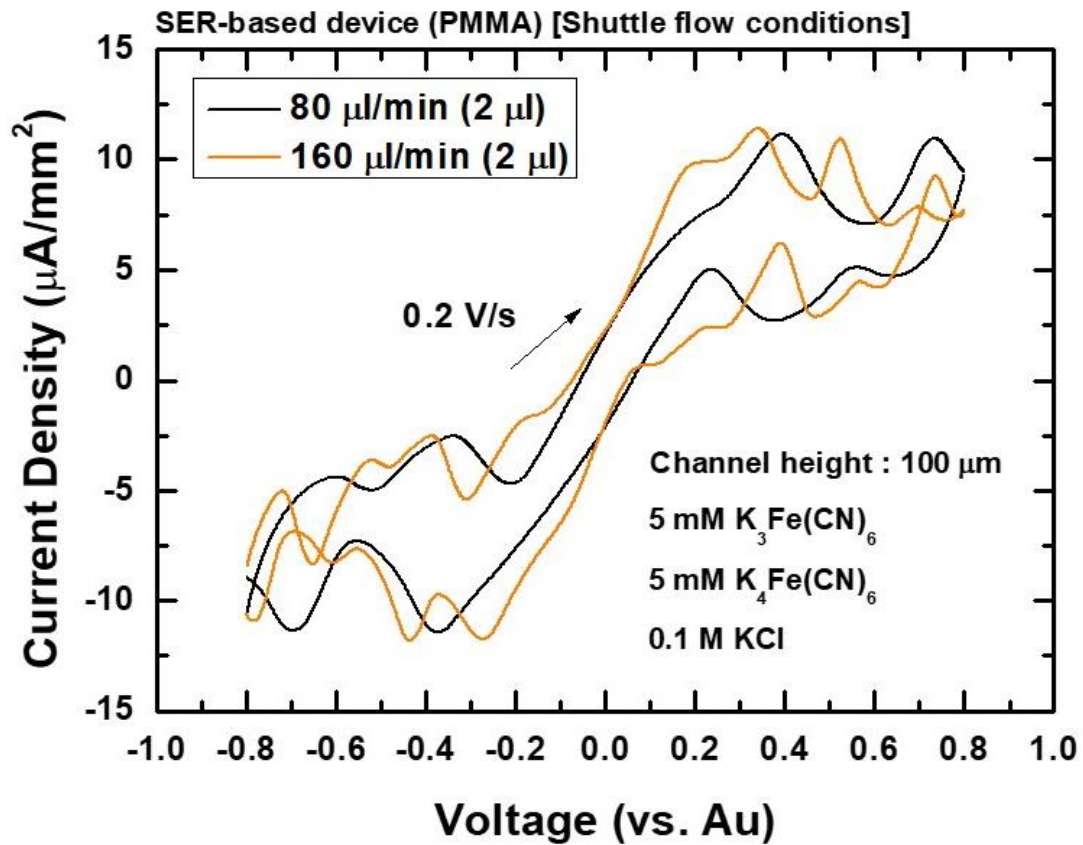
Figure 4.17 The CV diagrams of the redox mediator measured in the shuttle flow mode

using a device assembled with a PMMA microfluidic chip and a SER electrode chip

189

Furthermore, we fabricate four SER-based devices with different channel heights in the reaction zone (50 µm, 100 µm, 500 µm, and 1 mm) for one-way flow CV experiment. To prevent a possible collapse of the channel during operation, PMMA is used to replace PDMS here. The data are given in Fig. 4.18. Interestingly, we find that the enhanced mass transfer effect, featuring a wave-to-sigmoidal CV transition at an elevated flow rate, is only observed in the cases when the channel heights are 50 µm and 100 µm. When the channel height increases to 500 µm or 1 mm, the flow rate-tuned CV transition effect disappears. Although larger redox waves can still be observed at a higher flow rate, the shape of the CV diagrams remains a typical peak-shaped type for the large-channel devices (H = 500 µm or 1 mm). This tells that the enhanced mass transfer effect we discussed in this work does not merely mean the increase of current signal but also refer to the change of the behaviour of a microfluidic CV. The effect of the channel height on resulting the different CV dependence on the flow rate can be related to the ratio of the convective mass transport speed to the diffusional mass transport speed for the redox mediator. The convective mass transport resulted from the one-way flow is thought be more prominent in a small-channel device (H = 50 µm or 100 µm) than in a large-channel device (H = 500 µm or 1 mm). This can explain the difference between the devices' CV diagrams shown in Fig. 4.18.
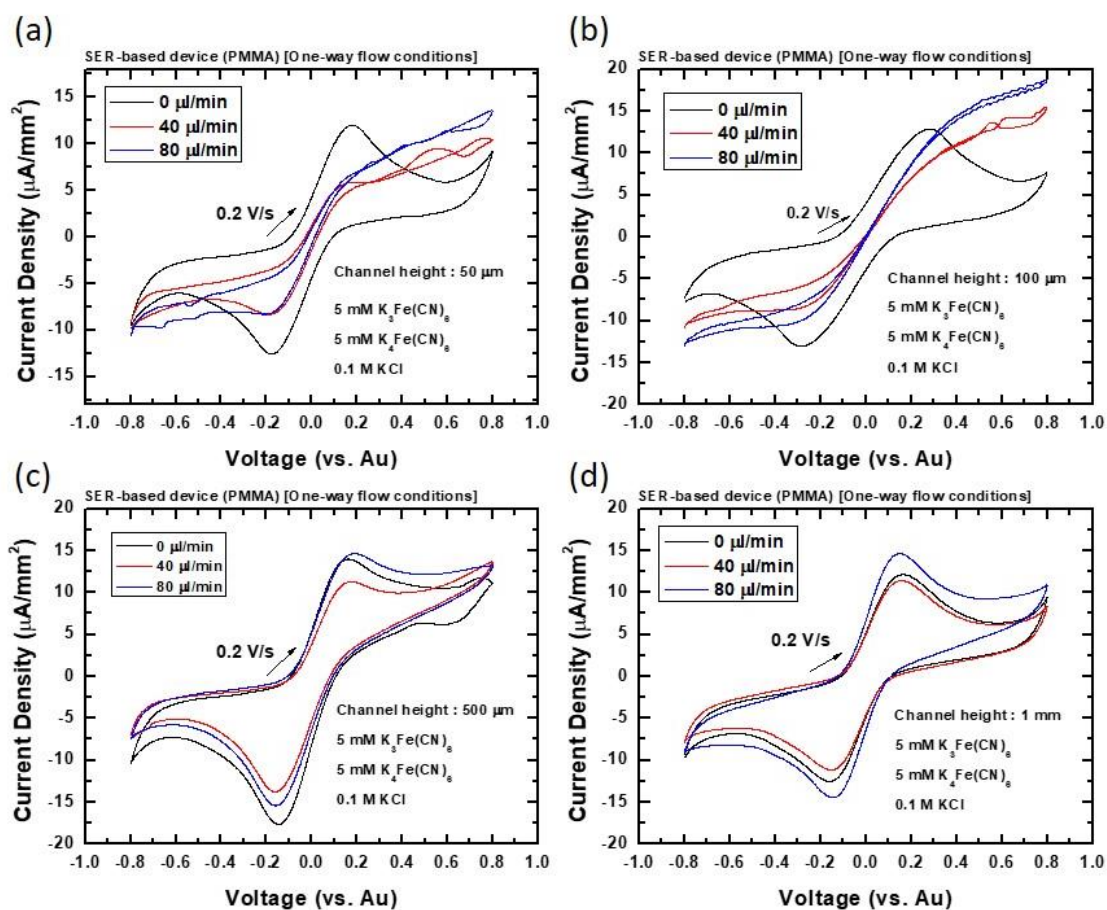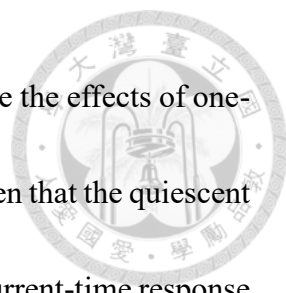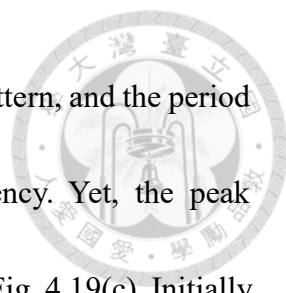
Figure 4.18 The CV diagrams of the redox mediator measured with SER-based devices in one-way flow mode at different flow rates. The devices are assembled with PMMA microfluidic chips having different channel heights in the reaction zone: (a) 50 μm (b) 100 μm (c) 500 μm (d) 1000 μm.

191

In addition to CV, we also perform CA measurements to compare the effects of one-way and shuttle flows. The results are plotted in Fig. 4.19. It can be seen that the quiescent SER-based device (at zero flow rate) yields a typical diffusion-type current-time response according to the Cottrell equation in both Fig. 4.19(a) and Fig. 4.19(c). When a one-way flow is introduced, a steady-state current response is attained (despite having some signal spikes) due to a stirring-like convection effect (Fig. 4.19(a)). Moreover, the current increases with the flow rate, while the response time to attain the steady-state current is greatly reduced accordingly (see Fig. 4.19(b)). In addition, an ultrafast speed in building a steady signal at a high flow rate (t < 0.1 s for v > 80 μl/min) is observed. This flow rate-dependent CA characteristics is highly consistent with the tunable CV behaviour observed in Fig. 4.13(a). In addition, it is found that the one-way flow CA response can be tuned in situ by speeding the flow rate in a step-wise way, which yields a steady-state current as a hyperbolic function of flow rate from 0 to 250 μl/min, which is shown in Fig. 4.20. In the case of the shuttle flow analysis, the CA response (Fig. 4.19(c)) also exhibits an oscillated profile as we observed in CV. Nonetheless, unlike the situation that CV oscillation in Fig. 4.13(b) produces complicated signals, there are periodic twin-peak currents in pairs developed with time and increased with the shuttle speed. The peak currents in pairs can not only be employed for reliable analysis but also be used as a measure for observing flow polarization and mixing effects. For instance, the shuttle

192

speed at 80 μl/min (0.3 Hz) gives a clear periodic twin-peak signal pattern, and the period of the twin-peak occurrence is consistent with the shuttle frequency. Yet, the peak symmetry in the paired signal varies with the shuttle cycle, as seen in Fig. 4.19(c). Initially, the advanced peak is sharp and high but the following peak is small and unclear. After several shuttles, the following peaks evolves and can match with, even exceed, the height of the advanced peak. The peak current data are further plotted and compared in Fig. 4.19(d). The crossover of two curves and increase in peak symmetry are the supporting evidence for the interchange in flow polarization direction and the effect of oscillatory mixing during the shuttle flow operation. Particularly, the micro-mixing effect of a shuttle flow is with the advantage on reducing the charge-transfer resistance for the redox reaction on the SER microelectrodes, which is evident from decreasing R_{ct} in EIS data with the shuttle speed as compared to the opposite phenomenon observed in the case of the one-way flow (see Fig. 4.21).
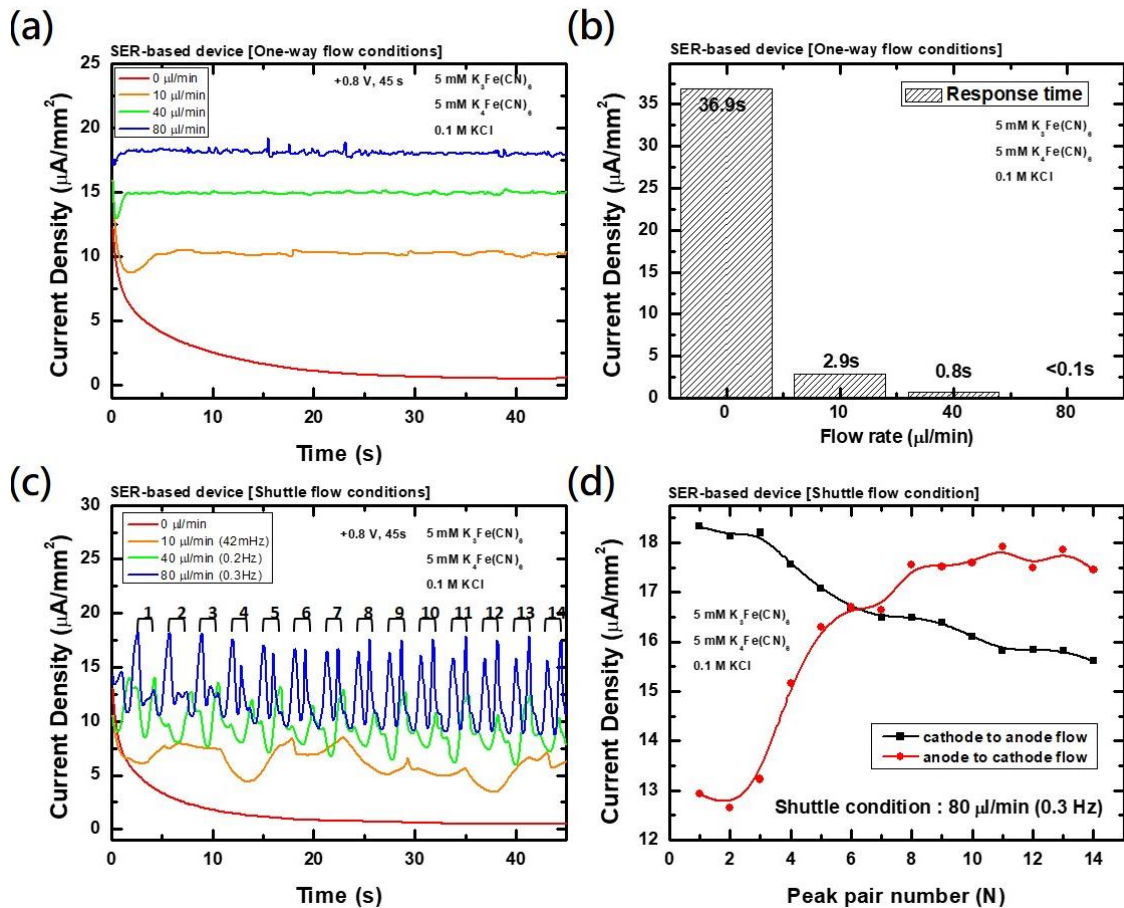
Figure 4.19 Two-electrode chronoamperometry for the ferricyanide redox reaction on the SER-based device measured at + 0.8 V: (a) Current-time data obtained under one-way flow condition with different flow rates. (b) Response time estimated from (a). (c) Current-time data obtained under shuttle flow condition with different shuttle rates. (d) Advanced and following peak currents as a function of the pair (shuttle cycle) number.

194
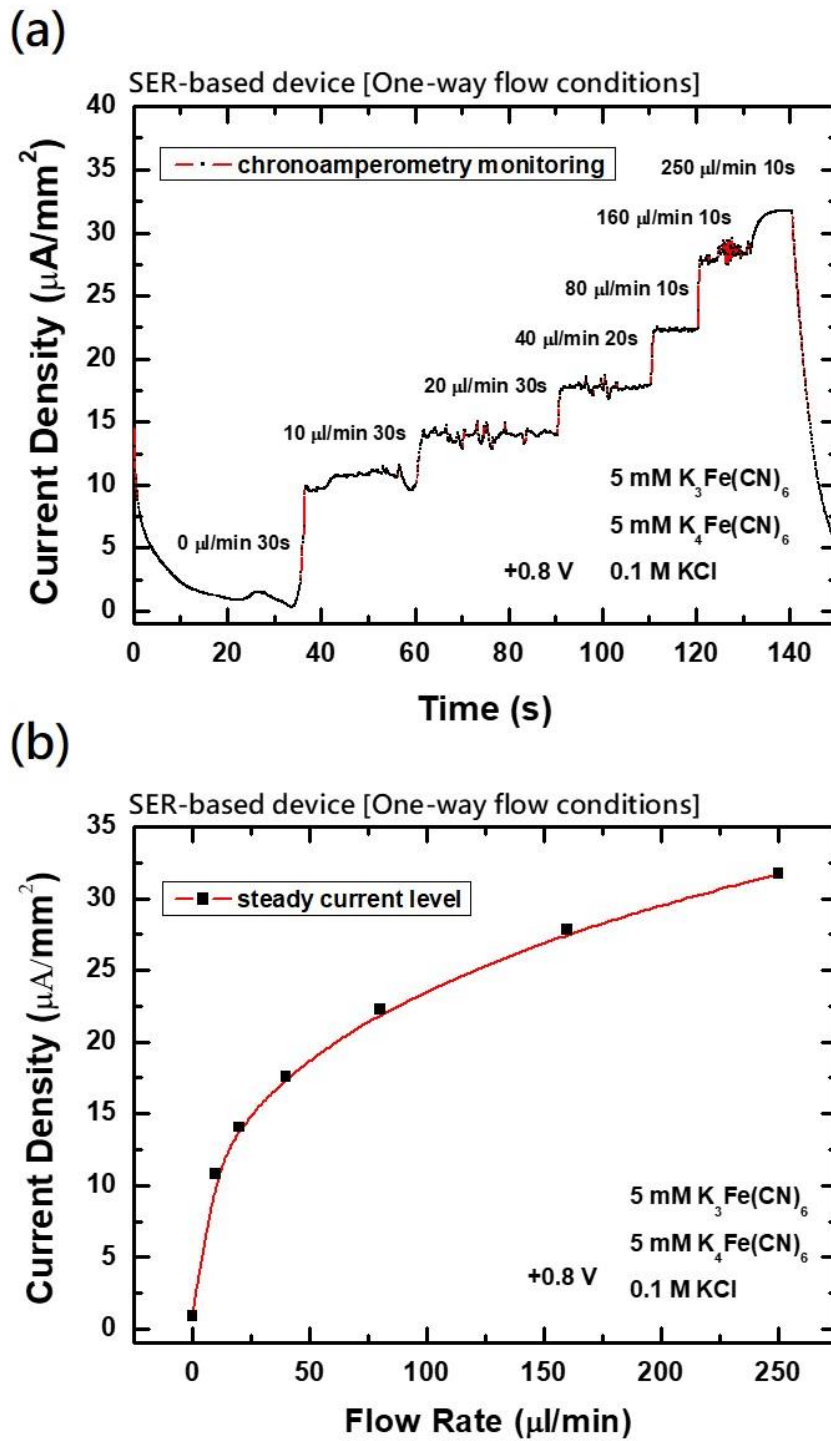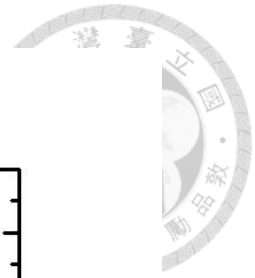
Figure 4.20 Chronoamperometry under step-accelerated one-way flow operation. (a) The

transient current measurement under step-wise increases of the one-way flow rate. (b)

The relationship between the steady current and the flow rate in (a).

195
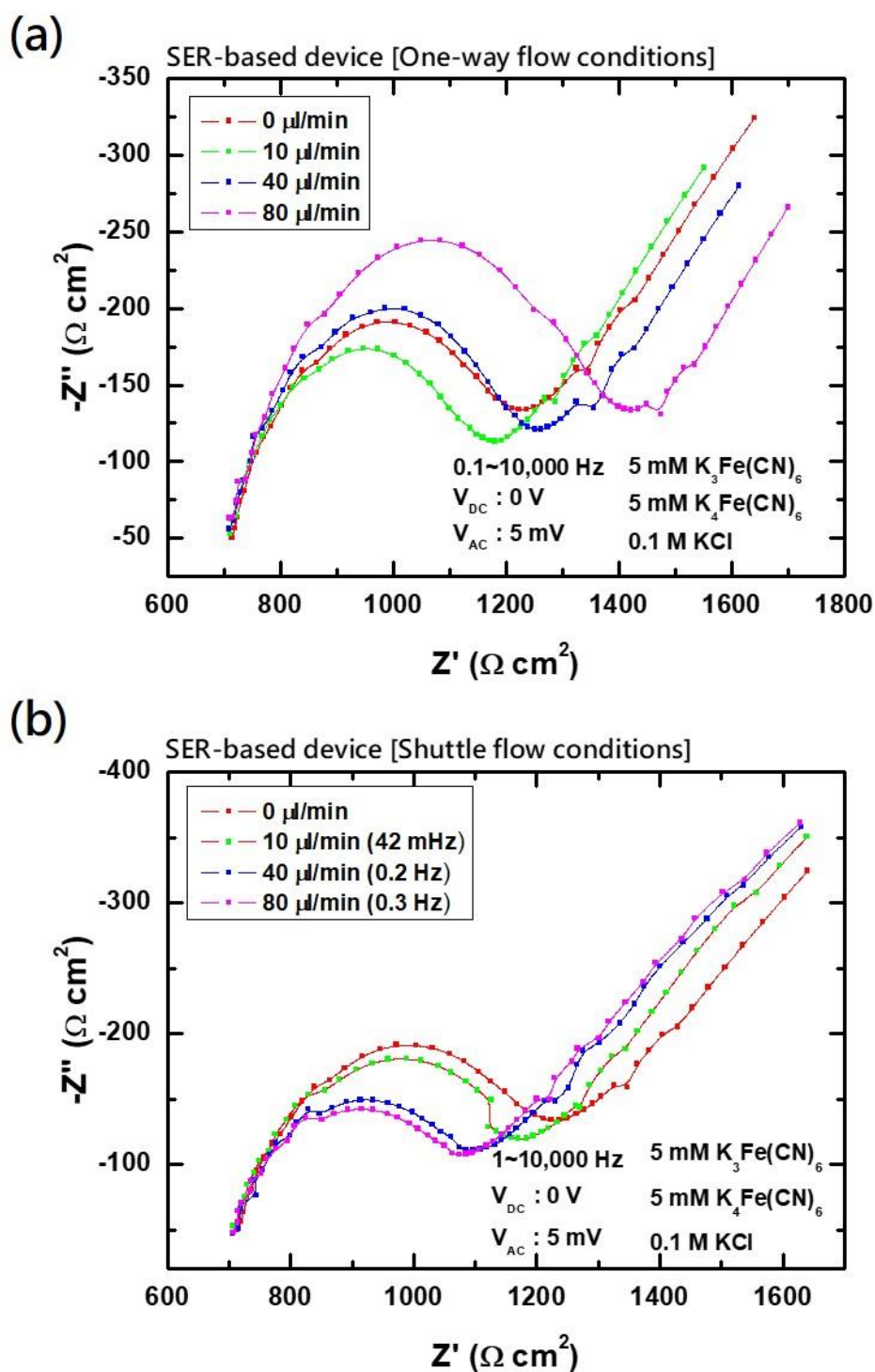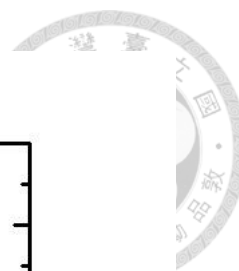
Figure 4.21 The Nyquist plots for the ferri/ferro-cyanide redox reaction from the EIS

analysis at different flow rates or flow speeds under (a) the one-way flow and (b) the

shuttle flow conditions.

196

4.4.4 Amperometry sensitivity enhancement under one-way flows
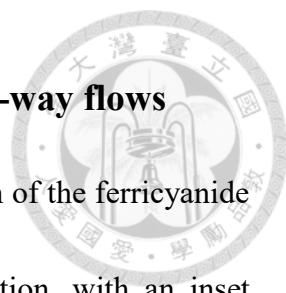
Fig. 4.22(a) plots the CA current (sampled at 45 s) as a function of the ferricyanide concentration for the SER microelectrodes under the static condition, with an inset showing the raw data. It can be seen that the CA current linearly increases with the ferricyanide concentration, and the detection sensitivity is calculated as 0.2 μA/(mm2· mM). From Fig. 4.22(b), it is proven that the CA detection sensitivity is greatly enhanced by applying a one-way flow. Even a slow flow rate as 10 μl/min can increase the CA sensitivity by a factor of 12.6 to 2.9 μA/(mm^2· mM). The CA sensitivity increases with the flow rate and attains 5.5 μA/(mm^2· mM) at 160 μl/min, which is a 24-fold enhancement as compared to the quiescent sensitivity. As discussed with Fig. 4.19(a), the sensitivity increase is attributed to the transition from a diffusion-type CA response to a stirring-like steady-state current from an enhanced mass transfer rate for the redox mediator. The evidence is further provided in Fig. 4.11, which shows that a steady, scan rate-independent I-V polarization curve is obtained instead of a wave-type CV profile for the SER-based device when the flow rate reaches 40-80 μl/min. The reversal occurred under 1mM ferri/ferro-cyanide condition may be resulted from insufficient refreshing rate due to a low mediator concentration and a slow flow speed. The CA quantification is carried out by measuring the endpoint current, which is supposed to be a steady current. Under the one-way flow condition with a 10 μl/min flow rate, the mediator might still

197

adsorb on the electrode surface at some degree that is similar to the static condition. This can lead to a higher current response at 10 µl/min than at 20 µl/min.

Figure 4.23 plots the LSV peak current (at 200 mV/s) as a function of the ferricyanide concentration for the SER-based device under the static condition, with an inset of the raw data. Because of the sweeping voltage effect, the static LSV sensitivity reaches 3.1 µA/(mm2· mM), which is 13.6-fold higher than that of static CA detection. The one-way flow effects on the LSV sensitivity are shown in Fig. 4.23(b). Similar to the data in Fig. 4.12(b), the LSV sensitivity decreases with the flow rate at the beginning (< 20 µl/min) but increases with the flow rate when the flow rate is higher than 40 µl/min. However, it should be noted that the LSV profile becomes a sigmoidal I-V curve at higher flow rates, as shown in Fig. 4.23. Thus, the steady-state currents, similar to the case of CA detection, are used for LSV analysis. As a result, the LSV sensitivity is approaching to CA detection sensitivity for the flow rates higher than 80 µl/min. In other words, microfluidic amperometry with a fast one-way flow results no difference between CA and CV (or LSV) detection modes. From the above discussions, we learn that both the CA and LSV characteristics and sensitivity for the SER-based device can be greatly improved with one-way flow and exhibit a similar redox behaviour like an IDA-based device bearing the UME advantages.
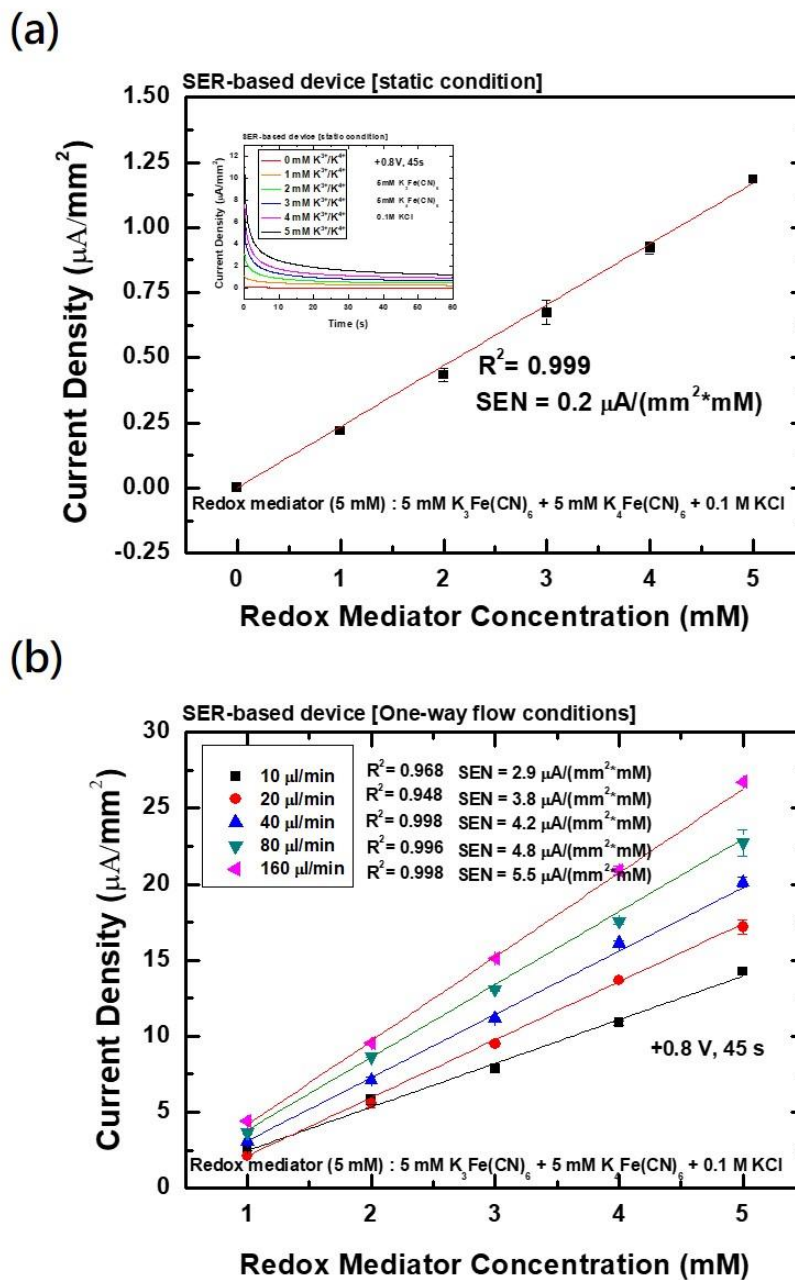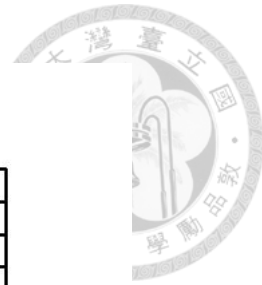
Figure 4.22 Ferricyanide detection with the SER-based device using micro-fluidic chronoamperometry (CA) under (a) static and (b) one-way flow conditions. Inset in (a): the current-time data measured at different ferricyanide concentrations. A constant voltage bias of +0.8V was applied, and the CA currents at the 45th sec were taken and plotted.
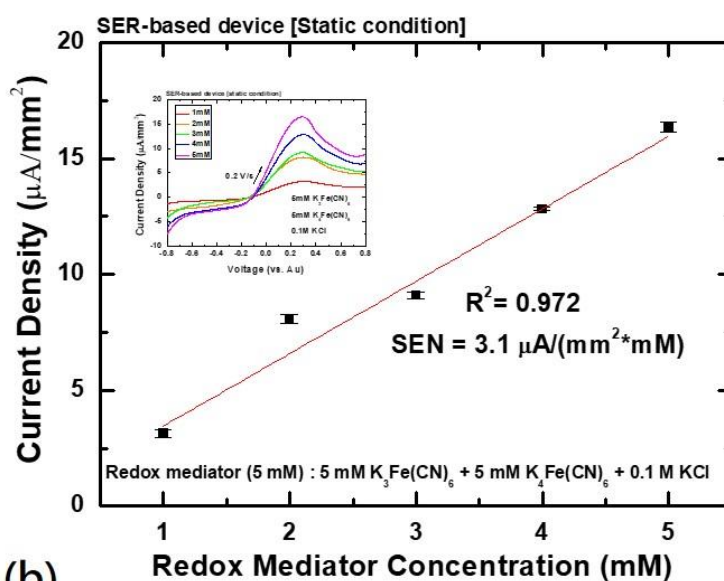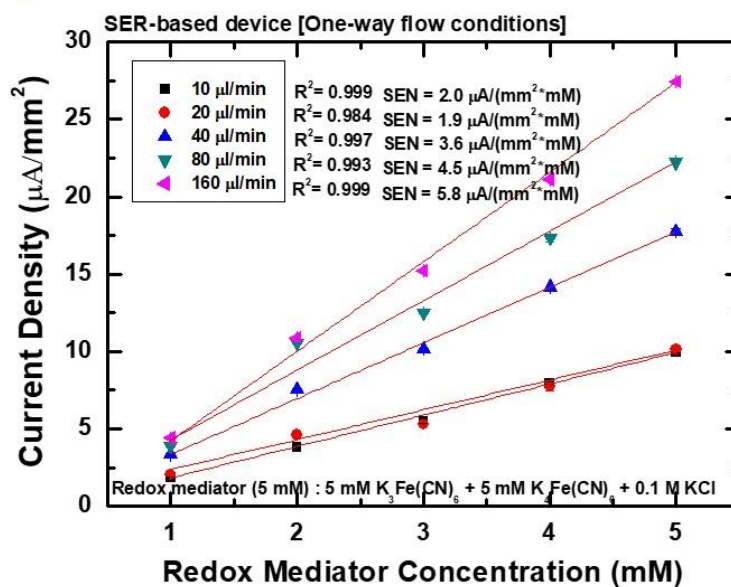
Figure 4.23 Ferricyanide detection with the SER-based device using linear-sweep voltammetry (LSV) under (a) static and (b) one-way flow conditions. Inset in (a): the current-voltage data measured at different ferricyanide concentrations. For detection, the applied voltage increased from -0.8 V to +0.8 V at a scan rate of 200 mV/s.

4.4.5 Amperometry sensitivity enhancement under shuttle flows

Similar to the one-way flow, the shuttle flow also increases the redox current response and enhances the sensitivity of the microfluidic amperometry. In addition, it simply needs a drop of analyte solution for the analysis. Because of the bi-directional sample shuttling, the resulted oscillating signals (Fig. 4.13(b)) make voltammetry analysis a difficult task. Thus, only CA detection is applied to the shuttle-flow analysis. Figure 4.24 compares two flow speeds with different moving volumes that yield different shuttle frequencies for the CA detection of ferricyanide. In this work, the shuttle frequency (f) is calculated with the flow speed (v) and moving volume (V). A shuttle duration time (T) is defined as the ratio of the double moving volume to the flow speed (T=2V/v), and the shuttle frequency is the reciprocal of the duration time (f=1/T). The data in Fig. 4.24 reveals the following facts for the CA detection with shuttle flows: (i) A shuttle flow also enhances the CA detection sensitivity despite less effective than a one-way flow. (ii) The CA sensitivity is higher at a faster flow speed (100 μl/min) than at a slower flow speed (50 μl/min) when the moving volume or shuttle frequency is fixed (e.g., it is almost 3-fold higher when f is 0.4 Hz). (iii) The CA sensitivity increases with the moving volume (i.e., decreases with the shuttle frequency), and the sensitivity can be modulated over 3 folds by tuning the shuttle frequency. From the facts, we consider that the sensitivity enhancement from the shuttle flow is resulted from the micro-mixing effect,

201

which is unlike the convective, continuous supplement of redox mediator by a one-way

flow Thus, the sensitivity increase is lower than that of one-way flow operation and

depends on flow speed and moving volume, which together determine the degree of

micro-mixing. Although the sensitivity enhancement is not very promising, the benefits

of repeated interaction with the electrodes, micro-mixing, and sample saving still make

the shuttle flow an ideal fluidic operation mode for microfluidic amperometry.
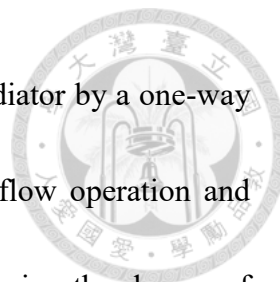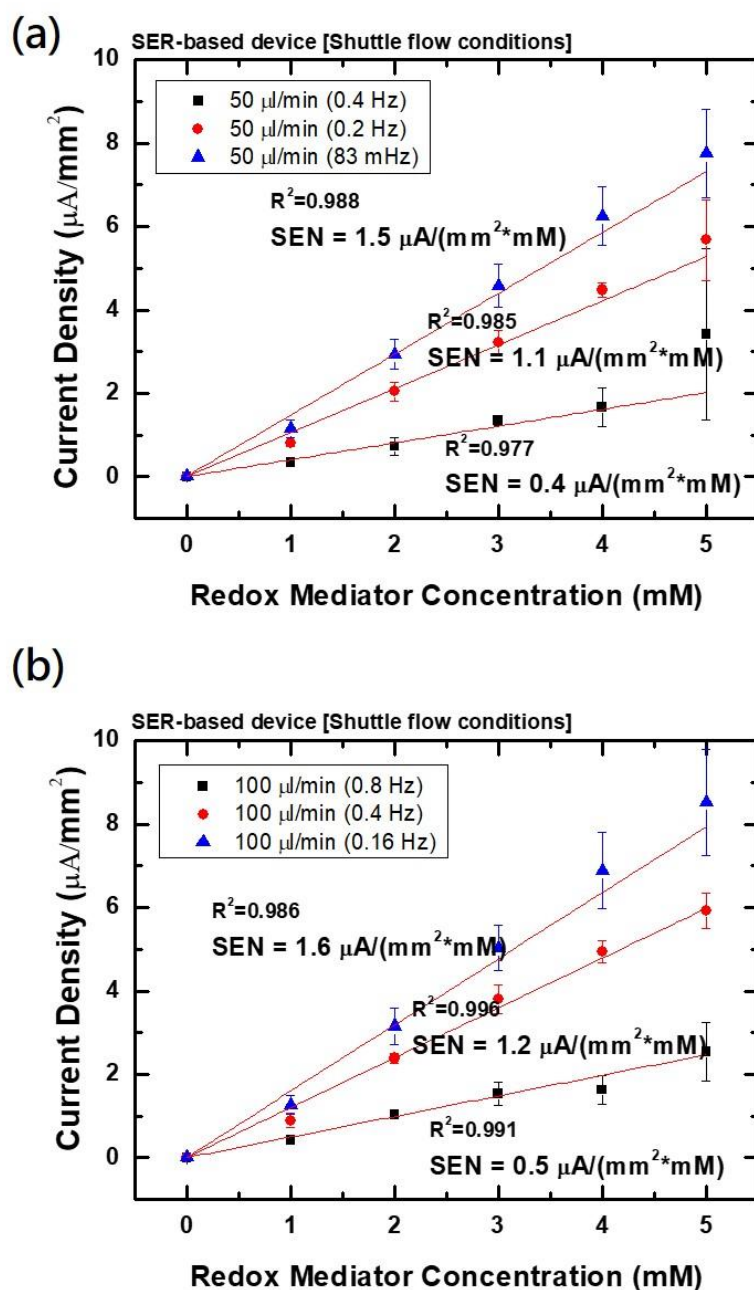
Figure 4.24 Ferricyanide detection with the SER-based device using micro-fluidic chronoamperometry (CA) under shuttle-flow conditions with different shuttle frequencies: (a) flow speed =50 μl/min and (b) flow speed =100 μl/min. The shuttle frequency (f) is calculated by dividing the flow speed (v) by the double moving volume (V), i.e., f = v/2V.

203

4.5 Chapter summary

In conclusion, microfluidic amperometry with two symmetric Au microelectrodes on a device has been demonstrated as an ideal platform method for µl-scale characterization or detection of a reversible redox mediator like ferricyanide. In particular, the method can be tuned with not only ordinary DC/AC parameters but also the microelectrodes design and microfluidic flow mode. For examples, the microelectrode pattern is proven to be a crucial factor to tune the shape of CV of ferricyanide under the static condition. In addition, one-way and shuttle flows are found especially effective for enhancing the micro-electroanalysis through exerting different flow effects. Increasing the flow rate, the one-way flow can bring in a facilitated mass transfer of ferricyanide as evidenced by both the CV shape change from a symmetric wave-type curve to a sigmoidal I-V polarization curve and the steady-state CA response. That makes the Au electrodes behave like a UME. Despite less efficient in reducing the sample volume, the one-way flow is also found effective in increasing the sensitivity of amperometric detection of ferricyanide, in which a 24-fold enhancement in CA sensitivity is demonstrated. In contrast, the shuttle flow has the advantages of single-drop analysis, micro-mixing and repeated interrogation of analyte. Although the shuttle flow is not as effective as the one-way flow in amperometry sensitivity enhancement and causes undesired oscillatory interference for CV, it yields a unique paired peak current pattern in CA, which can be

204

used for not only the redox mediator quantification but also the observation of the change in flow polarization and the assessment of mixing completeness. It also gives a new rate parameter for single-drop electroanalysis – shuttle frequency. With the conclusions, this study can inspire a new insight into microfluidic electrochemistry and can also be applied to versatile microfluidic biochip applications that use two Au electrodes instead of classical three-electrode design and ferricyanide as the electrochemical signal reporter.

205
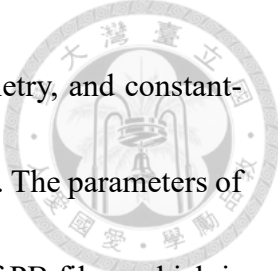
Chapter 5. Enhanced Prussian blue electrodepositions

5.1　Introduction

Prussian blue (PB) is a common dark blue pigment which is widely used in painting and porcelain. PB can be formed by oxidation of ferrous ferrocyanide salts. Actuarially, not only shows a beautiful color, but also PB can perform a variety of applications. In chemical engineering, PB is one of the electrochromic materials which can change colors according to the redox states of molecules (Itaya *et al.*, 1982). The PB film turns into a transparent state when a positive voltage is applied to it. With this feature, PB electrochromic has great potential to develop low power-consumption displays and smart windows. In biological engineering, PB is treated as an artificial redox catalyst which can catalyze the hydrogen peroxide (Karyakin *et al.*, 1998). The catalyzed reaction causes charge transfer and generates the current response. According to the redox current, the concentration of H_2O_2 can be quantitated. Besides, PB is also an ion-sensitive material (Krishnan *et al.*, 1990) that its redox reaction is affected by the concentration of Na^+ and K^+. In several biological reactions, the concentration of ions may be changed during the reaction, and the H_2O_2 served as a mediator to transfer the enzyme reaction. Therefore, PB film has a promising potential for biosensing applications.

In general, PB film can be electrodeposited on the electrodes by applying a positive potential to induce a reduction of ferricyanide, and the PB particles are accumulated on

the electrode surface. Including cyclic voltammetry, chronoamperometry, and constant-current, PB films can be formed by different electrochemical methods. The parameters of electrodeposition play an important role to influence the thickness of PB films which is related to the charge density. And, the rate of film formation also affects the quality of the PB film (stability and functionality). A lot of methods are proposed to enhance the performance of PB film, for example, adding the assisted component, layer-by-layer deposition (Li *et al.*, 2009), two materials co-deposition (Du *et al.*, 2010a), and preparation of nanomaterial (Du *et al.*, 2010b). However, fewer researches discuss the conditions and phenomena of electrodeposition in the microfluidic chips.
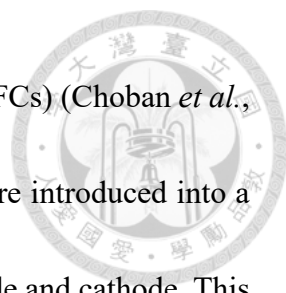
In this study, we try to electrodeposit the PB films on the microelectrodes in the microchannel with the two-electrode system and compare the flowing effect on the PB performance. The two-electrode system supplies a symmetric electrochemical reaction at both electrodes, so the electrodeposited parameters should be different in comparison to the typical three-electrode system. In the microchannel, the shorter diffusion distance may lead to a faster reaction rate, but the insufficient component supply due to the horizontal diffusion still limits the formation of stable PB films. Hence, the concept of laminated electrodeposition which has the effects of surface refreshment for providing sufficient components and shearing stress for removing the weak films during the depositing process.

5.2　Literature review

5.2.1　Interfacial effect in microfluidics
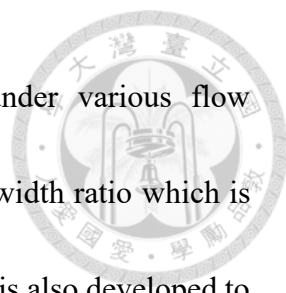
Reynold's number (Re) is an important dimensionless quantity which is the ratio of inertial forces to viscous forces within a fluid. The inertial force is related to the different fluid velocities, and the viscous force is dependent on the property of a liquid that indicates the frictional force arising between adjacent layers of fluid. Laminar flow in microfluidic reflects the liquid behavior with a low Reynold's number. Although the laminar flow causes an insufficient mixing, its unique features still have some advantage in microfluidic applications shown in Fig. 5.1. In laminar flow, two liquid streams can flow in parallel without obvious interference. Before the inter-diffusion zone in the downstream, the components in both liquids can only interact with each other along with the interface (Kamholz and Yager, 2001). With this interfacial reaction, the controllable chemical synthesis and selected molecule diffusion are achieved. Laminar flow patterning is used for various microfabrication including gold etching and silver deposition (Kenis *et al.*, 1999). Combining etching and deposition procedures, a three-electrode system can be easily in-situ manufactured in a microchannel. First, after the gold stripe is deposited on the substrate, the selective etching is applied to form two gold electrodes. And then, the AgX and reductant are injected into the channel in order to form a thin Ag wire as a reference electrode in the middle of the channel. Furthermore, the distinct interface can

be used as a pseudo-membrane for laminar flow-based fuel cells (LFFCs) (Choban *et al.*, 2004; Jayashree *et al.*, 2005). The liquid fuel and aqueous oxidant are introduced into a single channel which embeds two catalyst-covered electrodes as anode and cathode. This membrane-free configuration of LFFCs improves reaction kinetics and open cell potentials. Moreover, the shear stress attributed to the frictional force emerges at the liquid-to-liquid interface. With the designed microfluidic channels, the continuous liquid flow can be sheared into many sections to form droplets (Trantidou *et al.*, 2018). The size of the droplet is tunable with the various flow rates in sample flow and shear flow. Micro-droplet as a mini-reactor reduces the reagents and wastes as well as increases portability and controllability of assays. Droplet microfluidics benefits to single-cell analysis and cell culture, droplet synthesis, and high-throughput screening (Mashaghi *et al.*, 2016).

According to the laminar flow, when two liquid flows meet in a channel, they move forward side by side without turbulent mixing. Two parallel streams having the same width are formed due to the identical driving pressure at the symmetric inlets. The width of the stream can be confined by the modulation of flow velocity which is also related to the applied pressure and channel geometry. The relative width of each stream can be controlled by adjusting the ratio of inlet pressures. Hydrodynamic focusing lithography (HFL) is a novel method that creates stacked flows for particle synthesis (Bong *et al.*, 2010). To demonstrate this method, the manufacture of PEG particles consisted of
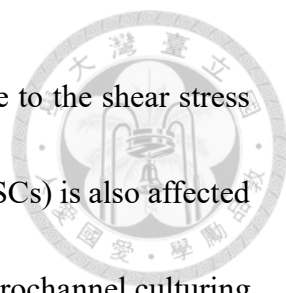
rhodamine acrylate and green fluorescent beads is presented under various flow

conditions. The particle images are further analyzed to quantify the width ratio which is

proportional to the estimate flow ratio. This special flow distribution is also developed to

versatile devices, such as T-sensors and H-filters (Kamholz *et al.*, 1999; Hatch *et al.*, 2001;

Osborn *et al.*, 2010).

Hydrodynamic focusing is an advanced technique based on the laminar feature and

the shear flow effect (Knight *et al.*, 1998). A central flow is compressed by two shear flow.

With the increasing shear stress, the width of central flow reduces into a tiny channel that

only allows single particle passing through. This mechanism is successfully demonstrated

in a wide variety of applications and flow cytometry is just an important one for single

cell analysis. Two flanked shear flow are applied to reduce the core flow which contains

the cells. Resulted from the narrow stream, the cells are forced to flow through the

detector one by one. Additionally, if the asymmetric shear flows are used to control the

direction of the central stream, the hydrodynamic guiding is achieved for addressable cell

immobilization (Brevig *et al.*, 2003), molecule sorting (Arakawa *et al.*, 2007) and array

pattering (Regenberg *et al.*, 2004; Kohlheyer *et al.*, 2008).

The shear stress can not only guide the liquid flow but also induce particular cell

behaviors. Effect of shear stress on endothelial progenitor cell (EPC) morphology is

presented with phase-contrast and fluorescent images. In comparison to the cells in a

static condition, the EPCs became elongated and aligned in response to the shear stress (Obi *et al.*, 2009). The differentiation of mesenchymal stem cells (MSCs) is also affected by the shear stress. When a gradient shear stress is applied to the microchannel culturing MSCs, endothelial differentiation is dominant in the high level of shear stress (Yamamoto *et al.*, 2003; Kim *et al.*, 2017).

According to the above evidence, the shear stress is known as a critical role in microfluidic laminar flow, especially at the liquid-channel interface. Instead of the cell immobilization, the microelectrodes used for the electrochemical reaction are assembled in the microchannel. The electrodeposition under static and flow conditions show different phenomena of film formation. The difference is attributed to the micro-mixing and shear-induced effects, and it results in different particle size, density and morphology. The chitosan-mediated biofilm assembly (Park *et al.*, 2006) and 3-D copper-core/carbon-sheath nanowalls (Parisi *et al.*, 2013) are demonstrated to discuss the flowing effect on electrodeposition at the electrode surface.
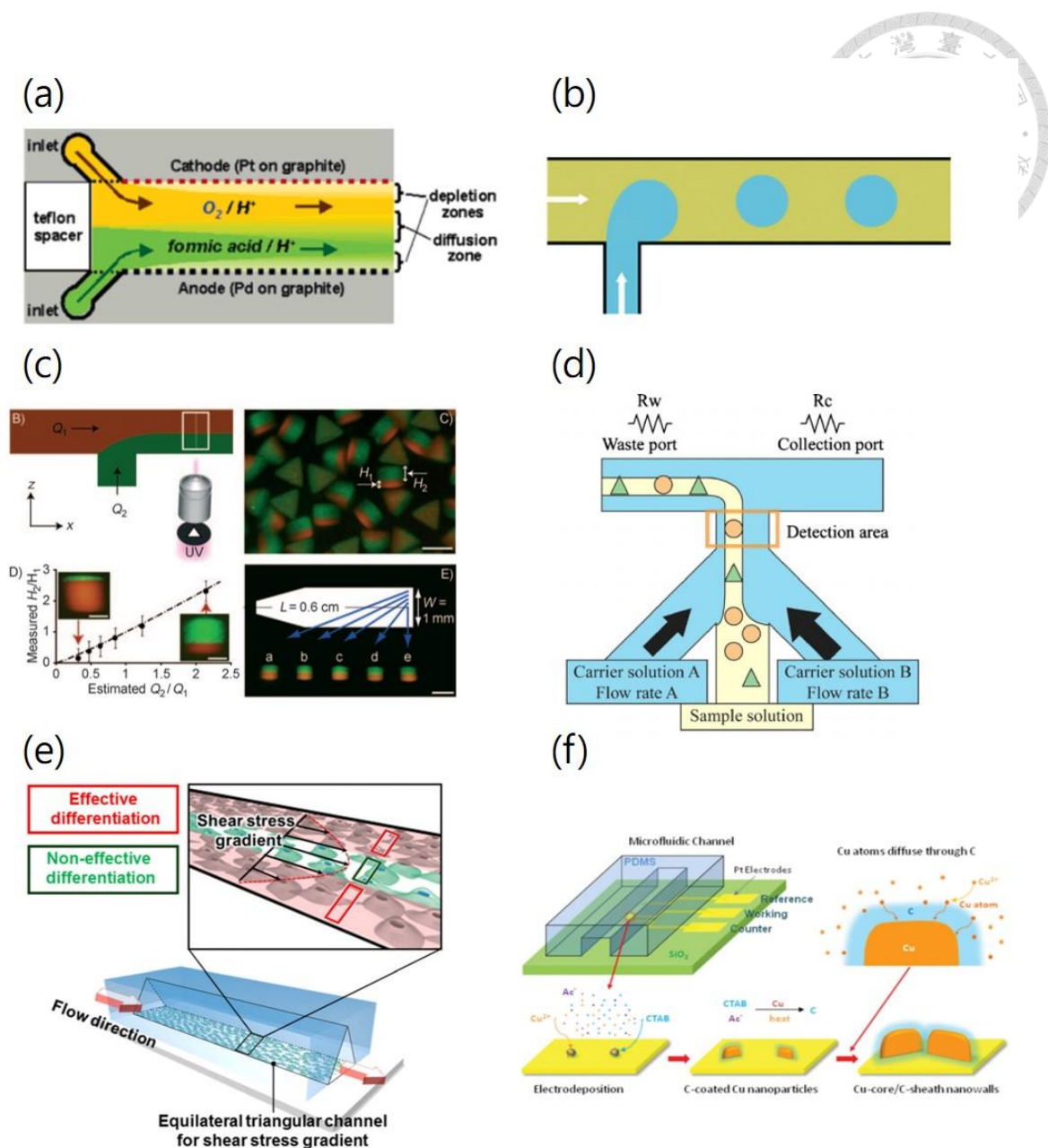
Figure 5.1 Interfacial effects in the laminar flow used for various applications. (a) Laminar Flow-Based Microfluidic Fuel Cell (Jayashree *et al.*, 2005). (b) Microdroplet formation (Trantidou *et al.*, 2018). (c) Hydrodynamic focusing lithography (Bong *et al.*, 2010). (d) Hydrodynamic focusing for particle sorting (Arakawa *et al.*, 2007). (e) Shear stress induces the endothelial differentiation (Kim *et al.*, 2017). (f) Growth of Cu-core/C-sheath nanowalls under flow conditions (Parisi *et al.*, 2013).

212
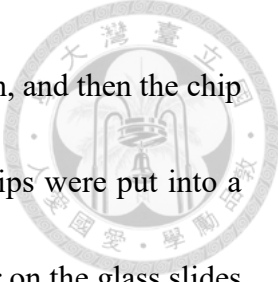
5.3　Experimental

● Reagents and materials

The redox mediator solution was prepared by equal-molar mixing, and the final concentration was 5 mM $K_3Fe(CN)_6$, 5 mM $K_4Fe(CN)_6$ and 0.1M KCl in ddH_2O. The PB plating solution contains 20 mM $K_3Fe(CN)_6$, 10 mM KCl and 20 mM $FeCl_3$ in 0.1M HCl. All reagents were purchased from Sigma-Aldrich. All organic solvents like ethanol, acetone, and isopropyl alcohol were obtained from HSIN MING chemical instruments Co., LTD (Taipei, Taiwan). The materials and reagents used for the device construction were obtained from commercial sources as follows: glass slide (FEA, 1"x3", 1-1.2 mm thickness); gold slugs, Cr pieces and boats (Guv Team International, Taiwan); S1813 photoresist (SHIPLEY); plastic photomask (TK, Taiwan); TMAH (Sigma); PDMS (BingBond, Taiwan); biopunch (MILTEX, Japan).

● Fabrication of the device

Two symmetric Au microelectrodes were fabricated on a glass slide by a standard lift-off process. Firstly, the glass slides were cleaned with acetone, isopropyl alcohol, and ddH_2O sonication, and then they were dried by N_2 and a 120 ℃ hotplate. Secondly, the positive photoresist S1813 was coated on the cleaned glass slides by spin coating at 1000 rpm for 20 s and then at 4000 rpm for another 60 s. After the soft baking at 115 ℃ for five minutes, the cured photoresist was exposed to UV light (15mW/cm^2) for 10 seconds.

213

Thirdly, the unexposed photoresist was developed in TMAH for 1 min, and then the chip was baked at 130 ℃ for 10 mins. Next, the photoresist-patterned chips were put into a thermal coater which deposited a Cr (30 nm) and an Au (80 nm) layer on the glass slides by heat evaporation. According to the lift-off principle, the electrode patterns appeared after the chips were immersed in acetone for a few minutes. The consistent areas of the two electrodes were defined by the microchannel. The microchannel was designed for reducing the fluidic resistance and enhancing the reaction efficiency. A shallow-height chamber was connected to two wide-height channels with a ramped diffuser, which smooths the liquid flow through the height-difference channel. For microchannel fabrication, PDMS (standard mixing ratio is 10:1) was poured into an aluminum mold (fabricated by a CNC machine) and cured at 120 ℃ for 10 mins. Later, the cured PDMS chip (4 mm in thickness) with microfluidic patterns were peeled off, and two tiny holes were punched for the tubing installing. Finally, the upper PDMS chip with micro-channels and the lower Au microelectrodes on a glass slide were bonded by oxygen plasma for a robust sealing through a relatively large contact area between PDMS and glass.

● Electrodeposition of Prussian blue

The plating solution is prepared by dissolving 20 mM $K_3Fe(CN)_6$ in 0.1M HCl and dissolving 10 mM KCl and 20 mM $FeCl_3$ in 0.1M HCl, individually. Two solutions are mixed only before the electrodeposition in order to prevent the oxidization of reagents.

214

The substrates including ITO glasses and gold electrodes are cleaned by sonicating in 0.1

M HCl to remove the contaminant and then dried by N_2. The working area is identified

by 3M tapes. After the electrodes are immersed in the plating solution, a voltage bias is

applied to drive the PB electrodeposition. In the three-electrode system, a Pt sheet as a

counter electrode and an Ag/AgCl reference electrode are used to carry out the

electrochemical reaction. After the electrodeposition is completed, the electrodes are

removed from the solution gently to prevent the film peeling, and the electrodes are rinsed

by DIW to wash the retained plating solution. The PB films are annealed at 120 °C for 1

hr.

● Electrochemical characterization

The prepared PB films are analyzed through a 20-cycle CV scanning in 0.1M KCl

in 0.1 M HCl. The charge density of PB films can be determined by integrating the CV

curves.

5.4 Results and Discussion

5.4.1 PB electrodeposition in the three-electrode system

To verify the experimental conditions in the typical PB electrodeposition with the three-electrode system shown in Fig. 5.2, the ITO glasses are used as the electrodes which are transparent so that the color change can be easily observed during the electrodeposition process. Two electrochemical methods including constant potential (CP) and cyclic voltammetry (CV) are chosen to induce the thin film deposition. In the CP-based method, a +0.7V potential (ref. to Ag/AgCl) is applied to the working electrode to supply a stable driving force for PB film formation. In Fig. 5.3(a), the CV characteristics of the PB films show increasing current responses along with the depositing time, and the blue color becomes darker on the ITO electrodes (shown in the inserted image). In the CV-based method, a cycling potential change (-0.3 V to +0.7 V) is applied to the ITO electrodes, and the cycling scan can repeatedly reduce and oxidize the PB films to obtain stable film structures. In Fig. 5.3(b), the CV characteristics of the PB films also show increasing current responses along with cycles, but the current is smaller compared to the film produced by the CP-based method. To measure the charge density of the PB films, the CV curves are integrated to calculate the charge intensity of the PB films (shown in Fig. 5.4). The CP-deposited PB films have a larger charge density that implies the thicker PB films.

216
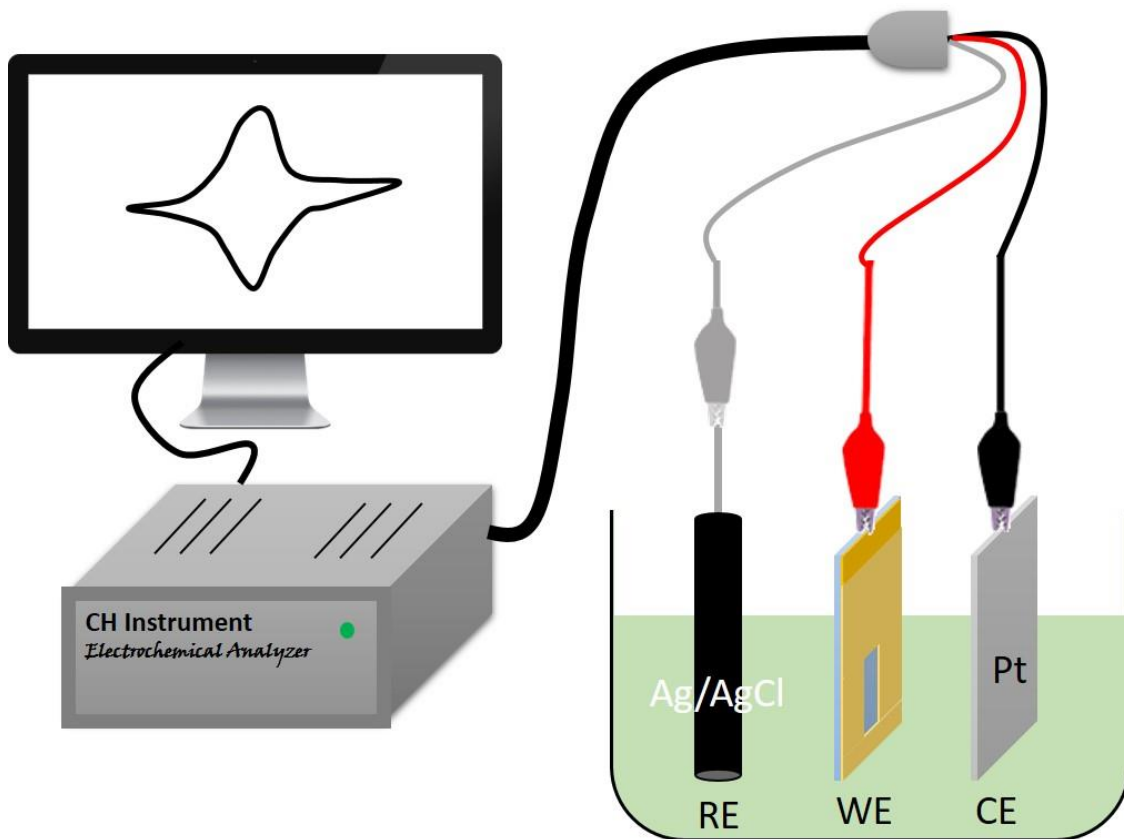
Figure 5.2 Three-electrode electrochemical analysis system contains a working electrode

(WE), a counter electrode (CE), and a reference electrode (RE). Three electrodes are

immersed in the plating solution for PB electrodeposition.
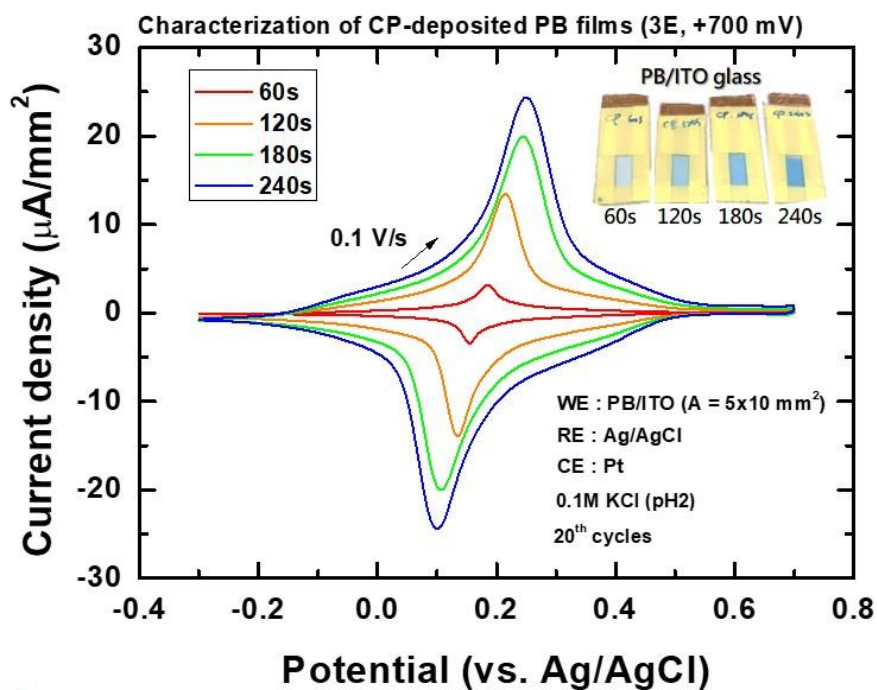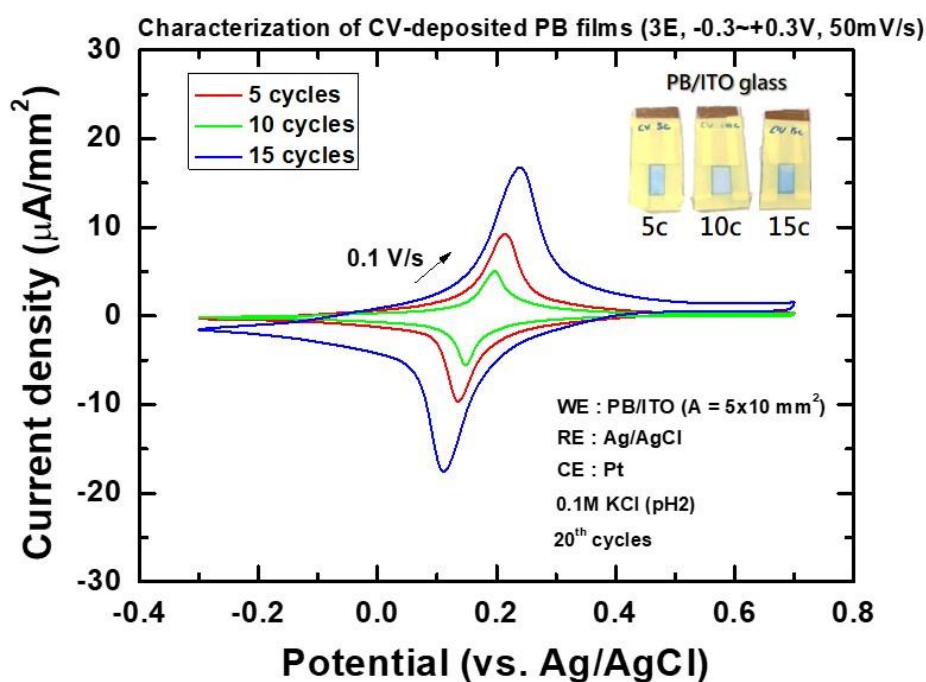
Figure 5.3 The CV characteristics of the PB films electrodeposited on the ITO glasses by

(a) the constant potential and (b) the cyclic voltammetry methods under different

conditions.

218

(a)

Characterization of CP-deposited PB films (3E, +700 mV)

PB/ITO glass

Charge density ($\mu C/mm^2$) vs Deposition time (s)

(b)

Characterization of CV-deposited PB films (3E, -0.3~+0.3V, 50mV/s)

PB/ITO glass

Charge density ($\mu C/mm^2$) vs Deposition cycle (N)
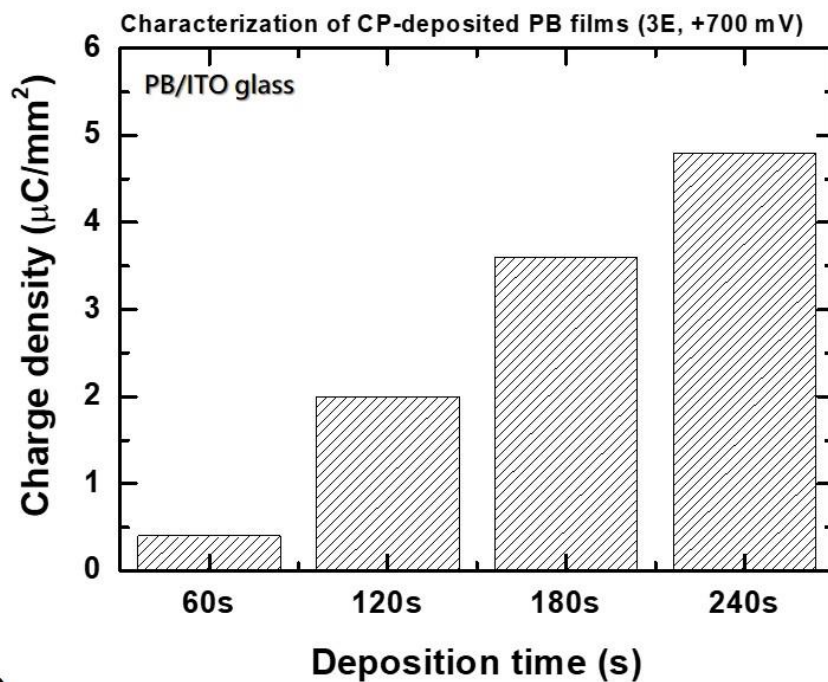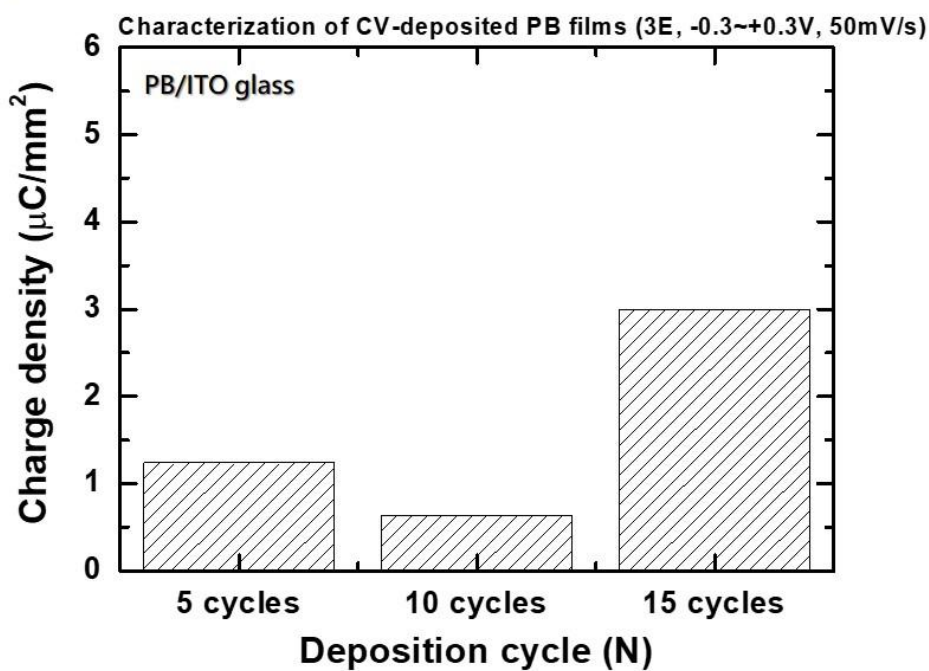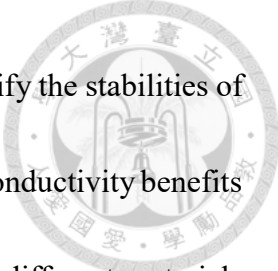
Figure 5.4 The charge densities of the PB films electrodeposited on the ITO glasses by (a)

the constant potential and (b) the cyclic voltammetry methods under different conditions.

219

The same experiments are executed on the gold electrodes to verify the stabilities of

the PB films on various substrates. The gold electrodes having better conductivity benefits

to the electrodeposition according to the small resistance. However, different materials

may lead to distinct electrode potentials, and it affects the electrodeposition performance.

In Fig. 5.5(a), seeing the dark blue color on the gold electrode surface, the CP-deposited

PB films are thick and uniform. The CV characteristics of PB films reveal the increasing

current responses along with deposition time. In contrast, the CV-deposited PB films are

fragile shown in Fig. 5.5(b). In these conditions, the PB films always peel off while the

electrodes are rising from the solution because the film growth rate is so fast that the PB

forms the unstable structures. Hence, the CV characteristics show smaller current

responses, and only a few pieces of PB dot can contribute to the redox reaction.

Comparing the PB films produced by both methods under the same deposition time (120s),

the CP-based method can provide darker blue colors that mean the thick PB films

formation. To measure the charge densities of the PB films, the CV curves are integrated

to calculate the charge intensity of PB films shown in Fig. 5.6. Although the redox

reaction can only occur at the shattered PB deposition, the thick films still supply large

charge densities. Nevertheless, the CV-deposited PB films seem to be more unstable than

the CP-deposited PB films.
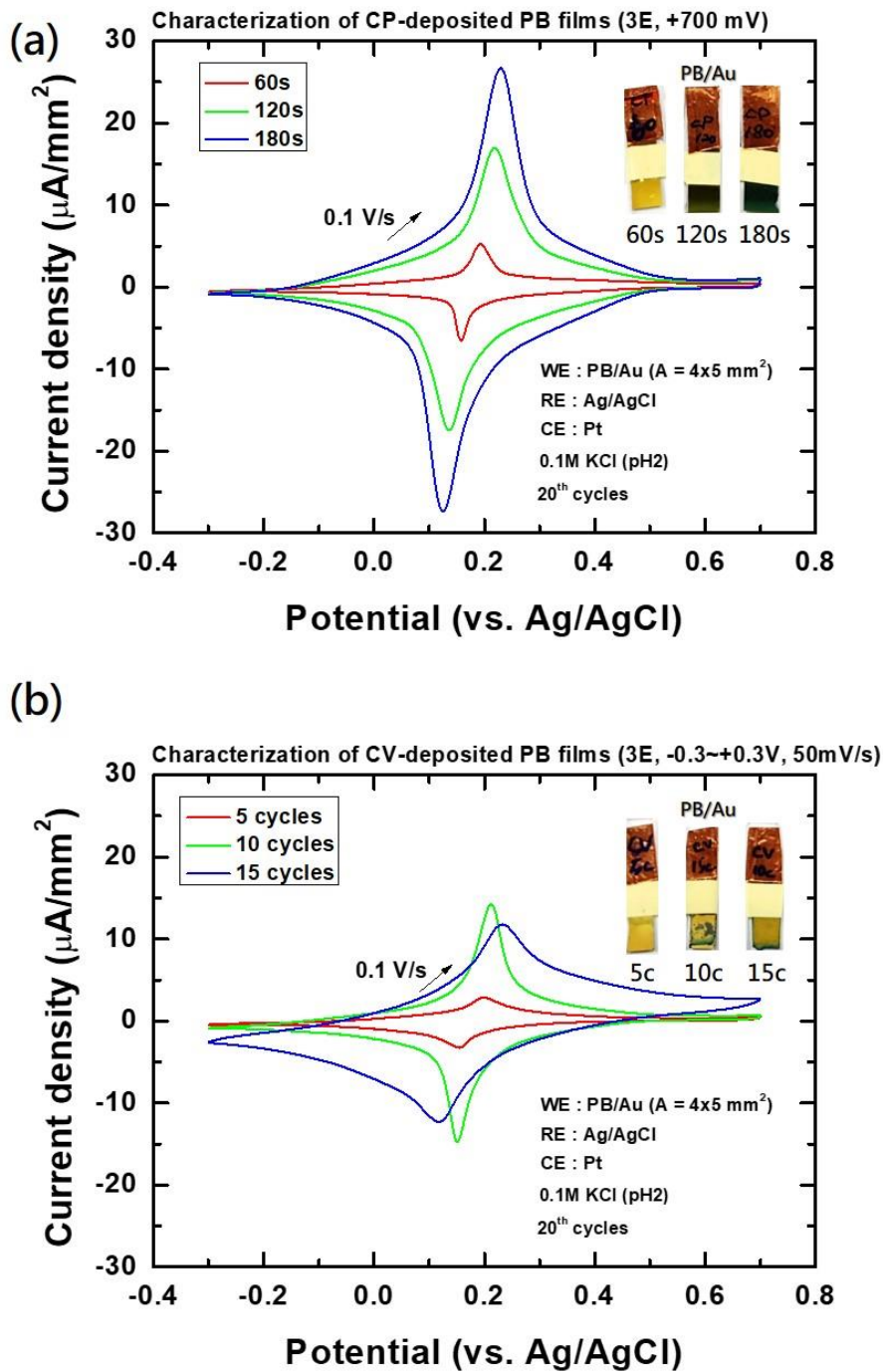
Figure 5.5 The CV characteristics of the PB films electrodeposited on the gold electrodes

by (a) the constant potential and (b) the cyclic voltammetry under different conditions.
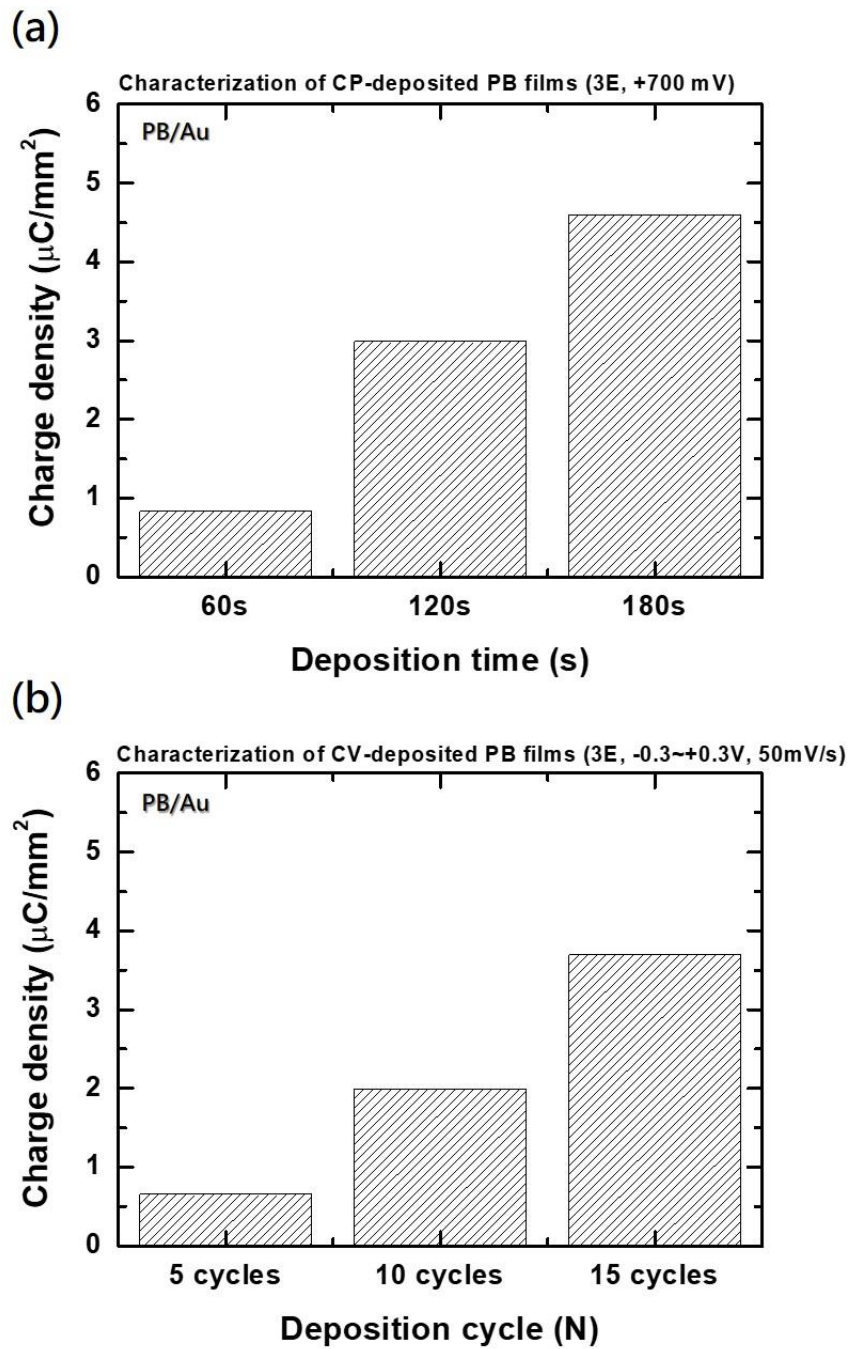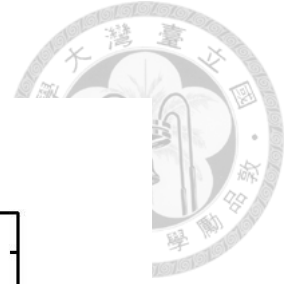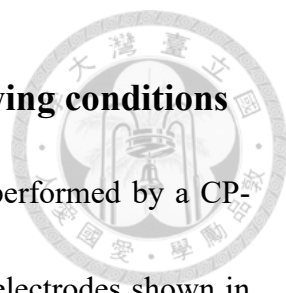
Figure 5.6 The charge densities of the PB films electrodeposited on the gold electrodes

by (a) the constant potential and (b) the cyclic voltammetry under different conditions.

222

5.4.2 Enhanced electrodeposition of PB film under flowing conditions

To study the in-channel reaction, the PB electrodeposition is performed by a CP-based method in microfluidic chips embedded the symmetric gold electrodes shown in Fig. 5.7(a). However, different from the three-electrode system demonstrated in the above experiments, the symmetric electrodes have a two-electrode configuration which needs to connect the reference electrode and counter electrode together. Without the aid of the Ag/AgCl reference, the voltage applied for PB electrodeposition should be re-calibrated to obtain the suitable parameters. A SER-based symmetric microelectrode is used to carry out the electrochemical reactions, and it's assembled with a PDMS microchannel via the O_2 plasma bonding. Loading the plating solution with static and flowing conditions, the performances of electrodeposition are compared to verify the assumption of flowing-induced enhancement.

In the static condition (shown in Fig. 5.7(a)), the plating solution is injected into the microchannel, and different voltages are applied to the electrodes. To fill the whole chip, at least 15 μl solution is needed. Observing the film images shown in Fig. 5.8(a), the PB films are uneven when the applied voltage increases to +0.3V, and the more serious film damage happens in the conditions of higher applied voltages. It may result from a too fast reaction rate due to the large potential drop between two electrodes. In spite of the dark blue color of PB films during the electrodeposition process, the films wash away as the

223

solution is discharged. The tendency observed from the images is also confirmed by the

chronoamperometry profiles during the electrodeposition process shown in Fig. 5.8(a).

The steady-state currents increase along with the applied voltages, and a saturated current

(40 μA) occurs as the voltage is +0.3 V. When the PB film forms on the electrode, the

substances in the diffusion layer around the surface are gradually consumed. The limited

concentration and low driving energy lead to a slow reaction rate, and this situation causes

the formation of thin PB films (shown in Fig. 5.9(a)). When the voltages rise to +0.5 V,

the deformed profiles imply the unexpected reaction. Instead of the steady-state signal, a

decreasing current is observed because the reduced concentration of plating solution in

the diffusion layer limits the reaction. Although the large driving energy provides a fast

reaction rate and forms thick PB films, the too fast film generation causes a weak structure

which is easy to be removed through a liquid flowing (shown in Fig. 5.9(a)).

In comparison, the plating solution is loaded into the microfluidic, and then a

continuous flow is executed to rapidly refresh the components around the electrode

surface that may also take away the waste of electrodeposition (shown in Fig. 5.7(b)).

According to the film images shown in Fig. 5.8(b), the flowing-deposited PB films have

more uniform surfaces but the films also break when the +0.7 V is applied to the electrode.

Compared to the static condition, the limited steady-state current is also observed as a

+0.3 V is applied under a flowing condition, and the current (c.a. 60 μA) is even higher

than the current response under the static condition (40 µA). The current enhancement

results from the flowing-induced surface refreshment which continuously removes the

diffusion layer and renews substances to eliminate the reaction limitation (shown in Fig.

5.9(b)). Interestingly, when the higher voltages are applied (+0.4~+0.6 V), the

chronoamperometry profiles still have the steady-state current (50 µA) shown in Fig.

5.8(b). Even though the high voltage leads to thick films with weak structures, the

shearing force in the flowing liquid can wash the fragile parts to selectively remain the

stable films. Further, the vacancy can provide a new space for re-electrodeposition of PB

films, and it can not only smooth the film surface but also carry on the growth of films

(shown in Fig. 5.9(b)). The oscillated curve of chronoamperometry obtained by applying

+0.7 V causes a fragile PB film, which is damaged easily under the flowing liquid

operation. It may be attributed to that the flow rate is not rapid enough to refresh the

diffusion layer in time. According to the limitation of the flowing effect for in-channel

electrodeposition, the kinetics of the reaction can be analyzed to optimize the parameters

of film production.

225
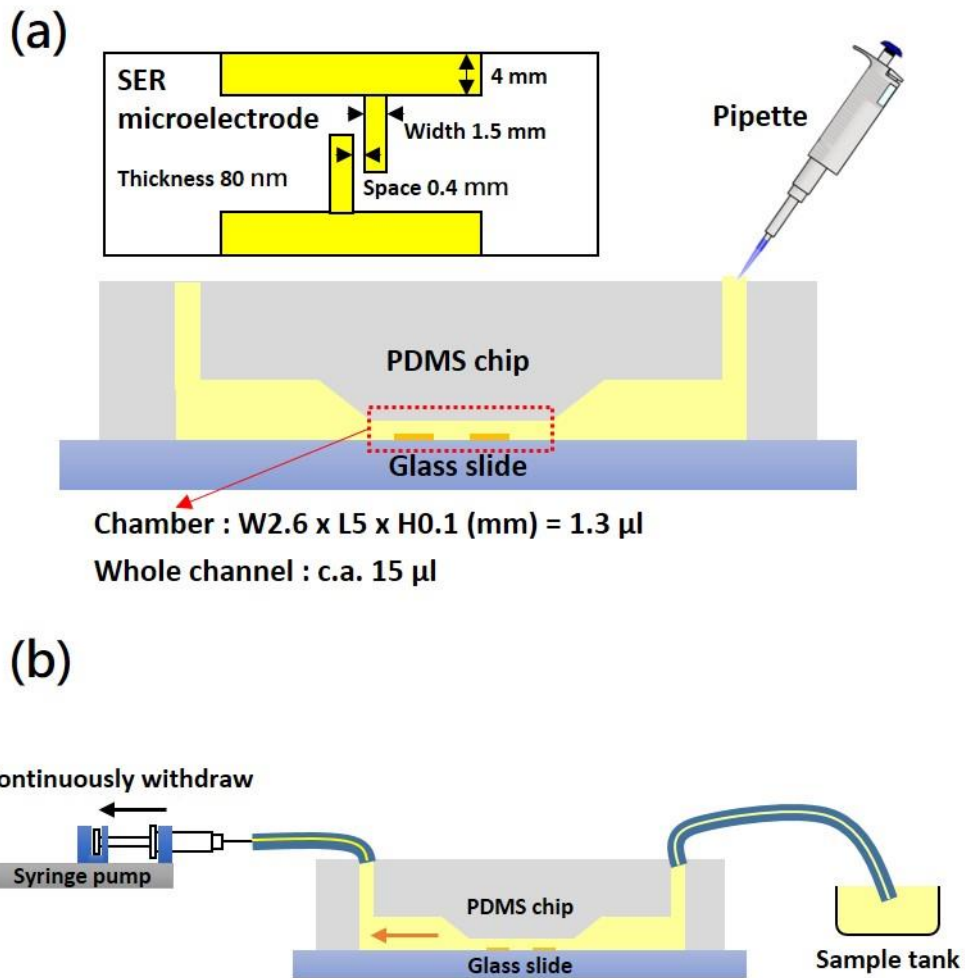
Figure 5.7 The in-channel electrodeposition of Prussian blue under (a) the static and (b)

the flowing conditions. The microelectrodes with the SER configuration are used to carry

out the electrochemical reaction after the plating solution is loaded into the microchannel.

A syringe pump is used to continuously withdraw the plating solution under a fixed flow

rate to provide a flowing condition for electrodeposition.
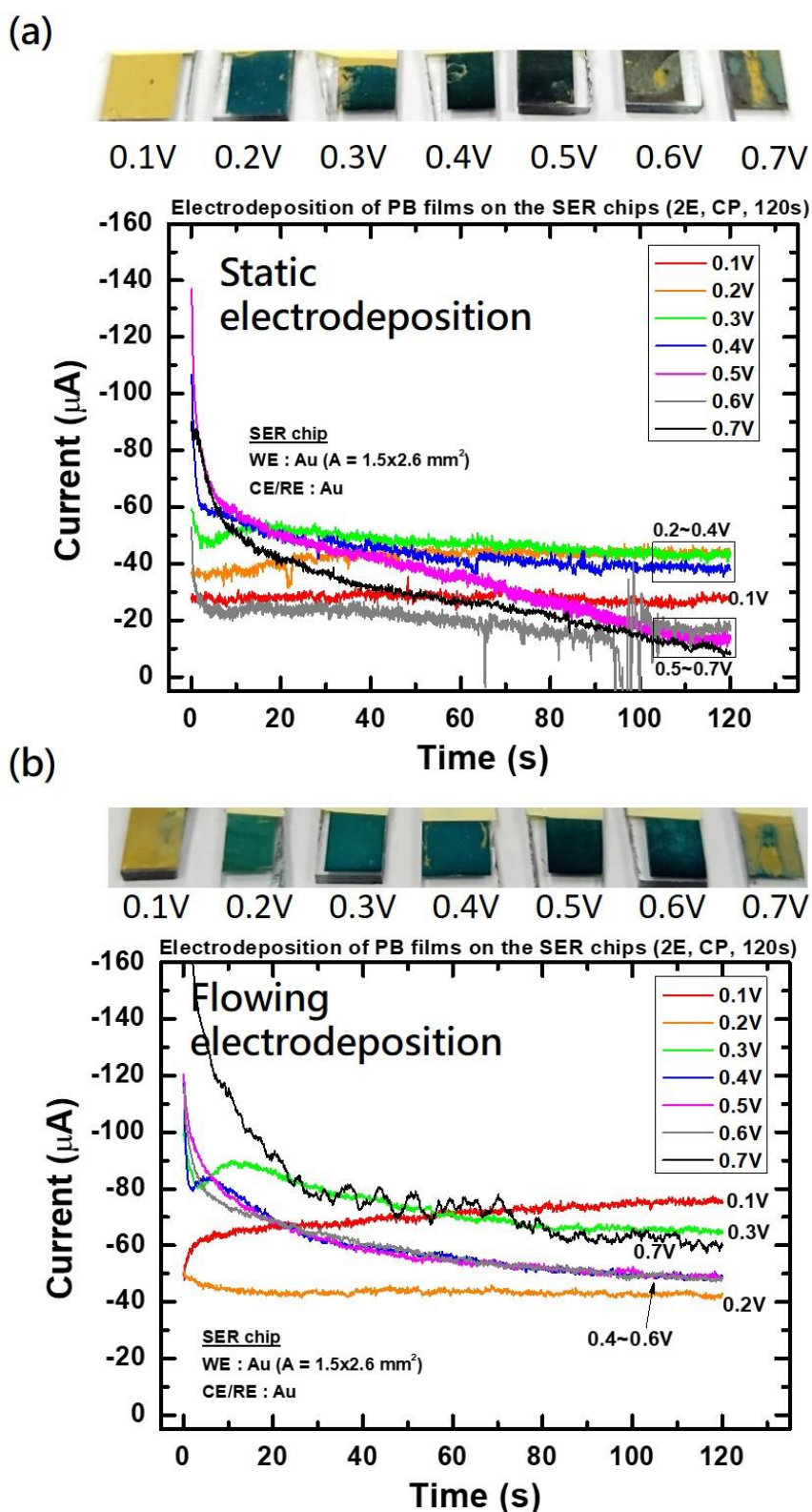
Figure 5.8 PB electrodeposition by the CP-based methods with different conditions under

(a) static and (b) flowing modes.

227
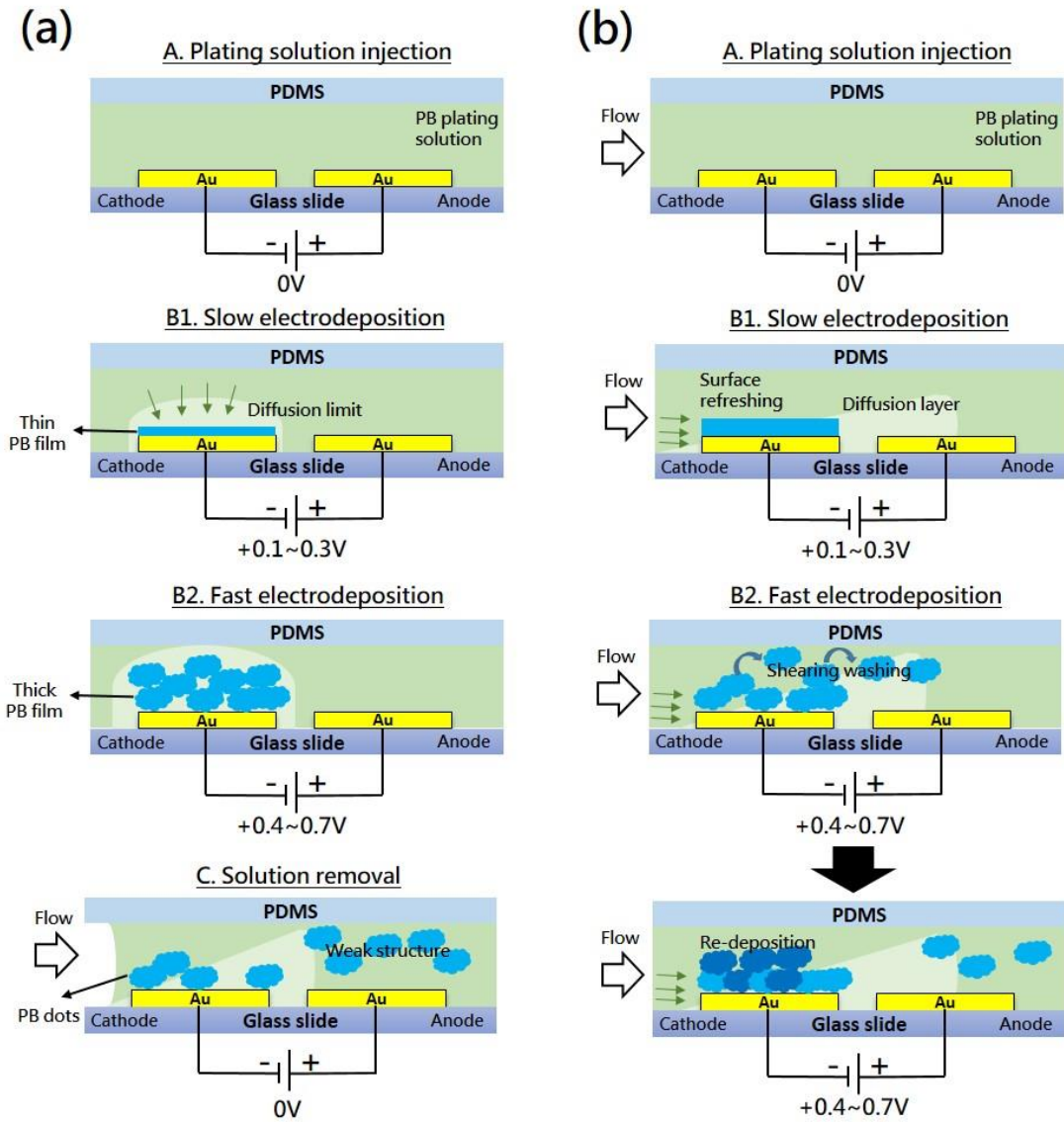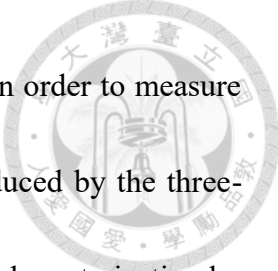
Figure 5.9 The concepts of in-channel PB electrodeposition under (a) static and (b) flowing conditions. The small voltages lead to slow electrodeposition, and large voltages lead to the fast electrodeposition.

The deposited PB films are characterized through CV analysis in order to measure the stability and charge density. To compare with the PB films produced by the three-electrode system, the in-channel PB films are cut to slice for the CV characterization by the three-electrode system. In the static-deposited PB films shown in Fig. 5.10(a), no obvious tendency of current peaks can be recognized, and the best PB film which has a large current peak and a small peak separation shown in Fig. 5.10(b) and (c) is produced by applying +0.2 V. The increasing peak separations shown in Fig. 5.10(c) result from the high charge resistance of thick PB films, and the signal drop at 0.7V may be attributed to the exposure of bare gold.

In comparison, the flowing-deposited PB films show growing current peaks along with applied voltages, and it reaches saturation at the +0.3V condition (shown in Fig. 5.11(b)). The peak separations also gradually increase which implies the increasing resistance of charge transfer on the PB-deposited electrodes (shown in Fig. 5.11(c)). To quantitate the performance of the PB films, the charge density is chosen to be an indicator for indicating the thickness of films and the efficiency of electrodeposition. The charge densities of PB films can be calculated by integrating the CV curves. In Fig. 5.12, most flowing-deposited PB films have higher charge densities than the static-deposited PB films, and it proves our assumption of flow-induced electrodeposition enhancement in the microfluidics.
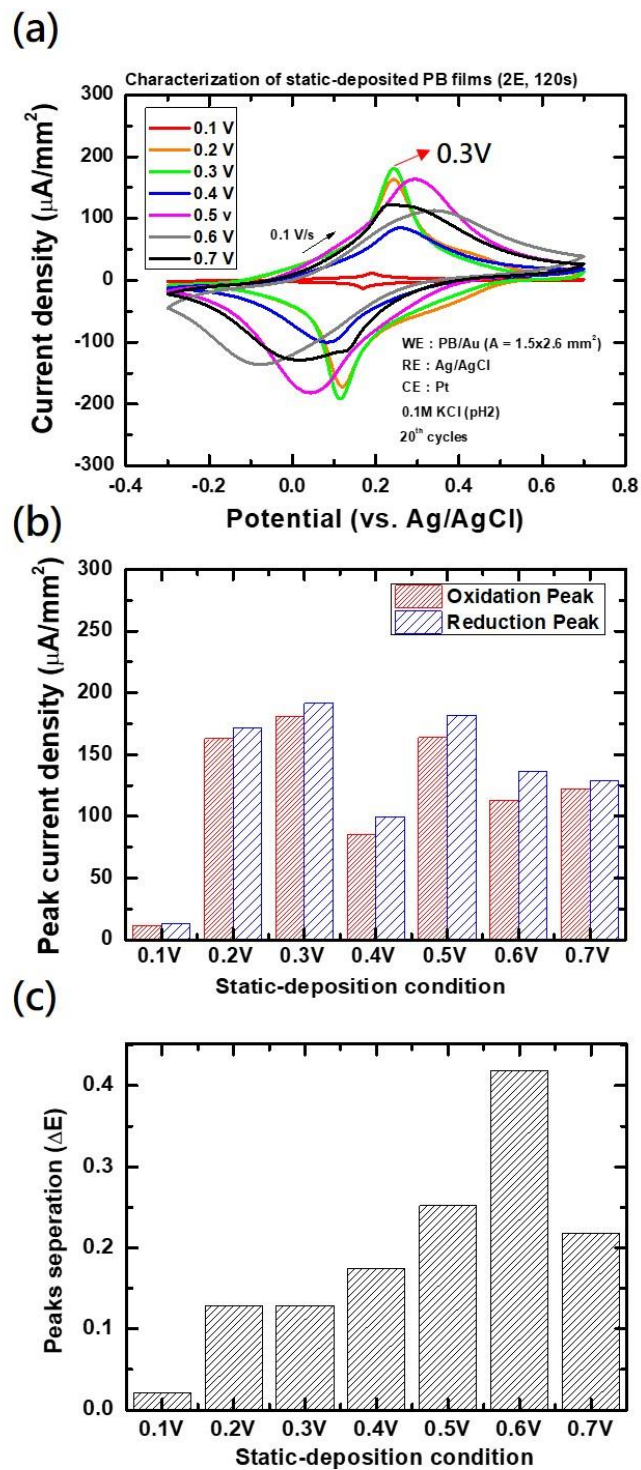
Figure 5.10 Under static modes, (a) The CV characteristics of the PB films electrodeposited on gold microelectrodes that can determine the (b) peak current and (b) peak separation.
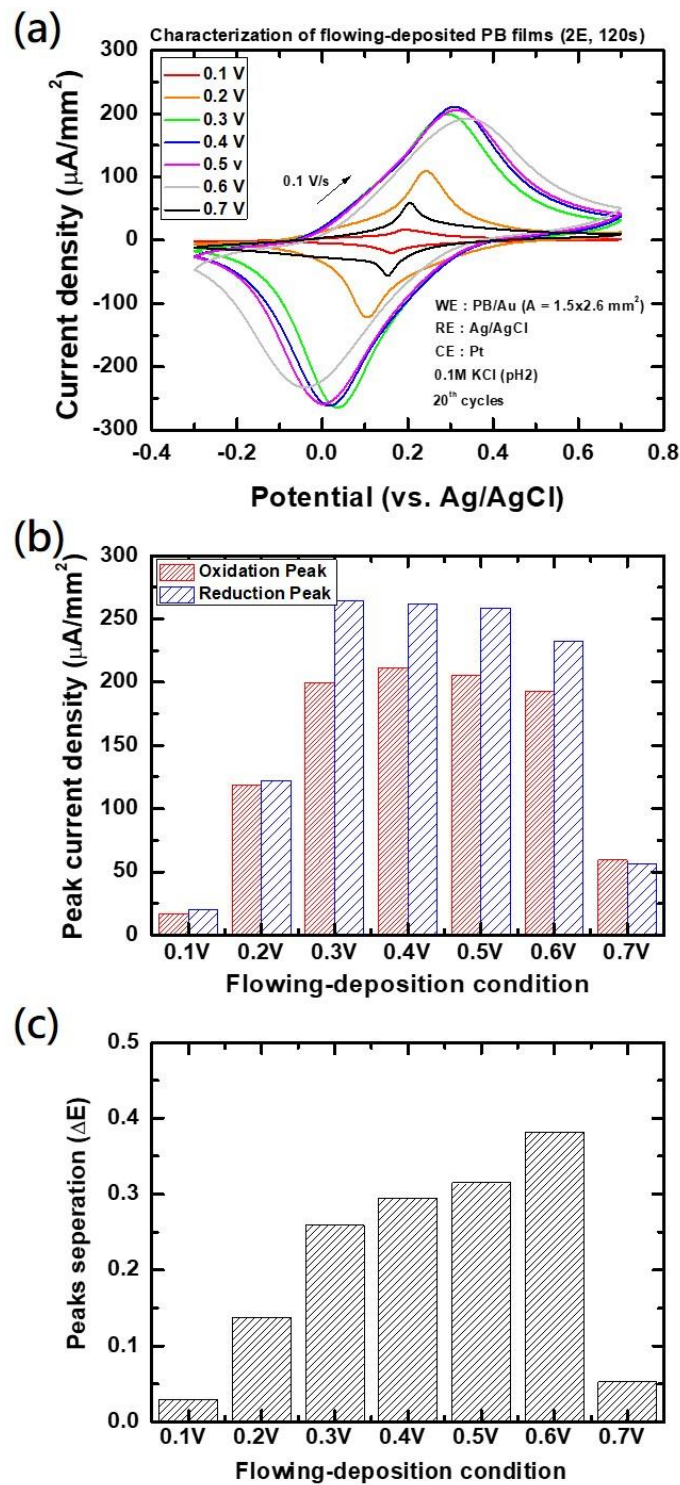
Figure 5.11 Under flowing modes, (a) The CV characteristics of the PB films electrodeposited on gold microelectrodes that can determine the (b) peak current and (b) peak separation.
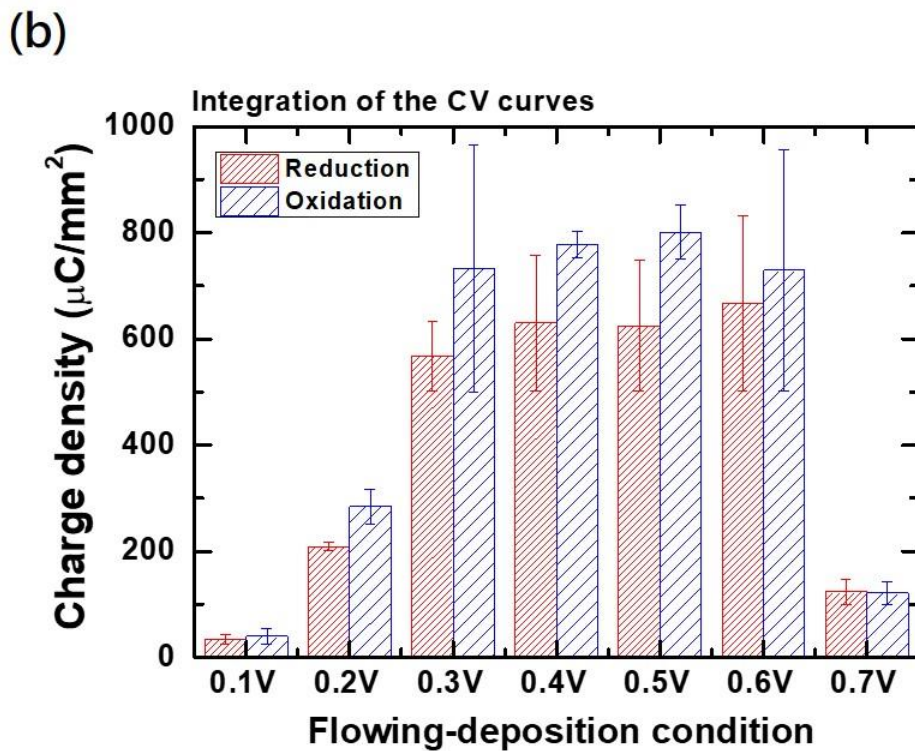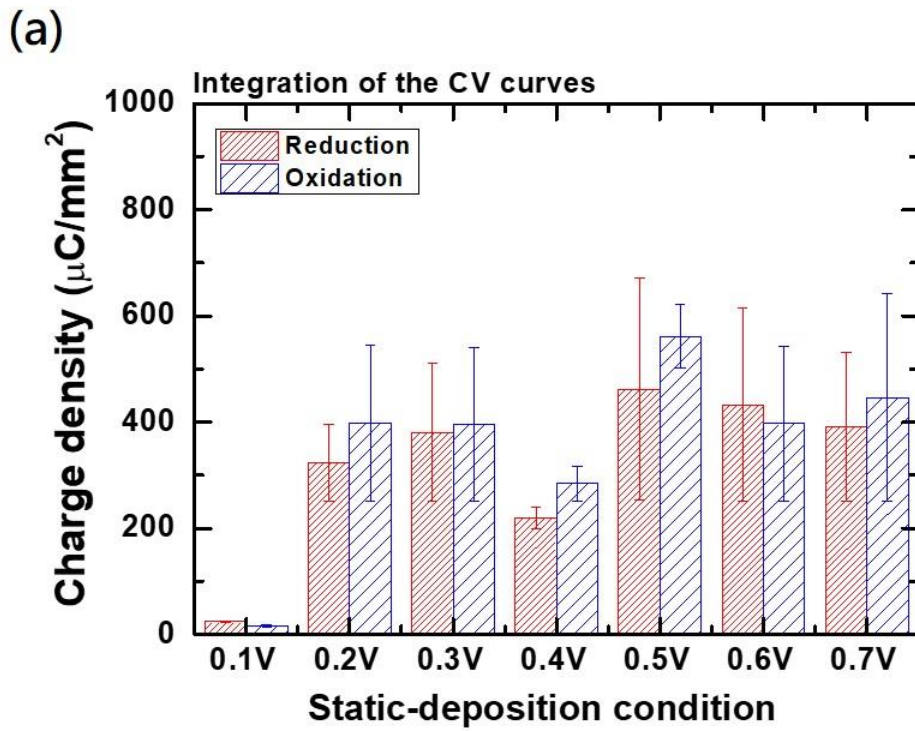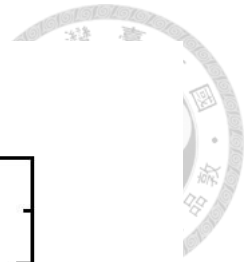
Figure 5.12 The charge densities of the PB films deposited by different voltages under (a)

static and (b) flowing modes. The charge densities are calculated by integrating the CV

curves.

232

5.4.3 Chapter summary

In this chapter, we demonstrate the Prussian blue electrodeposition under static and flowing modes in a microfluidic chip with the symmetric gold electrode. An enhanced electrodeposition observed in the flowing-deposited PB films is attributed to the surface refreshment via continuous liquid transportation. As the PB molecules generate on the surface, the concentration of ferricyanide salt reduces around the electrode surface forming a depletion zone that slows down the reaction rate. In the static condition, the fresh ferricyanide salt in bulk solution supplements to electrode surface through molecule diffusion, however, it costs a long time due to the poor mass transfer in laminar flow. With the facilitated mass transfer caused by liquid flow, the refreshed surface can enhance the electrodeposition efficiency. Furthermore, the laminar flow provides the shearing force on the outer of the liquid stream, so it can remove the weak films produced by improper deposition conditions. Only the stable film structure can be retained on the electrodes. With the flowing electrodeposition strategy, the PB films can be successfully formed on the microelectrodes, and the films show the higher charge density and stability. It provides the flowing-deposited PB film a great potential for developing the label-free biosensors.
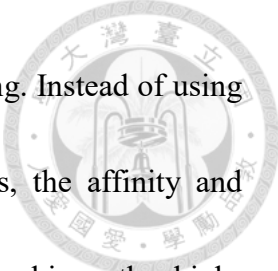
Chapter 6. Conclusions

Combining the features of shuttle mixing, shearing effect, and surface refreshment, the microfluidic platform evolves the improved techniques involving aptamer selection, electrochemical sensing, and electrodeposition. The platform reported in this study is a versatile tool proven by a series of proof-of-principle experiments. The shuttle mixing effect is preliminarily discovered by the Prussian blue reaction in a PMMA-based fluidic device. To further monitor the response in the flowing solution, the electrochemistry is introduced to provide a rapid and sensitive sensing strategy for real-time detection. The dynamic information obtained from flowing amperometry shows unique current responses and micro-mixing effect. The phenomenon can also be seen in the miniaturized device which integrated a PDMS microchannel and a microelectrode chip. Three-electrode and two-electrode systems are compared with different pattern configurations, and the two-electrode system can supply a simple amperometric analysis under flowing conditions
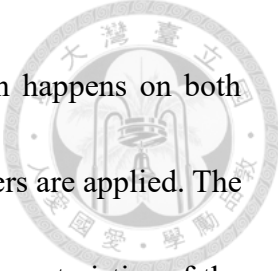
Microbeads-array microfluidic device is established for STAT3-specific aptamer selection. Combining the advantages of single-bead SELEX and the microfluidic characteristics, this device successfully identifies the STAT3-specific aptamers after several SELEX rounds. The microbeads array performs not only multiplex reactors, but also the obstacles for disturbing the laminar flow. The shuttle flow provides an efficient

234

selection condition consisted of repeated interaction and strict washing. Instead of using the traditional ELONA, which needs extra biotin-labeled aptamers, the affinity and specificity can be verified by an immuno-qPCR assay that can achieve the high-throughput aptamer validation. Moreover, the STAT3-specific aptamers are used as an inhibitor which regulates the gene expression in cancer cells. After the aptamer drugs are transfected into the cells by lipofectamine, the aptamer-bound STAT3 proteins are blocked from binding the promoter gene which leads to the apoptosis in cancer cells.

Microfluidic amperometry is adapted to study the electrochemical response under flowing conditions. SER, PAR and IDA configurations of microelectrode show various two-electrode electrochemical characterizations. The flow polarization found in the CV scan causes the asymmetric distribution of redox mediators on microelectrode surfaces. The facilitated mass transfer attributed to proactive liquid transportation leads to the micro-mixing effect. Eliminating the diffusion limit in microfluidic, the amperometric signal can be enhanced to get a better sensitivity of redox mediators like ferricyanide, which is a well-known molecule for label-free biosensing applications.

The enhanced electrodeposition of Prussian blue on the gold microelectrodes is demonstrated through a series of comparative experiments. According to the features of the gold electrode integrated into a microfluidic chip, the high conductivity and the short diffusion length lead to a fast electrodeposition rate but have non-robust film structures.
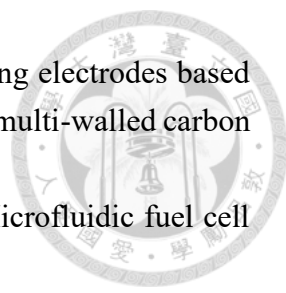
Especially, in the two-electrode system, a symmetric redox reaction happens on both electrodes so the gold electrode will be damaged if improper parameters are applied. The optimal deposition voltage is found according to compare the CV characteristics of the PB films. Too fast reaction rate induced by high applied voltage can result in an unstable film formation that is easily damaged through a flowing liquid. Interestingly, when continuous flow is applied during the electrodeposition process, the performance of PB films can be enhanced that is verified by measuring the charge densities. In addition, the flowing solution can not only provide a continuously refreshed solution on the electrode surface but also remove the unstable PB particles via the shearing force to obtain a uniform and stable film.
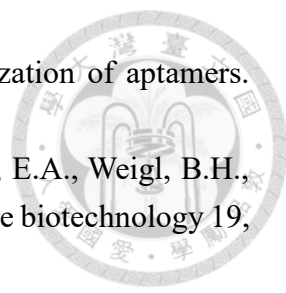
With the establishment of microfluidic devices for various applications involving the aptamer SELEX, electrochemical sensing, and electrodeposition, the concepts of flow effect in the microfluidic chips are verified. To wisely use the characteristics of microfluidic behaviors, the different liquid operation strategies are applied to produce the shuttle (droplet control) and one-way (continuous flow) conditions for achieving effects of the micro-mixing, surface refreshment, and shearing effect. The developed platforms basically improve the current techniques which have a great potential to develop a label-free electrochemical aptasensor for the highly sensitive disease diagnosis.

236

Reference
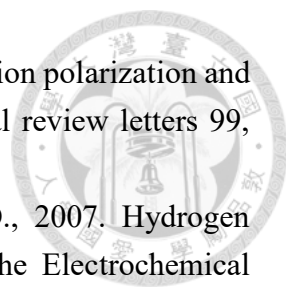
Abolhasani, M., Jensen, K.F., 2016. Oscillatory multiphase flow strategy for chemistry and biology. Lab Chip 16, 2775-2784.

Al Khatib, M., Bellini, M., Pogni, R., Giaccherini, A., Innocenti, M., Vizza, F., Lavacchi, A., 2018. Effect of Electrode Shape and Flow Conditions on the Electrochemical Detection with Band Microelectrodes. Sensors 18, 3196.

Ali, M.A., Jiang, H., Mahal, N.K., Weber, R.J., Kumar, R., Castellano, M.J., Dong, L., 2017. Microfluidic impedimetric sensor for soil nitrate detection using graphene oxide and conductive nanofibers enabled sensing interface. Sensors and Actuators B: Chemical 239, 1289-1299.

Amatore, C., Da Mota, N., Sella, C., Thouin, L., 2008. General concept of high-performance amperometric detector for microfluidic (bio) analytical chips. Analytical chemistry 80, 4976-4985.

Anderson, R.C., Bogdan, G.J., Puski, A., Su, X., 1998. Advances in integrated genetic analysis. Micro Total Analysis Systems' 98. Springer, pp. 11-16.

Arakawa, T., Shirasaki, Y., Aoki, T., Funatsu, T., Shoji, S., 2007. Three-dimensional sheath flow sorting microsystem using thermosensitive hydrogel. Sensors and Actuators A: Physical 135, 99-105.

Banerjee, K., Resat, H., 2016. Constitutive activation of STAT 3 in breast cancer cells: A review. International journal of cancer 138, 2570-2578.

Ben-Yoav, H., Dykstra, P.H., Bentley, W.E., Ghodssi, R., 2015. A controlled microfluidic electrochemical lab-on-a-chip for label-free diffusion-restricted DNA hybridization analysis. Biosensors and Bioelectronics 64, 579-585.

Bäcker, M., Rakowski, D., Poghossian, A., Biselli, M., Wagner, P., Schöning, M.J., 2013. Chip-based amperometric enzyme sensor system for monitoring of bioprocesses by flow-injection analysis. Journal of biotechnology 163, 371-376.

Bong, K.W., Bong, K.T., Pregibon, D.C., Doyle, P.S., 2010. Hydrodynamic focusing lithography. Angewandte Chemie International Edition 49, 87-90.

Brevig, T., Krühne, U., Kahn, R.A., Ahl, T., Beyer, M., Pedersen, L.H., 2003. Hydrodynamic guiding for addressing subsets of immobilized cells and molecules in microfluidic systems. BMC biotechnology 3, 10.

Carpenter, N., Roberts, E., 1999. Mass transport and residence time characteristics of an oscillatory flow electrochemical reactor. Chemical Engineering Research and Design 77, 212-217.

Cheng, Y., Luo, X., Payne, G.F., Rubloff, G.W., 2012. Biofabrication: programmable assembly of polysaccharide hydrogels in microfluidics as biocompatible scaffolds. Journal of Materials Chemistry 22, 7659-7666.
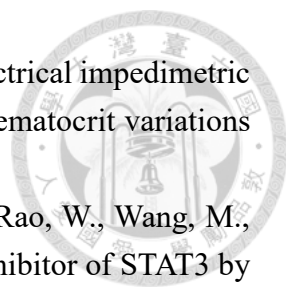
Chiu, J.-Y., Yu, C.-M., Yen, M.-J., Chen, L.-C., 2009. Glucose sensing electrodes based on a poly (3, 4-ethylenedioxythiophene)/Prussian blue bilayer and multi-walled carbon nanotubes. Biosensors and Bioelectronics 24, 2015-2020.

Choban, E.R., Markoski, L.J., Wieckowski, A., Kenis, P.J., 2004. Microfluidic fuel cell based on laminar flow. Journal of Power Sources 128, 54-60.

Comer, J., 1956. Semiquantitative specific test paper for glucose in urine. Analytical Chemistry 28, 1748-1750.

Cox, J.C., Ellington, A.D., 2001. Automated selection of anti-protein aptamers. Bioorganic & medicinal chemistry 9, 2525-2531.

Daniel, D., Gutz, I.G.R., 2003. Quick production of gold electrode sets or arrays and of microfluidic flow cells based on heat transfer of laser printed toner masks onto compact discs. Electrochemistry communications 5, 782-786.

Dennison, C., Beidaghi, M., Hatzell, K., Campos, J., Gogotsi, Y., Kumbur, E., 2014. Effects of flow cell design on charge percolation and storage in the carbon slurry electrodes of electrochemical flow capacitors. Journal of Power Sources 247, 489-496.

Du, D., Wang, M., Qin, Y., Lin, Y., 2010a. One-step electrochemical deposition of Prussian Blue–multiwalled carbon nanotube nanocomposite thin-film: preparation, characterization and evaluation for H_2O_2 sensing. Journal of Materials Chemistry 20, 1532-1537.

Du, J., Wang, Y., Zhou, X., Xue, Z., Liu, X., Sun, K., Lu, X., 2010b. Improved sensing in physiological buffers by controlling the nanostructure of Prussian blue films. The Journal of Physical Chemistry C 114, 14786-14793.

Elbuken, C., Glawdel, T., Chan, D., Ren, C.L., 2011. Detection of microdroplet size and speed using capacitive sensors. Sensors and Actuators A: Physical 171, 55-62.

Ellington, A.D., Szostak, J.W., 1990. In vitro selection of RNA molecules that bind specific ligands. nature 346, 818.

Esquivel, J., Del Campo, F., De La Fuente, J.G., Rojas, S., Sabate, N., 2014. Microfluidic fuel cells on paper: meeting the power needs of next generation lateral flow devices. Energy & Environmental Science 7, 1744-1749.

Fang, T.H., Ramalingam, N., Xian-Dui, D., Ngin, T.S., Xianting, Z., Kuan, A.T.L., Huat, E.Y.P., Hai-Qing, G., 2009. Real-time PCR microfluidic devices with concurrent electrochemical detection. Biosensors and Bioelectronics 24, 2131-2136.

Filali, L., Brahmi, Y., Sib, J.D., Bouizem, Y., Benlakehal, D., Zellama, K., Lemée, N., Bouhekka, A., Kail, F., Kebab, A., 2019. Local Surface Electric Field's Effect on Adsorbed Proteins' Orientation. Surfaces 2, 415-431.

Frey, O., Bonneick, S., Hierlemann, A., Lichtenberg, J., 2007. Autonomous microfluidic multi-channel chip for real-time PCR with integrated liquid handling. Biomedical microdevices 9, 711-718.
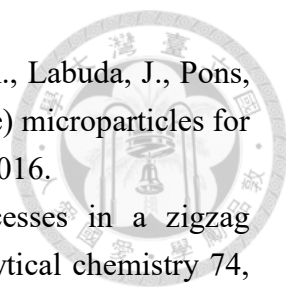
Gao, S., Zheng, X., Jiao, B., Wang, L., 2016. Post-SELEX optimization of aptamers. Analytical and bioanalytical chemistry 408, 4567-4573.

Hatch, A., Kamholz, A.E., Hawkins, K.R., Munson, M.S., Schilling, E.A., Weigl, B.H., Yager, P., 2001. A rapid diffusion immunoassay in a T-sensor. Nature biotechnology 19, 461.

Hindson, B.J., Ness, K.D., Masquelier, D.A., Belgrader, P., Heredia, N.J., Makarewicz, A.J., Bright, I.J., Lucero, M.Y., Hiddessen, A.L., Legler, T.C., 2011. High-throughput droplet digital PCR system for absolute quantitation of DNA copy number. Analytical chemistry 83, 8604-8610.

Ho, W., Lim, K., Yang, K.-L., 2016. In situ formation of leak-free polyethylene glycol (PEG) membranes in microfluidic fuel cells. Lab Chip 16, 4725-4731.

Horny, M.-C., Lazerges, M., Siaugue, J.-M., Pallandre, A., Rose, D., Bedioui, F., Deslouis, C., Haghiri-Gosnet, A.-M., Gamby, J., 2016. Electrochemical DNA biosensors based on long-range electron transfer: investigating the efficiency of a fluidic channel microelectrode compared to an ultramicroelectrode in a two-electrode setup. Lab Chip 16, 4373-4381.

Hosokawa, K., Fujii, T., Endo, I., 1999. Handling of picoliter liquid samples in a poly (dimethylsiloxane)-based microfluidic device. Analytical chemistry 71, 4781-4785.

Huang, C.-J., Lin, H.-I., Shiesh, S.-C., Lee, G.-B., 2010a. Integrated microfluidic system for rapid screening of CRP aptamers utilizing systematic evolution of ligands by exponential enrichment (SELEX). Biosensors and bioelectronics 25, 1761-1766.

Huang, C.-J., Lin, H.-I., Shiesh, S.-C., Lee, G.-B., 2012. An integrated microfluidic system for rapid screening of alpha-fetoprotein-specific aptamers. Biosensors and Bioelectronics 35, 50-55.

Huang, M.C., Ye, H., Kuan, Y.K., Li, M.-H., Ying, J.Y., 2009. Integrated two-step gene synthesis in a microfluidic device. Lab Chip 9, 276-285.

Huang, S., Li, C., Lin, B., Qin, J., 2010b. Microvalve and micropump controlled shuttle flow microfluidic device for rapid DNA hybridization. Lab Chip 10, 2925-2931.

Huang, W., Dong, Z., Wang, F., Peng, H., Liu, J.-Y., Zhang, J.-T., 2014. A small molecule compound targeting STAT3 DNA-binding domain inhibits cancer cell proliferation, migration, and invasion. ACS chemical biology 9, 1188-1196.

Hung, L.-Y., Wang, C.-H., Hsu, K.-F., Chou, C.-Y., Lee, G.-B., 2014. An on-chip Cell-SELEX process for automatic selection of high-affinity aptamers specific to different histologically classified ovarian cancer cells. Lab Chip 14, 4017-4028.

Hybarger, G., Bynum, J., Williams, R.F., Valdes, J.J., Chambers, J.P., 2006. A microfluidic SELEX prototype. Analytical and bioanalytical chemistry 384, 191-198.

Iles, A., Habgood, M., de Mello, A.J., Wootton, R.C., 2007. A Simple technique for microfluidic heterogeneous catalytic hydrogenation reactor fabrication. Catalysis

letters 114, 71-74.

Itaya, K., Shibayama, K., Akahoshi, H., Toshima, S., 1982. Prussian-blue-modified electrodes: An application for a stable electrochromic display device. Journal of Applied Physics 53, 804-805.

Jacobs, M., Nagaraj, V.J., Mertz, T., Selvam, A.P., Ngo, T., Prasad, S., 2013. An electrochemical sensor for the detection of antibiotic contaminants in water. Analytical Methods 5, 4325-4329.

Jayashree, R.S., Gancs, L., Choban, E.R., Primak, A., Natarajan, D., Markoski, L.J., Kenis, P.J., 2005. Air-breathing laminar flow-based microfluidic fuel cell. Journal of the American Chemical Society 127, 16758-16759.

Jin, S., Ye, Z., Wang, Y., Ying, Y., 2017. A novel impedimetric microfluidic analysis system for transgenic protein Cry1Ab detection. Scientific reports 7, 43175.

Jolma, A., Kivioja, T., Toivonen, J., Cheng, L., Wei, G., Enge, M., Taipale, M., Vaquerizas, J.M., Yan, J., Sillanpää, M.J., 2010. Multiplexed massively parallel SELEX for characterization of human transcription factor binding specificities. Genome research 20, 861-873.

Kamholz, A.E., Weigl, B.H., Finlayson, B.A., Yager, P., 1999. Quantitative analysis of molecular interaction in a microfluidic channel: the T-sensor. Analytical chemistry 71, 5340-5347.

Kamholz, A.E., Yager, P., 2001. Theoretical analysis of molecular diffusion in pressure-driven laminar flow in microfluidic channels. Biophysical journal 80, 155-160.

Karyakin, A.A., Karyakina, E.E., Gorton, L., 1998. The electrocatalytic activity of Prussian blue in hydrogen peroxide reduction studied using a wall-jet electrode with continuous flow. Journal of Electroanalytical Chemistry 456, 97-104.

Kenis, P.J., Ismagilov, R.F., Whitesides, G.M., 1999. Microfabrication inside capillaries using multiphase laminar flow patterning. Science 285, 83-85.

Kidner, N., Meier, A., Homrighaus, Z., Wessels, B.W., Mason, T.O., Garboczi, E., 2007. Complex electrical (impedance/dielectric) properties of electroceramic thin films by impedance spectroscopy with interdigital electrodes. Thin Solid Films 515, 4588-4595.

Kim, D., Lee, I.-H., Kim, S., Choi, M., Kim, H., Ahn, S., Saw, P.E., Jeon, H., Lee, Y., Jon, S., 2014. A specific STAT3-binding peptide exerts antiproliferative effects and antitumor activity by inhibiting STAT3 phosphorylation and signaling. Cancer research 74, 2144-2151.

Kim, D.S., Lee, S.W., Kwon, T.H., Lee, S.S., 2004. A barrier embedded chaotic micromixer. Journal of micromechanics and microengineering 14, 798.

Kim, H.W., Lim, J., Rhie, J.W., Kim, D.S., 2017. Investigation of effective shear stress on endothelial differentiation of human adipose-derived stem cells with microfluidic screening device. Microelectronic Engineering 174, 24-27.
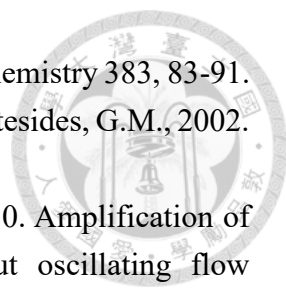
Kim, S.J., Wang, Y.-C., Lee, J.H., Jang, H., Han, J., 2007. Concentration polarization and nonlinear electrokinetic flow near a nanofluidic channel. Physical review letters 99, 044501.

Kjeang, E., Brolo, A.G., Harrington, D.A., Djilali, N., Sinton, D., 2007. Hydrogen peroxide as an oxidant for microfluidic fuel cells. Journal of the Electrochemical Society 154, B1220-B1226.

Knight, J.B., Vishwanath, A., Brody, J.P., Austin, R.H., 1998. Hydrodynamic focusing on a silicon chip: mixing nanoliters in microseconds. Physical review letters 80, 3863.

Ko, E., Tran, V.-K., Geng, Y., Chung, W.S., Park, C.H., Kim, M.K., Jin, G.H., Seong, G.H., 2017. Continuous electrochemical detection of hydrogen peroxide by Au-Ag bimetallic nanoparticles in microfluidic devices. Journal of Electroanalytical Chemistry 792, 72-78.

Kobayashi, H., Komanoya, T., Hara, K., Fukuoka, A., 2010. Water-tolerant mesoporous-carbon-supported ruthenium catalysts for the hydrolysis of cellulose to glucose. ChemSusChem: Chemistry & Sustainability Energy & Materials 3, 440-443.

Kohlheyer, D., Unnikrishnan, S., Besselink, G.A., Schlautmann, S., Schasfoort, R.B., 2008. A microfluidic device for array patterning by perpendicular electrokinetic focusing. Microfluidics and nanofluidics 4, 557-564.

Kopp, M.U., De Mello, A.J., Manz, A., 1998. Chemical amplification: continuous-flow PCR on a chip. Science 280, 1046-1048.

Kozicki, M., Maroufkhani, P., Mitkova, M., 2005. Valving in microchannels via electrodeposition on solid electrolytes. Technical Proceedings of the 2005 NSTI Nanotechnology Conference, pp. 716-719.

Krishnan, V., Xidis, A.L., Neff, V., 1990. Prussian blue solid-state films and membranes as potassium ion-selective electrodes. Analytica chimica acta 239, 7-12.

Kwakye, S., Goral, V.N., Baeumner, A.J., 2006. Electrochemical microfluidic biosensor for nucleic acid detection with integrated minipotentiostat. Biosensors and Bioelectronics 21, 2217-2223.

Latulippe, D.R., Szeto, K., Ozer, A., Duarte, F.M., Kelly, C.V., Pagano, J.M., White, B.S., Shalloway, D., Lis, J.T., Craighead, H.G., 2013. Multiplexed microcolumn-based process for efficient selection of RNA aptamers. Analytical chemistry 85, 3417-3424.

Lee, C.-Y., Chang, C.-L., Wang, Y.-N., Fu, L.-M., 2011. Microfluidic mixing: a review. International journal of molecular sciences 12, 3263-3287.

Lee, G., Lee, J., Kim, J., Choi, H.S., Kim, J., Lee, S., Lee, H., 2017. Single microfluidic electrochemical sensor system for simultaneous multi-pulmonary hypertension biomarker analyses. Scientific reports 7, 7545.

Lee, S., Kang, J., Ren, S., Laurell, T., Kim, S., Jeong, O.C., 2013. A cross-contamination-free SELEX platform for a multi-target selection strategy. Biochip Journal 7, 38-45.

241

Lei, K.F., Chen, K.-H., Tsui, P.-H., Tsang, N.-M., 2013. Real-time electrical impedimetric monitoring of blood coagulation process under temperature and hematocrit variations conducted in a microfluidic chip. PLoS One 8, e76243.
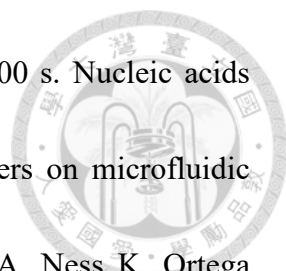
Leung, K.-H., Liu, L.-J., Lin, S., Lu, L., Zhong, H.-J., Susanti, D., Rao, W., Wang, M., Che, W.I., Chan, D.S.-H., 2015. Discovery of a small-molecule inhibitor of STAT3 by ligand-based pharmacophore screening. Methods 71, 38-43.

Li, Y., Liang, W.-B., Fang, L.-C., Huang, H., Deng, J., Zheng, J.-S., 2009. Disposable amperometric immunosensor based on layer-by-layer electro-depositing of the nanogold particles, prussian blue-modified indium tin oxide for determination of α-fetoprotein. Journal of Chemical Sciences 121, 1069.

Liby, K., Voong, N., Williams, C.R., Risingsong, R., Royce, D.B., Honda, T., Gribble, G.W., Sporn, M.B., Letterio, J.J., 2006. The synthetic triterpenoid CDDO-Imidazolide suppresses STAT phosphorylation and induces apoptosis in myeloma and lung cancer cells. Clinical Cancer Research 12, 4288-4293.

Lin, K.-C., Kunduru, V., Bothara, M., Rege, K., Prasad, S., Ramakrishna, B., 2010. Biogenic nanoporous silica-based sensor for enhanced electrochemical detection of cardiovascular biomarkers proteins. Biosensors and Bioelectronics 25, 2336-2342.

Liu, C., Qiu, X., Ongagna, S., Chen, D., Chen, Z., Abrams, W.R., Malamud, D., Corstjens, P.L., Bau, H.H., 2009. A timer-actuated immunoassay cassette for detecting molecular markers in oral fluids. Lab Chip 9, 768-776.

Liu, Y., Shi, X.-W., Kim, E., Robinson, L., Nye, C., Ghodssi, R., Rubloff, G., Bentley, W., Payne, G., 2011. Chitosan to electroaddress biological components in lab-on-a-chip devices. Carbohydrate Polymers 84, 704-708.

Liu, Y., Wang, C., Li, F., Shen, S., Tyrrell, D.L.J., Le, X.C., Li, X.-F., 2012. DNase-mediated single-cycle selection of aptamers for proteins blotted on a membrane. Analytical chemistry 84, 7603-7606.

Lou, X., Qian, J., Xiao, Y., Viel, L., Gerdon, A.E., Lagally, E.T., Atzberger, P., Tarasow, T.M., Heeger, A.J., Soh, H.T., 2009. Micromagnetic selection of aptamers in microfluidic channels. Proceedings of the National Academy of Sciences 106, 2989-2994.

Mali, S.B., 2015. Review of STAT3 (Signal Transducers and Activators of Transcription) in head and neck cancer. Oral oncology 51, 565-569.

Marschewski, J., Jung, S., Ruch, P., Prasad, N., Mazzotti, S., Michel, B., Poulikakos, D., 2015. Mixing with herringbone-inspired microstructures: overcoming the diffusion limit in co-laminar microfluidic devices. Lab Chip 15, 1923-1933.

Mashaghi, S., Abbaspourrad, A., Weitz, D.A., van Oijen, A.M., 2016. Droplet microfluidics: A tool for biology, chemistry and nanotechnology. TrAC Trends in Analytical Chemistry 82, 118-125.

Mayorga-Martinez, C.C., Hlavata, L., Miserere, S., López-Marzo, A., Labuda, J., Pons, J., Merkoçi, A., 2013. Nanostructured CaCO3-poly (ethyleneimine) microparticles for phenol sensing in fluidic microsystem. Electrophoresis 34, 2011-2016.

Mengeaud, V., Josserand, J., Girault, H.H., 2002. Mixing processes in a zigzag microchannel: finite element simulations and optical study. Analytical chemistry 74, 4279-4286.

Nguyen, N.-T., Wu, Z., 2004. Micromixers—a review. Journal of micromechanics and microengineering 15, R1.

Obi, S., Yamamoto, K., Shimizu, N., Kumagaya, S., Masumura, T., Sokabe, T., Asahara, T., Ando, J., 2009. Fluid shear stress induces arterial differentiation of endothelial progenitor cells. Journal of applied physiology 106, 203-211.

Osborn, J.L., Lutz, B., Fu, E., Kauffman, P., Stevens, D.Y., Yager, P., 2010. Microfluidics without pumps: reinventing the T-sensor and H-filter in paper networks. Lab Chip 10, 2659-2665.

Paredes, J., Fink, K.D., Novak, R., Liepmann, D., 2015. Self-anchoring nickel microelectrodes for rapid fabrication of functional thermoplastic microfluidic prototypes. Sensors and Actuators B: Chemical 216, 263-270.

Parisi, J., Liu, Y., Su, L., Lei, Y., 2013. In situ synthesis of vertical 3-D copper-core/carbon-sheath nanowalls in microfluidic devices. Rsc Advances 3, 1388-1396.

Park, J.J., Luo, X., Yi, H., Valentine, T.M., Payne, G.F., Bentley, W.E., Ghodssi, R., Rubloff, G.W., 2006. Chitosan-mediated in situ biomolecule assembly in completely packaged microfluidic devices. Lab Chip 6, 1315-1321.

Park, S.-m., Ahn, J.-Y., Jo, M., Lee, D.-k., Lis, J.T., Craighead, H.G., Kim, S., 2009. Selection and elution of aptamers using nanoporous sol-gel arrays with integrated microheaters. Lab Chip 9, 1206-1212.

Prasek, J., Adamek, M., Hubalek, J., Adam, V., Trnkova, L., Kizek, R., 2006. New hydrodynamic electrochemical arrangement for cadmium ions detection using thick-film chemical sensor electrodes. Sensors 6, 1498-1512.

Pristoupil, T., Kramlová, M., 1968. Microchromatographic separation of ribonucleic acids from proteins on nitrocellulose membranes. Journal of chromatography 32, 769-770.

Qian, J., Lou, X., Zhang, Y., Xiao, Y., Soh, H.T., 2009. Generation of highly specific aptamers via micromagnetic selection. Analytical chemistry 81, 5490-5495.

Rahimi, M., Mikkelsen, S.R., 2011. Cyclic biamperometry at micro-interdigitated electrodes. Analytical chemistry 83, 7555-7559.

Regenberg, B., Krühne, U., Beyer, M., Pedersen, L.H., Simón, M., Thomas, O.R., Nielsen, J., Ahl, T., 2004. Use of laminar flow patterning for miniaturised biochemical assays. Lab Chip 4, 654-657.

Ṙužička, J., Hansen, E., 1975. Flow injection analyses: Part I. A new concept of fast continuous flow analysis. Analytica Chimica Acta 78, 145-157.

Ruzicka, J., Hansen, E.H., 1988. Flow injection analysis. John Wiley & Sons.

Ruzicka, J., Hansen, E.H., 2000. Peer Reviewed: Flow Injection Analysis: From Beaker to Microfluidics. ACS Publications.

Saito, T., Tsujimoto, Y., Miyamoto, Y., Okamoto, N., Kondo, K., 2015. Electrochemical study of multi-component additive behavior during copper electrodeposition with a microfluidic device and an electrochemical quartz crystal microbalance. Japanese Journal of Applied Physics 54, 05EA04.

Sampson, T., 2003. Aptamers and SELEX: the technology. World Patent Information 25, 123-129.

Sansuk, S., Bitziou, E., Joseph, M.B., Covington, J.A., Boutelle, M.G., Unwin, P.R., Macpherson, J.V., 2012. Ultrasensitive detection of dopamine using a carbon nanotube network microfluidic flow electrode. Analytical chemistry 85, 163-169.

Sassa, F., Fukuda, J., Suzuki, H., 2008. Microprocessing of liquid plugs for bio/chemical analyses. Analytical chemistry 80, 6206-6213.

Schust, J., Sperl, B., Hollis, A., Mayer, T.U., Berg, T., 2006. Stattic: a small-molecule inhibitor of STAT3 activation and dimerization. Chemistry & biology 13, 1235-1242.

Sen, M., Thomas, S.M., Kim, S., Yeh, J.I., Ferris, R.L., Johnson, J.T., Duvvuri, U., Lee, J., Sahu, N., Joyce, S., 2012. First-in-human trial of a STAT3 decoy oligonucleotide in head and neck tumors: implications for cancer therapy. Cancer discovery 2, 694-705.

Sgrignani, J., Garofalo, M., Matkovic, M., Merulla, J., Catapano, C., Cavalli, A., 2018. Structural biology of STAT3 and its implications for anticancer therapies development. International journal of molecular sciences 19, 1591.

Shim, J.S., Rust, M.J., Ahn, C.H., 2013. A large area nano-gap interdigitated electrode array on a polymer substrate as a disposable nano-biosensor. Journal of Micromechanics and Microengineering 23, 035002.

Shirai, K., Mawatari, K., Kitamori, T., 2014. Extended nanofluidic immunochemical reaction with femtoliter sample volumes. Small 10, 1514-1522.

Shitanda, I., Takamatsu, S., Watanabe, K., Itagaki, M., 2009. Amperometric screen-printed algal biosensor with flow injection analysis system for detection of environmental toxic compounds. Electrochimica Acta 54, 4933-4936.

Skoog, D.A., Holler, F.J., Crouch, S.R., 2017. Principles of instrumental analysis. Cengage learning.

Stillman, B.A., Tonkinson, J.L., 2001. Expression microarray hybridization kinetics depend on length of the immobilized DNA but are independent of immobilization substrate. Analytical Biochemistry 295, 149-157.

Stoltenburg, R., Reinemann, C., Strehlitz, B., 2005. FluMag-SELEX as an advantageous

method for DNA aptamer selection. Analytical and bioanalytical chemistry 383, 83-91.

Stroock, A.D., Dertinger, S.K., Ajdari, A., Mezić, I., Stone, H.A., Whitesides, G.M., 2002. Chaotic mixer for microchannels. Science 295, 647-651.

Sugumar, D., Ismail, A., Ravichandran, M., Aziah, I., Kong, L., 2010. Amplification of SPPS150 and Salmonella typhi DNA with a high throughput oscillating flow polymerase chain reaction device. Biomicrofluidics 4, 024103.

Tadlaoui Hbibi, A., Laguillier, C., Souissi, I., Lesage, D., Le Coquil, S., Cao, A., Metelev, V., Baran-Marszak, F., Fagard, R., 2009. Efficient killing of SW480 colon carcinoma cells by a signal transducer and activator of transcription (STAT) 3 hairpin decoy oligodeoxynucleotide–interference with interferon-γ-STAT1-mediated killing. The FEBS Journal 276, 2505-2515.

Teixeira, M.F., Marcolino-Junior, L., Fatibello-Filho, O., Dockal, E., Bergamini, M.F., 2007. An electrochemical sensor for l-dopa based on oxovanadium-salen thin film electrode applied flow injection system. Sensors and Actuators B: Chemical 122, 549-555.

Trantidou, T., Friddin, M., Salehi-Reyhani, A., Ces, O., Elani, Y., 2018. Droplet microfluidics for the construction of compartmentalised model membranes. Lab Chip 18, 2488-2509.

Wang, C.-Y., Wu, C.-Y., Hung, T.-C., Wong, C.-H., Chen, C.-H., 2014a. Sequence-constructive SELEX: A new strategy for screening DNA aptamer binding to Globo H. Biochemical and biophysical research communications 452, 484-489.

Wang, J., Gong, Q., Maheshwari, N., Eisenstein, M., Arcila, M.L., Kosik, K.S., Soh, H.T., 2014b. Particle Display: A Quantitative Screening Method for Generating High-Affinity Aptamers. Angewandte Chemie International Edition 53, 4796-4801.

Wang, Y., He, Q., Dong, Y., Chen, H., 2010. In-channel modification of biosensor electrodes integrated on a polycarbonate microfluidic chip for micro flow-injection amperometric determination of glucose. Sensors and Actuators B: Chemical 145, 553-560.

Wang, Y., Liu, Y., Cheng, Y., Kim, E., Rubloff, G.W., Bentley, W.E., Payne, G.F., 2011. Coupling Electrodeposition with Layer-by-Layer Assembly to Address Proteins within Microfluidic Channels. Advanced Materials 23, 5817-5821.

Wang, Y., Ye, Z., Ping, J., Jing, S., Ying, Y., 2014c. Development of an aptamer-based impedimetric bioassay using microfluidic system and magnetic separation for protein detection. Biosensors and Bioelectronics 59, 106-111.

Wang, Z., He, L., Lv, J., Kimura, M., 2019. Electrodeposition of thin chitosan membrane in freestanding SU-8 microfluidic channel for molecular addressing by capillary effect. Materials Research Express.

Wei, C.-W., Cheng, J.-Y., Huang, C.-T., Yen, M.-H., Young, T.-H., 2005. Using a

microfluidic device for 1 μl DNA microarray hybridization in 500 s. Nucleic acids research 33, e78-e78.

Weng, C.-H., Huang, C.-J., Lee, G.-B., 2012. Screening of aptamers on microfluidic systems for clinical applications. Sensors 12, 9514-9529.

Wheeler, E., Benett, W., Stratton, P., Richards, J., Chen, A., Christian, A., Ness, K., Ortega, J., Li, L., Weisgraber, T., 2004. Convectively driven polymerase chain reaction thermal cycler. Analytical Chemistry 76, 4011-4016.

White, H.S., McKelvey, K., 2018. Redox cycling in nanogap electrochemical cells. Current Opinion in Electrochemistry 7, 48-53.

Williams, R., Peisajovich, S.G., Miller, O.J., Magdassi, S., Tawfik, D.S., Griffiths, A.D., 2006. Amplification of complex gene libraries by emulsion PCR. Nature methods 3, 545.

Wisitsoraat, A., Sritongkham, P., Karuwan, C., Phokharatkul, D., Maturos, T., Tuantranont, A., 2010. Fast cholesterol detection using flow injection microfluidic device with functionalized carbon nanotubes based electrochemical sensor. Biosensors and Bioelectronics 26, 1514-1520.

Wu, J., Tang, J., Dai, Z., Yan, F., Ju, H., El Murr, N., 2006. A disposable electrochemical immunosensor for flow injection immunoassay of carcinoembryonic antigen. Biosensors and Bioelectronics 22, 102-108.

Xu, W., Sandford, R.C., Worsfold, P.J., Carlton, A., Hanrahan, G., 2005. Flow injection techniques in aquatic environmental analysis: Recent applications and technological advances. Critical reviews in analytical chemistry 35, 237-246.

Yamamoto, K., Takahashi, T., Asahara, T., Ohura, N., Sokabe, T., Kamiya, A., Ando, J., 2003. Proliferation, differentiation, and tube formation by endothelial progenitor cells in response to shear stress. Journal of Applied Physiology 95, 2081-2088.

Yang, D.-K., Chen, L.-C., Lee, M.-Y., Hsu, C.-H., Chen, C.-S., 2014. Selection of aptamers for fluorescent detection of alpha-methylacyl-CoA racemase by single-bead SELEX. Biosensors and Bioelectronics 62, 106-112.

Yang, S.-Y., Lien, K.-Y., Huang, K.-J., Lei, H.-Y., Lee, G.-B., 2008. Micro flow cytometry utilizing a magnetic bead-based immunoassay for rapid virus detection. Biosensors and Bioelectronics 24, 855-862.

Zou, Z., Jang, A., MacKnight, E., Wu, P.-M., Do, J., Bishop, P.L., Ahn, C.H., 2008. Environmentally friendly disposable sensors with microfabricated on-chip planar bismuth electrode for in situ heavy metal ions measurement. Sensors and Actuators B: Chemical 134, 18-24.

Appendix

● The sequences of STAT3-specific aptamers

Name	Sequence (5'-3')
S102	TCCCTACGGCGCTAACCGGGGTGATGGGCCGACCGATACGTCCTGAGCCACCGTGCTACAA
S204	TCCCTACGGCGCTAACTATACTACTGCAGCCACCACTTTGCTCGGAGCCACCGTGCTACAA
S206	TCCCTACGGCGCTAACAGTACTAAAACGGTGATGGGGGGCCCTCTGGCCACCGTGCTACAA
S213	TCCCTACGGCGCTAACGGACTACCGAAACGATGGGAGGGAATGTCTCGCCACCGTGCTACAA
S216	TCCCTACGGCGCTAACCCCCTATGCAAGTCCCAGATCCGCGGTGAGGCCACCGTGCTACAA
S304	TCCCTACGGCGCTAACTGTAGCTTTTCCGACTGTTGCTACGACGATGCCACCGTGCTACAA

● Immuno-qPCR assay for measuring the STAT3 aptamer affinity
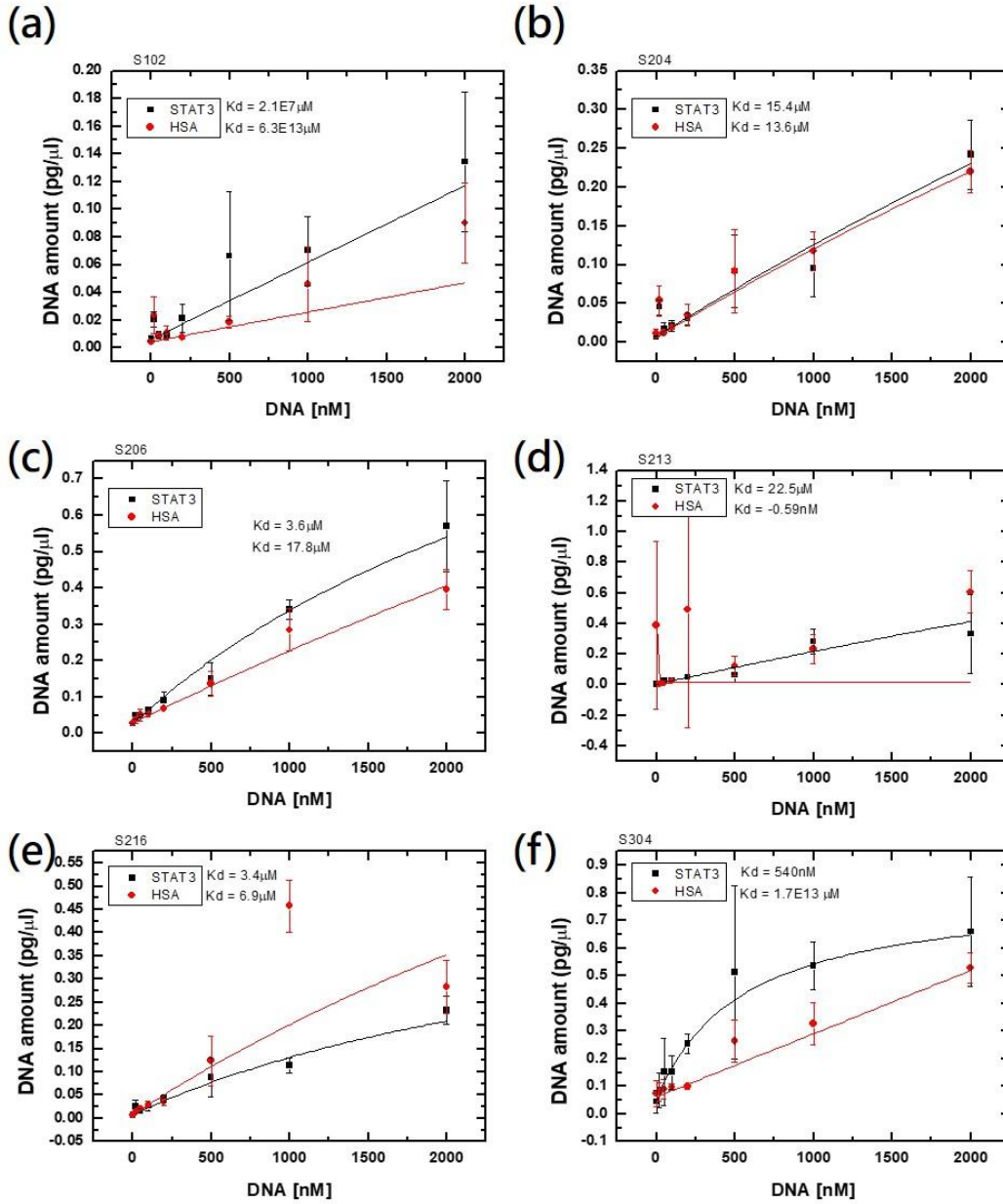
- Calculation of diffusion constants according to cyclic voltammetry

According to the Randles–Sevcik equation, the peak current (i_p) is not only related to the concentration of redox mediator but also corresponded to the scan rate in the cyclic voltammetry. Using ferro-/ferri-cyanide couple as the example, the square roots of the scan rate are plotted across the x-axis and its corresponding current peaks are plotted on the y-axis, and the slopes of the fitting curves can be used to calculate the diffusion constant. The original Randles–Sevcik equation is described as below.

$$i_p = 0.4463nFAC(\frac{nFvD}{RT})^{\frac{1}{2}}$$

Ip : current maximum (A)
n : number of electrons transferred in the redox event
A : electrode area (cm^2)
D : diffusion constant (cm^2/s)
C : concentration (mol/cm^3)
v : scan rate (V/s)
R : gas constant (J/K・mol)
T : temperature (K)
F : Faraday constant (C/mol)

If the experiments are executed with 5 mM (=5×10^{-6} mol/cm^3) ferro-/ferri-cyanide solution (n = 1) at 25°C, the equation can be simplified as below.

$$i_p = 1.343AD^{\frac{1}{2}}v^{\frac{1}{2}}$$

The slopes of fitting curves obtained from the plots of i_p and $v^{1/2}$ can be depicted:

$$m = 1.343AD^{\frac{1}{2}}$$

Hence, diffusion constants can be calculated:

$$D = \frac{m^2}{1.8A^2}$$

- Calculation of the Reynolds number (Re)

The Reynolds number is defined as the ratio of inertial forces to viscous forces.

$$Re = \frac{\rho V D}{\mu} = \frac{\rho Q D}{\mu A}$$

ρ : density of the liquid (kg/m^3)
V : velocity of the fluid (m/s)
D : characteristic linear dimension (m)
μ : dynamic viscosity of the fluid (Pa·s or N·s/m^2)
Q : volume flow rate of the liquid (m^3/s)
A : Cross-sectional area (m^2)

If the cross-section is rectangular, the hydraulic diameter of the pipe (D$_H$) can be modified:

$$D_H = \frac{4A}{P} = \frac{4ab}{2(a+b)} = \frac{2ab}{a+b}$$

where P is the perimeter of cross-section, a and b are width and length of the rectangle.

If the liquids are aqueous solutions, the density and viscosity can be 1000 kg/m^3 and 8.94x10^{-4} Pa·s.

$$Re = \frac{\rho Q D}{\mu A} = \frac{1000 \times Q(m^3/s) \times 4}{8.9 \times 10^{-4} \times P(m)} = 0.0745 \times \frac{Q(\mu l/min)}{P(mm)}$$

250
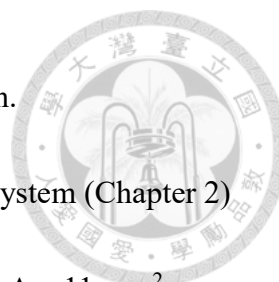
- The tables of the flow-operating parameters used in this research.

One-way flow and shuttle flow controlled by the home-made pump system (Chapter 2)

In PMMA channel-based reactor: a = 5.5 mm, b = 2 mm, P = 15 mm, A = 11 mm^2

Input	Measured flow rate (µl/min)	Calculated flow velocity (mm/s)	Re
5 V	474	0.72	2.35
6 V	825	1.25	4.10
7 V	825	1.25	4.10
8 V	1,155	1.75	5.74
9 V	1,155	1.75	5.74
10 V	1,444	2.19	7.17
11 V	1,914	2.90	9.51
12 V	1,932	2.93	9.60
14 V	2,300	3.48	11.42

In the peristaltic pipe: P = 3.6 mm, A = 1.04 mm^2

Input	Calculated flow rate (µl/min)	Measured flow velocity (mm/s)	Re
5 rpm	418.1	6.7	8.65
10 rpm	842.4	13.5	17.4
20 rpm	1,684.8	27	34.8
40 rpm	3,307.2	53	68.4
80 rpm	6,533.3	104.7	135.2
100 rpm	8,161.9	130.8	168.9
150 rpm	11,001.1	176.3	227.6

In the PDMS chip: P = 3.2 mm, A = 0.15 mm^2

Input	Known flow rate (µl/min)	Calculated flow velocity (mm/s)	Re
5 rpm	418.1	46.4	9.73
10 rpm	842.4	93.6	19.6
20 rpm	1,684.8	187.2	39.22
40 rpm	3,307.2	367.5	77.0
80 rpm	6,533.3	725.9	152.1
100 rpm	8,161.9	906.9	190.0
150 rpm	11,001.1	1,222.3	256.1
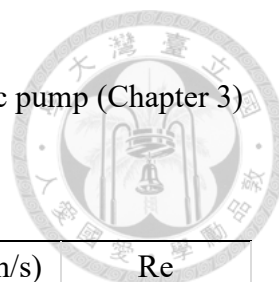
One-way flow and shuttle flow controlled by a commercial peristaltic pump (Chapter 3)

In the microbeads-array chip: P = 2.8 mm, A = 0.4 mm^2

Input	Set flow rate (μl/min)	Calculated flow velocity (mm/s)	Re
Scale 8	1,920	80	51.1
Scale 6	1,760	73.3	46.8
Scale 4	1,240	51.6	33.0

One-way flow and shuttle flow controlled by a commercial syringe pump (Chapter 4, 5)

In the microbeads-array chip: P = 5.4 mm, A = 0.26 mm^2

Input	Set flow rate (μl/min)	Calculated flow velocity (mm/s)	Re
10 μl/min	10	0.64	0.14
20 μl/min	20	1.28	0.28
40 μl/min	40	2.56	0.56
80 μl/min	80	5.12	1.10
150 μl/min	150	9.62	2.07